STIFFNESS AND ANISOTROPY CHARACTERIZATION OF MECHANICALLY-COMPRESSED COHESIVE SOILS USING DIRECTIONAL WAVE PROPAGATION

A dissertation

submitted by

Deniz Ranjpour

in partial fulfillment of the requirements

for the degree of

Doctor of Philosophy

in

Civil and Environmental Engineering

TUFTS UNIVERSITY

July 2020

Adviser: Dr. John T. Germaine

Abstract

Compressional and shear wave velocity (V_p and V_s) measurement is a powerful tool to study material behavior including elastic stiffness. The elastic stiffness and stress-velocity-porosity characterization can facilitate safer well designs and improve seismic imaging interpretations. Also, the nondestructive nature of wave velocity measurements makes it possible to assess the characteristics of the same specimen as it is deformed over a significant stress range. This research focuses on the high porosity clay, transitioning into low porosity mudrocks, under pressure.

Naturally occurring cohesive soil deposits are inherently anisotropic, most often transversely isotropic (TI). A novel directional velocity measurement technology was designed and fabricated using piezoelectric elements, allowing for meaurements of V_p in three and V_s in two directions. The velocities were measured on resedimented specimens, deforming (up to 25% axial strain) under K_0-consolidation (vertical effective stress (σ'_v) =1-10 MPa) in a triaxial cell. The triaxial P-wave velocities increased by nearly 300 m/s (+17%) while the S-wave velocities increased by 350 m/s (+250%). The measured velocities were used to calculate the TI stiffness and compliance matrices, which were in turn used to calculate the elastic stiffness parameters at different stress levels. The results showed very low P and S anisotropy (<0.1) in resedimented Gulf of Mexico-Eugene Island (RGoM-EI) and not much anisotropy change over the 9 MPa increase in σ'_v.

Another point of interest in this research was the wave velocity behavior in high porosity material (0.25-0.45 porosity) under high pressures (10 MPa $< \sigma'_v$). A second testing setup was developed for this purpose (TCRS) which was used to run K_0-consolidation (σ'_v =1-25 MPa) tests on resedimented specimens. Vertical V_p and V_s were measured throughout these tests, expanding the vertical velocity measurement range (1-10 MPa) on deformable material by 2.5 times. The TCRS results showed a 450 m/s (+26%) increase in the P-wave velocity and 550 to 600 m/s (+283% to +300%) increase in the S-wave velocities, depending on the material.

Finally, the velocity measurements were compared to in-house and published data, suggesting an increasing velocity trend with decreasing porosity over 1-100 MPa vertical effective stress. Also, the anisotropy results were compared to some published data, pointing out the anisotropy dependency on porosity and velocity ratios.

Acknowledgements

The past five years and this research would not have been possible without the love and support of so many people, a handful of which I would like to mention here.

I feel extremely blessed to have had Prof. Jack Germaine, better known as Dr. G among his students, as a mentor and academic advisor. His vast array of knowledge has pushed me to keep asking why and to try to "expand my horizons", as he likes to call it. More importantly, his humorous and caring personality has certainly made the intense PhD work an enjoyable experience. I will be forever grateful to him.

I would like to thank the rest of my committee including Prof. Laurie Baise, Dr. Keith Katahara and Prof. Robert White for their invaluable advice and constructive feedback. I am also grateful to Dr. Richard (Dick) Plumb for his always fresh academic point of view, constant encouragement and heartfelt emails over the past few years.

I was supported by the GeoFluids consortium, both financially and academically. I thank Dr. Peter Flemings and Dr. Maria Nikolinakou and the rest of the UT GeoFluids Austin team. Dr. Lucy Jen has also been an amazing resource and a great female role model in an otherwise male-dominated field.

Some of the parts and equipment used in this research were fabricated by Mr. Steve Rudolph at MIT, for which I am thankful.

Special thanks go to my Tufts friends that have come and gone over the years, leaving an abundance of fond memories. Special acknowledgments must go to the people with whom I have shared the lab space, as well as numerous meals and drinks: Tony, Jana, Liz, Amanda, Liam, Mark, Chunwei, Jim, Stephen and Nick. I cannot leave out my other Tufts friends Jason, Tiffany, Marshall, Parker, Amy, Sofia, Karin and Gabrielle. Outside of Tufts, I owe a big thank you to my friends Amer and Maha (and their bundle of joy, Rami) for being my family in the US.

I would like to thank my family, Elnaz and Ali, for being my rock, for their unconditional love and for getting me where I am. Lastly, I would like to thank John, for making my life so much better with his love and understanding, and for making this pandemic bearable for me over the past few months.

Contents

List of Tables

List of Figures

Stiffness and Anisotropy Characterization of Mechanically-Compressed Cohesive Soils Using Directional Wave Propagation

Chapter 1

Intodcution

1.1 Problem Statement

Soil stiffness properties have been mostly studied in two independent categories. Geotechnical engineers have focused on "clays", or sands which are fundamentally different and will not be included in this study, and geologist and rock mechanics experts have studied "rocks". The clay category consists mainly of high porosity, deformable material under low pressure (<1 MPa), whereas rocks are lithified, low porosity, non-deformable materials tested under higher pressures. There has been a lack of study focusing on the high porosity material, clay, transitioning into low porosity material, under pressure. The higher the applied pressure on a drained clay specimen gets, the closer the material gets to what is considered a mudrock. The velocities depend on the elastic stiffness of the materials, thus rendering velocities a useful parameter in the stiffness characterization of soils. Velocity measurements, both in-situ and in a laboratory, have also been performed in one of the two distinctive categories, clay or rock, making velocity measurements during the clay to rock transitional phase highly desirable. Another characteristic that has been largely overlooked in clays is anisotropy. Truly isotropic soil behavior is hard to come by in nature, if not impossible. Velocity (or seismic) anisotropy is in fact dependent on the elastic properties in each direction. For deep depositional soil layers where attaining an intact sample and running tests in a lab is hard if at all possible, velocity measurements and methods such as seismic imaging are desirable, especially by the oil and gas industry. While many researchers have tried to understand the directional dependence of stiffness properties in rocks by measuring velocities in more than one direction (usually perpendicular to bedding), the same level of effort has been missing from the geotechnical realm for the most part.

With an understanding of how the elastic stiffness of clays varies as a function of stress level, direction, soil type, and loading conditions, the small strain stiffness behavior can be predicted, with applications to subsurface construction projects. Furthermore, the stress-velocity-porosity characterization can facilitate safer well designs and improve seismic imaging interpretations.

This research focuses on developing velocity measurement technologies that can help: 1) expand the stress level at which the velocities are measured on clay specimens as much as possible to connect the high and low porosity behavior, 2) measure velocities in different directions to understand anisotropy and calculate the full stiffness matrix. The aim of this work will be to study directional compressional (P) and shear (S) waves propagating through resedimented Gulf of Mexico-Eugene Island and Boston Blue Clay, under medium-high pressures.

1.2 Scope and Objectives

This research will focus on two major goals, understanding the wave velocity behavior in clays in medium-high pressure stress span, and understanding the directional component of wave velocity behavior resulting from the material anisotropy. All tests will be performed on resedimented specimens.

The most important objective of this study is to develop the technology to measure directional compressional and shear velocities in resedimented clay specimens that are deforming under K_0 consolidation in a medium pressure triaxial cell. Several challenges lie ahead, most important of which is the electronic setup, as generating and receiving interpretable signals in three directions while keeping the specimen isolated from the surrounding chamber oil is a crucial part of the process. Another important step is specimen preparation protocol, to generate repeatable results. Results from directional velocity measurements can then be used to calculate full TI stiffness matrices of the same specimen at various stress levels, as well as to understand anisotropic behavior of certain resedimented materials.

Another major objective of the work in hand is developing a testing setup and

process where the existing piezoceramic technology can be used to measure vertical velocities in higher stress levels. These experiments can help close the gap between high and low porosity material velocity behaviors.

Lastly, this research will compare the testing results to the previous in-house (tests performed in Dr. Germaine's lab on the same materials by various researchers) and other similar published results, in an attempt to verify the accuracy of the newly developed technology.

This work is part of the UT Geofluids Consortium, populated with members from Tufts University and UT Austin. This consortium provides a wide breadth of data on all the materials tested in this research, focusing on the "evolution of pressure, stress, deformation and fluid migration through experiment, models, and field study".

1.3 Organization of Thesis

The content of this research is as follows:

Chapter 2 includes the motivations behind this research. It also includes the groundwork for this study laid out by other researchers. An extensive background on elastic stiffnesses and various studies on measurement methods is provided. Also, some previous works on velocity measurements and velocity anisotropy are discussed. Moreover, a summary of clay microstructure and its implications on compression behavior and anisotropy is provided. Finally, the effects of attenuation and dispersion, as well as input frequency on signal and velocity behavior are investigated.

Chapter 3 discusses the materials tested in this research by introducing the origins of the source materials, as well as providing their index properties such as chemical composition, gradation and Atterberg limits. Next, the resedimentation method used to make the specimens is explained from drying and grinding the source material to incremental loading and extrusion.

Chapter 4 describes the apparatus and procedures in detail. It includes the details of triaxial and Tall Constant Rate of Strain (TCRS) testing setups, control

and data acquisition systems, as well as the wave propagation electronics. There is also a comprehensive discussion on the design and fabrication of the new directional velocity measurement technology.

Next, in Chapter 5, signal interpretation and the most important factors, propagation direction, testing setup and tested material, affecting the waveforms are explained. The chapter also includes the reasoning and methodology behind vertical effective stress corrections for the excess pore fluid pressure and sidewall friction.

Chapter 6 is arguably the most important and data heavy chapter of this thesis. First the compression behavior of the tested materials is studied, and the compression curves are compared to similar curves produced by other researchers on the same materials. Next, the velocity data and their trends are presented as a function of stress and density. Also, a repeatability analysis investigating the quality of the experimental results is provided. After that, the isotropic and anisotropic elastic stiffness parameters are shown and compared, and the anisotropy parameters (Thomsen's parameters) are presented. Finally, the velocity and elastic anisotropy parameters produced in this research are compared to various other in-house and published data.

Chapter 7 is a summary of the purpose of this study, as well as the conclusions. It ends with some ideas that could be helpful in guiding other researchers to continue the work on the topic.

Chapter 2

Background

The elastic properties of deformable material are important in both geological and geotechnical practices. The stiffness behavior of soils and rocks has been extensively tested using many different techniques. Soft soils have been tested using both destructive and nondestructive methods, including triaxial, torsional shear, resonant column and bender element testing. Alternatively, hard materials such as rocks have been tested using piezoelectric transducers as well. The geotechnical field has mostly tested soft clay (porosity (n) >0.45), low-stress regime (σ'_v <1 MPa) , while the geophysics field has tested the hard clay (n <0.25), high-stress regime (10 MPa < σ'_v). Although there are some studies that have compared different testing techniques, such as Brignoli et al. [21], Abdulhadi and Barghouthi [1] and Valle-Molina [162], there have been no studies that bridge the two fields and cover a wide range of stresses (0.1 < σ'_v <100 MPa).

Naturally occurring cohesive soil deposits are inherently anisotropic. This anisotropy is primarily due to the process of sedimentation followed by predominantly one-dimensional consolidation. Also, studies on clays have shown that platy clay particles tend to become perpendicularly oriented with respect to the major principal stress during one dimensional consolidation ([110], [14], [13] and [131]). The strain-induced component of anisotropy is often incorrectly confused with the stress- induced component, but, for example, an overconsolidated natural clay might currently be under an isotropic stress state while having anisotropic properties that are related to its one-dimensional strain history [82].

As a result, soil characteristics can be significantly different in various directions. Much research has been done on the effect of anisotropy on soil properties such as permeability [102], slope stability [6] and strength [108]. This chapter aims to introduce various velocity measurement technologies, elastic properties and stiffness

measurements, and material anisotropy.

2.1 Motivation

Nondestructive nature of wave velocity measurements makes it possible to assess the characteristics of the same specimen as it is deformed over a significant stress range, as opposed to a destructive test providing one data point for each specimen. The resulting stress-velocity-porosity characterization can directly facilitate safer borehole designs, improve interpretation of geophysical surveys, constrain in-situ pore pressure predictions, and improve seismic imaging interpretations. Velocity measurements have been a key component in understanding soil behavior under various loading conditions and histories, hence assisting geologists in predicting the structure and composition of rocks in the Earth. Seismic imaging techniques enable a rather detailed subsurface characterization based on multiple wave sources and many staggered acoustic receivers or geophones. The interpretation of the signals acquired by receivers can be greatly altered with an incorrect interpretation or assumption, such as an incorrect V_p/V_s ratio, or not accounting for anisotropy. In fact, the relation of V_p and V_s can be used as an indicator of hydrocarbon saturation [28] or overpressure [129]. An important portion of the interpretations and assumptions used for in-situ data comes from the laboratory test results on either intact or resedimented specimens. In a laboratory setting we have much higher control over the testing conditions and parameters as well as much higher accuracy in measurements. Historically, different velocity measurement technologies (bender elements, piezoelectric elements, etc) have been used on specimens tested in various laboratory testing conditions (hydrostatic or 1-D, drained or undrained, etc). Most bender element tests cover a limited stress range of up to 400 kPa, which is relatively low, and only measure the shear wave velocity. Piezoelectric elements do provide both shear and compressional signals and velocities under higher pressures, but almost all velocity measurements under high pressure testing conditions are performed on low porosity rocks, with a negligible amount of plastic deformation during compression.

Marjanovic [103], however, measured vertical P and S velocities in one dimensionally consolidated triaxial specimens under vertical effective stresses up to 10 MPa, providing the foundation for this research.

Moreover, directional velocity measurements can be used in computing elastic stiffness moduli and stiffness matrix. Depending on the material type, a different number of velocity measurements are needed for stiffness matrix determination. For example, sedimentary deposits are by nature Transverse Isotropic (TI) with the vertical axis as axis of symmetry. The resedimentation process used in this study (explained in Chapter 3) simulates natural sedimentation process, producing TI materials. Five independent velocities, vertical P and S, horizontal P and S, and one inclined P with θ angle are needed to determine the stiffness matrix for TI material. Most of the previous research on velocity anisotropy has focused on rocks ([80], [168], [79]), with porosity ranging from 0.01 to 0.16, and have mostly ignored anisotropy in materials plastically deforming and transitioning from high porosity to low porosity with increasing stresses.

This study focuses on high porosity ($n > 0.5$) and deformable resedimented clay specimens and tries to shed light on two problems, velocity anisotropy under medium pressure (1-10 MPa), evolution of elastic parameters during K_0-consolidation (1-10 MPa), and the behavior of vertical velocities in specimens under higher pressures (1-30 MPa).

2.2 Elastic Moduli and Material Anisotropy

Wave velocity measurements are nondestructive , hence the specimen can be tested continuously over a wide stress range while plastically deforming, whereas a destructive test usually provides only one data point at a single stress level. The peizoelectric transducers used in this study propagate and measure both the S-wave and the compressional wave (P-wave). The strains induced by wave propagation are within very small strain range ($\epsilon < 0.0001\%$), the measured properties are linear elastic as a result.

This research encompasses test results obtained from two stress regimes: medium (triaxial), and high (Tall Constant Rate of Strain (TCRS)). These ranges correspond to 1 - 10 MPa, and 1- 30 MPa respectively. The focus of this work is on directional measurements in medium stress range and uninterrupted vertical velocity measurements in specimens under low to high stresses. Both the medium and high stress regimes use piezoelectric transducers, which are described in Section 4.4, to measure P and S-waves.

In the laboratory, pulses are applied at the boundary of the specimen and are detected using transducers of a finite size. The compressional and shear waves are body waves since they propagate inside the specimens. The wavelength (λ) is also an important factor when it comes to the wave type, especially relative to the transducer and specimen dimensions. In an ideal situation, the wavelengths are small compared to the transducer dimensions, which are in turn smaller than the specimen dimensions. This is when the waves are collimated at the source and propagate through the specimen as a plane wave, without interference from boundary effects. In this research, the wavelength range is $\lambda = 1 - 1.8$ cm for P-waves and $\lambda = 1 - 8$ cm for S-waves, whereas the specimen diameter is 3.5 cm and the transducer dimensions are 1×1 cm, so it may not exactly satisfy the plane wave requirements. Nonetheless, plane waves will be assumed here. To the extent the measured ultrasonic modes are not plane waves, the velocities may be a little too slow.

The V_s measurements are used to calculate the shear modulus (G), depending on the propagation direction of the shear signal, when the bulk density of the material (ρ) is known. Relative to the P-wave, the velocity is controlled by the stiffness of the material in the direction of propagation. For solids this will depend on the lateral constraint. If the deformation is one dimensional (zero lateral deformation) the velocity is controlled by the constrained modulus (M). If the lateral deformation is unconstrained (constant lateral stress) the velocity is controlled by Young's modulus (E). These two conditions represent the upper and lower limits. Laboratory triaxial experiments are conventionally interpreted to give M.

Elastic moduli for linearly elastic and isotropic material are computed using well

established equations. G is calculated using the shear wave velocity and the bulk density (ρ):

$$G = \rho \times V_s^2 \tag{2.1}$$

P-wave velocity on the other hand provides the constrained modulus (M):

$$M = \rho \times V_p^2 \tag{2.2}$$

While the constrained modulus is directly calculated from the compressional velocity, the more commonly used modulus to describe the behavior of materials is the bulk modulus (K) [112]. K can be calculated using the following relationship:

$$K = M - \frac{4G}{3} \tag{2.3}$$

All the elastic parameters, including the moduli and Poisson's ratio, are related to each other. More extensive derivations can be seen in Stein and Wysession [152],but the final versions can be seen as follows:

$$G = \frac{E}{2(1+\nu)} \tag{2.4}$$

$$\nu = \frac{M - 2G}{2M - 2G} \tag{2.5}$$

$$E = \frac{G(3M - 4G)}{M - G} \tag{2.6}$$

where ν is Poisson's ratio and E is Young's modulus.

Although these equations are commonly used in the geotechnical field, truly isotropic soils are pretty rare. The materials tested in this study are Transverse Isotropic (TI), which is a result of depositional nature of most soil bodies, including resedimented samples. The vertical axis in these materials are usually (but not

always) the axis of symmetry and the material is isotropic in the plane normal to the symmetry axis, as shown in Figure 2.1

The elastic equations explained above do not apply to anisotropic material, including TI. A symmetrical matrix with five independent parameters (C_{11}, C_{33}, C_{44}, C_{66} and C_{13}) represents the stiffness behavior in TI material. Thomsen's [158] method is used to determine each of the elements in the stiffness matrix shown in Figure 2.2 using the five independent velocities (Vertical P (V_{pv}), Vertical S (V_{sv}), (Horizontal P (V_{ph}), Horizontal S (V_{sh}), which propagates horizontally and is polarized horizontally, and Inclined P ($V_{p(\phi)}$), shown in Figure 2.3), the angle at which the inclined velocity was measured with respect to the vertical axis(ϕ) and the bulk density (ρ). The C_{ij} parameters can then in turn be used to calculated the elastic moduli for TI material. But before, the one intermediate step is converting the measured inclined velocity and angle ($V_{p(\phi)}$ and ϕ) to the phase velocity and angle ($V_{P(\theta)}$ and θ) using Byun's [23] method, as Thomsen's equations use the inclined phase velocity.

The Group or Ray velocity is the velocity of propagation of particle disturbance or the energy propagation. Phase velocity on the other hand is the velocity of a single particle, or the speed at which the wave surface is expanding. The group and phase velocities are equal in directions parallel and perpendicular to bedding, since the ray is normal to the wave surface. The relationship between the group and phase velocity is discussed in Postma [127]. Figure 2.4 illustrates the following relationships graphically. Byun [23] parameters are used to calculate the compressional phase velocities and angles from the measured group velocities.

$$\tan(\phi - \theta) = \frac{1}{V(\theta)} \frac{d\nu(\theta)}{d\theta} \tag{2.7}$$

$$V^2_{(\phi)} = V^2_{(\theta)} + \left(\frac{d\nu(\theta)}{d\theta} \right)^2 \tag{2.8}$$

Once the compressional inclined phase velocity and angle are determined, C_{ij} elements are calculated. Thomsen gives both exact and approximate weak anisotropy

equations, the details of which can be found in Thomsen's "Weak Elastic Anisotropy" [158]. The exact equations were used in this study.

The stiffness matrix can then be inverted to determine the compliance matrix (S_{ij}) (Figure 2.5) [51], the elements of which are used to calculate the Young's moduli in TI material:

$$E_h = \frac{1}{S_{11}} = \frac{1}{S_{22}} \tag{2.9}$$

$$E_v = \frac{1}{S_{33}} \tag{2.10}$$

$$\nu_{hh} = \frac{-S_{12}}{S_{11}} \tag{2.11}$$

$$\nu_{vh} = \frac{-S_{13}}{S_{33}} \tag{2.12}$$

$$G_{hh} = \frac{1}{2S_{55}} = \frac{1}{2S_{66}} \tag{2.13}$$

$$G_{vh} = \frac{1}{2S_{44}} \tag{2.14}$$

It is also possible to generate the directional dependence of both shear and compressional velocities using the stiffness matrix [32].

$$\rho V_p^2(\theta) = \frac{1}{2}[C_{33} + C_{44} + (C_{11} - C_{33})\sin^2\theta + D(\theta)] \tag{2.15}$$

$$\rho V_{sv}^2(\theta) = \frac{1}{2}[C_{33} + C_{44} + (C_{11} - C_{33})\sin^2\theta - D(\theta)] \tag{2.16}$$

and

$$\rho V_{sh}^2(\theta) = C_{66}\sin^2\theta + C_{44}\cos^2\theta \tag{2.17}$$

where

$$D(\theta) = ((C_{33} - C_{44})^2 + 2\left(2(C_{13} + C_{44})^2 - (C_{33} - C_{44})(C_{11} + C_{33} - 2C_{44})\right)\sin^2\theta + \left((C_{11} + C_{33} - 2C_{44})^2 - 4(C_{13} + C_{44})^2\right)\sin^4\theta)^{\frac{1}{2}} \quad (2.18)$$

2.3 Previous Studies Measuring Wave Velocities Using Various Technologies

The most common technology for laboratory velocity measurement is based on Piezoelectric elements. Much research has been done to investigate the properties of relatively rigid rocks using the piezoelectric technology. Most of these studies have been performed on cylindrical rock samples (0.1 < n), where velocities are predominantly measured in the axial direction and the pore and confining pressures are controlled. When a piezoelectric element is electrically stressed by a voltage, its dimensions change. When it is mechanically stressed by a force, it generates an electric charge. When the electrodes are isolated, a voltage associated with the charge appears. A piezoelectric element is therefore capable of acting as either a sensing or transmitting element. Depending upon the configuration and polarity, these elements will behave differently, changing in shape, dimension or both. Piezoelectric elements include Bender Elements, Extender Elements and Shear Plates. The most appropriate element for each testing condition should be chosen based on stress level, material type and stiffness, as well as electronic layout and limitations.

Much research has been done to investigate the properties of relatively rigid rocks using the piezoelectric technology, some of which will be discussed in this section. Hughes [71] introduced quartz crystals and the pulse technique for velocity measurement in metal rods in 1949. Hughes and Cross [72] measured elastic dilatational (compressional) and torsional velocities in rocks using the pulse technique, showing

an increase in the velocities with confining pressure (Figure 2.6).

Wyllie et al. [180] used piezoelectric elements to measure longitudinal (compressional) velocities in brine-oil and brine-gas saturatied samples of natural sedimentary rock and compared their laboratory test results to Gassmann model [50] (Figure 2.7).

Winkler and Nur [176] measured attenuation of compressional and shear waves in sandstones and shales using piezoelectric elements built into caps and directly bonded to the specimen showing that attenuation is much more sensitive to changes in rock properties than is velocity. They studied the effects of strain amplitude, confining pressure, pore pressure, and degree of water saturation. Their results suggested that pore fluids dominate attenuation in the upper part of the earth's crust, S-wave attenuation increases with degree of saturation, reaching a maximum at total saturation and P-wave attenuation increases with saturation at low degrees of water saturation and is larger than S-wave attenuation. Finally, they pointed out that the amplitude dependence disappears at low strain amplitudes and is strongly inhibited by moderate confining pressures.

Hovem [69] studied the wave propagation in layered media to determine how the media structure and properties influence the velocity. He also mathematically showed that for wavelengths long compared to the dimension of the layer, the medium behaves as a homogenous material with compressibility and density given as the weighted averages of the compressibility and density of the constituents. Wulff et al. [179] carried out uniaxial compression tests of sandstone and granite to evaluate the influence of increasing microfracture on wave attenuation and used wave velocities to assess the damage parameter. A common measure for attenuation is the inverse of the quality factor (Q) related to the attenuation coefficient α by:

$$\frac{1}{Q} = \frac{\alpha V}{\pi f} \tag{2.19}$$

(e.g. Toksöz et al. [159]) where f is the wave frequency and V is the velocity.

Wulff et al. [179] presented their data on multiple sandstone samples. Figure 2.8 is an example of their velocity and attenuation data for P and S-waves with

increasing uniaxial strain for a main frequency of 400 kHz.

Pellet and Fabre [123] used P-wave velocity measurements to monitor damage evolution during uniaxial strain in controlled compression tests and long-term creep tests. Darot and Reuschle [33] measured the P-wave velocity of cracked granite under different confining pressures and pore pressures to interpret the relationship between crack behavior evolution and imposed pressures. They concluded that the increase in acoustic velocities and decrease in permeability are both results of crack closure in the damaged rock. Adam [3] investigated the variation of wave velocity to reflect the change of rock microstructure caused by the action of carbon dioxide and water. Many researchers have studied the effect of clay content on velocity such as Ayres and Theilen [11], Han et al. [56], Castagna et al. [29] and Tosaya [160], each suggesting a set of equations calculating the velocity using porosity and clay content, some of which will be discussed in Section 2.10.2. The problem with such equations though is that they disregard the depositional environment, pore space evolution and the type of clay.

There is also extensive research and a long history of testing deformable soil specimens where the piezoelectric elements are embedded in platens and protruded into the specimen. Lawrence Jr [92] described one of the first applications of piezoelectric transducers in shear wave testing of soil specimens. Shear plate transducers and a triaxial cell were used in these studies. The transducers were housed in the base pedestal and top cap and used to test clay and sand specimens. An example of his velocity measurements during load, unload and reload of Boston Blue Clay is shown in Figure 2.9. It should be noted that one of the reasons that the literature's focus has been mostly on shear wave velocities is the effect of water on compressional velocities. P-wave velocities in saturated soft materials are dominated by the effect of pore fluid and provide limited information about the soil itself.

A different transducer scheme was developed by Shirley and Anderson [147]. They employed transducers consisting of two transverse-expansion mode piezoelectric elements (benders) that were able to generate and detect shear waves. The bender transducers developed by Shirley and Anderson have been used widely in the

field. Horn [65] measured shear wave velocities in sand and Richardson et al. [133] measured shear wave velocities in marine sediments. Brignoli et al. [21] measured shear wave velocities in soil specimens tested in triaxial cells, using 3 different technologies: Bender elements, shear plate (piezoelectric) transducers and resonant column. This study showed good agreement in S-wave velocities measured in intact offshore clay using different technologies (Figure 2.10). They discussed the near-field effect that dominates the shear signal arrival in some material. This effect will be discussed in more details in Section 5.1.1.

Mondol et al. [112] measured P and S velocities in the two endmember clay minerals, smectite and kaolinite, both dry and brine saturated. They are "end members" in the sense that smectite is the most fine-grained clay found in nature and has a high cation exchange capacity and large surface area (700 m^2/g), while kaolinite is coarser grained and has a much lower cation exchange capacity and smaller surface area (10 m^2/g) compared to other clay minerals. They consolidated their slurries up to a relatively high pressure (50 MPa), and the porosities varied by nearly 25%. Figures 2.11 and 2.12 show the changes in P and S velocities with increasing stress and decreasing porosity. It should be noted that Mondol et al. [112] tested dry and brine saturated clay powders which are not representative of natural sediments. Moreover, they loaded the slurries to 50 MPa in 21 days, which is not enough time to guarantee primary consolidation completion.

Marjanovic [103] developed a new testing setup using piezoelectric elements in a medium pressure triaxial cell and tested a variety of resedimented and intact materials, with different clay composition and plasticity, under K_0 loading and unloading conditions (0-10 MPa). Marjanovic measured P and S velocities perpendicular to the bedding. The specimens underwent significant axial strain, hence changing in porosity (by up to 25%), given the nature of drained consolidation tests. She studied the dependence of vertical P and S velocity behavior on stress level, loading history, plasticity and OCR. She also investigated how the dynamic elastic moduli and velocity ratios (V_p/V_s) varied with stress level. Some of her testing results are shown in Figures 2.13 through Figure 2.20.

The V_p/V_s ratio is widely used to predict soil and rock properties such as saturation, lithology, stress state and elastic moduli. The factors dominating the V_p/V_s ratio are not yet well understood. Some believe that lithology dictates the V_p/V_s behavior [125], while others argue that the pore geometry has a stronger effect on it than the mineral elastic constants and that the inferred link with lithology is rather controlled by the dominant pore sizes and distributions in those respective lithologies [155]. This ratio has been well documented mostly for sands and rocks. Gardner et al. [48] reporting ratios of greater than 2 for water-saturated unconsolidated sands, and less than 2 for consolidated rocks or gas- saturated sands. Zimmer [181] also reported the V_p/V_s ratio as a function of stress for various sands. Fawad et al. [43] showed that for eight different dry sands, the V_p/V_s ratio converges to 1.7 - 1.85 at 50 MPa.

2.4 Velocity Anisotropy

Material anisotropy is an umbrella term describing a material's directional dependence of a physical properties, such as stiffness, deformability, velocity behavior and permeability. Materials where all the physical properties are independent of the direction are called isotropic. The materials tested in this study however are TI or transverse isotropic, the characteristics of which were explained in Section 2.2. Directional velocity measurements have been used by various researchers to understand rock anisotropy and the effects of saturation, stress level, cracks, kerogen and the damage level. It has been shown that velocity anisotropy in rocks tends to increase with kerogen levels and microcrack concentration, but decrease with stress level.

There has been a significant effort in studying velocity anisotropy in sedimentary rocks, especially in low porosity domain ($n<0.1$). Podio et al. [126] measured P and shear wave velocities in 0, 30, 45, 60 and 90 angles between the bedding planes and the propagation direction, in dry and water-saturated Green River shale specimens. Their results showed an increasing trend in velocities with stress level, and the trend varied with direction (Figure 2.21). They also calculated the stiffness matrix

elements (C_{ij}) (Figure 2.22).

Jones and Wang [80] measured P and shear velocities in two Cretaceous shales from two different depths in directions perpendicular and parallel to bedding and showed that both P and S-waves propagate faster parallel to bedding (Figure 2.23).

Thomsen [158] reviewed virtually all published data on velocity anisotropy in sedimentary rocks (sandstone, shale, siltstone, etc) and proposed three parameters quantifying seismic anisotropy:

$$\epsilon = \frac{C_{11} - C_{33}}{2C_{33}} \tag{2.20}$$

$$\gamma = \frac{C_{66} - C_{44}}{2C_{44}} \tag{2.21}$$

$$\delta = \frac{(C_{13} + C_{44})^2 - (C_{33} - C_{44})^2}{2C_{33}(C_{33} - C_{44})} \tag{2.22}$$

where ϵ and γ represent compressional and shear wave anisotropy respectively and δ controls most anisotropic phenomena of importance in exploration geophysics. ϵ, γ and δ are known as Thomsen's anisotropy parameters. The δ value includes the effect of P and S anisotropies, as well as the effect of the stiffness in the inclined direction (at θ angle). Thomsen suggests that all three anisotropies (ϵ, γ and δ) are usually of the same order of magnitude, however there is no particular correlation between them as demonstrated in Figure 2.24.

Agarwal and Ishibashi [5] studied directional velocities of waves propagating through a dry granular material in a cubical specimen with rigid walls in order to quantify anisotropic characteristics of glass sphere assembly. Vernik and Nur [168] measured horizontal, vertical and inclined velocities in kerogen-rich shales, and concluded that seismic anisotropy is higher in more mature samples with a higher concentration of horizontal microcracks. Their results also showed higher anisotropy with an increase in kerogen content (Figure 2.25).

Johnston and Christensen [79] measured directional P and S velocities and studied the clay particle alignment through X ray diffraction and electron microprobe backscatter (BSE) imaging. Their results showed a strong positive correlation between the degree of preferred orientation and seismic anisotropy. They also reported a V_p anisotropy range of 20%-30% and a V_s anisotropy range of 19%-35% at elevated pressures (Figure 2.26), which are fairly low.

Vernik and Liu [167] measured ultrasonic velocities and anisotropy in various shale samples (dry, oil saturated and brine saturated) with different clay minerology, kerogen contents and relatively low porosities. They suggested that the velocities measured in their study were phase velocities, thus could be used directly in calculating stiffness and anisotropy parameters. Hornby [66] measured P and S velocities in vertical, horizontal and inclined directions in fluid saturated specimens under compression. Despite most studies that are run on either dry or undrained (constant volume) specimens, Hornby tested drained specimens, which means the specimen porosities were changing, although not significantly ($\approx 2\%$). He reported up to 26% compressional wave anisotropy (Thomsen's ϵ) and up to 48% shear wave anisotropy (Thomsen's ϵ) and found that both ϵ and γ decreased as a function of increasing confining pressure (Figure 2.27). Sarout et al. [137] studied the anisotropic elastic properties of Jurassic shale under undrained conditions by measuring ultrasonic velocities. In contrast to majority of the previous studies that used specimens trimed in different directions, the five velocities in this research were measured on a single undrained (and low porosity) rock sample while being hydrostatically loaded. Measuring the velocities in a single core, minimizes the errors due to the particular difference between two samples of the supposedly same lithology or same physical state (stress, saturation history and recovery process). The anisotropy parameters calculated based on the measured velocities follow a decreasing trend with increasing axial stress (Figure 2.28). They also developed a micromechanical model to quantify the damaged state of the shale which allows for the identification of the pertinent parameters. The model is used for a general transversely isotropic orientational distribution of microcracks, superimposed on the intrinsic transverse isotropy of the

rock. Wong et al. [178] used arrays of specially constructed transducers with different modes of vibration that were mounted on samples trimmed from natural cores and measured wave velocities of over-consolidated shale samples in horizontal, vertical and 45° directions. They calculated the elastic moduli which are more or less constant with increasing stress (Figure 2.29) (from the compliance matrix) and analyzed the difference with static tests results. Piane et.al. [124] measured velocities in vertical, horizontal and 45° directions during an undrained triaxial test. They studied the intrinsic and crack-induced anisotropic properties of brine-saturated shale samples and their response to external stresses. They concluded that when estimating anisotropic elastic wave velocities and their effects on pore pressure predictions, anisotropic stress fields should be considered.

Lastly, Horne [67] compiled and statistically analysed some published anisotropic elastic properties of mudrocks. They observed that Thomsen's ϵ and γ parameters are almost always positive, Thomsen's ϵ and γ parameters are well correlated, Thomsen's δ is mostfrequently small and Thomsen's ϵ is generally larger than Thomsen's δ.

While the studies mentioned in this section have helped us understand seismic anisotropy and directional velocity in sedimentary materials significantly better, they have mostly ignored one important domain: velocity anisotropy in high (and changing) porosity, deformable material under medium to high pressures. This study attempts to focus on anisotropy in such materials by measuring directional velocities in deforming specimens under K_0 consolidation in a triaxial setup.

2.5 Compression Behavior in Clay

The correlation between the void ratio and the stress level in clays, as well as the corresponding changes in material characteristics are important both in the civil engineering field (foundation, tunnel, excavation and earth support system design) and the oil industry (exploration and drilling). The term consolidation, or compaction as it is called in the oil industry, is used when clay undergoes plastic deformation

as a result of an increase in the effective stress. This is usually accompanied by the excess pore fluid dissipating and the porosity decreasing. Clay materials can be consolidated following different loading paths, such as hydrostatic, one-dimensional (or K_0) or non-K_0. However, one-dimensional consolidation best represents typical geostatic soil behavior and is consequently used in many studies, including this one.

The compression behavior of clays is well studied in the geotechnical field. Mondol et al. [111]summarized multiple published studies in a depth-porosity graph, representing the compression curves in shales and argillaceous sediments (Figure 2.30).

Mondol et al. [111] conducted compression tests (up to 50 MPa) on a variety of dry and brine-saturated clay aggregates, ranging from pure smectite to pure kaolinite, in the laboratory. They showed that the physical properties (porosity, density, acoustic velocity, etc.) of mudstones vary greatly with increasing effective stress, clay mineralogy and fluid content. Casey [26] tested an extensive variety of fine-grained materials, including the ones tested in this study (Resedimented Gulf of Mexico-Eugene Island (RGoM-EI) and Boston Blue Clay (RBBC). He provided compression curves for materials K_0-consolidated in a high pressure (1-100 MPa) triaxial setup (Figure 2.31).

There are several theories attempting to explain the evolution of compression in clays. A few examples are: Olsen [120] suggested that high porosity compression is controlled primarily by cluster rearrangement. Lambe [89] and Mitchell [110] however believed that it was the particle orientation driving the clay behavior as a function of stress. Another theory is that a "collapsing aggregate structure" is at play during compression [35]. While the compression behavior is most likely the result of a combination of the suggested factors, the exact mechanism, both at a microstructural and a macrostructural level, is yet to be understood.

2.6 Clay Microstructure

In geotechnical engineering, clays are usually characterized by their macroscopic or engineering properties, that is at the scale of laboratory specimens or in-situ testing. The most common and perhaps useful macrostructural analysis are the correlations between engineering parameters such as stress level, stress history, strain and porosity. Microstructural properties on the other hand are governed by a combination of the geometrical arrangement of particles (or fabric) and the forces operating between them. These properties include physio-chemical structure, particle orientation, diffuse double layer characteristics and cation exchange rates. The microstructural approach is a completely different but necessary process of characterizing clays.

All clay minerals have a similar chemical composition, plate like particles, a layered structure, and a great affinity for water (or oil in case of some kaolinites). They consist of particles that contain anionic layered silicates and metal cations. The platy particles can theoretically be positioned at any angle between 0° to 90° from the bedding direction, which is called the particle orientation. They are part of the phyllosilicate group of minerals. Most have the "sandwich" structure with 2 layers of sheet silicates bonded to octahedral cations. Other, weakly bonded cations are located between layers and are solvated by water. Tournassat et al. [161] studied the structure and the surface properties of clay minerals in details (Figure 2.32).There are four main classes of clay minerals: Kaolinite, Montmorillonite/Smectite, Illite and Chlorite. The two clay types were tested in this study are Illite (Boston Blue Clay) and Illite-Smectite (Gulf of Mexico- Eugene Island), which will be discussed in detail in the next chapter.

Different types of clay particles have different sizes and geometries. The two clay materials used in this research are Gulf of Mexico-Eugene Island (smectite) and Boston Blue Clay (Illite). Smectite has a thickness of 1-10 nm and diameter-to-thickness ratio of 3-10, Illite has a thickness of 10-200 nm and a diameter-to-thickness ratio of 10 [90]. Kaolinite clay which has be largest particles (30-1000 nm) was not studied in this research.

The diffuse double layer water is electrostatically attached to the particle surface. The thickness of the double layer depends on the type of material, Specific Surface Area (SSA) of the particles and the pore fluid chemistry. Higher pore fluid salinity can shrink the diffuse double layer [64]. Moreover, smaller particles (such as smectite) have higher SSA, and larger amounts of exchangeable ions. The Cation Exchange Capacity (CEC) is a measure of exchangeable ions present on a clay particle, required to neutralize its net charge. Smectite has a higher CEC (100 $meq/100g$) than Illite (20-30 $meq/100g$) for the same mass quantity. Particles with higher CEC (smectite) attract more water and form a thicker diffuse double layer. All of these mircostructural characteristics affect the velocity behavior of clays.

2.6.1 Compression Behavior

There has been a great effort to study the correlation between 1-D consolidation, soil fabric, particle orientation and void distribution. Martin and Ladd [105] studied 50 kaolinite specimens under 1-D consolidation (0.01-100 MPa pressure) using X-ray diffraction (XRD) method. They showed an increase in horizontal alignment (prependicular to loading direction) with increased 1-D consolidation, mostly under 0.1 kg/cm^2 and concluded that the ease with which the particles are oriented depends on the initial soil structure. As a result, they believe it is very unlikely that one would observe a unique relation between particle orientation and either void ratio or applied anisotropic stress (Figures 2.33 and 2.34).

Similar studies on illitic clays ([130], [118] and [131]), and on montmorillonite [41] have shown similar positive correlations between orientation and one-dimensional consolidation.

Griffiths and Joshi [55] ran an experimental program examining the response of clay fabric and void distribution to consolidation. They used Mercury Intrusion Porosimetry (MIP) to test 4 different soil types and observed that although the total and entrapped void volume in a soil sample are related to the maximum consolidation stress; the higher the consolidation stress the lower the total void volume in a soil sample, the volume of free voids is not related to the maximum consolidation stress.

Also, deformation of clays during consolidation is mainly due to the loss of inter-assemblage pores. Figure 2.35 shows the pore classes and re-intrusion.

Delage and Lefebvre [35] used Scanning Electron Microscopy (SEM) and MIP in parallel to study the structure of Champlain clay. They studied intact, remolded and oven dried samples, as well as one dimensionally consolidated. Their observation of clay structure at various stress levels show that the collapse of the structure is progressive, the largest interaggregate pores being the first affected. As the consolidation proceeds, smaller and smaller pores are affected. Their SEM images in different planes showed an increase in anisotropy with consolidation.

Day-Stirrat et.al [34] studied the development of a preferred orientation of clay minerals in response to changes in vertical effective stress and composition in resedimented Boston Blue Clay. They assessed the clay mineral preferred orientation quantitatively using a single-crystal diffractometer, in resedimented specimens loaded up to 10 MPa in a CRS device. Their results showed a slight increase in preferred orientation in mica and chlorite with increasing vertical effective stress (Figure 2.36).

2.6.2 Anisotropy

Despite lack of experimental studies focusing on microstructural anisotropy of clays, it is thought to be caused both by the orientation distribution of crystallites and high-aspect-ratio pores. Loon [98] used high-energy and high-intensity X-rays from a synchrotron source to obtain diffraction images that were then analyzed using the Rietveld method, with the primary aim to obtain quantitative information about the preferred orientation of clay minerals in shales. According to Loon's results, the observed mineral orientation correlates with anisotropy of macroscopic properties such as acoustic wave propagation and transport parameters. Hicher et al. [63] studied the evolution of clay structure (shape, size, concentration and orientation of the elements) by means of scanning and transmission electron microscopes. They observed a structural re-organization during one- dimensional and triaxial testing, which led to a very strong anisotropy under high consolidation stresses. They used rose diagrams to illustrate the degree of preferred orientation of particles from photos

obtained by the SEM. Their diagrams showed an increase in preferred orientation with increasing uniaxial strain.An example of a rose diagram of particle orientation for a K_0 consolidated bentonite specimen is shown in Figure 2.37, the details of which are beyond the scope of this study.

They concluded that the anisotropy in the arrangement of the particles is what creates and anisotropy in the mechanical behavior of clay. Also, the difference between horizontal and vertical stiffnesses in conventional K_0 consolidation triaxial tests is consistent with the particle orientations observed by Hicher et al. [63]. The rigidity of the particle assembly is stronger when the load is applied in a direction perpendicular to the main direction of particle orientation, rather than in the same direction. It is important to note, however, that macro-level anisotropy is dependent on loading condition as well and cannot be independently correlated with particle orientation.

2.7 Other Methods of Stiffness Characteristics Determination

Soil stiffness properties and elastic behavior have significant importance in the geotechnical engineering field, especially to help understand the stress-strain relationships. Several methods can be used to measure these characteristics in a laboratory such as triaxial test, torsional shear, resonant column and bender elements, and others can been used in-situ, like soil stiffness gauge (SSG), seismic dilatometer test (SDMT), in-situ wave propagation, dynamic cone penetrometer, cross hole and down hole tests. Some of these methods will be briefly discussed in this section.

2.7.1 Triaxial Testing

Stiffness parameters of clays can be measured in two main ways, using the triaxial testing setup: internal small strain measurements with specimen-mounted yoke apparatus during undrained triaxial compression, and external strain measurements

using one or more Linear Variable Differential Tansformers (LVDT), during conventional K_0 consolidation undrained compression test (CK_0UC). Atkinson and Sallfors [10] categorized the strain levels into three groups: the very small strain level (ϵ<0.0001%, linear elastic) , where the stiffness modulus is constant in the elastic range; the small strain level ((0.0001%<ϵ<0.1%, non-linear elastic), where the stiffness modulus varies non-linearly with the strain; and the large strain level (0.1%<ϵ, plastic), where the soil is close to failure and the soil stiffness is relatively small. Likitlersuang et al [96] illustrated this explanation using the stiffness degradation curve and showed the strain ranges for various geotechnical laboratory testing and in-situ loading conditions. (Figure 2.38).

Measuring the small strain behavior in a triaxial setup is challenging, due to the generally large strains exhibited during this type of testing. Santagata [136] used two LVDTs mounted on the specimen that measured displacement with reference to the spring anchor post also attached onto the specimen. Santagata was able to achieve strain resolution at 0.0001%, which is within the linear small strain region. A stiffness degradation curve measured by Santagata et al. [135] for RBBC can be seen in Figure 2.39. The figure indicates that although the typical limit quoted for the linear small-strain region is 0.001% (i.e. [31]), for RBBC the limit for the linear region appears to be at 0.005%. Note that measurements performed by Santagata [136] were done during undrained shearing of the specimen, thus the undrained Young's modulus (E_u) is measured.

Santagata's testing program isolated the roles of: overconsolidation ratio (OCR), consolidation stress level, void ratio, lateral stress ratio, pre-shear consolidation path, strain rate and duration of laboratory aging. Ther results indicate that the stress-strain behavior of RBBC is linear, independent of the testing condition and OCR (Figure 2.40). They also found that at any OCR, for a strain rate of at least 25-30 times the pre-shear creep rate, initial Young's modulus is a direct function of effective stress and suggested the following equations for RBBC:

$$E_{u,max} = 617 \times OCR^{0.15} \times {p'_{mc}}^{0.8} \tag{2.23}$$

$$E_{u,max} = 273 \times e^{-2.44} \times {\sigma'_{vc}}^{0.44} \tag{2.24}$$

where $E_{u,max}$ is the initial Young's modulus, e is the void ratio, σ'_{vc} is the vertical effective stress and p'_{mc} is the mean effective stress calculated as:

$$p'_{mc} = \frac{(\sigma'_1 + 2\sigma'_3)}{3} = \frac{(\sigma'_v + 2\sigma'_h)}{3} \tag{2.25}$$

While the work does have a thorough analysis of the small strain behavior, it is limited to low pre-shear stress levels ($\sigma'_{vc} < 1.5$ MPa) and does not address the stress levels that are of interest in the geology field. Furthermore, the destructive nature of a static shearing test prevents multiple measurements on one specimen. The study in hand will try to address both of these issues in the following chapters.

The second method of measuring Young's modulus using a triaxial setup is the use of conventional K_0 consolidation undrained compression test (CK_0UC) and external strain measurements. Although not truly within the small strain zone, Abdulhadi [2] successfully measured normalized undrained secant modulus. His results on normally consolidated RBBC are shown in Figure 2.41.

2.7.2 Torsional Shear

Torsional shear test can be performed using a single device together with a resonant column test ([73], [86], [153] and [100]), or alone in an independent device. Torsional shear test is a non-destructive test where a small static or dynamic torque is applied to one end of a solid or hollow cylindrical specimen, and the shear modulus of the specimen is measured, as well as the damping properties in case of dynamic loading. The shear strains in torsional shear testing are relatively high and non-uniform. A comprehensive description of torsional shear test can be found in ASTM D6467. Iwasaki et al. [75] ran dynamic torsional shear tests, as well as resonant column, on various sands to evaluate the degree of reduction in the shear modulus with increasing shear strain. They compared their results to other available research (Figure 2.42). They also suggested a curve representing the reduction in shear modulus to be used

in conducting earthquake response analysis (Figure 2.43).

Teachavorasinskun et al. [156] investigated the stiffness and damping behavior in drained sand specimens, under monotonic and dynamic loadings, at different strain levels (Figure 2.44). They concluded that for a range of shear strain less than about 7×10^{-6} the secant stiffness of the sands was scarcely affected by the type of dynamic and monotonic loadings. Hence the shear modulus in this small strain region is elastic. They also showed that the relationship between shear modulus ratio and the damping was unaffected by the confining pressure (Figure 2.45).

2.7.3 Resonant Column

The resonant column test, first introduced in the 1960's, consists of a cylindrical soil specimen with a fixed plate attached to one end and a vibrating plate attached to the other end. A simple illustration of the setup is shown in Figure 2.46. The sinusoidal vibration is generated by a coil and magnet system that generates an electromagnetic force, moving the top plate. The resulting behavior yields the shear modulus and shear velocity. A detailed description of the test can be seen in ASTM D4015. The resonant column can only test one stress state at a time, however once the specimen is tested, it can be consolidated to a higher stress and tested again repeatedly.

Ellis et al. [40] used resonant column testing to study the effect of pore fluid viscosity on the stiffness, damping, and liquefaction characteristics of sands. Sas and Gabrys [138] measured small strain shear modulus (G_0) in natural cohesive soils from Warsaw area investigations site, under a variety of the confining pressures and mean effective stresses. Figure 2.47 shows the summery of their results for different mean effective stresses, and suggests higher normalized shear stiffnesses for higher mean effective stresses.

2.7.4 Bender Elements

The piezoceramic bender element is an electro-mechanical transducer which is capable of converting mechanical energy (movement) either to or from electrical energy. They are usually inserted directly into the soft soil specimen, generating and receiving shear waves. When placed parallel to the specimen surface however, bender elements can generate compressional signals propagating perpendicular to that surface. Bender elements can be installed in a variety of standard laboratory equipment, for example triaxial, direct simple shear and oedometer devices. While this technology is ideal for lower stress levels, at higher stresses soil stiffness restrains the vibration and weakens the signals, eventually making the arrival interpretation impossible. Shirley and Hampton [148] were first to use bender elements in 1978 and measure shear wave velocity and shear modulus in kaolinite. Many more researchers have since used bender elements to measured soil stiffness parameters and anisotropy ever since. Jovičić and Coop [81] measured the stiffness of coarse-grained soils and in [82] investigated the anisotropy of small strain stiffness of fine-grained soils using bender elements in a triaxial specimen under mean effective stress up to 0.6 MPa mean effective stress. Similar anisotropy studies have been performed by other researchers such as Lings et al. [97] and Kang et al. [83].

Marjanovic and Germaine [104] tested Ticino sand and resedimented Boston blue clay (RBBC) to develop the characteristics of the bender element behavior and to isolate the parameters that most closely need to be monitored during the experimental procedure. They used the shear velocities to calculate shear stiffness as a function of vertical effective stress (0.05-2 MPa) and compared their results to the data available in the literature, as shown in Figure 2.48.

2.7.5 Soil Stifness Gauge

The soil stiffness gauge (SSG), also known as GeoGauge, is a portable, user-friendly and nondestructive in-situ testing device that directly and rapidly measures the in-situ stiffness of soils. The ASTM D6758-18 standards discusses SSG testing in detail.

The SSG vibrates and produces small changes in vertical force and deflections at 25 steady-state frequencies between 100 and 200 Hz. The soil stiffness is determined at each frequency and its average value is displayed. The SSG stiffness can be used to determine directly Young's modulus. In a 2002 study Sawangsuriya et al. [139] conducted a laboratory investigation to better understand the SSG measurement characteristics and limitations and concluded that caution needs to be exercised in interpreting the results from the SSG when it is used on multilayer systems, especially those with geosynthetic separators. The presence of a geosynthetic separator, commonly used for separating the aggregate from the subgrade in pavement construction, between the layers may cause a stiffness decoupling of the layers.

2.7.6 Seismic Dilatometer Marchetti Test

The Seismic Dilatometer Matchetti Test (SDMT) is the combination of the flat dilatometer with an add-on seismic module for the measurement of the shear wave velocity. Marchetti et al. [101] first proposed the possible use of the SDMT for deriving in-situ elemental soil stiffness variations with strain level. An example of SDMT results is shown in Figure 2.49. Amorosco at al. [7] thoroughly investigated the potential of the using SDMT to assess the decay of in-situ stiffness with strain level in different soil types.

2.7.7 Stiffness Testing Comparison

Many researchers have tried to compare the mentioned stiffness measurement technologies, in an attempt to find how the elastic moduli and velocity measurements from each test compare to one another, and the results from which method are the most representative of the elastic behavior of the material.

Brignoli et al. [21] performed laboratory tests on Ticino sand, Pontida silty clay and offshore clay to compare data from different types of transducers. They compared the piezoelectric results to bender element and resonant column data. The P-wave velocities from bender element and piezoelectric plates are virtually the same (Figure 2.50, whereas S-wave velocities show a stronger dependence on testing

method and soil type (Figures 2.51 and 2.52). All in all, Brignoli et al. [21] found the use of piezoelectric technology in P and S velocity measurements to be promising.

Valle-Molina [162] combined 4 of the most common methods by installing bender element and piezoelectric elements into a combined resonant column and torsional shear (RCTS) device and tested washed mortar sand that was prepared using under-compaction method. The shear velocity (V_s) was higher when using bender elements versus resonant column (Figure 2.53). Valle-Molina concluded that the difference in velocity values were caused by differences in frequency and strain level. Figure 2.54 shows the shear wave velocity results from torsional shear, resonant column and bender element methods, with different driving frequency. Higher frequencies yield slightly higher shear wave velocities. The results covered only low stress levels and mostly shear wave velocities.

Winkler and Nur [176] studied the effect of the testing strain amplitude on attenuation and velocity as well. Using a technique similar to that of Gardner et al. [49], they made a long, thin bar of rock to resonate in either a torsional or extensional normal mode while being rigidly supported at its center.They concluded that at strains 10^{-7} and lower, there is an insensitivity; however, strains above this limit show a marked increase in attenuation and decrease in velocity as a function of increasing strain (Figure 2.55). Similarly, Iwasaki et al. [75] tested sands using cyclic torsional shear and showed that shear modulus is significantly higher for testing strains of less than 10^{-5}.

2.7.8 Stiffness Anisotropy Testing

Although similar to this research, stiffness anisotropy in soils has mainly been studied through directional velocity measurements, a few researchers have used other stiffness measurement techniques for that purpose. Lings et al. [97] carried out triaxial testing on natural Gault Clay from Madingley, UK, involving multiple drained stress path excursions and orthogonal determinations of horizontal shear wave velocity using bender elements. Three independent elastic moduli were determined from the triaxial tests (E_v, E_v, ν_{vh}, (or ν_{hh})), and the two anisotropic elastic shear moduli

(G_{vh} and G_{hh}) from the bender elements mounted in two directions on the specimen. Combining results from both sets of tests, they calculated all 5 independent transverse isotropic elastic parameters. Teng et al. [157] determined the anisotropy ratios (horizontal to vertical ratio) for both the shear modulus and the Young's modulus in natural Taipei silty clay (Figure 2.56)under vertical effective stresses lower than 0.25 MPa. They performed K_0-consolidated small-strain undrained shear triaxial tests to get the Young's moduli and used bender elements to get the shear modulus.

2.8 Attenuation and Dispersion

Seismic attenuation is an intrinsic property of rocks reflecting dissipation of energy as seismic waves propagate away from the source. It is manifested by the decay of amplitude of the seismic waves. Attenuation is proportional to frequency [159] and is related to velocity dispersion [15]. Dispersion is when the velocity differs as a function of frequency. The squirt-flow mechanism is proposed to explain velocity dispersion. It describes describes how fluid is squeezed from one pore to another due to the passing wave (pore/micro level) [38]. At low frequencies, the fluid pressure does have time to equilibrate and the contacts remain soft. At high frequencies, pressure does not have enough time to equilibrate, which stiffens the contacts, increasing the shear moduli, and dispersion occurs. The Biot mechanism describes how the fluid moves with the solid due to viscous friction and inertial coupling (macroscopic level). The squirt-flow mechanism describes how fluid is squeezed from one pore to another due to the passing wave (pore/micro level) [38]. The squirt flow dispersion is dominant at medium/high frequencies (10-100 kHz) and Biot's dispersion is dominant at ultrasonic frequencies (around 1 MHz). In materials with high porosity and well-connected pores, the Biot mechanism is the dominant driver of dispersion rather than the squirt mechanism [150]. A unified model, named the Biot-squirt (BISQ) model was introduced by [38]. The model however, is limited to high pressure rocks with closed compliant cracks. The testing performed in this thesis is on the order of sonic logging frequencies (P-wave=100-260 kHz, S-wave=5-50 kHz), thus it is

uncertain which dispersion mechanism is at play.

Numerous mechanisms have been proposed, trying to explain attenuation behavior. Each of the mechanisms is assumed to have a different effect depending on the material type and physical conditions.

Durek and Ekstrom [36] suggested that propagating seismic waves loose energy due to the following:

- **Geometrical Spreading**: As the wavefront moves out from the source, the initial energy released in the seismic wave is spread over an increasing area and therefore the intensity of the wave decreases with distance. Shearer [144] explained geometrical spreading using ray theory.

- **Absorption (Anelastic Attenuation)**: Internal friction during wave propagation causes a loss in energy [142] This is called intrinsic or anelastic attenuation. Intrinsic attenuation occurs mostly during shear wave motion associated with lateral movements of lattice and grain boundaries.

- **Scattering (Elastic Attenuation)**: Scattering occurs when there are discontinuities or heterogeneities present. If the heterogeneities are much smaller than the wavelength, then the wave will likely pass through them as it does through the medium.

- **Multipathing**: When the heterogeneities are much larger than the wavelength, multipathing takes over. Multipathing is when the wave is focused or defocused by changes in refractive properties of the medium.

Johnston et al. [77] listed some of the most important mechanisms as: 1) matrix anelasticity, including frictional dissipation due to relative motions at the grain boundaries and across crack surfaces [170] 2) dissipation of high frequency waves in a fully saturated rock due to relative motion of the frame with respect to fluid inclusions ([18], [154]) 3) squirting phenomena ([107], [119]) 4) partial saturation effects such as gas pocket squeezing ([174]) 5) Energy absorbed in systems undergoing phase changes [151] and 6) fluid flow, including relaxation due to shear motions

at pore-fluid boundaries ([171] and [172]). Fluid flow occurs when size of the pore (a_{pore}) is much smaller than the size of the heterogeneity (such as pores), which is much, much smaller than the wavelength of the propagating wave (λ) ([115]).

In this research, the wavelength of the P-wave is between $\lambda = 1 - 1.8$ cm, while the wavelength of the S-wave is between $\lambda = 1 - 8$ cm. Since this wavelength is much bigger than the average size of the clay particles and pores, hence scattering is unlikely to occur. Also there is no multipathing since the arrivals are measured directly and not from surface reflections. Moreover, the strains induced by wave propagation are within very small strain range ($\epsilon < 0.001\%$) and elastic behavior real, ruling out the occurrence of anelastic attenuation. This leaves geometric spreading as the most likely mechanism causing attenuation in the study in hand.

2.9 Input Frequency

The frequency of the input signal is generally believed to affect both the arrival time and the quality of the output signal. Blewett et al. [19] used a continuous sinusoidal wave with frequencies varying between 200 Hz and 10 kHz and suggested that shear-wave velocities in sand measured using bender elements in triaxial setup are dependent upon the excitation frequency and exhibit a maximum velocity for a specific frequency. Leong et al. [93] measured S-wave velocities using bender–extender elements in compacted residual soil specimens. The excitation frequencies were varied from 1 to 16 kHz. The specimen was subjected to isotropic effective confining pressures of 50, 100, 200, and 400 kPa. They also measured the P-wave velocities under the same conditions and varying input frequencies of 10 to 30 kHz. Leong et al. [93] suggested that while the S-wave velocity is dependent on the input frequency, the P-wave velocity is unaffected. Marjanovic [103] evaluated the frequency dependency of the arrival time in saturated Presumpscot clay (Figure 2.57 and Figure 2.58). She set the input frequency of the square step at a high enough frequency so that the input is both excited and grounded before the arrival of the output signal (36.2 kHz for P and 40 kHz for S). Alternatively, the converse scenario was to have a

square pulse with a low enough frequency so that it entirely encompasses the arrival (6.6 kHz for P and 4 for S). Her results showed that the quality of the signal greatly deteriorates when using high frequencies. She concluded that while the input frequency does not expressly change the arrival time, it does affect the interpretation of the arrival time, thus leading to potential erroneous velocity values due to the ambiguity of the arrival selection.

2.10 Empirical Equations

2.10.1 Stiffness

Researchers have long tried to come up with equations correlating soil characteristics such as stiffness, stress state, stress history and porosity, to laboratory or in-situ measurements. Some of these correlations and their underlying assumptions and findings will be discussed in this section. Hardin [58] formulated elastic constitutive equations to describe the small strain shear modulus as a function of stress:

$$\frac{G_0}{p_a} = S \times f(e) \times OCR^k (\frac{p'}{p_a})^n \tag{2.26}$$

Where G_0 is the small strain shear modulus, p_a is atmospheric pressure, $f(e)$ is a decreasing function of the void ratio, p' is the mean effective stress, and OCR is the overconsolidation ratio. The terms S, K, and n are material constants. Hardin and Blandford [59] formulated three-dimensional elastic constitutive equations in terms of two scaler functions representing effects of void ratio and stress history, a reference fabric matrix, a stress-compliance matrix, and a Poisson's ratio matrix. However, the earlier equations (including modifications by Hardin [57]) were not formulated to assure objectivity. Transformation of coordinates and the definition of reference fabric are carefully considered in the developed formulation:

$$G^e{}_{ij} = \frac{\mathrm{OCR}^k}{f(e)} \frac{S_{ij}}{2(1+\nu)} {p_a}^{1-n} (\sigma'_i \sigma'_j)^{n/2} \tag{2.27}$$

where ν is Poisson's ratio (assumed to be isotropic) and terms i and j indicate

the directions of wave propagation and particle motion, respectively. These two equations are most commonly used for sands.

Shibuya et al. [146] introduced a new void ratio term on the basis of characteristics of the small-strain shear modulus of soft clays, from in-situ and laboratory measurements of shear wave velocity:

$$f(e) = (1+e)^{\alpha} = \nu^{\alpha} \tag{2.28}$$

where α is an empirical constant. m in equation 2.28 is the constant relating the increase of stress with increase of shear modulus as follows:

$$\frac{G_{max}}{G_{maxr}} = (\frac{\sigma'_v}{\sigma'_{vr}})^m \tag{2.29}$$

Shibuya et al. [146] proposed the following expression for estimating the depth profile of G_{max}:

$$G_{max} = A(1+e)^{-2.4}{\sigma_r}^{0.5}{\sigma'_r}^{0.5} \tag{2.30}$$

where A is a constant that accounts for different soils, and includes an aging effect present between reconstituted versus intact samples (Figure 2.59).

For fine-grained soils and isotropic stress conditions, Viggiani [169] proposed the following expression for G_0:

$$\frac{G_0}{p_r} = S^*(\frac{p'}{p_r})^{n^*} OCR^m \tag{2.31}$$

where OCR is the overconsolidation ratio, S^*, n^*, and m are material constants, p' is mean effective stress, and p_r is a reference stress used to eliminate units. Rampello et al. [132] performed an experimental investigation on the effects of anisotropic stress states and histories on the small-strain shear stiffness of reconstituted clays as measured with bender element tests. Rampello et al. [132] concluded that for a clay under isotropic stress conditions, one of the following in Vigginani [169] is redundant and not needed: e (void ratio), p' (mean effective stress), and OCR. They took the

rational link that exists between void ratio, state of stress and overconsolidation ratio into account and proposed the following equation:

$$\frac{S_\eta}{S} = exp(\frac{c}{\lambda}(N - N_\eta))\beta^{\frac{n}{2}} \tag{2.32}$$

where η represents the shear stress ratio to the mean effective stress, S and S_η are stiffness multipliers for isotropic and anisotropic stress histories respectively, c is the exponent of $\frac{p'_e}{p'}$ and $\frac{p'_{e\eta}}{p'}$, λ is compression index in natural log scale, N is specific volume and N_η specific volume at the reference stress for constant η virgin compression, n is the exponent of mean effective stress, and β is the function of stress ratio η, capable of accounting for the different strain histories experienced by the samples during anisotropic constant η and isotropic compression paths.

Vardanega and Bolton [163] analyzed a database of the secant shear stiffness of 21 clays and silts was compiled from 67 tests from 10 publications. They proposed 2 equations which together predicted over 90% of the $\frac{G}{G_{max}}$ ratios within a margin of ±3% across the full range of values from 0 to 1.0 for all soils (Figure 2.60), with the exception of certain London Clay data, which is significantly underpredicted:

$$\frac{G}{G_{max}} = \frac{1}{1 + (\frac{\gamma}{\gamma_{ref}})^{0.943}} \tag{2.33}$$

where γ_{ref} is:

$$\gamma_{ref} = J\left(\frac{I_P}{1000}\right) \tag{2.34}$$

I_P is the plasticity index and J is a static adjustment constant.

Not many studies have tried to consider the effects of anisotropy on the correlations between the elastic stiffness parameters and other soil characteristics such as stress state and porosity.

Jamiolkowski et al. [76] first introduced directional shear modulus of clays at very small strains in 1995 as:

$$G_{vh} = S_{vh} e^{-x} {p_a}^{(1-nv-nh)} ({\sigma'}_v)^{nv} ({\sigma'}_h)^{nh} \tag{2.35}$$

$$G_{hh} = S_{hh} e^{-x} {p_a}^{(1-2nh)} ({\sigma'}_h)^{nh} ({\sigma'}_h)^{nh} \tag{2.36}$$

$$G_{hv} = S_{hv} e^{-x} {p_a}^{(1-nh-nv)} ({\sigma'}_h)^{nh} ({\sigma'}_v)^{nv} \tag{2.37}$$

where p_a is atmospheric pressure, S_{vh} is a material constant reflecting the current soil structure, σ'_v is the vertical stress, σ'_h is the horizontal effective stress and nv and nh are exponents.

More recently Mašín and Rott [106] proposed the following equation for anisotropy coefficient:

$$\alpha_G = b_1 + b_2 \ln \frac{p_e}{p_r} + b_3 (K_0 - K_{0NC}) \left(\frac{p}{p_e} \right)^{b_4} \tag{2.38}$$

where $\alpha_G = G_{vh}/G_{hh}$, $b_1 - b_4$ are material coefficients, b_1 represents the initial α_G, b_2 controls the rate of α_G increase (positive b_2) or decrease (negative b_2) with p, p is mean effective stress, P_e is Hvorslev equivalent pressure, pr is reference pressure 1 kPa, and K_{0NC} is the value of K_0 in normally consolidated state. Under K_0 normally consolidated conditions, K_0 is equal to K_{0NC} thus only the first two terms of the equation, which represent the contribution of inherent anisotropy, are active. The model assumes that the current pe was reached by one-dimensional compression, which is a reasonable assumption for natural clays; it is thus not applicable to reconstituted clays consolidated under conditions other than K_0.

2.10.2 Velocity

There are numerous models describing the stress, porosity, clay content ([134], Butcher and Powell [22], etc) or depth dependence ([95], [9], [122], etc) of shear or compressional (although mostly shear) velocity behavior based on empirical data. Some of the most relevant and commonly used models will be discussed here.

Gardner et al. [47] studied various rocks and proposed an empirical equation to calculate the compressional velocity using the bulk density (Figure 2.61).

$$\rho = aV_p{}^b \tag{2.39}$$

where a and b are fitting parameters, and ρ is density. Later Castagna and Backus [28] suggested extending the equation to:

$$\rho = aV_p{}^2 + bV_p + c \tag{2.40}$$

Tosaya and Nur [160] presented an empirical, material dependent correlation between P-wave velocity, porosity and clay content, which Castagna et al. [29] used to calculate compressional velocities, and suggested the following equation for mudrocks (Figure 2.62):

$$V_s = 0.862V_p - 1.172 \tag{2.41}$$

Eberhart-Philips et al. [39] used a multivariate analysis to investigate the influence of effective stress σ_r' (difference between confining stress and pore pressure), porosity n , and clay content C on the compressional and shear velocity of rocks using laboratory measurements on 64 water-saturated sandstones under low stress levels (0-0.15 MPa). They suggested the following fit for the material tested. The predictions are compared to the test results in Figure 2.63.

$$V_p = 5.77 - 6.9n - 1.73\sqrt{C} + 0.446(\sigma_r' - e^{-0.16.7\sigma_r'}) \tag{2.42}$$

and

$$V_s = 3.70 - 4.9n - 1.57\sqrt{C} + 0.361(\sigma_r' - e^{-0.16.7\sigma_r'}) \tag{2.43}$$

Sayers and den Boer [140] compared the density versus velocity data for two deep water subsalt wells in the Green Canyon area to predictions of Gardner's relation,

assuming the parameters given by Castagna et al. [27] for sands (blue curve) and shales (red curve), as well as Mori-Tanaka rock physics model [114] (Figure 2.64), and the mudrock line from Castagna et al. [29](Figure 2.64), to see which one most closely predicts the behavior of this mudrock. They showed that the best model that described the data was the effective field theory of Mori- Tanaka, which includes a pore aspect ratio assumption, approximately 0.02 for the P-wave and 0.015 for the shear wave.

Bowers-type fit is commonly used for P-wave velocity prediction in the geotechnical and geology fields to describe the loading and unloading behavior of shales and rocks [20]. It was specifically developed to improve pore pressure predictions and accounts for the unloading effect. The equation is as follows:

$$V_p = C + A(\sigma'_{max}\left(\frac{\sigma'}{\sigma'_{max}}\right)^{\frac{1}{U}})^B \tag{2.44}$$

where A, B and C are fitting parameters, it is assumed that $C = 5000 ft/s$ in all cases, U is a fitting parameter for the unloading portion, σ'_{max} max is the maximum past stress, and σ' is the current effective stress. U is referenced by Bowers [20] as falling between 3-8, with $U = 1$ being a perfectly elastic unloading, and $U = \infty$ being a perfectly plastic unloading. For normally consolidated soils the equation is simply:

$$V = C + A\sigma'_B \tag{2.45}$$

Similar power equations for both P and S velocities in different directions are used in many recent studies, including Landon et al. [91] and Moon and Ku [113].

Although some of the models explained above could theoretically be used to predict velocities in different directions, such as power equations, there are very few studies available focusing specifically on velocity determination under anisotropic conditions. Roesler [134] was first to consider the effect of directionality on velocity trends in 1979. He suggested that V_s depends primarily on the stresses in the direction of wave propagation and in the direction of particle motion, with the third principal stress having a negligible effect on V_s, and proposed the following equation:

$$V_s = C_s(\sigma'_a)^{n_a}(\sigma'_b)^{n_b}(\sigma'_c)^{n_c} \tag{2.46}$$

where C, is a shear wave velocity constant dependent on soil state, σ'_a (direction of propagation), σ'_b (direction of particle motion), σ'_a (perpendicular to the other two) are the principal effective stresses, n_a, n_b, n_c are exponents for each direction.

Fioravante [44] tested Kenya and Ticino sand in a triaxial cell and measured velocities in different directions, using piezoelectric transducers. They suggested a general form for V_p and V_s determination based on current stress state (vertical and horizontal effective stresses, σ'_v and σ'_h).

$$V_p = C_p \times e^d \times \left(\frac{\sigma'_v}{p_a}\right)^{nv} \times \left(\frac{\sigma'_h}{p_a}\right)^{nh} \tag{2.47}$$

$$V_s = C_s \times e^d \times \left(\frac{\sigma'_v}{p_a}\right)^{nv} \times \left(\frac{\sigma'_h}{p_a}\right)^{nh} \tag{2.48}$$

where C_P and C_S are experimentally determined material constants, e is void ratio, and d, n_v and ${}_nh$ are nondimensional function exponents to be determined experimentally. Fioravante et al. [45] modified the velocity equations to account for stress history (OCR) and the stress ratio (K):

$$V_p = C_p \times e^d \times \left(\frac{\sigma'_v}{p_a}\right)^{nv} \times \left(\frac{\sigma'_h}{p_a}\right)^{nh} \times OCR^K \tag{2.49}$$

$$V_s = C_s \times e^d \times \left(\frac{\sigma'_v}{p_a}\right)^{nv} \times \left(\frac{\sigma'_h}{p_a}\right)^{nh} \times OCR^K \tag{2.50}$$

It is clear from the number of proposed models and empirical corelations that establishing a relationship between stiffness parameter or velocity and porosity and stress is highly desirable. Although empirical fits to data are often preferred over theoretical models in the field. Most of the models mentioned are appropriate for rocks, sands, and in some cases a certain amount of clay content added to a primarily rock or sand formation. Few attempts have been made, besides most notably Hardin and Blandford [59], to describe clay behavior. There is an insufficient amount

of data and empirical attempts at describing how velocities behave through clays, including different clay types and their plasticities, and as a function of evolving stress conditions and porosity.

2.11 Sidewall Friction

The standard one-dimensional compression tests like oedometer or constant rate of strain (CRS) are usually carried out on specimens with low aspect ratios. According to ASTM standard [ASTM D2435-04], for incremental loading, the height to diameter ratio of the specimen should be greater than 0.17 (to avoid disturbance during trimming), but less than 0.4 to reduce the influence of friction along the lateral surface. By ensuring that specimen dimensions remain within these limits, any effect of wall friction can be ignored, and a uniform initial excess pore pressure distribution can be reasonably assumed. If the height of the sample is much greater than its diameter, stress transfer occurs between the soil mass and the adjacent rigid wall. As a result, the actual stress felt by the specimen is lower than the applied stress, resulting in significant stress, effective stress and lateral stress ratio calculatin errors. The magnitude of the sidewall friction increases with the height to diameter ratio, soil cohesiveness and equals to a higher portion of the applied stress at lower stress levels. Wickland and Wilson [175] estimated in their large column tests (1.7 aspect ratio) that wall effects reduce vertical applied stresses by as much as 10–25%.

He et al. [60] ran three tests on slurried Jeeropilly coal tailings in a fixed-wall slurry consolidometer (H=41 cm, D=15 cm) under three different loading sequences and considered the simulation of slurry consolidation test results using the finite element method to study the friction losses quantitatively. Wall friction was modelled using the test results of Potyondy [128], which gave a friction angle for saturated soil on steel, under low normal stress, of 24.5°. They measured the stress applied via a cap to the top of the specimen is measured by the top load cell connected to the loading piston, and the stress transmitted to the base is measured by the base load cell. The difference between the measured applied load at top and transmitted load

to the base gives an indication of the combined piston and wall friction losses.

The total stress is a maximum where it is applied to the top piston and decreases with depth due to accumulating wall friction. The pore water pressure drains rapidly at the only drainage boundary at the top of the specimen, and increases with depth, while the effective stress does the opposite. They ran one of their tests under constant rate of stress conditions (up to 300 kPa, at a 0.2 kPa/min rate for a total of 1500 minutes) and compared the applied loads to the measured stresses at the bottom of the specimen and the model outcome (Figure 2.65). Their results indicated a 11.1% to 34.2% vertical effective stress loss due to friction. The high magnitude of the friction loss could be due to the use of fixed wall consolidometers and more importantly, the high rate of loading.

Variations in vertical effective stress with depth for a fixed wall consolidometer (or the top half of a floating consolidometer) can be derived as [99]:

$$\sigma_Z = \frac{\gamma D - 4c}{4K\tan\delta}\left[1 - e^{4K\tan\delta(\frac{Z}{D})}\right] + qe^{4K\tan\delta(\frac{Z}{D})} \tag{2.51}$$

where σ_Z is the vertical effective stress at depth Z, q is the applied vertical stress, D is the specimen diameter, c is the soil cohesion, K is the lateral stress ratio, δ is the wall–soil interface friction angle, and γ is the dry unit weight of the soil. Although the soil is saturated, the derivation will be carried out using dry unit weight in preparation for the final expression in terms of effective stress. The vertical effective stress within the soil at a depth Z is the combination of two components: the soil self-weight and the external applied pressure:

$$Self-weight: \quad \sigma_{S_W} = \frac{\gamma D - 4c}{4K\tan\delta}\left[1 - e^{4K\tan\delta(\frac{Z}{D})}\right] \tag{2.52}$$

$$\text{Applied Pressure}: \quad \sigma_P = qe^{4K\tan\delta(\frac{Z}{D})} \tag{2.53}$$

Lovisa and Sivakugan [99] suggests that for a high enough applied stress (q/γ D$>$10) and a small enough aspect ratio ($H/D<2$), the self-weight portion of the

equation could be disregarded. Using the above method, Kang et al. (2014) [84] calculated the average friction corrected vertical effective stress for kaolinite samples for unloading and reloading. Their results, presented in Table 1, suggest that for a normally consolidated kaolinite specimen, the vertical stress loss due to interface friction does not exceed 3%. However, for high-OCR cases, the vertical stress decrement was as much as 14% (at an applied vertical stress of 16 kPa), because the OCR led to a significant increase in K_0.

Casey [24] investigated the sidewall friction effect on resedimentation stresses. Figure 2.66 plots the ratio of vertical stresses within a RBBC sample normalized with respect to the applied vertical stress as the sample undergoes resedimentation to σ'_P = 10 MPa (H/D of approximately 3). As the sample height reduces dramatically during resedimentation, the height for each load increment is normalized by the distance to the bottom porous stone. The actual stresses within the sample are calculated by dividing the sample into multiple layers and assigning a coefficient of friction (f) which acts between the soil and the wall of the consolidometer. This will be discussed further in Section 5.2.2.

			1 mol/l Sample				0.005 mol/l Sample			
Applied σ_z', kPa	OCR	k_0	Friction Corrected σ_z', kPa	Height, mm	$\Delta\sigma_z'$, kPa	$\Delta\sigma_z'/\sigma_z'$, %	Friction Corrected σ_z', kPa	Height, mm	$\Delta\sigma_z'$, kPa	$\Delta\sigma_z'/\sigma_z'$, %
16	6	1.230	14	97	2	10%	15	79	1	8%
48	2	0.848	46	96	2	4%	46	79	2	4%
96	1	0.661	93	94	3	3%	94	76	2	2%
192	1	0.661	187	90	5	2%	188	71	4	2%
416	1	0.661	408	84	8	2%	409	68	7	2%
800	1	0.661	785	80	15	2%	789	60	11	1%
416	2	0.825	407	82	9	2%	409	63	7	2%
192	4	1.072	186	83	6	3%	187	63	5	3%
96	8	1.356	91	84	5	5%	93	64	3	4%
48	17	1.715	45	85	3	7%	45	65	3	5%
16	50	2.488	14	87	2	14%	14	66	2	11%
8	100	3.147		-			7	67	1	1%

Table 2.1: Friction corrected vertical effective stress calculation spreadsheet for 0.005 and 1 mol/l kaolinite samples

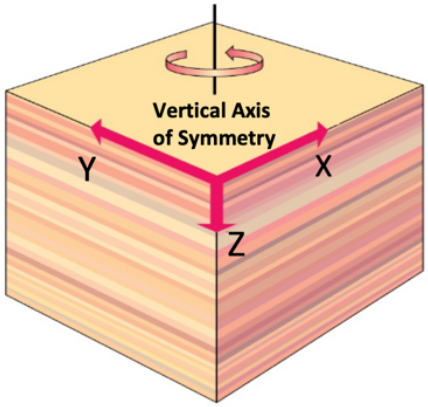

Figure 2.1: Axis of symmetry in TI material

$$\begin{bmatrix} \sigma_{11} \\ \sigma_{22} \\ \sigma_{33} \\ \sigma_{23} \\ \sigma_{13} \\ \sigma_{12} \end{bmatrix} = \begin{bmatrix} C_{11} & C_{12} & C_{13} & 0 & 0 & 0 \\ C_{21} & C_{22} & C_{23} & 0 & 0 & 0 \\ C_{31} & C_{32} & C_{33} & 0 & 0 & 0 \\ 0 & 0 & 0 & C_{44} & 0 & 0 \\ 0 & 0 & 0 & 0 & C_{55} & 0 \\ 0 & 0 & 0 & 0 & 0 & C_{66} \end{bmatrix} \begin{bmatrix} \epsilon_{11} \\ \epsilon_{22} \\ \epsilon_{33} \\ 2\epsilon_{23} \\ 2\epsilon_{13} \\ 2\epsilon_{12} \end{bmatrix}$$

Figure 2.2: Hooke's law for TI material

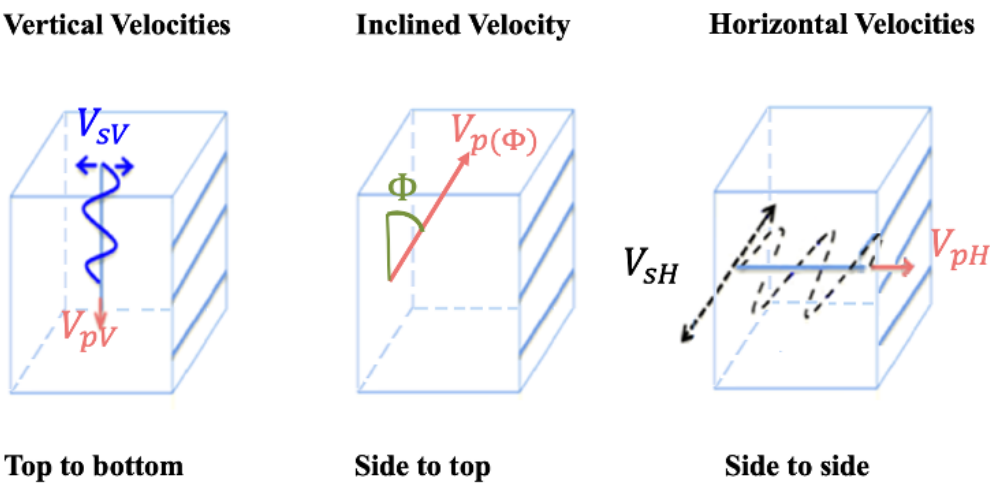

Figure 2.3: P and S Waves in vertical, inclined and horizontal directions

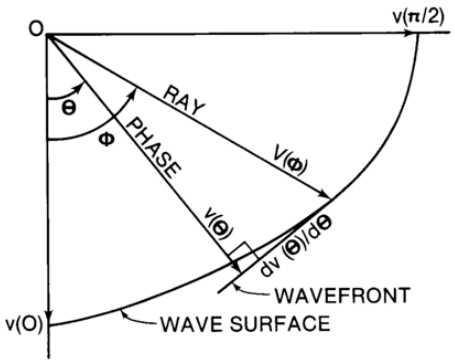

Figure 2.4: Ray (group) and phase velocities in anisotropic material

$$\begin{bmatrix} \frac{1}{E_h} & \frac{-\nu_{hh}}{E_h} & \frac{-\nu_{vh}}{E_v} & 0 & 0 & 0 \\ \frac{-\nu_{hh}}{E_h} & \frac{1}{E_h} & \frac{-\nu_{vh}}{E_v} & 0 & 0 & 0 \\ \frac{-\nu_{hv}}{E_h} & \frac{-\nu_{hv}}{E_h} & \frac{1}{E_v} & 0 & 0 & 0 \\ 0 & 0 & 0 & \frac{1}{2G_{vh}} & 0 & 0 \\ 0 & 0 & 0 & 0 & \frac{1}{2G_{vh}} & 0 \\ 0 & 0 & 0 & 0 & 0 & \frac{1}{2G_{hh}} \end{bmatrix}$$

Figure 2.5: Compliance matrix for TI material

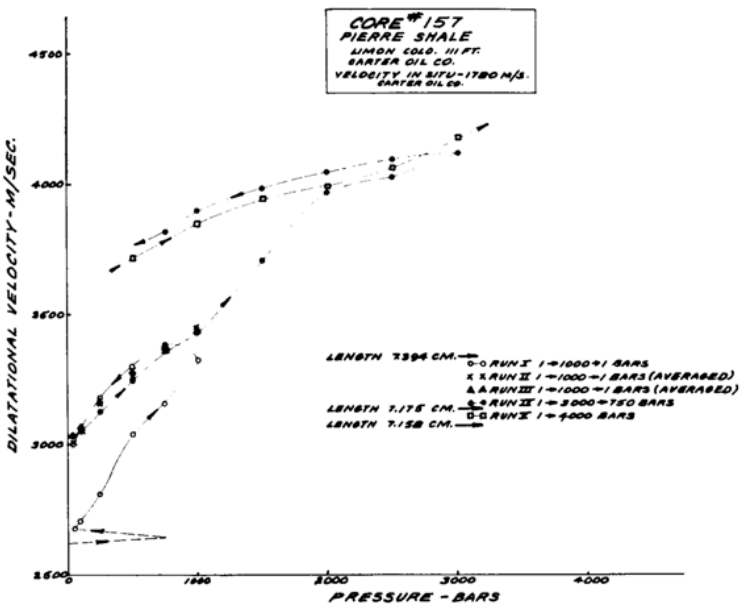

Figure 2.6: Measured dilatational (compressional) velocities with increasing confining pressure [72]

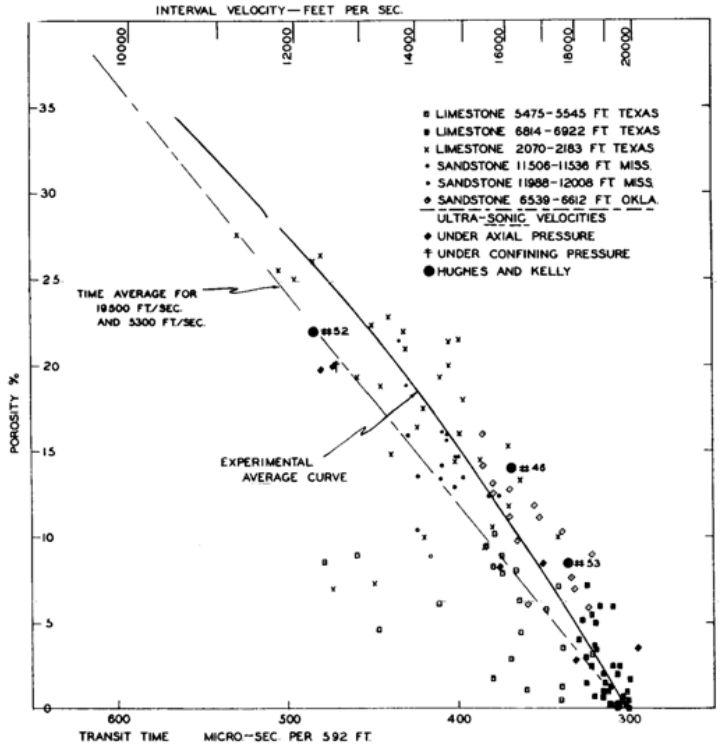

Figure 2.7: Measured compressional velocities compared to Gassmann's model [180]

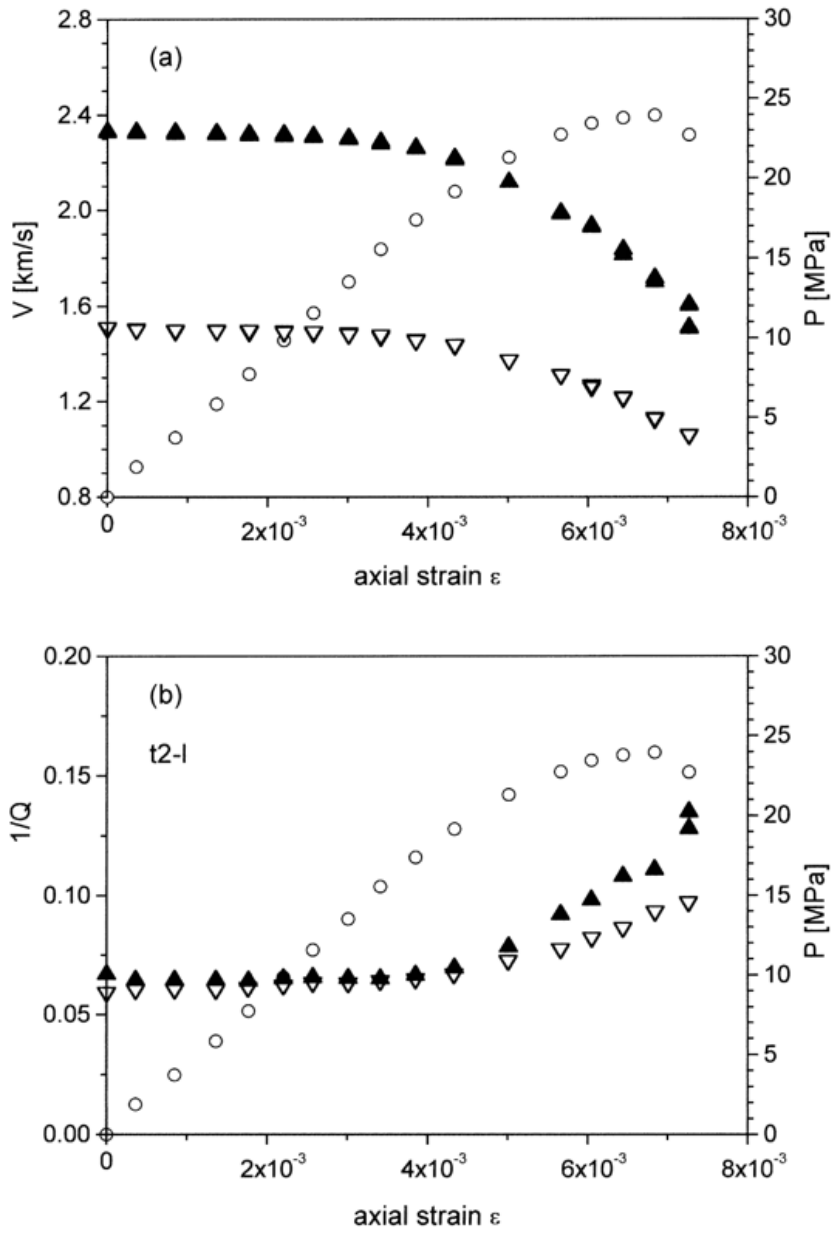

Figure 2.8: Measured P (solid triangles) and S (white triangles) wave velocities changing with axial strain, and the corresponding uniaxial stresses (white circles) [179]

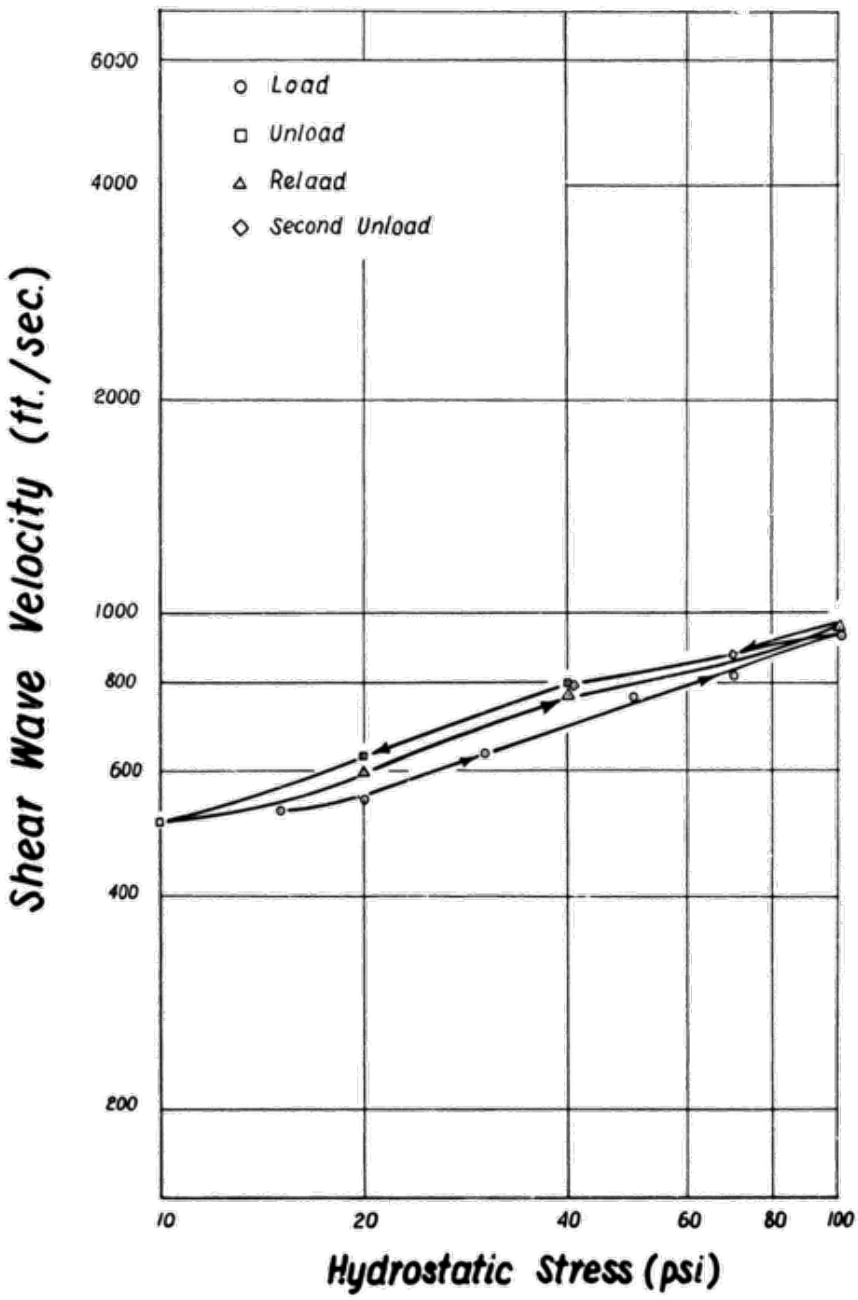

Figure 2.9: Measured shear velocities are shown during load, unload and reload [92]

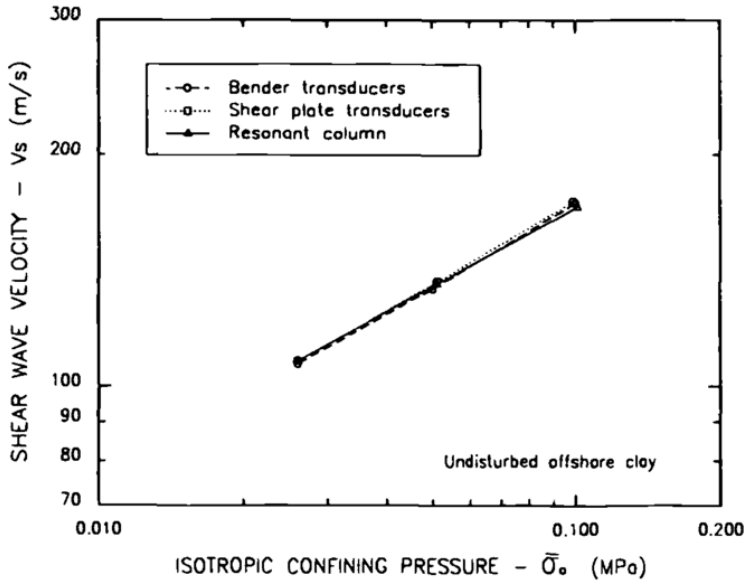

Figure 2.10: Variation of the shear wave velocity with isotropic confining pressure for undisturbed offshore clay [21]

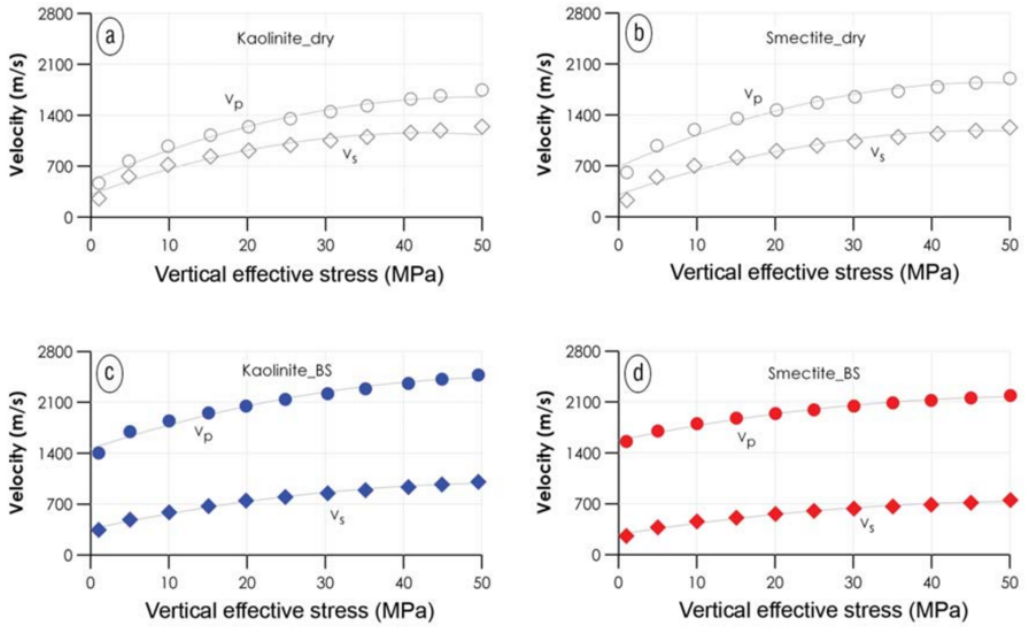

Figure 2.11: V_p and V_s plotted against vertical effective stress of mechanically compacted dry and brine-saturated kaolinite (a and c) and smectite (b and d) aggregates [112]

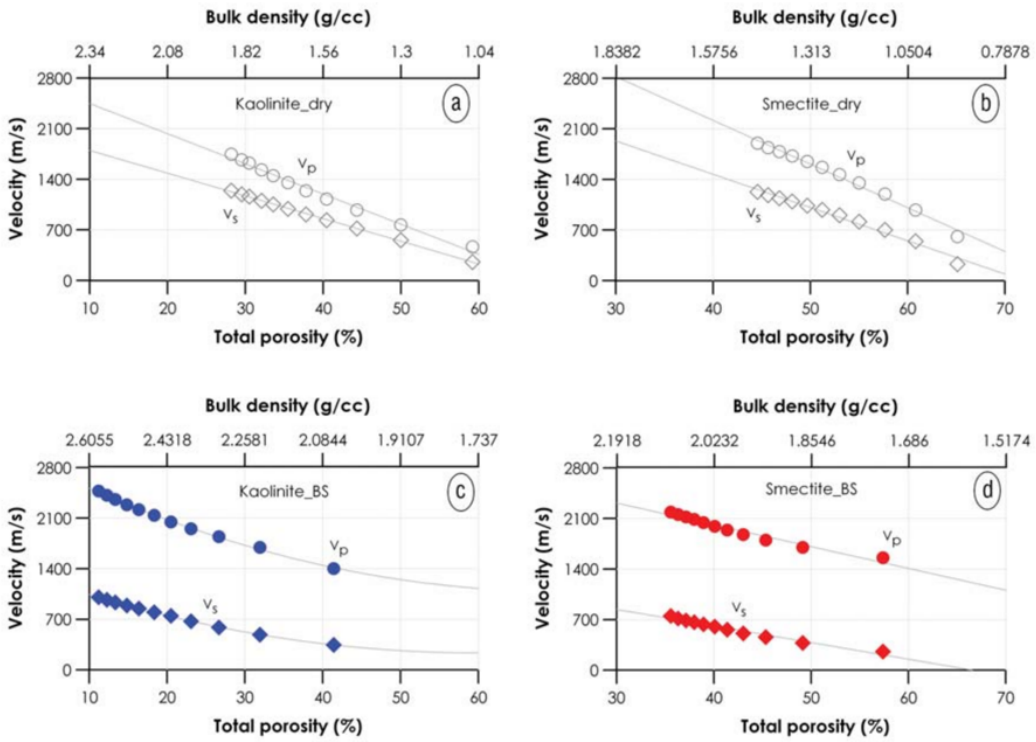

Figure 2.12: V_p and V_s plotted against porosity and bulk density of mechanically compacted dry and brine-saturated kaolinite (a and c) and smectite (b and d) aggregates [112]

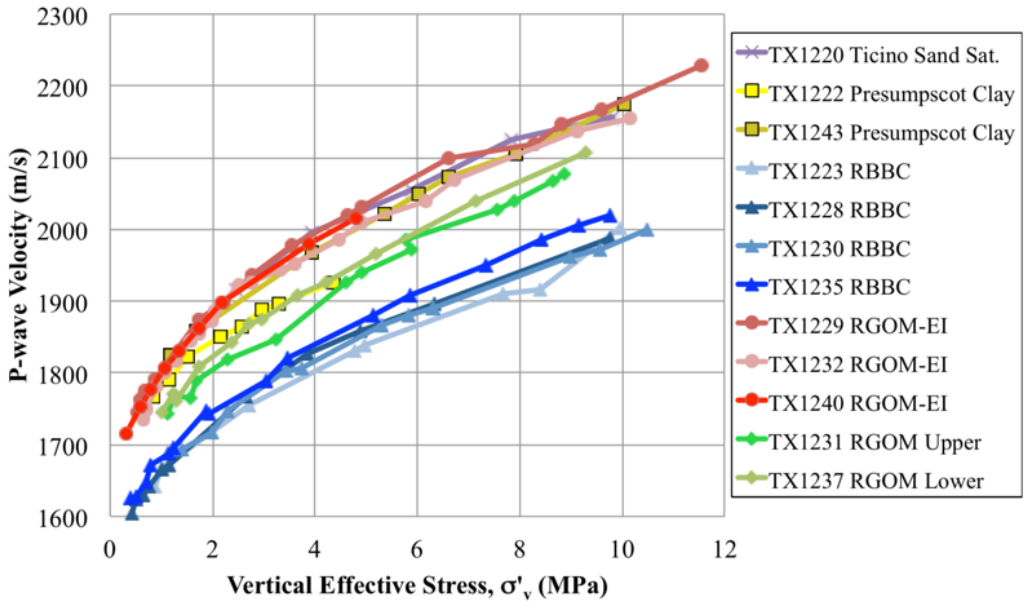

Figure 2.13: P-wave velocity results as a function of vertical effective stress for all saturated materials tested [103]

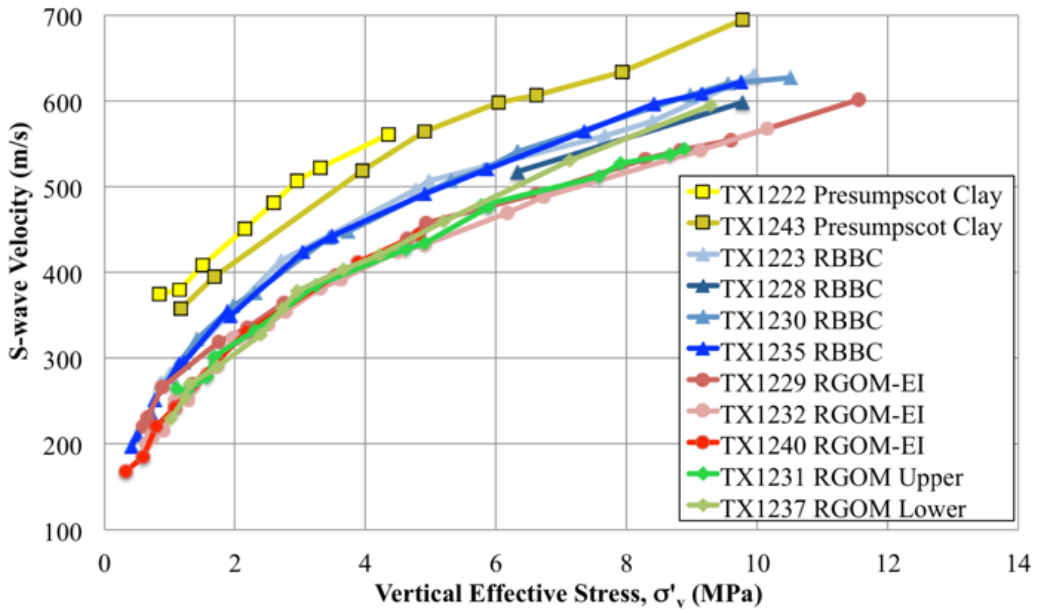

Figure 2.14: S-wave velocity results as a function of vertical effective stress for all saturated materials tested [103]

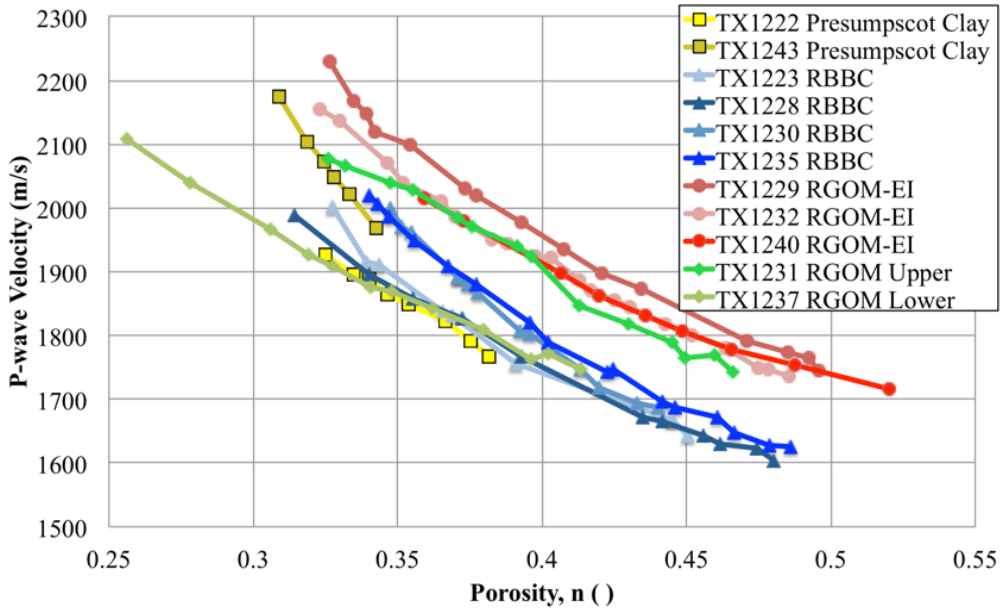

Figure 2.15: P-wave velocity results as a function of porosity [103]

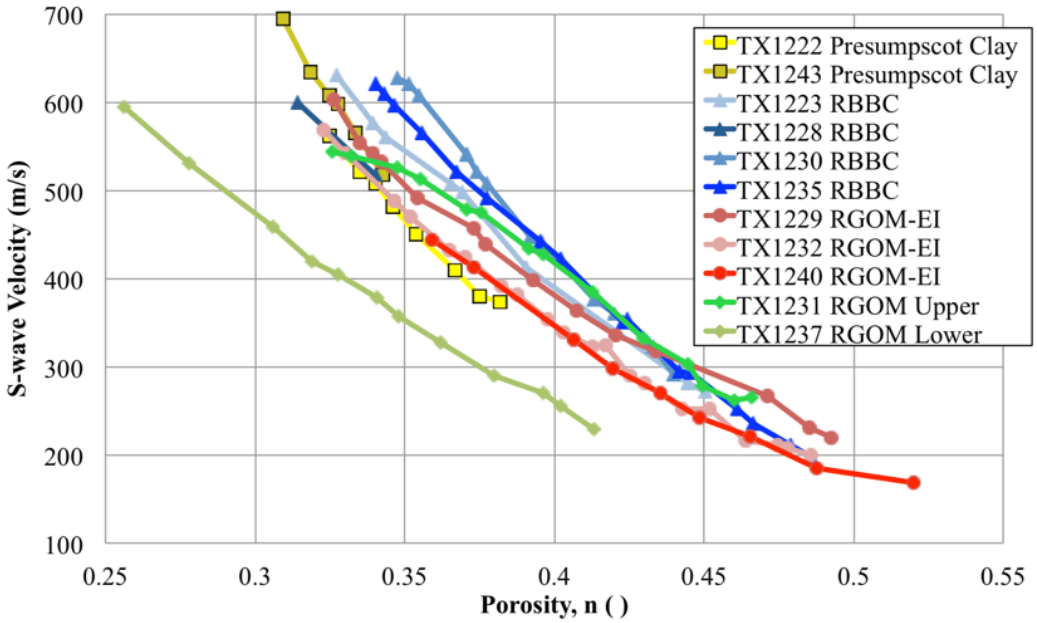

Figure 2.16: S-wave velocity results as a function of porosity [103]

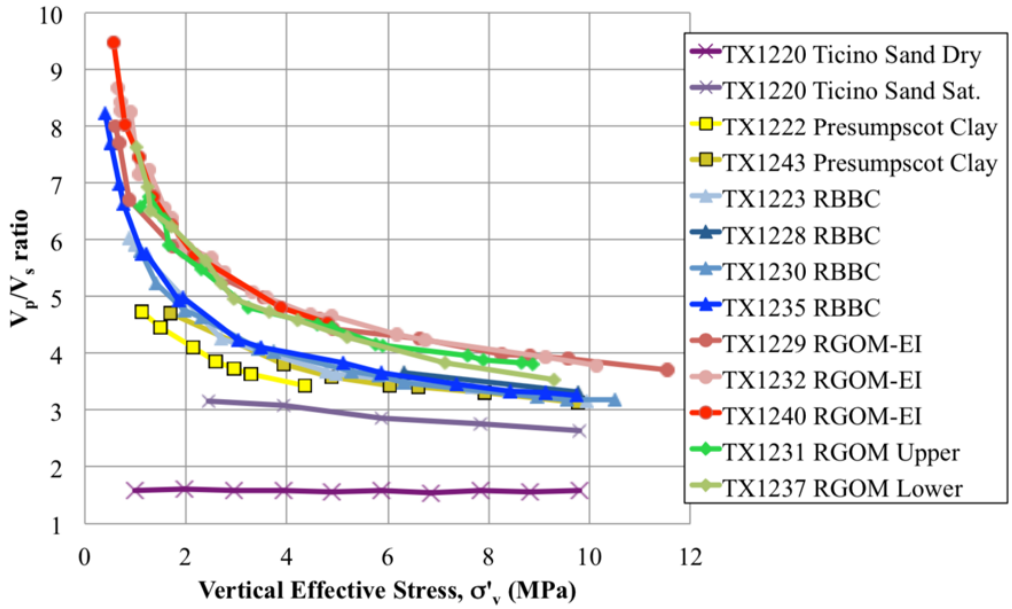

Figure 2.17: The ratio of P-wave to S-wave velocity is shown as a function of vertical effective stress [103]

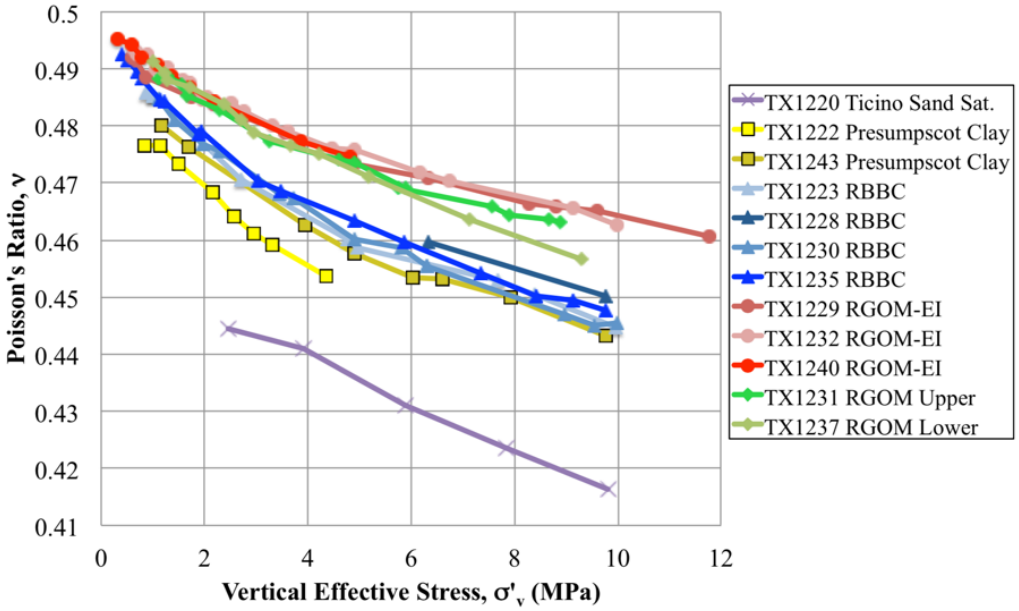

Figure 2.18: Velocity-derived Poisson's ratio for normally consolidated material as a function of stress [103]

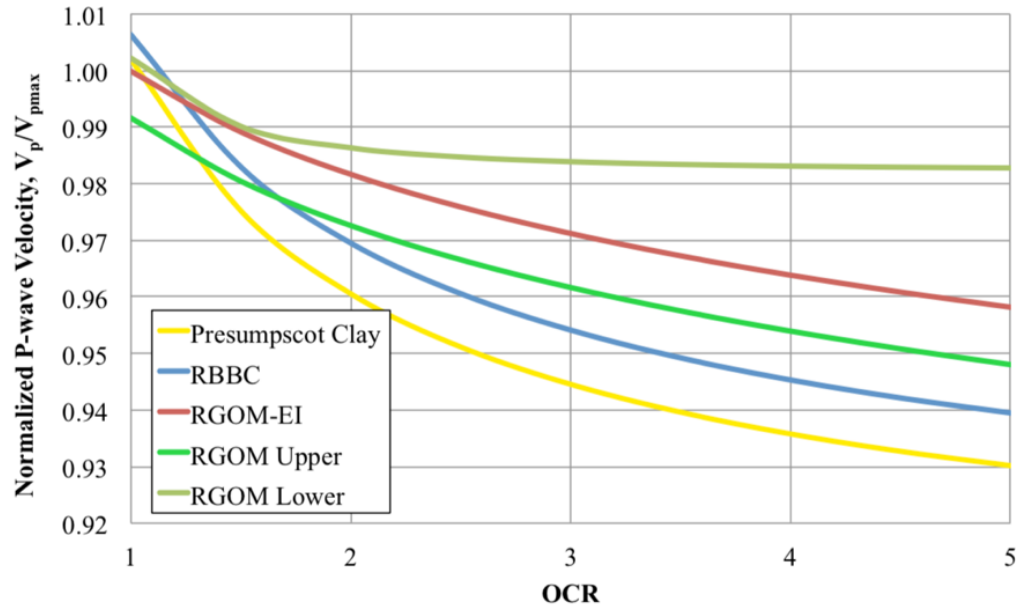

Figure 2.19: The normalized unloading P-wave velocity curves are shown for all the clays. These are best-fit lines intended to describe the general behavior [103]

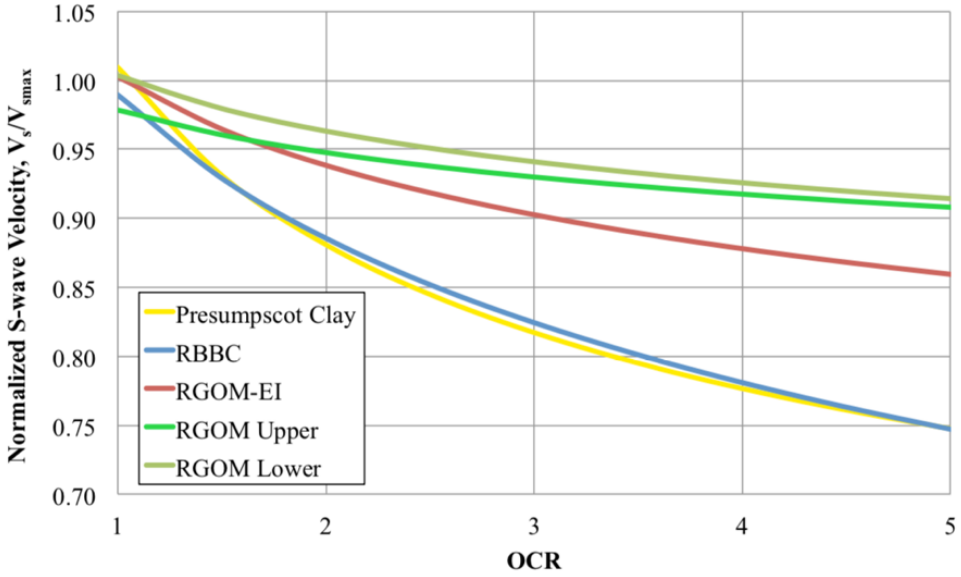

Figure 2.20: The normalized unloading S-wave velocity curves are shown for all the clays. These are best-fit lines intended to describe [103]

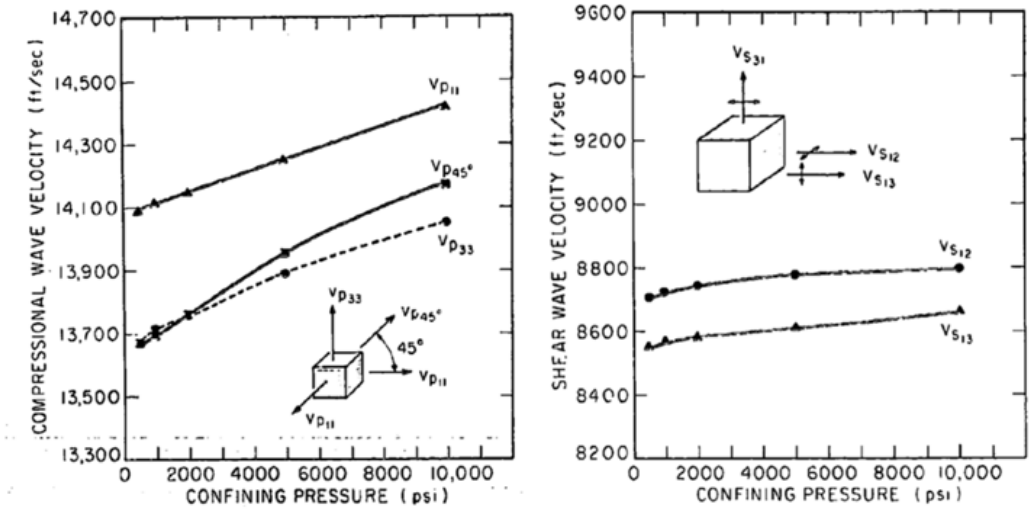

Figure 2.21: Measured directional velocities with increasing confining stress level in dry Green River shale [126]

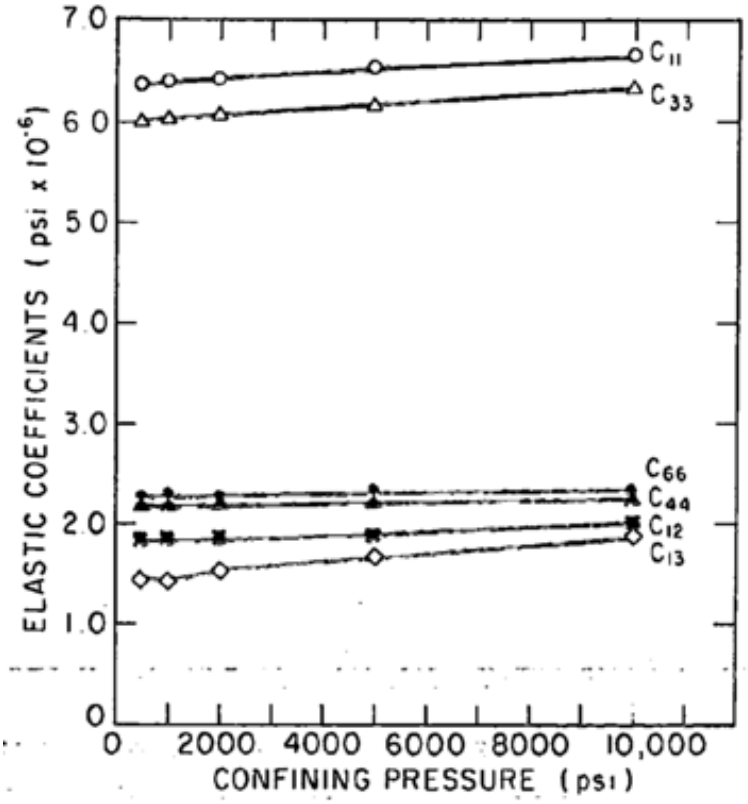

Figure 2.22: Stiffness matrix elements calculated based on the measured directional velocities [126]

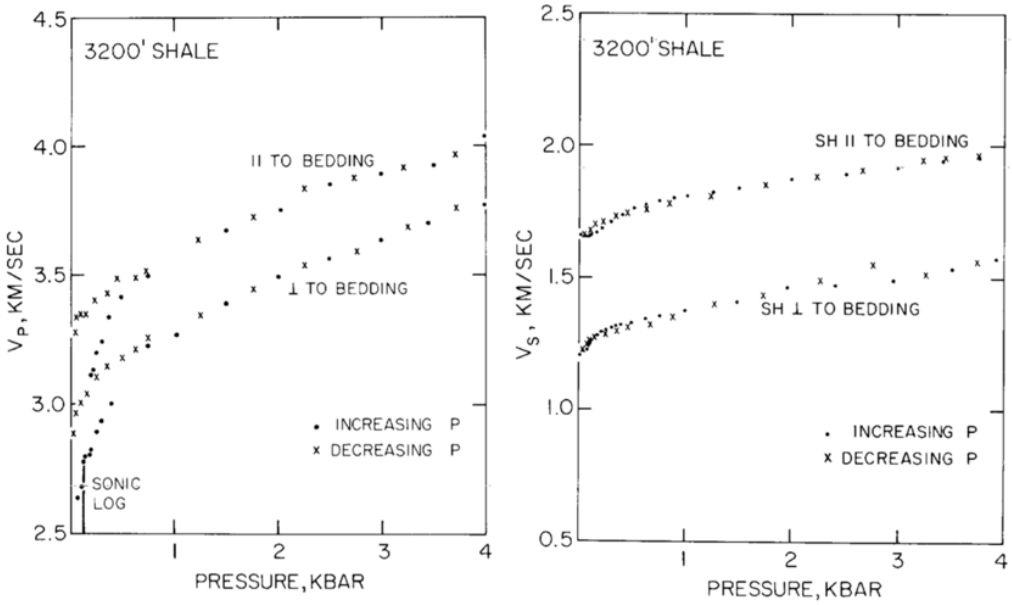

Figure 2.23: Compressional and shear velocities parallel and perpendicular to bedding in shale samples retrieved from 3200 ft, under loading and unloading conditions [80]

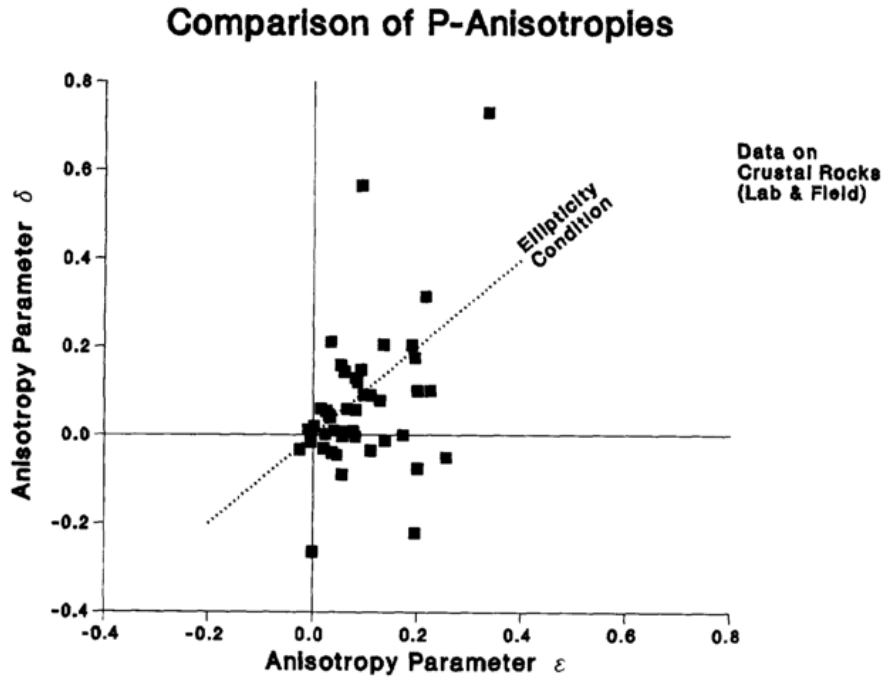

Figure 2.24: This figure indicates the noncorrelation of the two anisotropy parameters ϵ and γ [158]

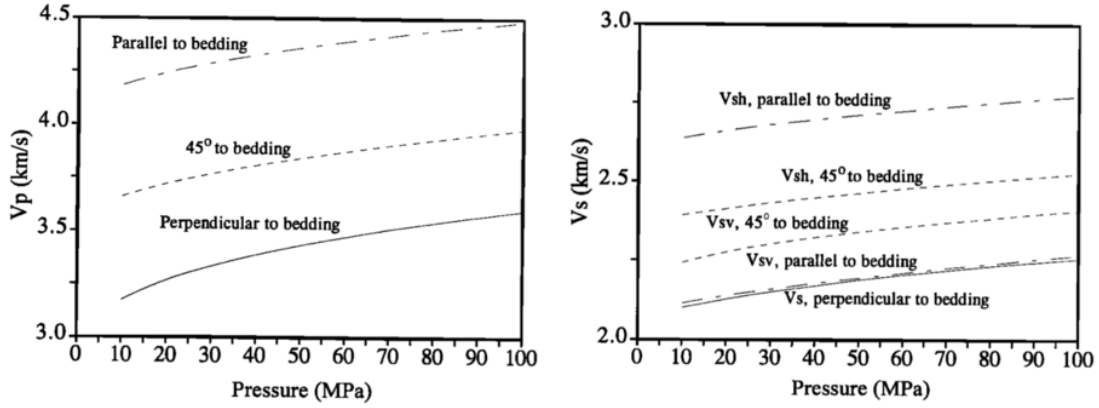

Figure 2.25: P and shear velocities in specimens with different kerogen content [168]

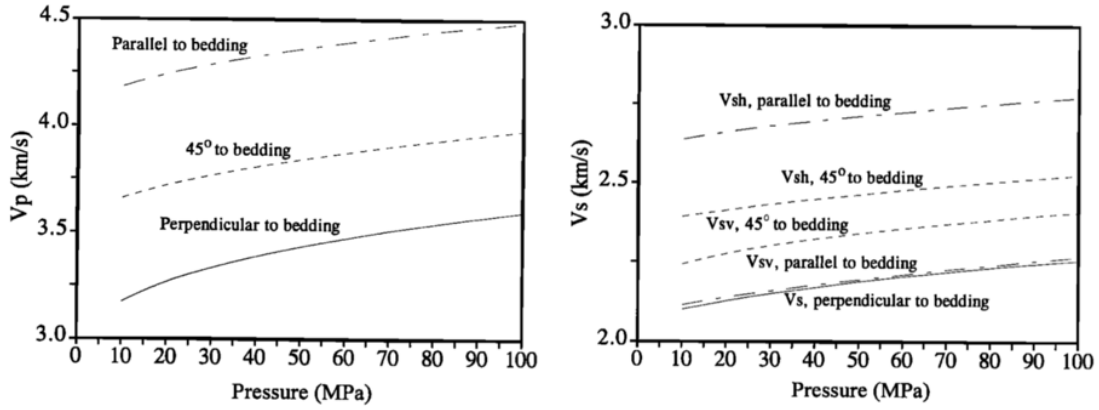

Figure 2.26: P and shear velocities in different directions as a function of confining pressure [79]

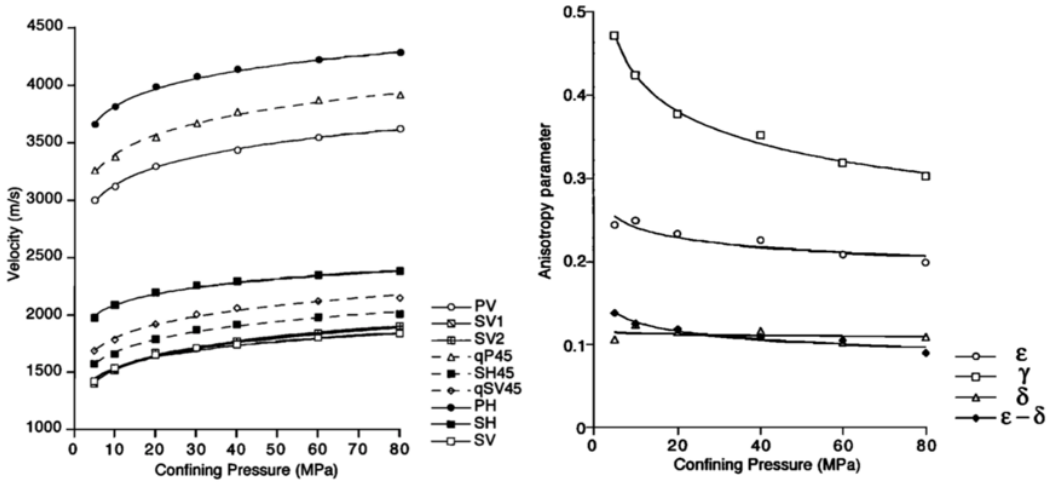

Figure 2.27: Directional velocities and anisotropy parameters with increasing confining pressure in Jurassic shale [66]

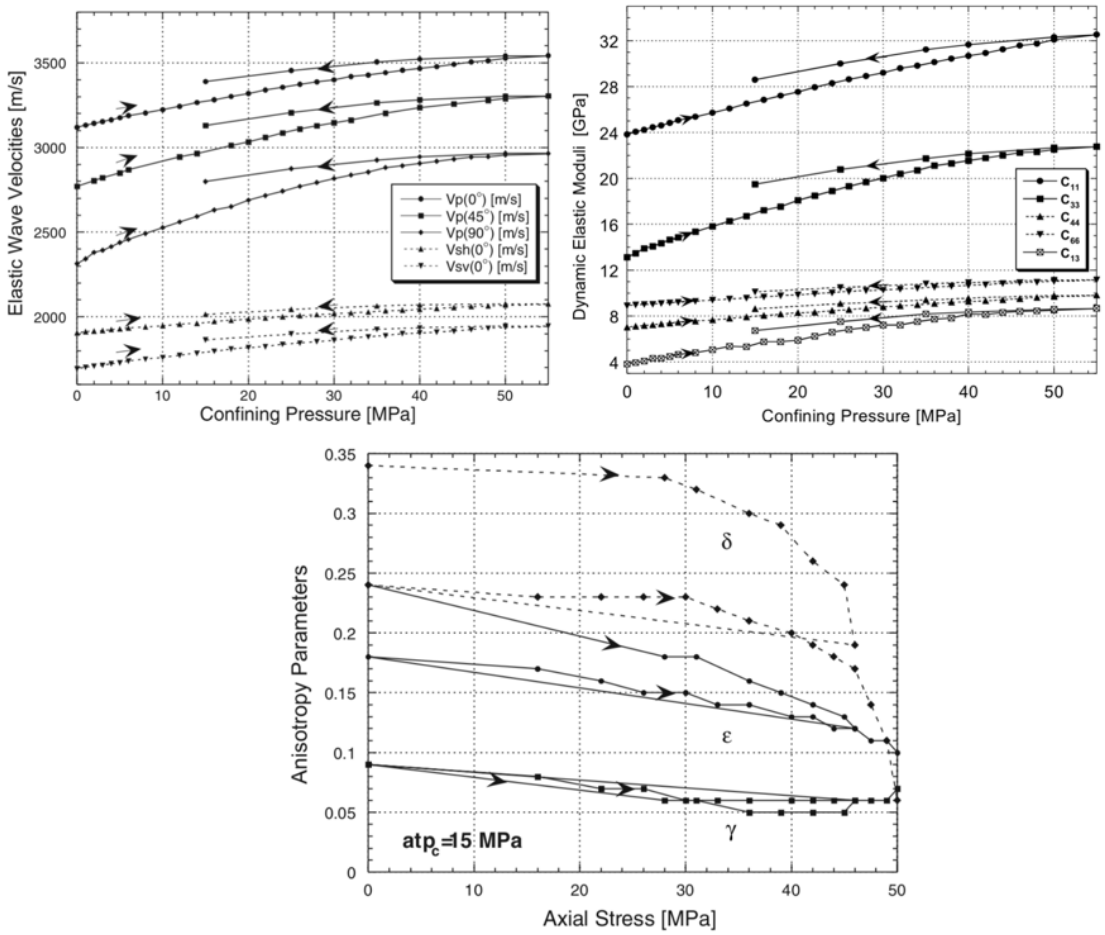

Figure 2.28: Directional velocities, Cijs and anisotropy parameters (The loading starts with a confining pressure cycle between 0 and 55 MPa, then unloading from 55 to 15 MPa, at 15 MPa confining pressure, a deviatoric stress is applied) [137]

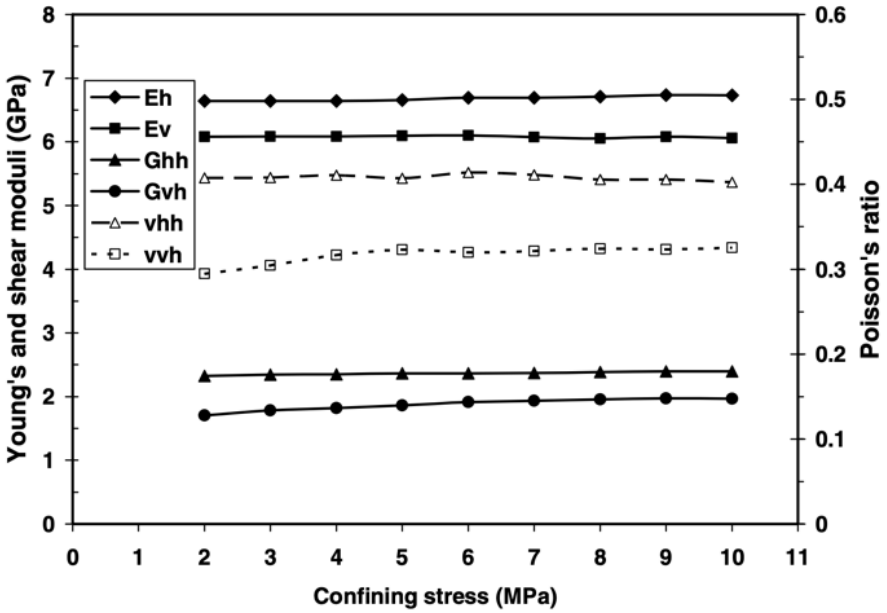

Figure 2.29: Dynamic elastic constants derived from ultrasonic wave velocities versus confining stress [178]

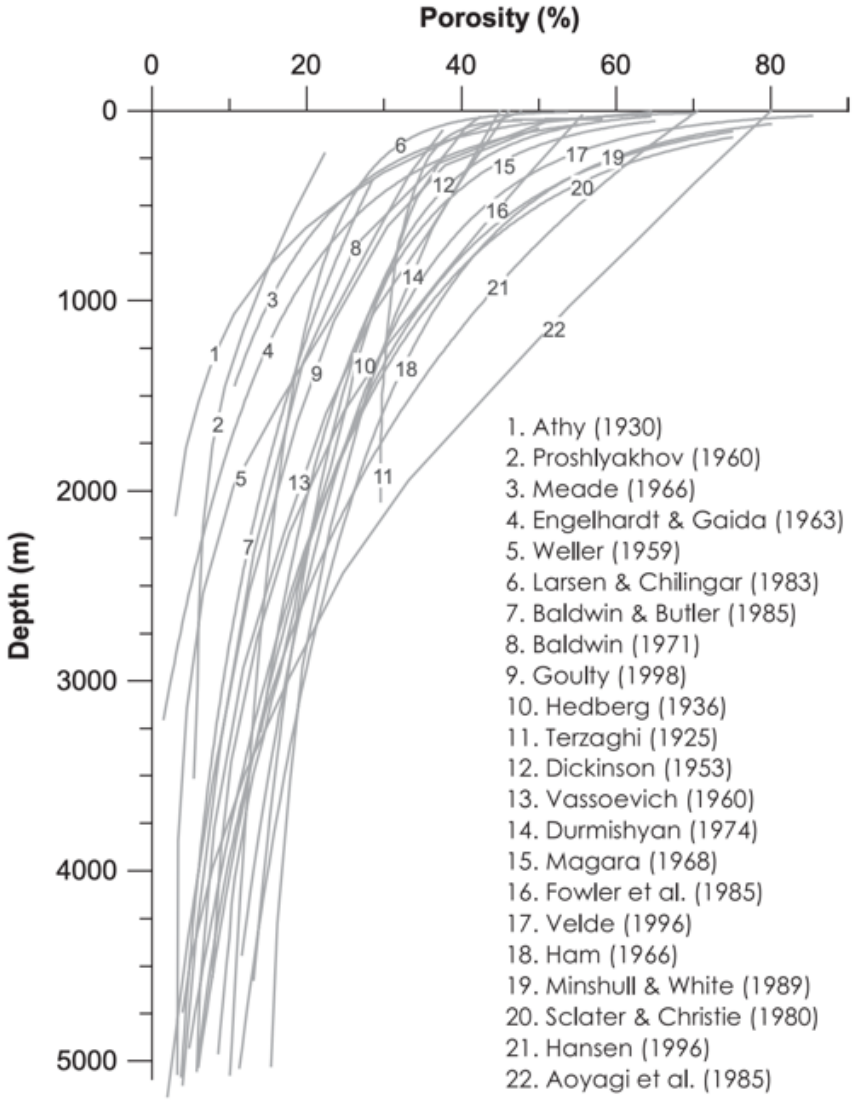

Figure 2.30: Dynamic elastic constants derived from ultrasonic wave velocities versus confining stress [178]

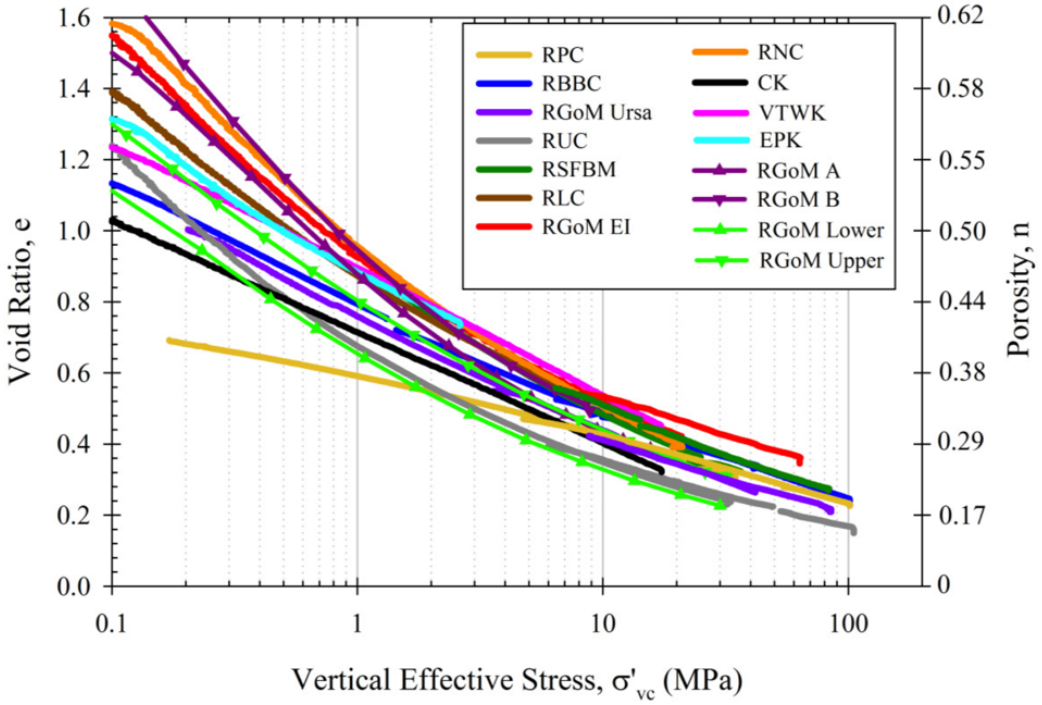

Figure 2.31: One dimensional virgin compression behavior of different materials [26]

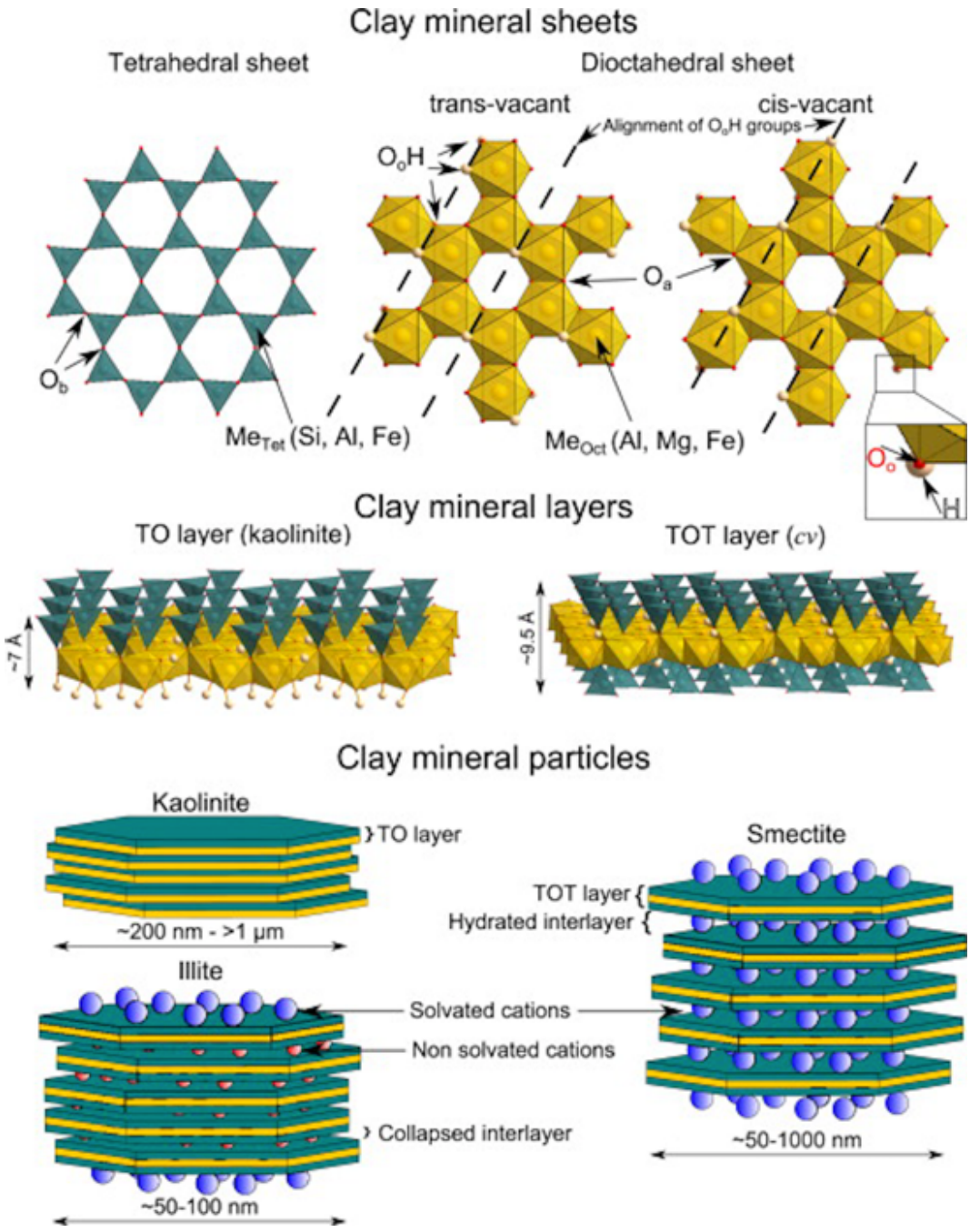

Figure 2.32: Clay mineral structure [161]

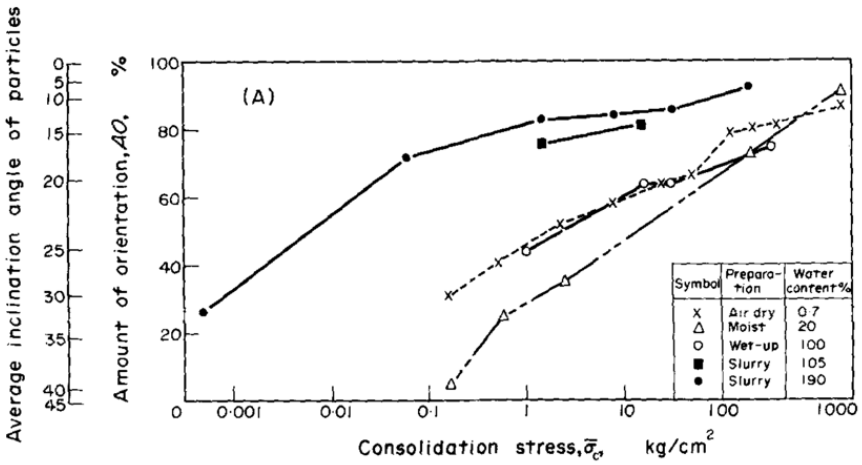

Figure 2.33: Effect of one-dimensional consolidation of kaolinite on fabric [105]

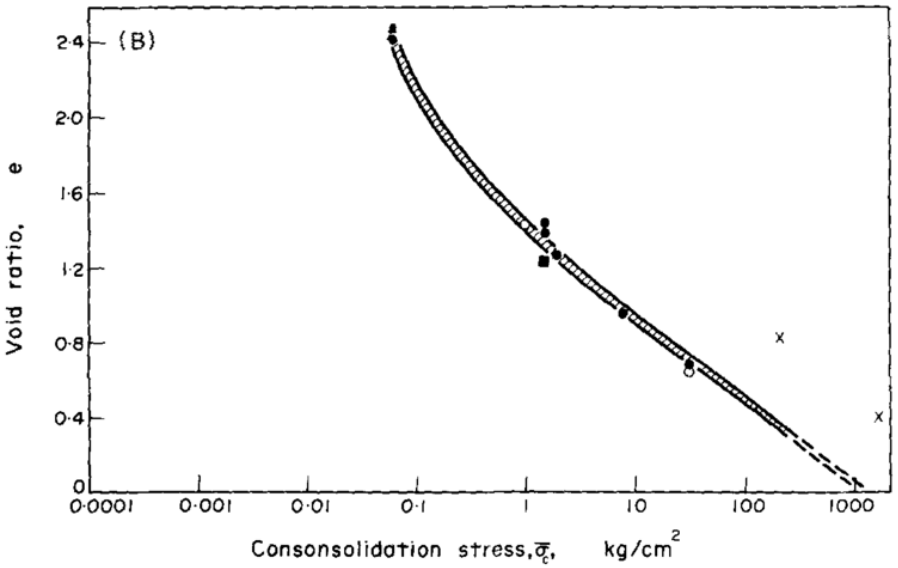

Figure 2.34: Effect of one-dimensional consolidation of kaolinite on void ratio [105]

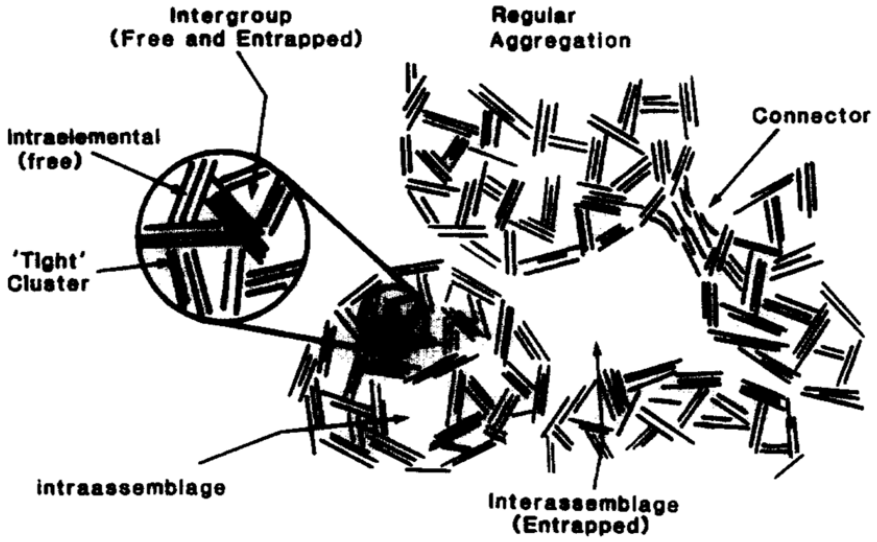

Figure 2.35: Free pores are pores through which fluid can flow freely, represented by second intrusion. Entrapped pores are pores in which fluid is trapped and does not flow, represented by the difference in volume of mercury intruded in first and second intrusion [55]

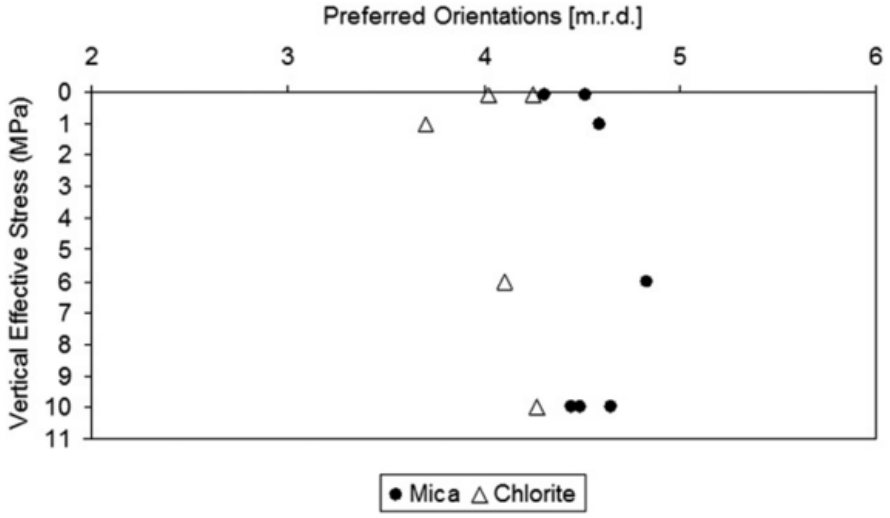

Figure 2.36: Resedimented Boston Blue Clay (BBC) with 57% clay-size particles by mass shows a small increase in preferred orientation (maximum pole density) with increasing vertical effective stress over a range of $0.1e^{10}$ MPa for both mica and chlorite [34]

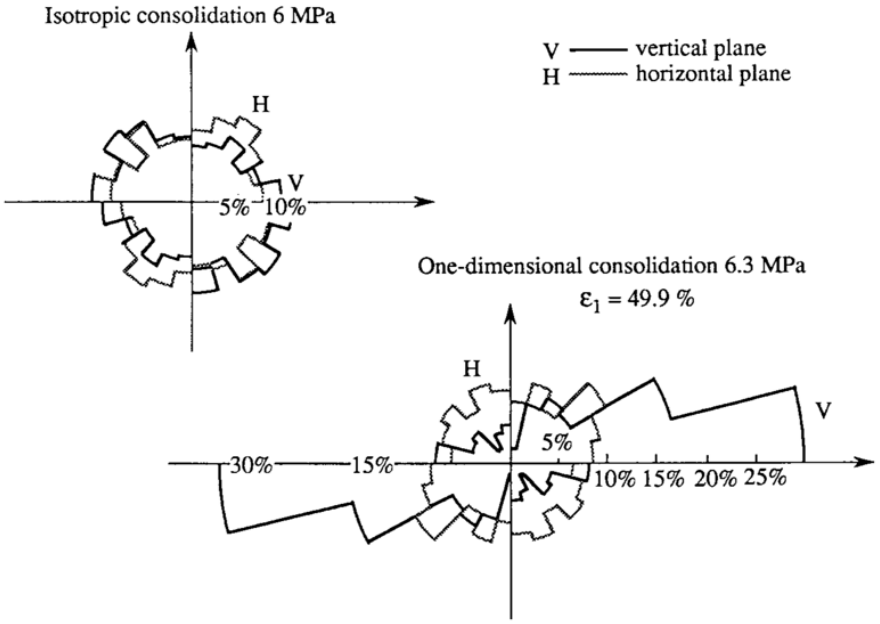

Figure 2.37: Rose diagrams of bentonite particle orientation after 1-D consolidation tests [63]

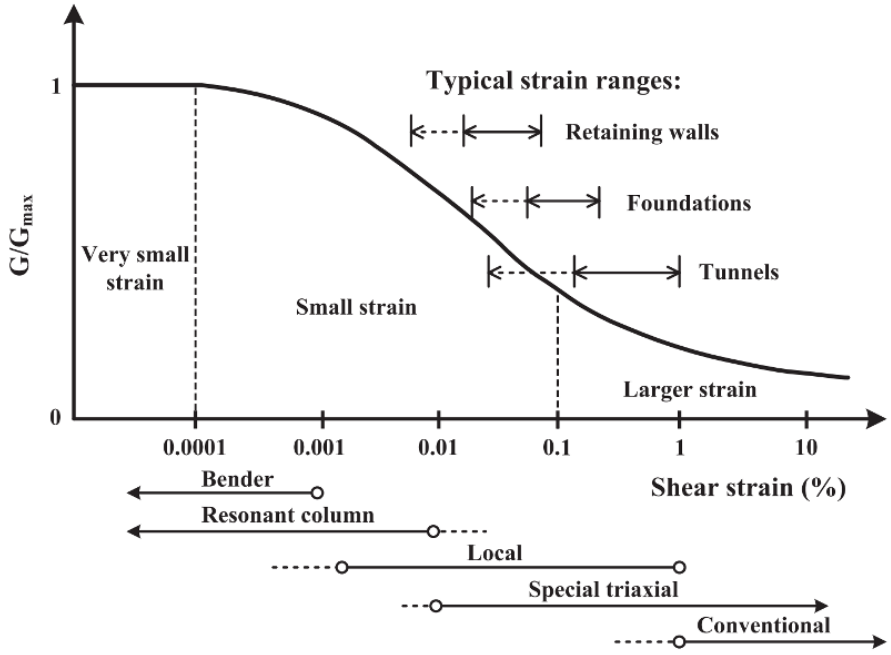

Figure 2.38: Normalized stiffness degradation curve [96]

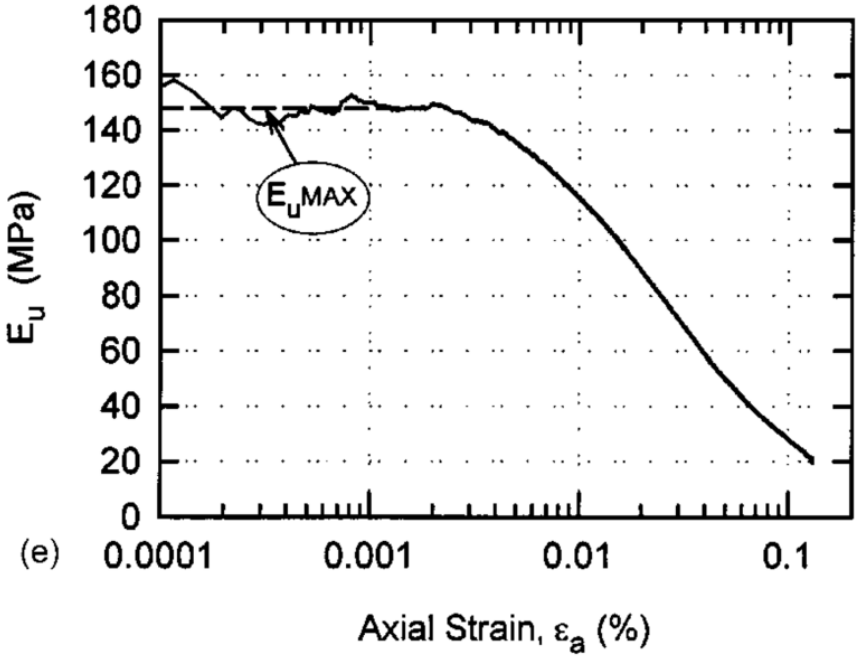

Figure 2.39: Stiffness degradation curve for RBBC shows that linear behavior prevails until a strain of 0.005% [135]

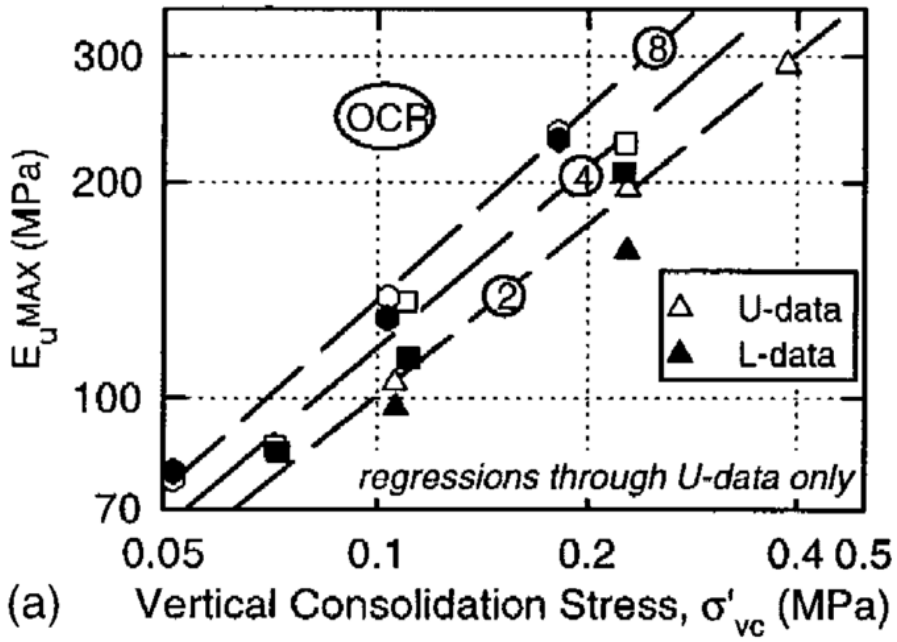

Figure 2.40: Relationship between initial stiffness of OC resedimented Boston Blue Clay and pre-shear vertical effective stress for loading and unloading consolidation paths [135]

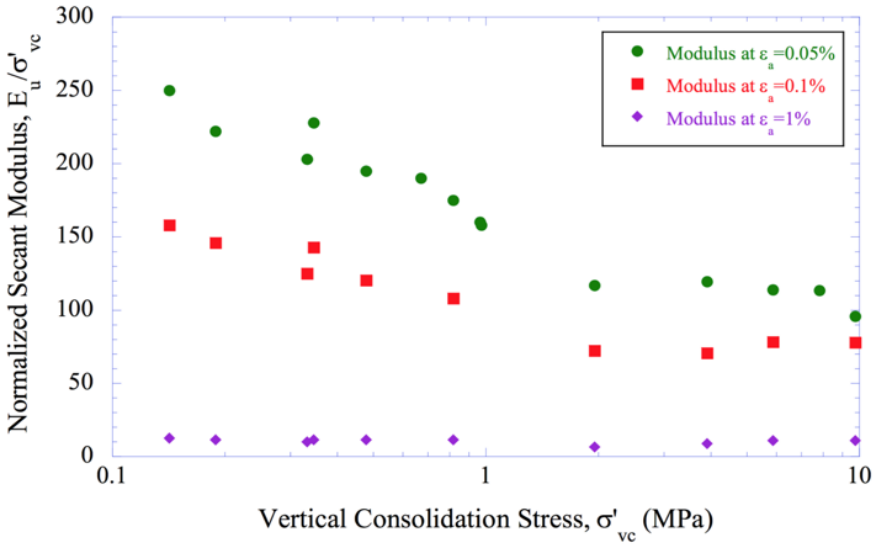

Figure 2.41: Normalized undrained secant modulus versus stress level for NC RBBC from CK_0UC triaxial tests [2]

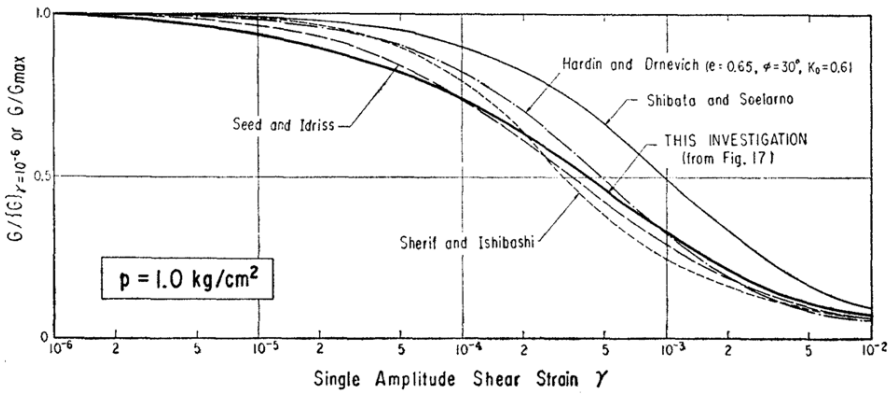

Figure 2.42: Research comparison for strain-dependency of shear modulus for mean effective stress of 1 kg/cm^2 [75]

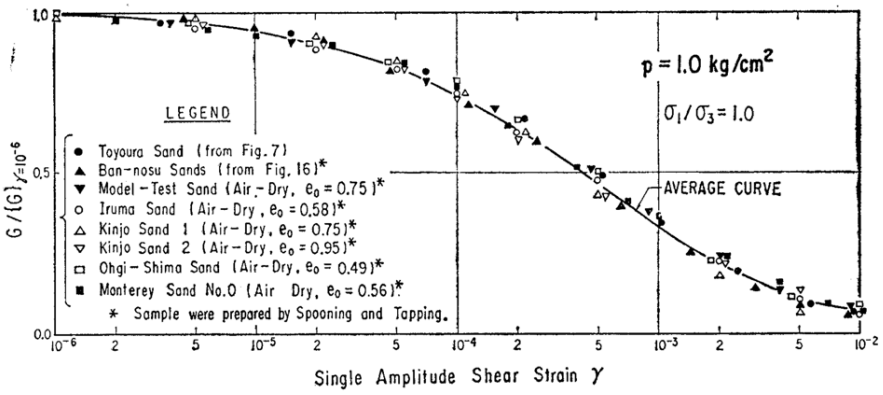

Figure 2.43: Shear modulus degradation curve for tested sands [75]

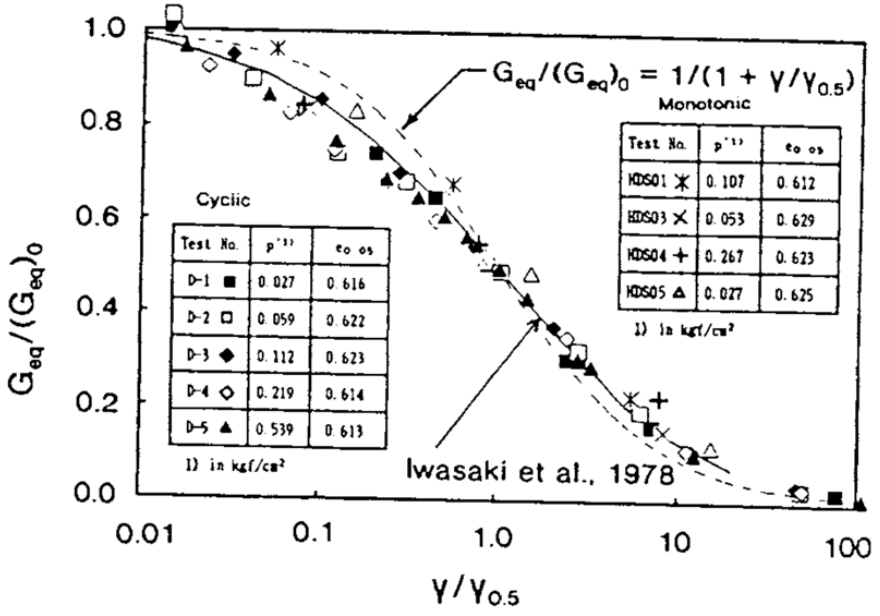

Figure 2.44: Degradation curve for Hamaoka sand [156]

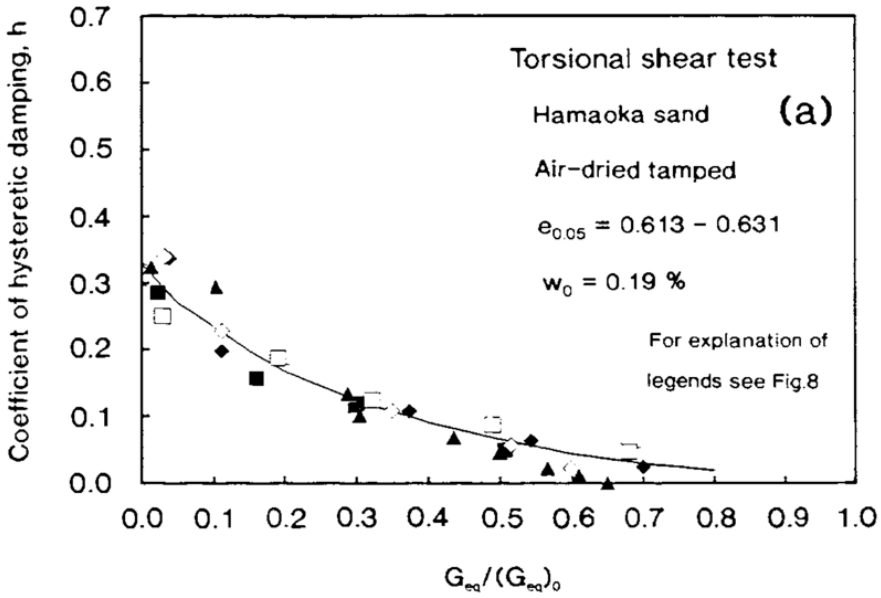

Figure 2.45: Decreasing coefficient of hysteretic damping with increasing shear modulus ratio [156]

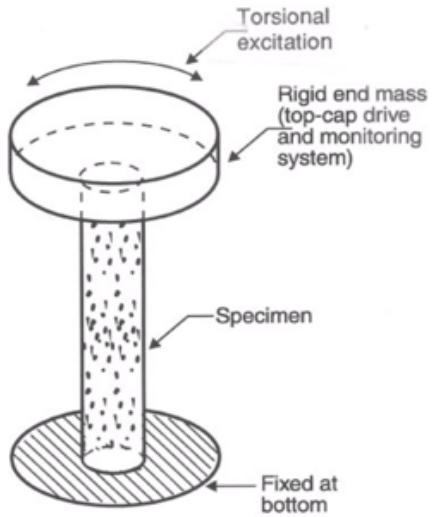

Figure 2.46: Resonant column test (NGI)

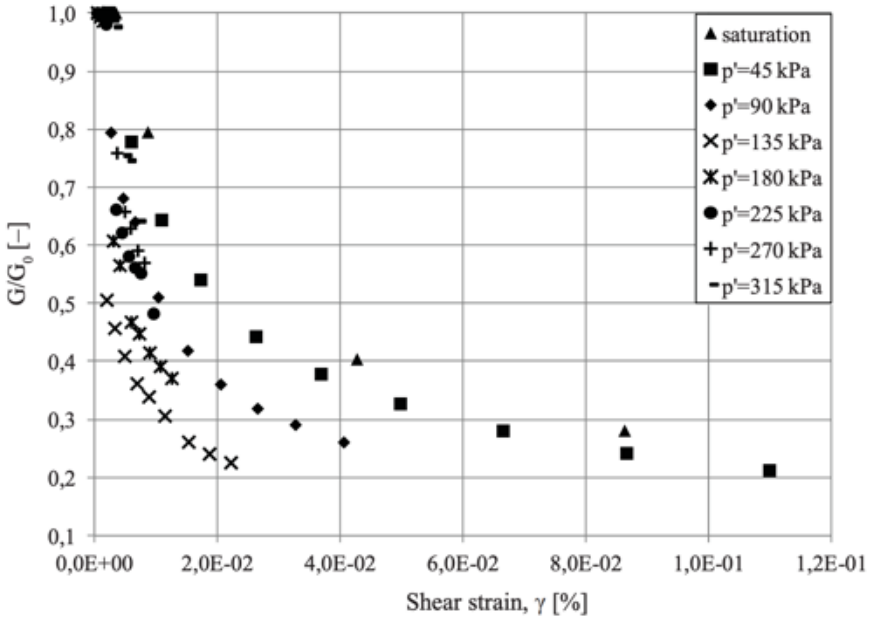

Figure 2.47: Shear stiffness degradation curve for Warsaw area soil with different mean effective stresses [138]

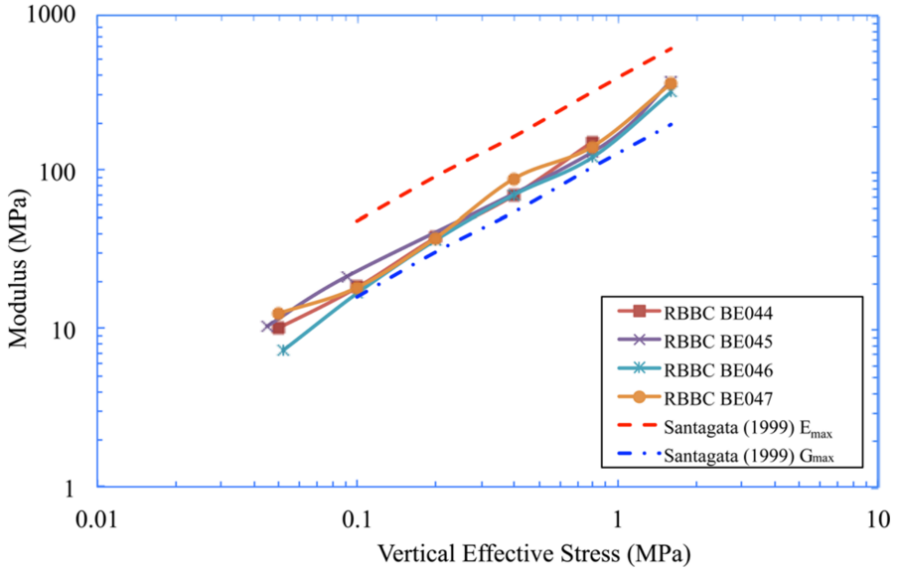

Figure 2.48: Experimental shear modulus values for RBBC compared to published results [104]

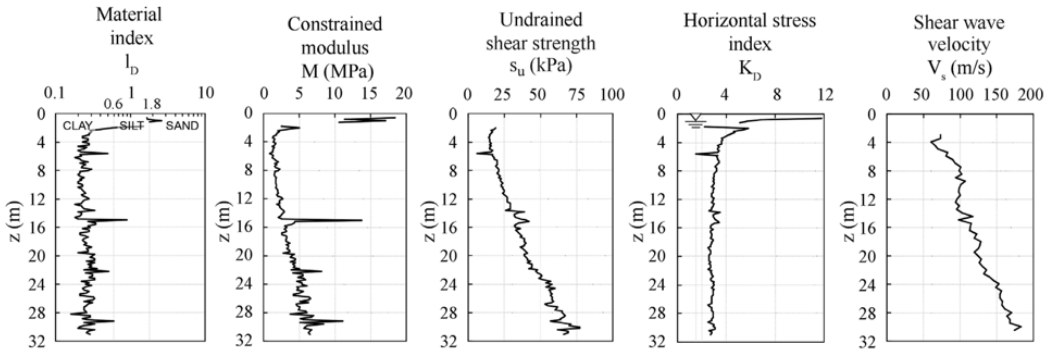

Figure 2.49: SDMT profiles at Fucino plain [101]

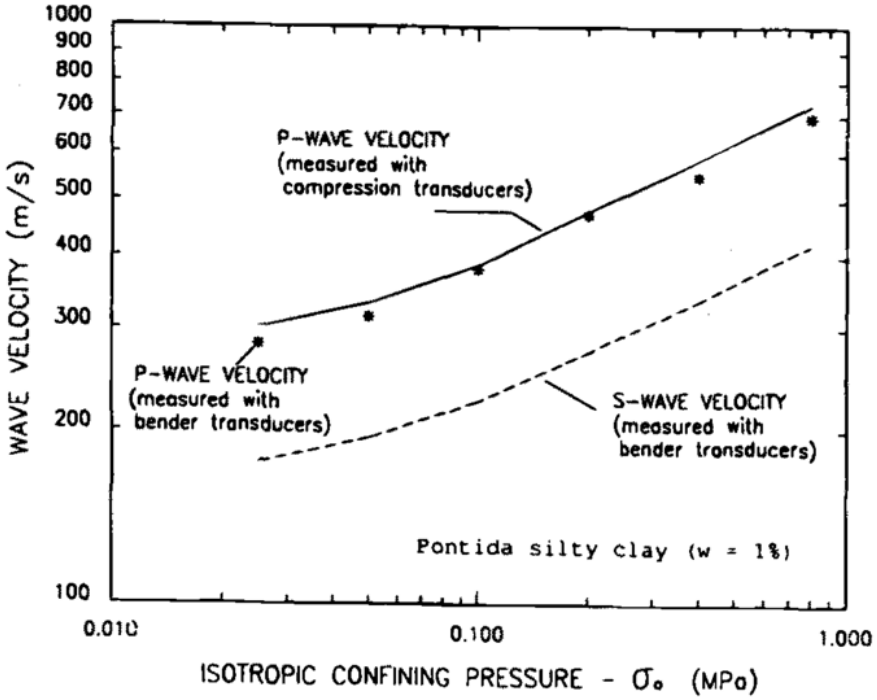

Figure 2.50: Compression and shear wave velocity measurements of dry Pontida silty clay [21]

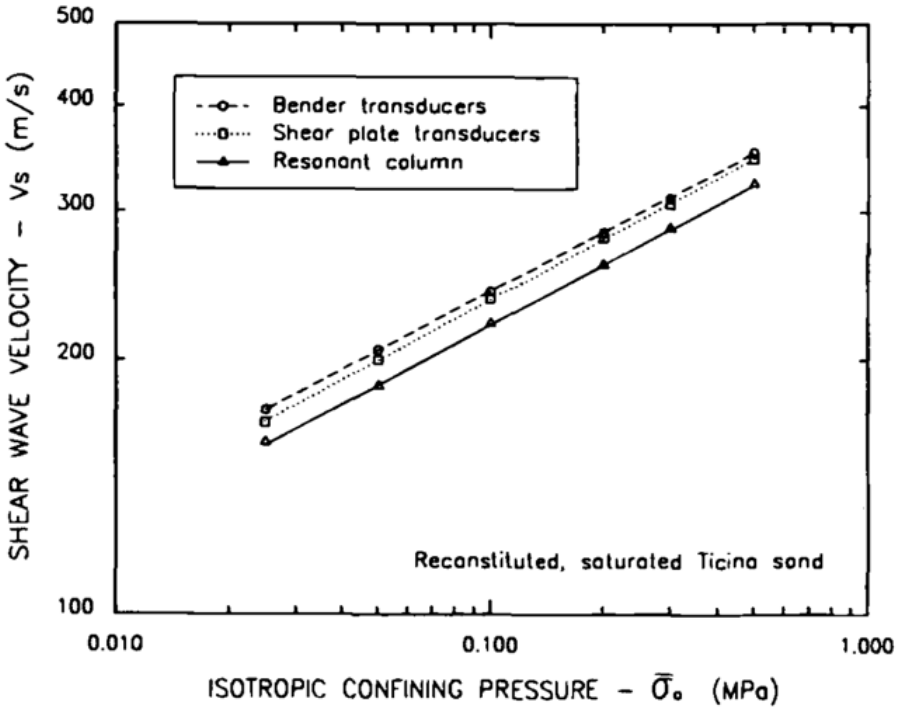

Figure 2.51: Variation of the shear wave velocity with isotropic confining pressure for reconstituted, saturated Ticino sand [21]

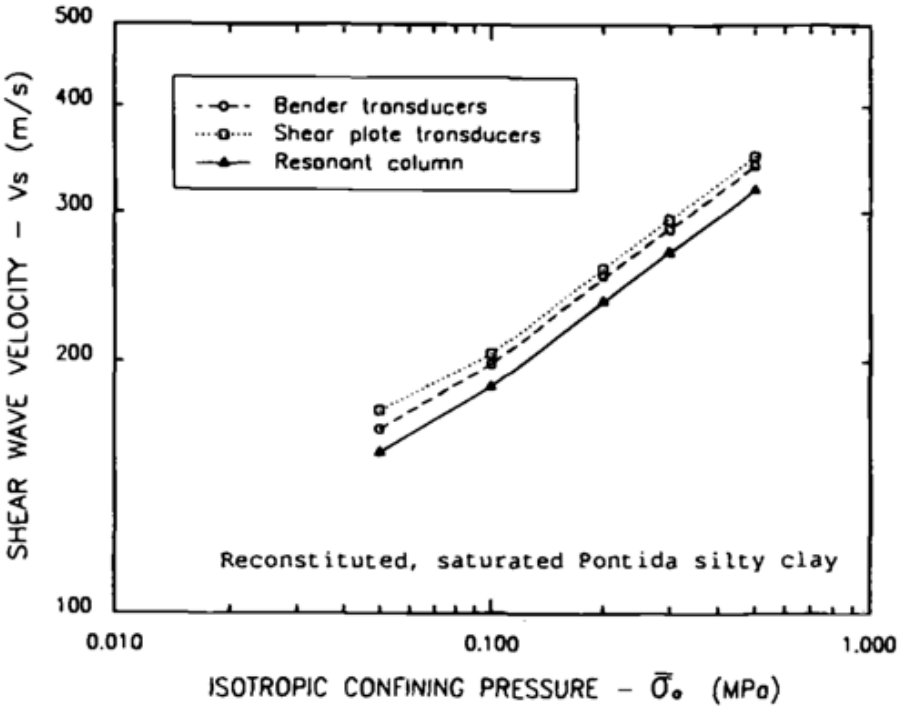

Figure 2.52: Variation of the shear wave velocity with isotropic confining pressure for reconstituted, saturated Pontida silty clay [21]

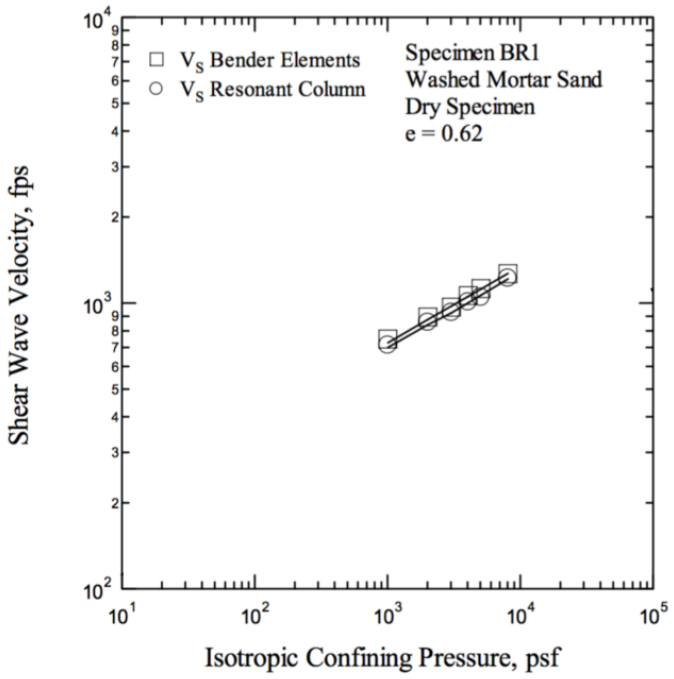

Figure 2.53: V_s results for both resonant column and bender elements [162]

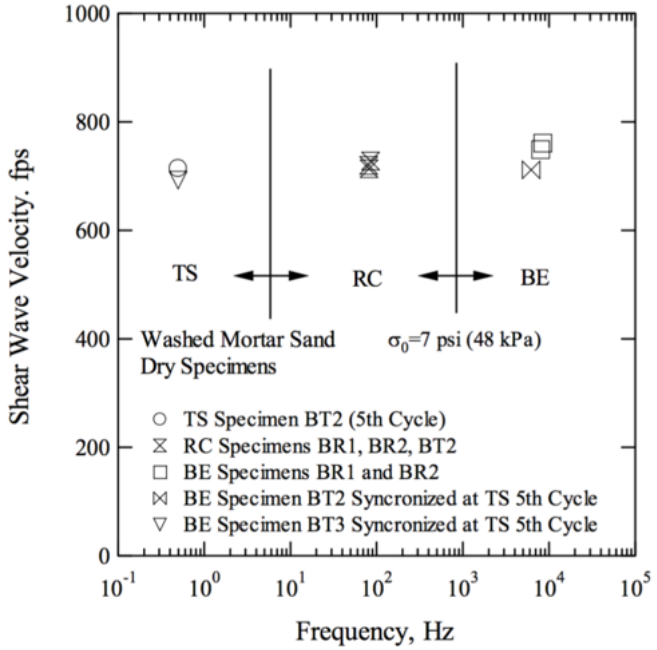

Figure 2.54: Comparison of torsional shear, resonant column, and bender element tests on washed mortar sand specimens at 48 KPa, with varying driving frequencies [162]

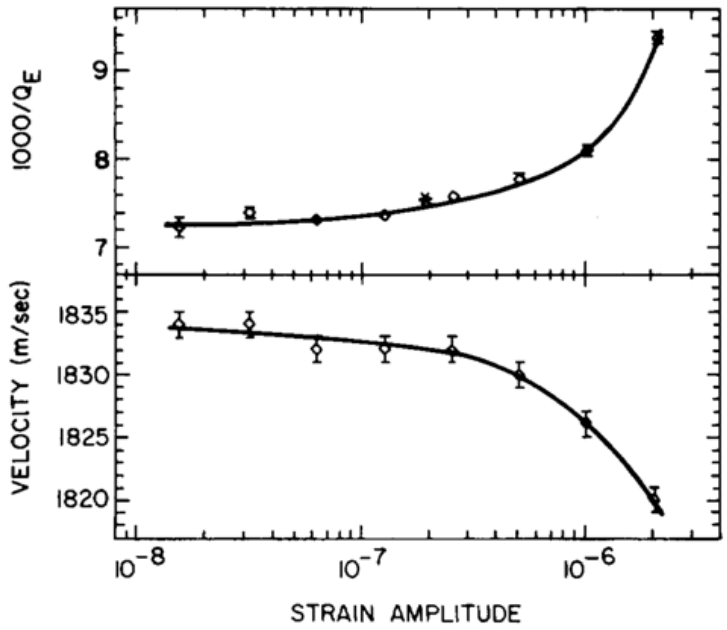

Figure 2.55: Variation of attenuation ($1000/Q_E$) and velocity with strain amplitude for dry Massilon sandstone in extensional resonance. The star indicates the value found from the resonance peak half-width. All other values are from resonance decay [176]

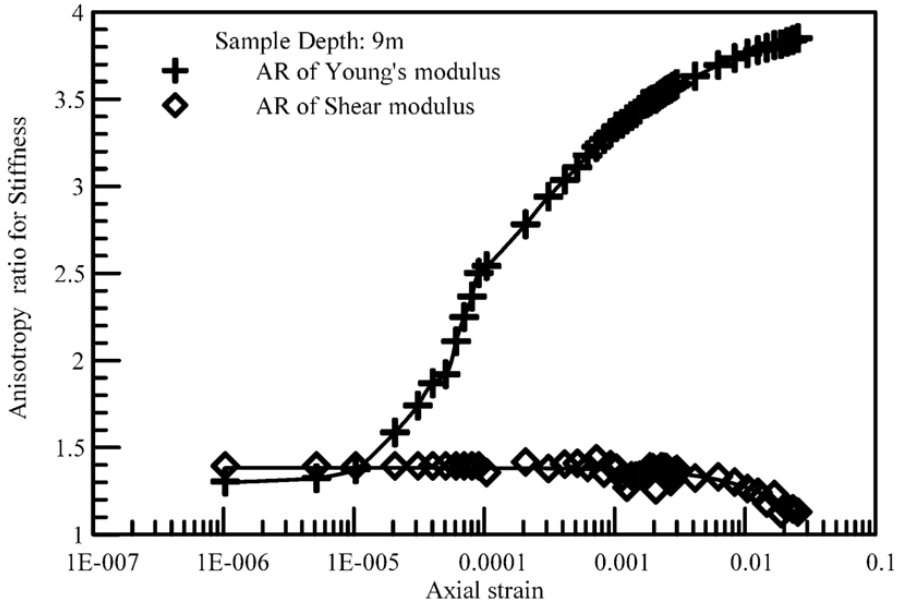

Figure 2.56: Variation of anisotropy ratios for the stiffness during undrained shearing [157]

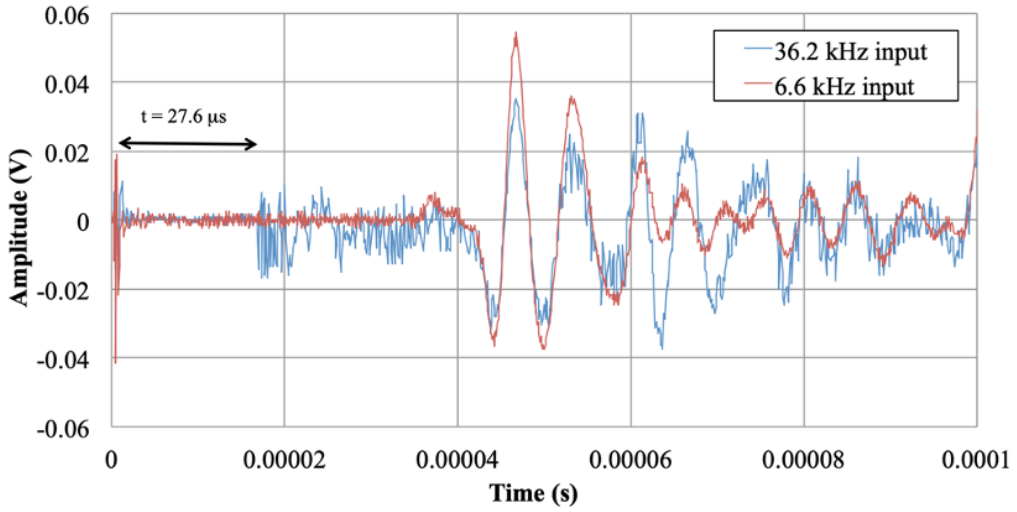

Figure 2.57: Saturated Presumpscot clay confined by 0.1 MPa [103]

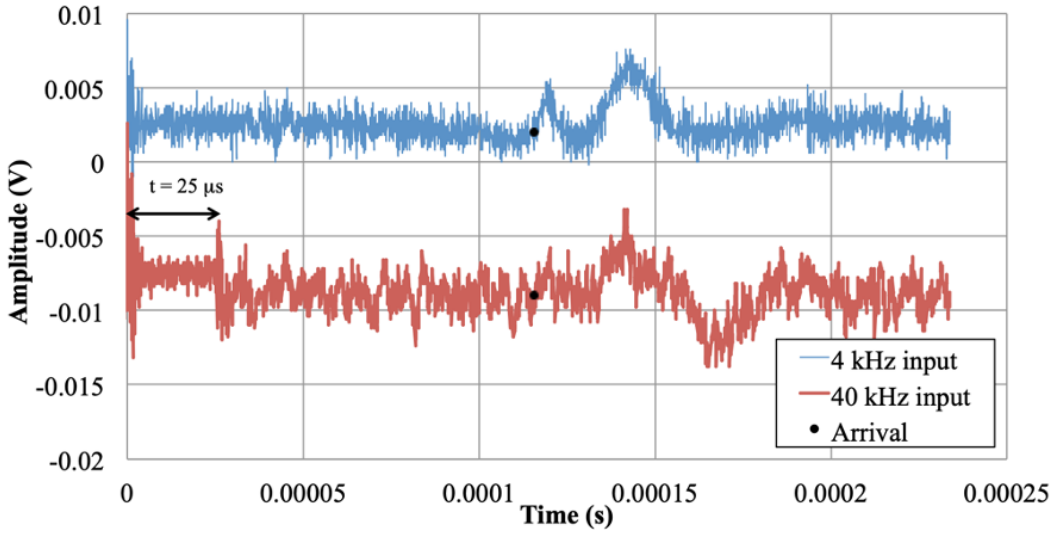

Figure 2.58: Saturated Presumpscot clay confined by 2.1 MPa (The black dots are the arrival time) [103]

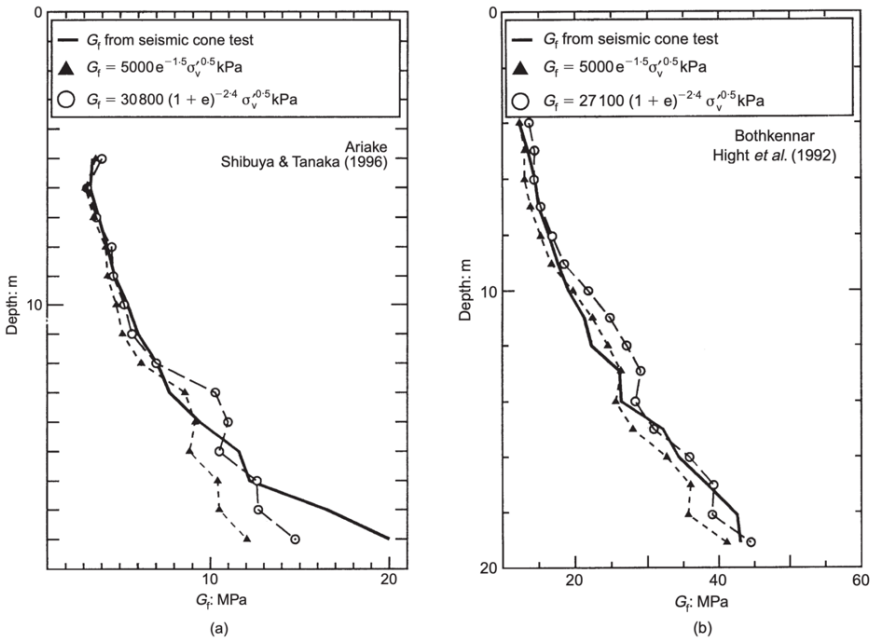

Figure 2.59: Two examples to demonstrate the performance of the newly proposed expression given in equation above for estimating the G_{max} profile with depth [146]

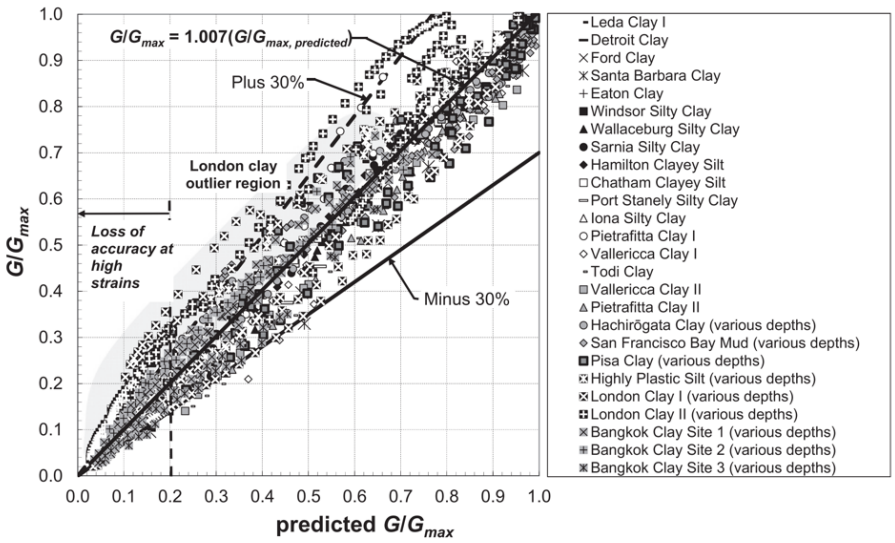

Figure 2.60: Measured data compared to the predicted G_{max} ratios [163]

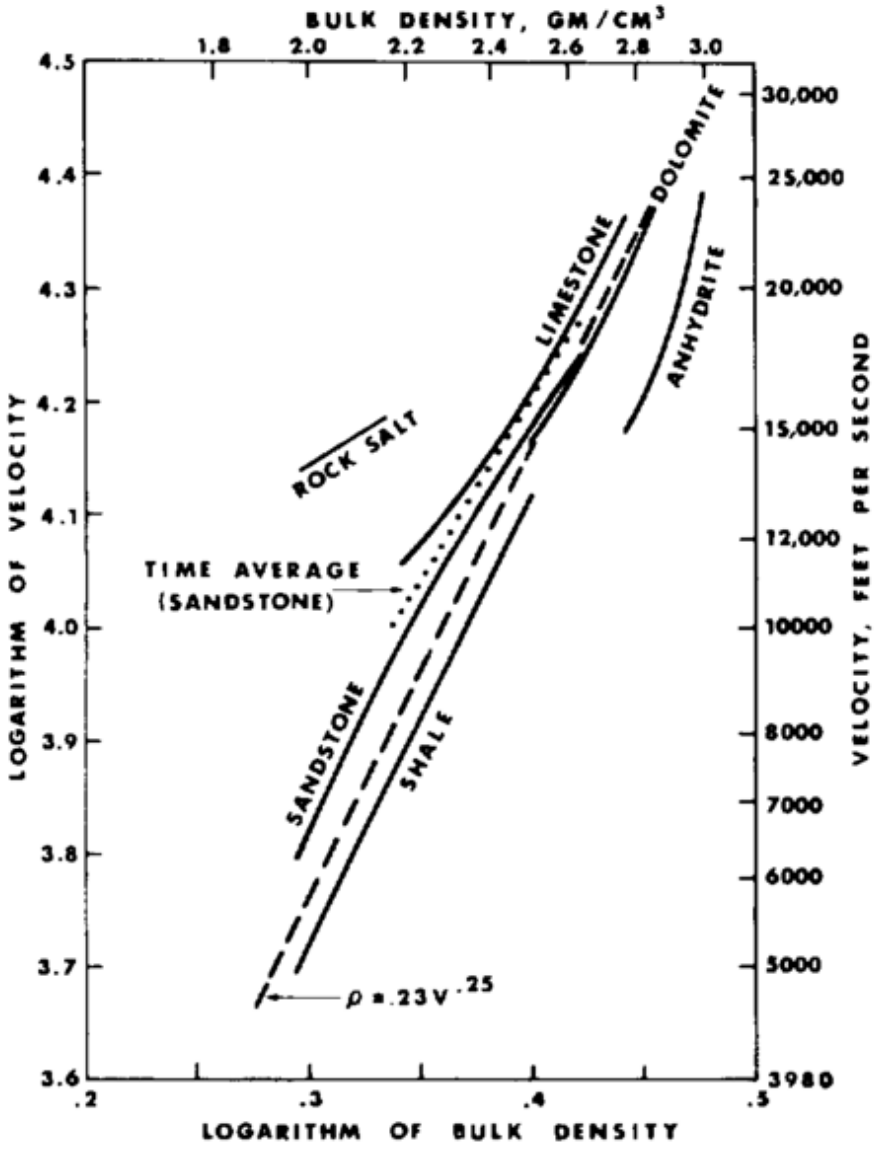

Figure 2.61: Compressional velocity as a function of bulk density [47]

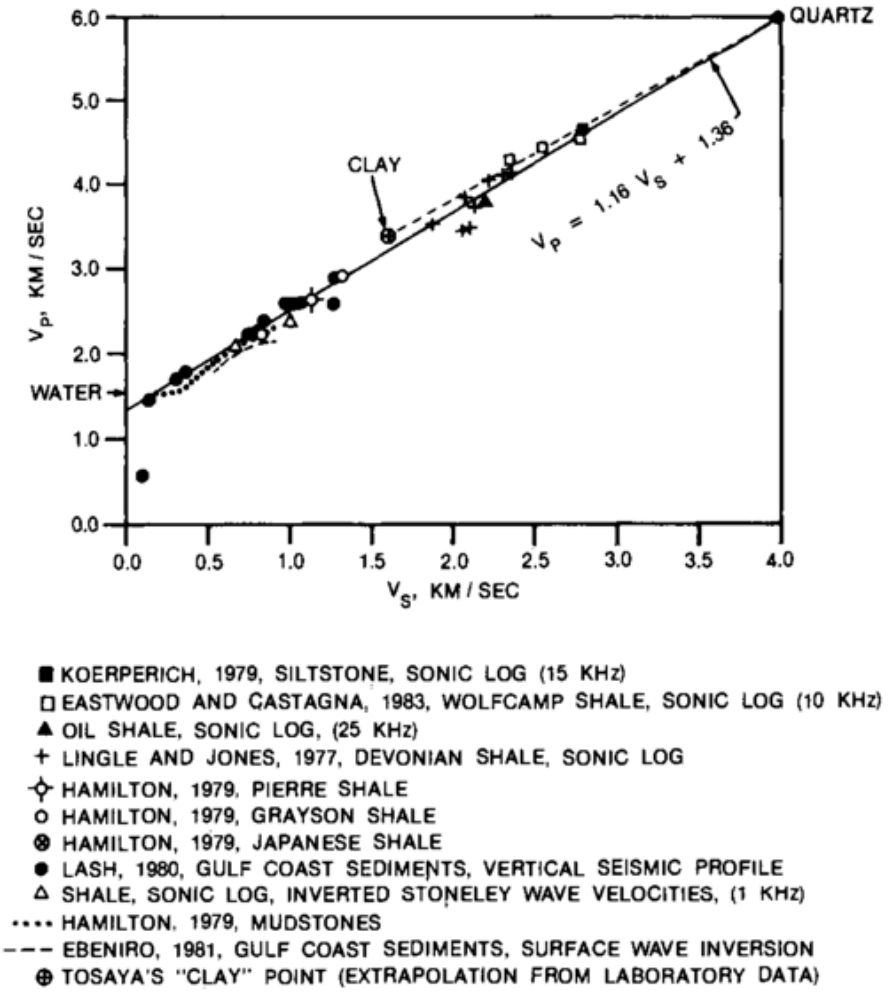

Figure 2.62: Compressional and shear wave velocities for mudrocks from in-situ and field seismic measurements [47]

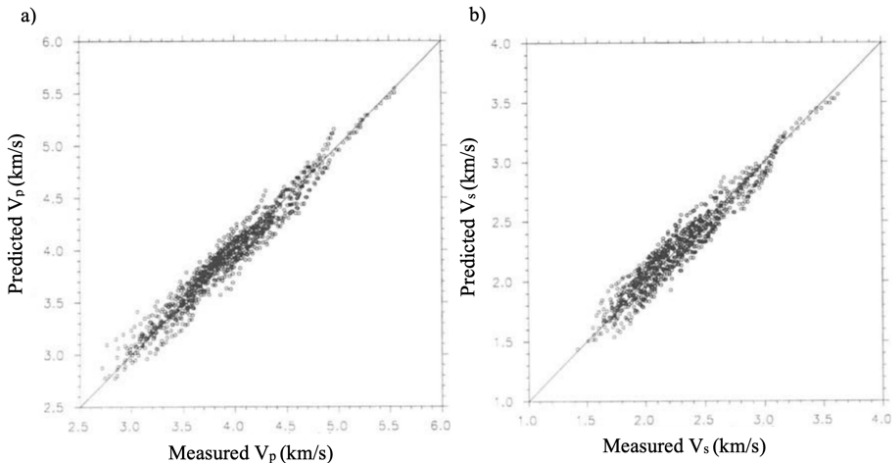

Figure 2.63: Velocity predictions compared to the measured a) P-wave velocity, b) S-wave velocity [39]

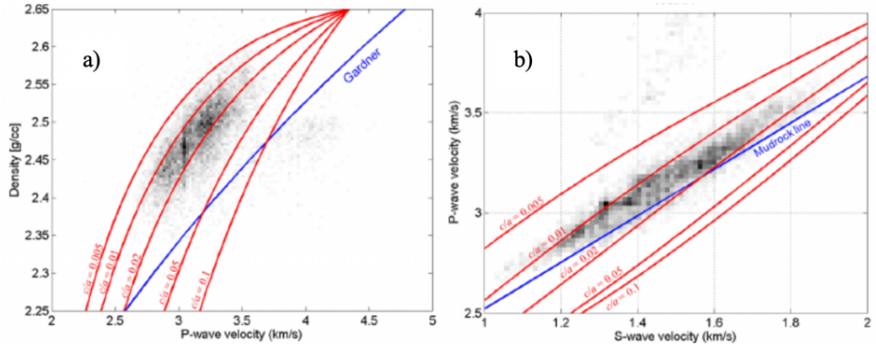

Figure 2.64: 2D histograms for a well with intensity of grey- scale shading, proportional to point density: a) bulk density vs. P-wave velocity compared to predictions from Gardner's relation (blue) and Mori-Tanaka effective field theory (red) for various aspect ratios, b) P-wave velocity vs S- wave velocity compared to Castagna's mudrock line (blue) and predictions from Mori-Tanaka effective field theory for various aspect ratios (red curves) [140]

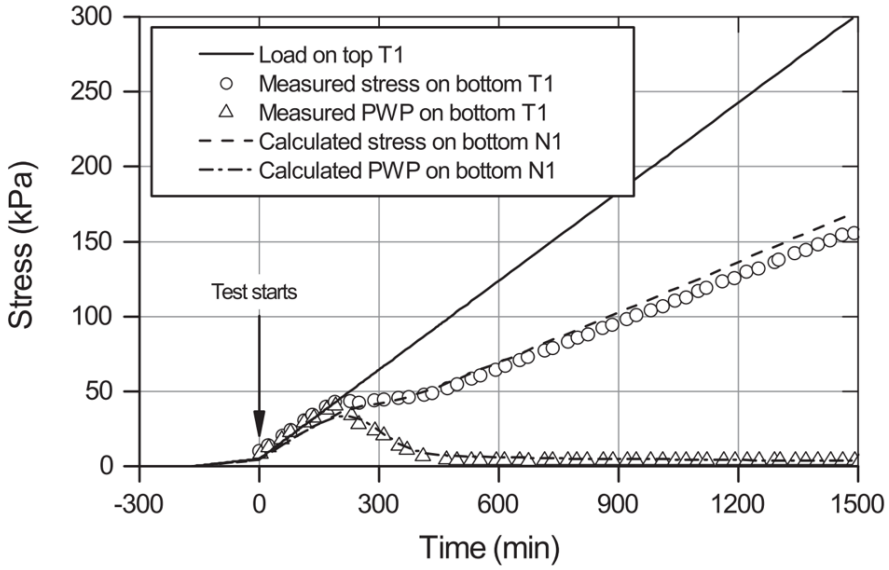

Figure 2.65: Comparison of calculated and measured stresses for tests [60]

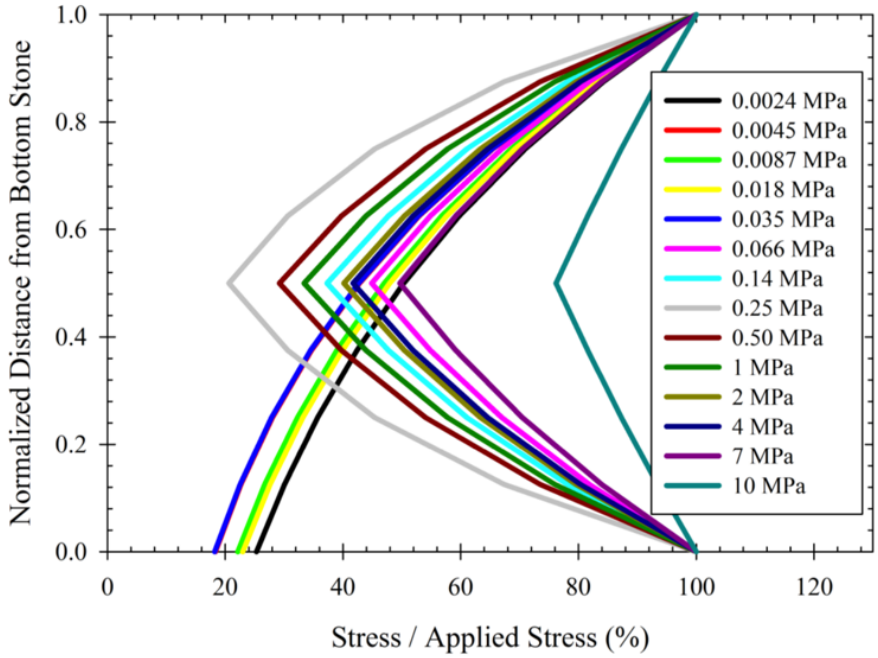

Figure 2.66: The ratio of vertical stresses within RBBC sample normalized with respect to the applied vertical stress as the sample undergoes resedimentation [24]

Chapter 3

Materials and Resedimentation

3.1 Introduction

The first part of this chapter will focus on the origin of the soils tested in this study, and their index properties such as gradation and Atterberg limits. Boston Blue Clay (BBC) and Gulf of Mexico- Eugene Island (GoM- EI) clays, which have significantly different characteristics, were tested in this work. The GoM samples were used in both triaxial and high-pressure CRS testing, whereas BBC was only used in CRS testing. Both of these materials have been extensively investigated by other researchers in particular those working at the MIT Geotechnical Laboratory and Tufts Advanced Geomaterials (TAG) Laboratory, including Fahy [42], Casey [24] and Marjanovic [103]. The two materials represent different characteristics and minerology in terms of plasticity grain size distribution and permeability. The plasticity of the materials was obtained from the liquid limit and plastic limit, where the liquid limit was determined using either the Casagrande cup method (ASTM D4318) or the falling cone method (BS 1377). Figure 3.1 shows RGoM-EI at the higher end of plasticity, and RBBC at a relatively low plasticity. The grain size distribution was obtained using the hydrometer method (ASTM D422) and presented in accordance with Unified Soil Classification System (USCS) (ASTM D2487). Figure 3.2 demonstrates the particle size distribution curves, where RGoM-EI and RBBC seem to have similar size distributions, with RGoM-EI particles being slightly finer. Figure 3.3 compares the permeability in the two materials as a function of porosity. While in both materials the permeability changes at the same rate with porosity, RBBC is much more permeable than RGoM-EI. Tables 3.1-3.4 summarize these characteristics as well as the specific gravity, a measure of the grain density of the soil measured based on ASTM D854-14 as well as the Cation Exchange Capacity (CEC), performed with a

Cu-complex at University at Buffalo, SUNY, and Specific Surface Area (SSA) that was performed by Adams [4] using MB Spot Test Method. The clay mineralogy of each material was determined using X-ray Diffraction (XRD) and was performed and interpreted by Macaulay Scientific Consulting Ltd. of Aberdeen, U.K. Both a sample of the bulk material and the clay fraction ($< 2\mu m$) was tested. The clay fraction was separated using timed sedimentation and then it was glycolated, heated, and air dried.

The second part of this chapter will describe the resedimentation process, which is the method used to produce samples in this study. This method allows one to produce multiple samples with identical material source, preconsolidation stress, pore fluid salinity (and the salt composition), and diameter. Unlike natural intact samples that have varying compositions, saturation ratio and disturbance levels, resedimented samples make it possible to run laboratory tests on uintact and fully saturated samples with known composition, pore fluid salinity and stress history. This is particularly important in velocity testing since isolating the parameter that is being tested is essential. Testing identical samples also makes it possible to verify the accuracy of the testing equipment and procedure. Moreover, test results obtained by different researchers on samples produced using the same resedimentation protocol can be compared to one another. An evaluation of sample uniformity will be presented at the end of this chapter.

3.2 Test Materials

All of the samples tested in this research were made using the resedimentation method. The source materials (Boston Blue Clay and Gulf of Mexico-Eugene Island) will be discussed in detail in Sections 3.2.1 and 3.2.2.

3.2.1 Boston Blue Clay

Natural Boston Blue Clay is a glacio-marine clay of low sensitivity and plasticity. It consists mainly glacial outwash that was originally deposited about 12,000 to 14,000

years ago [85] in a marine environment, immediately following deglaciation of the Boston basin. BBC can be found mostly in the shallow ground layers throughout the Boston area, with a varying thickness of 20-40 m. While the top 12-20 m forms a stiff and overconsolidated (OCR of 2-5) crust, the lower layers (>20m) tend to be normally consolidated ([136]. Although BBC samples sourced from different sites and depths are fairly similar, there can be slight variations in index properties depending on several factors including particle size distribution, pore fluid chemistry and mineralogy. The material used in this research is Series IV BBC powder. The series number corresponds to the location of the source material. While Series I-III were obtained from various regions around Boston, Series IV was obtained from an excavation site at MIT's Koch Biology Building (Building 68) in Cambridge, MA in 1992. Approximately 2500 kg of BBC was excavated at a depth of about 12 m where the OCR of the clay varied from 1.3 to 4.3 [16]. In order to prepare the natural BBC for resedimentation, it was mixed with tap water to form a thick slurry which was then passed through a #10 sieve (2 mm opening) to remove debris such as shells and twigs. The resulting slurry was oven-dried at $60°C$ and the dry material was ground to 95% passing a #100 sieve (0.15 mm opening). The grinding process was done by the Sturtevant Company using a roller mill. Finally, the material was manually blended to produce a homogenous powder and stored in 40 gallon buckets [30]. The RBBC tested in this study was transferred to Tufts University in 5 gallon buckets and stored.

Resedimented and intact BBC has been extensively tested over the last few decades by researchers on Dr. Germaine's team (first at MIT and then at Tufts University since 2015), starting with Bailey [12] and more recently Casey [24], Adams [4] and Marjanovic [103]. Its engineering behavior is very similar to many natural uncemented clays, including its low to medium sensitivity, stress-strain behavior, strength anisotropy, significant strain rate dependency and typical consolidation characteristics. Most recently its strength properties are known up to 100 MPa as well as its resistivity, resistivity anisotropy, and permeability anisotropy. BBC has a liquid limit of w_L = 46.5%, clay fraction (percentage of total dry mass) of 56%, and

specific gravity of G_s = 2.778. BBC's bulk material is primarily quartz, plagioclase, and muscovite, while the clay fraction is about 92% illite. Berman [16], Casey [25], House [68] and Horan [64] compared the intact BBC samples to resedimented ones. Marjanovic [103] and [104] measured vertical P and S velocities in BBC material deforming under K_0 stresses up to 10 MPa stress.

3.2.2 Gulf of Mexico-Eugene Island

This highly plastic clay comes from the Eugene Island area in the Gulf of Mexico, located off the coast of Luisiana, as shown in Figure 3.4. In this area, the basin consists of over 4 km of Pliocene and Pleistocene sedimentary fill deposited over a salt-weld. The RGoM-EI material used in this research was obtained by mixing the materials from two 10.2 cm cores drilled in the 1990's: A-20ST2 well in Block 330 and the A-12 well in Block 316 [46]. A large quantity of core material was collected from each borehole at depths ranging from approximately 2200 m to 2500 m and was processed at the University of Texas at Austin [17]. First the sandy intervals in the core were discarded while the clayey material was broken into fist-sized pieces and air dried for 18 days on plastic sheeting. The dried material was then ground to 99% passing a #100 sieve by an external company, and hand blended into a fine, homogenous powder. GoM has a liquid limit of w_L = 87%, clay fraction of 65%, and specific gravity of G_s = 2.775. Its bulk material is primarily comprised of quartz, illite and illite-smectite, while the clay fraction is over 65% interlay smectite, which is calculated using the expandability and illite-smectite percentage. Resedimented GoM-EI has been tested for both mechanical properties and velocity behaviors. Fahy [42] conducted a large number of triaxial test results in low and medium pressure cells. Casey [24] tested RGoM-EI in a high pressure triaxial cell and measured mechanical properties of specimens under high stresses (up to 100 MPa). In-situ compressional velocity measurements were obtained by wireline logging tools for well A-20ST2. Furthermore, Stump and Flemings [46] conducted laboratory velocity measurements on intact samples from both the A-12 and A-20ST2 wells. Marjanovic [103] measured vertical velocities in GoM-EI material under up to 10 MPa stress.

3.3 Resedimentation

Bailey [12] introduced resedimentation to the MIT Geotechnical Laboratory in 1961, as a reliable method to produce multiple identical clay samples for laboratory testing. The method was initially used to produce partially saturated BBC that could only be subsequently saturated using a 200 kPa back-pressure. Germaine [52] revised the resedimentation technique in 1982 to produce fully saturated and uniform samples with a known salt concentration. Later the method was further refined to produce fully saturated, high pressure (40 MPa) samples to be produced. Resedimented specimens are highly desirable for laboratory testing since the researcher has control over characteristics such as salt concentration, salt chemistry, soil composite and dimensions. It allows for isolating a particular factor that affects soil behavior.

3.3.1 Salinity

Natural pore fluid salinity varies greatly depending on the material type and location. When batched for resedimentation in the laboratory, the researcher needs to decide on the appropriate salt concentration based on multiple factors: Natural and actual salinity, slurry workability, and the desired characteristics of the final specimen for the specific testing purpose (whether or not to vary salinity from material to material). The natural salinity of a clay is the existing salt (g) in 1 kg of dry powder, and the actual salinity is final amount of salt (g) in 1 L of pore fluid.

The different measures of salinity used in this research are shown in Table 3.5. It is clear that the batching salinity (resedimentation salinity) was different than the natural salinity. The author batched both the GoM and BBC slurries with saline water with 80 g/l of sea salt concentration, producing 89.1 g/l and 81.8 g/l "Actual Salinity" after the "Natural Salt" was taken into account. This was to minimize the effect of pore fluid salinity in the measured velocities in different materials (as Marjanovic [103] has shown an increasing trend in V_p with increasing pore fluid salinity at a constant stress). It is worth noting that the salinity at which the specimen is

originally made during mixing is assumed to remain constant during the consolidation. Also, the evaporated water from the bath, housing the resedimentation tube, was regularly replaced with only water, to keep the salinity as close to the original value as possible.

3.3.2 Resedimentation Process

All the specimens tested in this research were resedimented by the author using the same type of salt (Wholefoods sea salt) and salt concentration, with the same equipment and following the same steps (as shown in Figures 3.5-3.9):

- **Powdering**: The natural material obtained from the field is broken down, dried and ground into a powder 95% passing through a #100 sieve. The broken down and dried pieces of GoM Upper interval clay is shown in Figure 3.5. While there are minor differences in the way each material is processed into a powder depending on the specific conditions and, the general idea is essentially the same. The processed clays are hand blended into homogenous powder and stored in 5 gal buckets to minimize humidity reabsorption.

- **Slurry**: Once the powdered material is available, it is mixed with salt and water to form a slurry (Figure 3.6). Other soils can also be added to the mix if needed (like silt). The produced slurry needs to be watery enough to be easily pourable into the resedimentation tube, but not too watery to form free water at the surface or cause the specimen to lose too much water (and height as a result) during consolidation. It also needs to be viscous enough to prevent any large particle separation. Water content of 105% was found to work well for both GoM and BBC for this study. The slurry is mixed thoroughly with an electric blender at low speed and left to hydrate overnight. Next, it is de-aired by applying a vacuum (15 to 25 inches of mercury) to a large sealed vacuum container (Figure 3.7).

- **Deposition**: The prepared slurry is poured into an acrylic tube (Figure 3.8). The inside of the tube is lubricated using WD-40 spray, to minimize sidewall

friction, then the tube is placed inside a bath that is filled with saltwater (with the same salinity that the slurry was batched with). The slurry is poured into the tube using a flexible tube and a funnel. Porous stones and nylon filter papers are placed on both ends of the slurry to allow double drainage.

- **Consolidation**: Once in the tube, the slurry is incrementally loaded with a load increment ratio of one, doubling the load each time. The first load is the weight of the porous stone, followed by various PVC spacers, and then the load frame and hanging weights (Figure 3.9). The ratio of one is to guarantee minimal slurry extrusion around the side of the porous stone. Each load increment is maintained at least until the end of primary consolidation as determined by the root time method. Once the slurry is thick enough to stay in the tube when picked up (usually after consolidating with a 10 kg load), a one inch tall PVC spacer is placed on the bottom of the tube under the porous stone (without touching the tube) to ensure a floating setup for two reasons: 1) reducing the effect of sidewall friction (by ensuring that the load is not transfered to the base by the sidewall friction and is applied to the specimen directly), 2) provide water content uniformity (by letting the specimen drain from the top and the bottom). The gravity hanger system is limited to 80kg of weigh. This means that for a sample made to be the size of a triaxial specimen (Area = 9.93 cm^2) reaches approximately 0.8 MPa. If further loading is needed (which was not the case for this research), the pneumatic actuator is used, which has the capability of applying up to 1000 kgf of load.

  When the target stress is reached (which is 80 kg/cm2 for this research) the sample is maintained at that stress level for an extra full log cycle after the end of primary, to achieve primary compression. The sample is then unloaded to an OCR=4 in a single load increment. When at OCR=4, the sample is at isotropic stress state where K_0=1, and there is minimal shearing during extrusion

- **Extrusion**: The last step before the specimen can be trimmed to the appropriate diameters and shape for the specific testing types, is extrusion. It can be extruded from the tube either manually or with a hydraulic jack. The trimming processes will be discussed in Sections 4.1.3 and 4.2.3.

3.3.3 Evaluation of Specimen Uniformity

The two main causes of nonuniformity in a resedimented sample are vertical variation in composition of the sample and the radial heterogeneity introduced by the sidewall friction. Germaine [52] and Seah [141] evaluated the uniformity of their resedimented large diameter (30 cm) soil cakes via water content measurements, checking vertical and radial slices for stratification, and x-ray diffraction pattern methods, all confirming adequate homogeneity. However, the samples in this research are resedimented in acrylic tubes with the inner diameter of 3.45 cm, which means the initial height to diameter ratio is more than 6, for a typical sample, dropping to nearly 3 at the end of resedimentation (to 10 MPa), as opposed to the 0.4 ratio for a resedimented soil cake.

Casey [26] compared the virgin compression curve of RBBC measured in a typical CRS test (0.35> H/D ratio) against the compression curves exhibited by two RBBC samples undergoing resedimentation under maximum stresses of 2 and 10 MPa. Figure 3.10 shows that the void ratios of the samples in the consolidometers are higher than in the CRS test. This is due to the fact that the stress applied to a sample in a consolidometer only acts fully at the top and bottom of the sample, as side wall friction reduces the applied stress to a lower value away from the ends. As a result, the void ratio of a resedimented sample is lowest at the ends and highest in the middle.

Casey accounted for the effect of sidewall friction and calculated the actual stresses within the resedimented sample by dividing the sample into multiple layers and assigning a coefficient of friction (f), to represent the sidewall friction. The f values are adjusted for each load increment so that the calculated average void ratio of each layer is equal to the average void ratio measured for the corresponding

stress level during CRS testing. Figure 3.11 shows that the f values increase with the stress level up to a certain point (0.1 MPa) and starts decreasing afterwards as a result of two factors: 1) load being applied from both top and bottom, 2) H/D ratio decreasing. Based on these results, the sidewall friction effect was considered negligible during the resedimentation process, especially considering the stress levels these specimens are tested at. However, it will be taken into account for TCRS tests run for this research as will be discussed in Section 5.2.2.

	RBBC	RGoM-EI
Quartz	21.3	27.8
Plagioclase	20.5	5.3
K-Feldspar	8.2	4.0
Calcite	0.5	1.2
Dolomite	0.8	0.8
Siderite	-	1.0
Pyrite	-	0.7
Anatase	-	0.2
Barite	-	3.2
Halite	0.2	0.2
Muscovite	13.8	1.9
Illite+Illite-Smectite	7.3	44.4
Kaolinite	2.9	9.1
Chlorite	6.2	0.4
Amphibole	3.8	-
Tri-mica	9.2	-
Hydrobiotite	5.4	-

Table 3.1: The mineralogy obtained from performing XRD on the bulk materials is shown here in % (Testing performed by Macaulay Scientific Consulting LTD)

Material	Chlorite (%)	Kaolinite (%)	Illite (%)	Illite-Smectite (%)	Expandibility (%)
RBBC	5	2	65	28	5
RGOM-EI	1	4	8	87	70-80

Table 3.2: The mineralogy obtained from performing XRD on the ($< 2\mu m$) is shown here in % (Testing performed by Macaulay Scientific Consulting LTD)

Material	CEC (meq/100g)	SSA (m^2/g)
RBBC	10.7	49
RGoM-EI	32.8	267

Table 3.3: CEC and SSA for the materials tested in this research

Material	Abbreviation	Origin	Liquid Limit, w_L (%)	Plastic Limit, w_P (%)	Plasticity Index, I_p (%)	Clay Fraction (%)	USCS Classification	Specific Gravity, G_s	Performed by
Boston Blue Clay	RBBC	Boston, Massachusetts	46.5	23.8	22.7	56	CL	2.778	Casey (2014), Horan (2012), Abdulhadi (2009), Santagata (1998)
Gulf of Mexico - Eugene Island	RGOM-EI	Eugene Island, Gulf of Mexico	87.0	24.0	63.0	65.0	CH	2.775	Casey (2014), Fahy (2014), Betts (2014)

Table 3.4: Index properties and origin of soils tested (UT GeoFluids archive)

Material	Natural Salts (g/kg)	Resedimentation Salinity (g/l)	Water Content (%)	Actual Salinity (g/l)
RBBC	2.19	80	105	81.8
RGOM-EI	10.95	80	105	89.1

Table 3.5: Salinity and water content at which the materials were mixed during resedimentation (Tests performed by members of UT Geofluids Consortium)

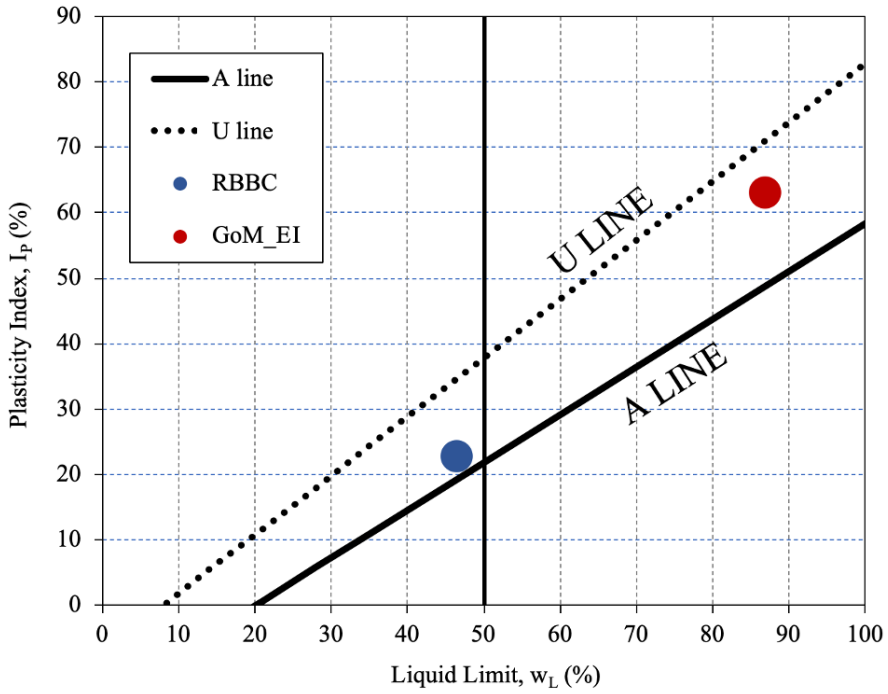

Figure 3.1: The materials used in this research are plotted on the plasticity chart

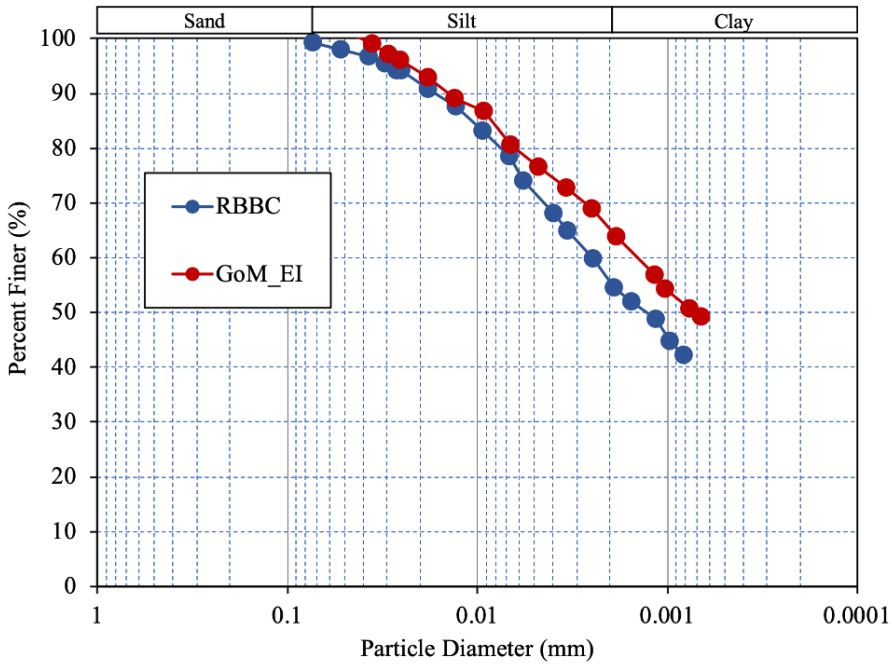

Figure 3.2: This grain size distribution chart shows the spread of the particle size as a function of % passing. The clay fraction ($< 2\mu m$) was obtained using a hydrometer test

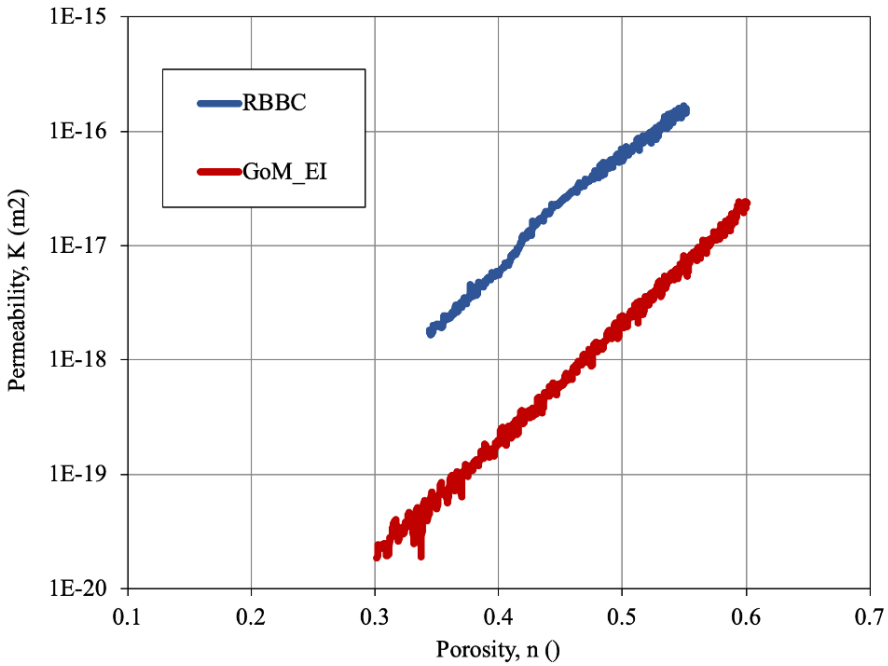

Figure 3.3: Permeability curves of all the materials tested (Tests performed by members of UT Geofluids Consortium)

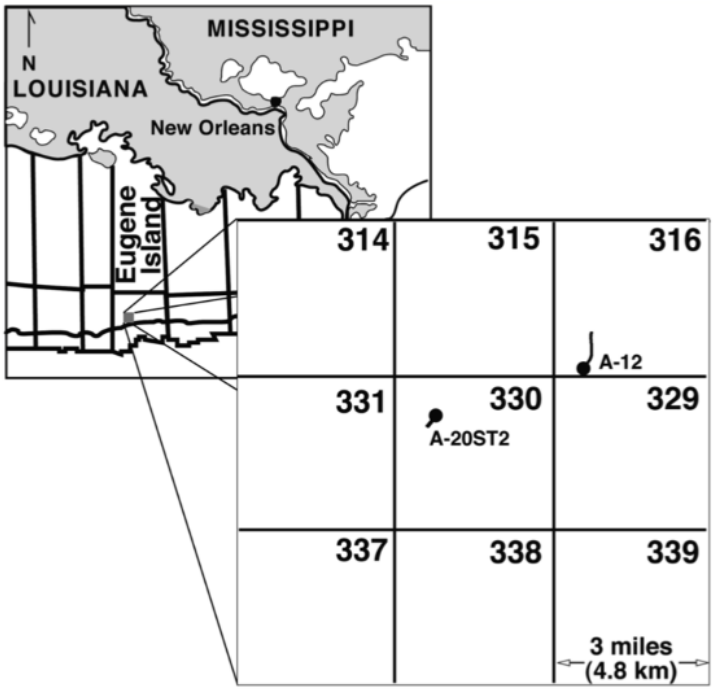

Figure 3.4: Location of the two blocks from which the RGOM-EI source material was obtained – blocks 316 and 330

Figure 3.5: Cleaned and dried natural material (RGoM Upper interval clay) before grinding [42]

Figure 3.6: Clay powder is mixed with salt and water until thoroughly homogenized and no lumps are present

Figure 3.7: The slurry is vacuumed in a sealed container

Figure 3.8: The slurry is poured into the acrylic tube using a flexible tube and a funnel

Figure 3.9: The tube is placed in a salt-water bath and loaded using a gravity hanger system

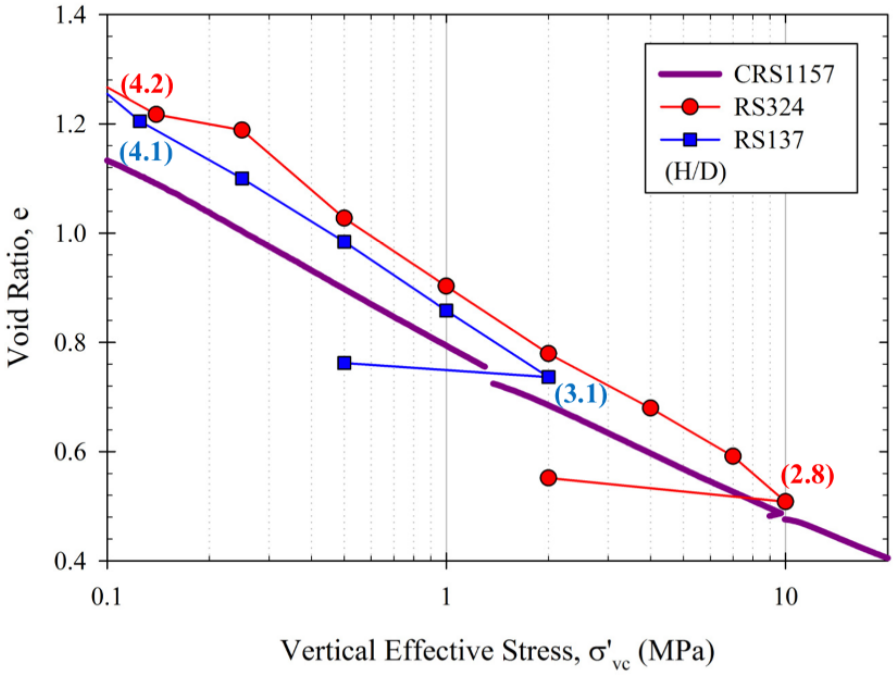

Figure 3.10: Comparison of virgin compression curves for RBBC as measured in a typical CRS test and during resedimentation in consolidometers [26])

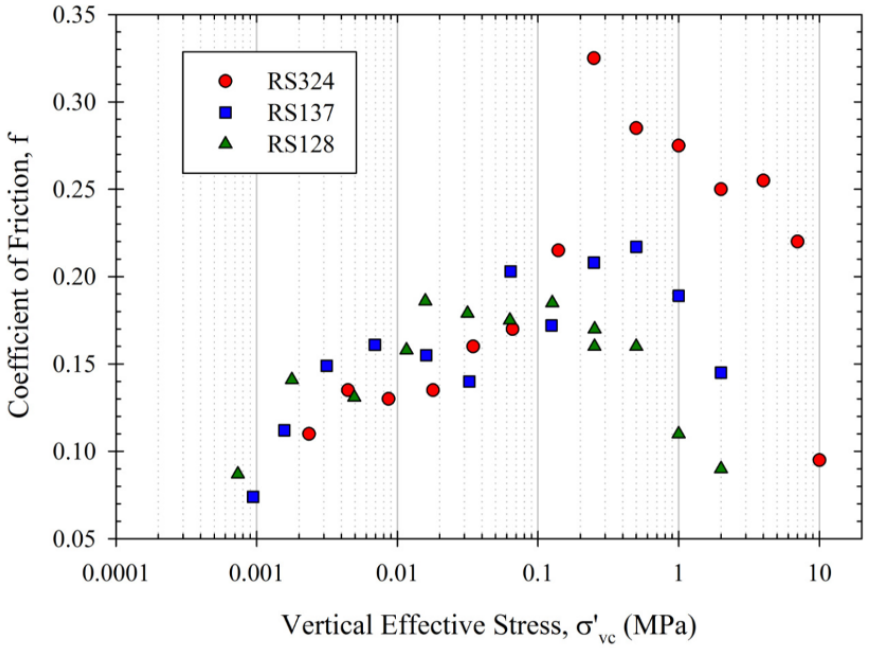

Figure 3.11: Variation in the calculated coefficients of friction as a function of stress level for three samples undergoing resedimentation [26])

Chapter 4

Testing Equipments and Procedures

As mentioned in Chapter 2, this study has two main purposes: 1) To understand the velocity anisotropy in fine-grained resedimented materials, 2) Expand the stress level of vertical velocity measurements, that was previously achieved by Marjanovic ([103], [104]). Two separate apparatus and testing setups were used in this study. Medium pressure triaxial testing device was used to study anisotropy by means of directional velocity measurements, which will be discussed in Section 4.1. A new setup called thw Tall Constant Rate of Strain (TCRS), was used to measure vertical velocities continuously, in a specimen undergoing consolidation with up to 25 MPa vertical effective stress. The TCRS device and the testing process will be presented in Section 4.2.

4.1 Triaxial Testing

4.1.1 Overview of Triaxial Systems

All of the triaxial tests in this research were performed in a medium pressure triaxial system. This device was initially developed for the testing of frozen sand by Anderson [8] but was modified for the testing of fine-grained soil by Abdulhadi [2]. A typical triaxial test setup consists of a triaxial cell connected to three Pressure Volume Actuators (PVAs, controlling the axial load, cell pressure and back presuure) that are controlled by a control box that is connected to a computer (running a custom-made feedback loop), and a data acquisition system (collecting and saving the data from the station computer) (Figure 4.1 shows a slightly older version that only had the cell and back pressure PVAs).

triaxial apparatuses used at Tufts Advanced Geomaterials Laboratory (TAG Lab) are capable of imposing K_0 consolidation and stress path loading conditions, as well

as shearing the specimen both in extension and compression. Although many researchers (Abdulhadi [2], Casey [25], and Fahy [42]) had previously taken advantage of the many capacities of the medium pressure triaxial equipment at MIT Geotechnical Laboratory, the author has only focused on K_0 consolidation up to 10 MPa for this research.

4.1.2 Triaxial Cell and Load Frame

A typical triaxial specimen is a cylinder with 3.5 cm diameter and ~8 cm height. However, in this research, two narrow slices, parallel to one another, were cut from the sides of the cylindrical specimen, to provide the flat surface needed for mounting the horizontal velocity setup, while keeping a uniform cross section, which will be discussed more in Section 4.3.1. Marjanovic [103] modified the top cap and the pedestal by hollowing them out and mounting the piezoelectric actuators in the cavities. She also made an annular cut around the pedestal for the hollowed porous stones to be placed in. This was done to eliminate the effect of having a second material between the actuators and the soil specimen and provide better coupling, while allowing for appropriate drainage. The pedestal was further modified by the author to accommodate for the side actuators that will be explained in Section 4.4.1. Although not shown in the schematics, the specimen is drained both from the top and the bottom through drainage lines that are connected to the top cap and the pedestal. The drainage line is copper tubing coiled around the specimen to allow for large vertical deformations. The top and bottom drainage lines connect to a pressure transducer through a series of valves and tubes that measure the pore fluid pressure directly. The specimen is sealed with two thick membranes ordered from Humboldt Manufacturing Co. The membranes have 0.024 inches thickness and fit a 3.5 cm diameter specimen, as opposed to the two thin membranes 0.03 cm (0.012 in) that was previously used by Marjanovic [103]. While thin membranes (rubber membrane or unlubricated condoms) can be effective under lower confining pressures ($<$3.5 MPa) and in tests completed in shorter periods of time, the author found that thicker membranes provide more reliable sealing for tests run for longer periods of

time at higher stress levels.

A three-dimensional schematic of a triaxial cell is provided in Figure 4.2 and a section view including the dimensions (in inches) can be seen in Figure 4.3. The chamber used in this study has a 10 mm zinc-plated carbon steel wall and was designed to withstand up to 10 MPa pressure. The chamber is filled with 20 centistokes silicone oil (Dow-Corning "200 fluid"). This particular fluid was selected due to its non-conductive nature since both the load cell and the velocity actuators have wires running from the inside of the cell, through the triaxial base. Also, silicon oil is known to have exceptionally low viscosity at a wide range of temperatures, thus can be used in many different testing conditions. Finally, it does not react with the latex membranes used in testing and leakage is not an issue.

The axial load is applied with a 9 ton (89 kN) hydraulic load frame controlled by a PVA filled with silicon oil. The hydraulic pressure generated in the PVA pushes the pedestal upward against a stationary cross bar. The pressure is then transmitted to the specimen through a 2.54 cm diameter hardened steel piston that is sealed with an O-ring. The load is measured using an internal, 2000 lb (8.9 kN) capacity load cell, attached directly to the piston. This configuration (shown in Figure 4.4) eliminates the effect of the frictional resistance, between the piston the cell, on the measured load.

In addition to the axial load PVA, two other PVAs are used in the triaxial testing setup: One to control the cell pressure and another one to control the pore fluid pressure. These PVAs have a pressure capacity of 14 MPa and a volume capacity of 47 cm^3 and accommodate a 0.5 tone Duff-Norton inverted ball screw jack, which can be driven by a Maxon Motors servomotor with 80 mNm continuous output (geared at 84:1) (Figure 4.5). All the PVAs have a limit switch at both extreme ends of the stoke, which shuts down the servomotor when the limit is reached. The cell pressure and pore pressure PVAs are connected to 2000 psi (14 MPa) capacity pressure transducers. The pore pressure PVA has a string pot attached to it that measures the displacement of the PVA piston directly, which in turn allows for volume change determination considering the constant cross-sectional area of the

PVA piston (2.85 cm^2). This is a critical component to the PID (proportional-integral-derivative) control algorithm that allows for K_0 consolidation.

4.1.3 Triaxial Testing Procedure

This section will focus on the setup procedure for a medium pressure triaxial test. Since this study is meant to cover the velocity behavior and anisotropy in normally consolidated specimens under medium pressures (1-10 MPa), the specimens were resedimented to a preconsolidation pressure of 0.8 MPa (80 kg of load). This is to shorten the consolidation time inside the triaxial cell (specially for highly plastic materials such as GoM), as well as to ensure that specimen is stable enough to withstand the setup procedure. The resedimentation tubes in this study have a diameter of 3.75 cm which is slightly higher than the triaxial pedestal diameter (3.5 cm). The specimens were trimmed to the correct diameter using a mitre box and a large razor blade. The trimming also eliminates the smeared surface, and any lateral nonuniformities. The specimen is then placed inside a split sleeve and the two ends are cut using a wire saw to ensure they are parallel, and smoothened with the razor blade. The initial height of the specimens range between 8-9 cm. Once the specimen has the desired cylindrical dimensions, it is placed on a flat surface, lightly pushed down to keep in place, and a wire saw is used to cut two narrow slices vertically parallel to one another, to ensure a flat, smooth surface for the side actuators to be placed on. Schematics of the specimen are shown in Figure 4.6. The dimensions of the specimen (diameter, height and the width after the sides are cut) are measured and recorded. The water content of the trimmings is determined by drying them for 24 hours in a 105° oven. Although not used for the void ratio calculations, and generally 2-4% drier than the actual specimen, this initial water content provides a good reference point for final water content comparison.

The top cap, the pedestal and the flat surface of the side actuators are covered with a thin layer of vacuum grease to help seal the specimen and provide better coupling between the actuators and the specimen. Although vacuum grease is inevitably used, both the porous stones and the nylon filter papers are hollowed out in

order to minimize mechanically interfering materials between the specimen and the actuators. The trimmed specimen is then placed between the pedestal and the top cap, both of which have a hollowed porous stone (Figure 4.7). The side actuators are placed on the cut side surfaces facing one another, at exactly the same vertical distances from the pedestal. The side actuators are secured on the specimen with a small band of unlubricated condom, which prevents the actuators from sliding down on the specimen throughout the setup process (Figure 4.8). A thick membrane is stretched out using a membrane stretcher attached to a vacuum. The stretcher needs to have a big enough diameter to go over the large top cap and not touch the side actuator as it is slid over them. Once the membrane is in position, the vacuum is released and the membrane fits onto the specimen. Next, four O-rings are stretched out using a two-piece O-ring stretcher and two are placed on each end, where the membrane overlaps with the endcap. Then the second membrane is placed the same way, covering both the specimen and the four O-rings. The last O-ring on each side is placed on top of the second membraned to sit between the first two. The side actuator wires sit on the brass pedestal and are covered with caulk (as described in Section 4.4). A circular metal belt is tightened around the bottom O-rings to provide better seal for the specimen. Finally, the drainage line is connected to the top and the bottom caps and the acoustic components are connected to a nine-pin connecter mounted inside the base. The final arrangement of the specimen is shown in Figure 4.9. The O-ring configuration explained here can seal the specimen mechanically, when an external hydrostatic pressure is applied. To mimic this pressure before the chamber is placed, and to check the specimen for internal leak, a vacuum is applied to a salt-water (80 g/l) filled sidearm flask, which is connected to the specimen from the pore fluid transduce connection. If the specimen is properly sealed, the fluid inside the flask should stop bubbling after a while (which is when the air inside the system and the specimen is all sucked out). Before the vacuum is applied to the specimen, an alignment frame is screwed onto the base and the top plate of the frame is lowered on the top cap to ensure the specimen is properly aligned and centered.

The frame is removed when the vacuum is in place. The vacuum is maintained until there is a minimum of 5 kg/cm^2 cell pressure on the specimen. Also, when the vacuum is released while the drainage lines have free access to fluid, the specimen sucks salt-water in and flash saturation occurs.

Next, the steel chamber is lowered down using a cantilever pulley system. The load cell is connected to the second nine-pin connector in the base before the chamber reaches its final position and the voltage (zero load) is recorded. This also allows the load cell to "warm up". The load cell voltage is closely monitored while the chamber is lowered and the washers and nuts are tightened, to ensure that no axial load is being applied. Tightening the nuts pushes the chamber down against an O-ring on the bottom of the triaxial base, which provides the proper seal for the pressurized cell fluid (silicon oil). The piston is slowly tapped down with a rubber mallet, while the load cell voltage is still being monitored, until contact is established between the alignment cap and top endcap. The chamber is filled with silicon oil and a small amount of cell pressure (usually 5 kg/cm^2 which is around the sampling effective stress) is applied. Finally the suction is released, filling the drainage lines with salt water, and the pore pressure transducer is connected.

For the first few minutes a small axial load (1 kg) is applied to ensure that the top cap and the alignment cap are in contact. The axial load motor is then turned off to prevent excess loading caused by creep. At this point the specimen has entered the "pressure up" stage, where the 0.5 MPa cell pressure is maintained on the specimen over-night, while the drainage lines are closed, letting the specimen equilibrate. The drainage lines are then opened, and the specimen is back-pressure saturated until a satisfactory B-value (the ratio of change in pore pressure divided by change in applied cell pressure while the pore pressure valves are closed off) is observed. Back pressure saturation is performed by a stepwise increase in the pore pressure, while the cell pressure is adjusted accordingly to keep the effective stress constant. Pore pressure is typically kept near 0.025 MPa.

Once the specimen is back pressure saturated, the volume change due to saturation needs to be zeroed so that the total volume change only reflects the effect of

consolidation. This is done by equating the volumetric strain (%) to the axial strain (%) and adjusting the zero on volumetric LVDT.

The next stage is K_0-consolidation. The PID control algorithm used to control consolidation is set to a strain rate of 0.15%/hr for RBBC and 0.08%/hr for RGoM. The strain rates depend of the clay's permeability. The pore pressures are only measured at the bottom of the specimen, but assumed to be uniform throughout the specimen. The feedback loop monitors the volumetric strain measured from the pore water being expelled from the specimen and applies just the right amount of cell pressure to keep the specimen area constant. Also the final diameters of the specimen are measured after it is out of the cell to ensure uniform corss sectional area along the length of the specimen. The no lateral deformation condition ($\epsilon_v = A_0 \times \epsilon_a$) is by definition a prerequisite of K_0-consolidation. The specimen is continuously consolidated up to almost 10 MPa vertical effective stress, to ensure a state of normally consolidated (NC) at all times. Vertical stress, cell pressure, axial strain, volumetric strain and pore pressure are measured with consistent intervals throughout the tests. Velocity measurements are taken periodically (usually every 1 MPa), using a custom-made setup connected to an oscilloscope, which will be discussed in Sections 4.4 and 4.5.

Once the test is done, the specimen is carefully taken out and the dimensions are measured, as well as the wet mass. Finally, the specimen is oven dried in 105°C and measured again for dry mass. The oven dried specimens are archived in labeled plastic bags.

4.2 Tall Constant Rate of Strain (TCRS) Testing

4.2.1 Overview of TCRS Setup

The oedometer test has been used and continuously improved for decades. Before collaborating on consolidation research with Arthur Casagrande at MIT, Karl Von Terzaghi published his "theory of consolidation" in 1923. Oedometer is a simple, yet effective way of studying one dimensional consolidation behavior under incremental

loading. In 1971 Wissa [177] introduced another consolidometer that was capable of loading the specimen at a constant rate of strain, while also measuring the pore pressure. The setup used in this research, Tall Constant rate of Strain (TCRS), is a modified combination of a conventional oedometer and a constant rate of strain device, which will be discusses in the next section.

4.2.2 TCRS Testing Setup

TCRS setup simply consists of a specimen placed inside a stainless-steel ring, and a load frame controlled by a feedback loop, similar to the ones used for triaxial testing. The load frame has a loading capacity of 10,000 lbf. The screw driven piston is connected to a manual transmission and driven by an AC motor. It is controlled by the computer which used a DC relay to turn the motor on and off. When the motor is on, the jack pushes the bottom platen up, against the stationary cross bar. There is a 10,000 lbf capacity load cell attached to the cross bar, measuring the applied axial load. The strain rate of the load frame (which is equivalent to the strain rate of the specimen) is determined by the mechanical gear configuration that is set manually, depending on the material being tested. Since the excess pore pressure is not measured in this testing setup, the strain rate is kept low enough to ensure full drainage at all times. The axial strain is measured with an external Linear Variable Differential Transformer (LVDT) attached to the stationary side bar, with the coil moving only with the platen, as the specimen vertically deforms. The specimen is placed inside a stainless steel ring, that has a 35.5 mm diameter and an 80 mm height. It is drained from both ends with drainage lines connected to free water surface, in a reservoir filled with salt-water with salt concentration same as the batching salinity. The ring is stiff enough to prevent any lateral deformations, hence ensuring K_0-consolidation. Also, the load is applied from both sides (floating wall), minimizing the sidewall friction. The final configuration of the testing setup is shown in Figure 4.10. Note that the velocity actuator wires in this setup are connected directly to the wave source and the oscilloscope, eliminating any interference caused by the wires going through various connections.

4.2.3 TCRS Testing Procedure

TCRS specimens were prepared with a method close to CRS or oedometer methods. The resedimented specimen was slowly pushed out of the acrylic tube using PVC spacers and the part or the specimen outside of the acrylic tube was pushed inside the lubricated ring. Next the excess material was removed in preparation for the next push. This process was performed with utmost caution to minimize disturbance. Once the specimen was inside the ring, two hollow porous stones were placed at the top and the bottom of the specimen so they were flush with the ring. Next the ring, stones and the specimen are weighed to get the wet mass, and the distance between each end of the ring and the specimen is subtracted from the ring height to get the specimen height (usually between 6 and 6.5 cm). Two identical caps, housing velocity actuators (top caps from the triaxial setup) were lubricated and placed on each side of the specimen. Hollowed out porous stones and nylon filter papers were also used to provide drainage. A thin rubber membrane was used around the ring to prevent any contact with air. The flexible drainage lines are connected to the top and the bottom and placed inside a salt-water reservoir open to the atmosphere to provide drainage from both ends. The specimen is then placed in the load frame and both the LVDT and load cell values are zeroed. At this point the consolidation is started and the load is increased up to 30 MPa. The specimen is continuously consolidated and the vertical V_p and V_s measurements are taken while loading to ensure that there is no secondary compression effect in the measured velocities. The specimens can also be unloaded, simply by reversing the direction of the load frame, which was not done in this research.

Lastly, the ring is taken out of the frame, and the specimen is pushed out using a hydraulic jack. The height and the wet mass of the specimen are measured, and it is oven dried for 7 days before being weighed for dry mass.

4.3 Control System and Data Acquisition

Sheahan [143] originally developed the control system automating the manual system. The control system allows for precise, automated stress path control without continuous supervision. Anderson [8] integrated the automation system into the medium stress triaxial setup. Test variables are measured using internal and external transducers, that are connected to the control motor which itself is controlled by a computer program. The analog signal collected by the transducers is converted into digital data and is recorded by a central data acquisition system. The details of above will be discussed in this section.

4.3.1 Transducers and Computer Control System

The test variables are measured by transducers, depending on the type of the test. Note that the velocity transducers used in this research will be discusses in the next two sections. The following transducers are used in TCRS test:

- External LVDT (Linear Variable Differential Transformer) that measures vertical displacement
- External load cell measures vertical deviator load applied to the specimen

An external LVDT is also used in a triaxial test, however the load cell is placed inside the cell, between the piston and the specimen, to eliminate the piston friction effect on the recorded load. Four other transducers are used in triaxial testing in addition to the LVDT and the load cell:

- Pore pressure transducer that can measure the back pressure and specimen pressure
- Cell pressure transducer for chamber pressure
- String pot that measures linear displacement but is subsequently transformed into volumetric strain based on changes of pore fluid

The analogue outputs from each transducer need to be converted to a digital signal. Sheahan [143] developed a Multichannel Analogue-to-Digital converter (MADC), which is based on the Analog Devices AD1170 analog to digital (A/D) converter. The AD1170 has a high degree of signal averaging, thus eliminating noise and producing a very stable reading. The signal is then sent to a USB interface card (also housed in the MADC box, Figure 4.11), which is then sent to the computer. This interface card is specifically used for newer computers that do not have an expansion slot to house the A/D converter. For the TCRS tests run for this research, ARS interface cards (developed by ARS technologies) were used as the USB interface connector [121]).

The computer runs a control program written in QBASIC and uses this signal to evaluate which commands to send back out to the motors controlling the pressures and loads in the test, implementing either intermittent proportional or continuous proportional–integral–derivative (PID) control. USB to ISA emulator (support assistant)requires DOSBOX, which hosts the QBASIC software, which is capable of running all aspects of a test including initial pressure-up, back pressure saturation, consolidation (K_0 or stress path) and shearing, depending on the test type.

A digital to analog (D/A) converter board made by Strawberry Tree Inc. is also in the MADC box. It converts the digital signals sent by the computer program into 12 bit analog signals that control the motors and the PVAs. Then sends the analog signals to a custom-designed control card, housed in the control box which will be discussed in the next section.

4.3.2 Control Box and Central Data Acquisition Center

The computer control box is the main junction box between the computer program and the testing motors. Parry [121] developed an updated version of previous computer control boxes (Figure 4.12) with new Maxon Escon motor controllers and a newly designed printed circuit board (PCB) control card (Figure 4.13). The computer control card directs voltage commands from the computer to the correct motor controller to cause a physical change in the experiment. An Autotonics W50NT500

is used in the control box to supply power to the motors. The motor controllers send the command signals to the cell, axial load and pore pressure PVAs. The computer control box can operate in either "Manual" or "Computer" control mode. The manual mode allows the user to bypass the computer signals and control the motor using a potentiometer that is on the front panel of the box. Throughout the triaxial testing process, however, the box is set to computer control for the most part. For the TCRS testing setup, a third box, called load frame junction box, is also used (Figure 4.14). The load frame junction box houses an AC/DC converter, a relay, a power inlet and a power outlet, and a manual switch. This junction box can also operate both controlled manually and by the computer. When on computer control, the on/off relay responds to the signal sent by the computer. The control signal is based on a comparison between the current calculated stress in the system and the target value. This control loop is the reason the load frame automatically shuts off when the test reaches a target stress level, and the relay and prevents the load cell from being overloaded.

The data from both the triaxial tests and the TCRS tests are collected by the TAG Lab central data acquisition center, which has 200 channels in total. These 200 channels are connected to and HP 3497A data acquisition unit controlled by a PC. The user has control over which channels to record the data from, reading intervals, as well as the total reading number.

4.4 Directional Wave Propagation Equipment

The wave propagation technology used in this study was designed and fabricated at TAG Lab. The endcaps designed by Marjanovic [103] only allowed for velocity measurements in one direction (vertical in this case). The setup was modified to include horizontal actuators, capable of propagating horizontal waves on the same specimen. It is also possible to measured velocities in non-major directions (inclined) using one vertical and one horizontal sandwich.

4.4.1 Equipment Fabrication

Two different types of piezoelectric elements are used in this study, extender elements (Noliac NAC2015) for compressional signals and shear plates (Noliac CSAP03) for shear signals. These two elements are assembled into bidirectional sandwiches. The transducers work on the principle of piezoelectric effect. When mechanical stress or forces are applied to some materials along certain planes, they produce electric voltage. This electric voltage can be measured by high impedance measuring instruments. The compressional plate element NAC2015 is $10 \times 10 \times 2$ mm, has a stiffness of 1273.0 N/µm, a capacitance of 760.0 nF, and provides a free stroke of 3.3 µm. The Noliac shear plate elements are characterized by providing a large stroke for a very compact design. The shear plate CSAP03 element measures $10 \times 10 \times 0.5$ mm and provides a free stroke of 1.5 µm and a capacitance of 3.321 nF. The P and S-wave elements are shown in Figure 4.15.

Each piezoelectric sandwich is built using the method described in Marjanovic [103]. A compressional and a shear piezoceramic element, two Brass Shim stock plates, two Dupont Kapton plates and various epoxies are used (Figure 4.16). The two plates ($12 \times 12 \times 0.8$ mm) of Brass Shim stock are epoxied to the sides of the shear plate using conductive epoxy product (silver-filled adhesive). There is a wire soldered to each Brass plate, making one the ground wire and one the power wire. Then a small piece (12×12 mm) of DuPont Kapton is glued to the sides of the compressional transducer using Loctite E30-CL, a brittle non-conductive epoxy, which isolates the shear and compressional transducers. The two sets are then epoxied together using Loctite E30-CL. The two ground wires are soldered together, reducing the number of wires coming out of each sandwich into 3; positive shear, positive compression and the ground. The outlet wires are then attached to a 3-hole pitch socket receptacle.

One set of piezoceramic sandwiches is fitted into a cavity machined out of the top and the bottom endcaps, as shown in Figure 4.17. The empty space around the sandwich in the cavity is then filled with soft epoxy (Loctite E-90FL). And finally, the hard epoxy (Loctite E30-CL) is used to coat the surface of the metal shim stock

and fill in any gaps at the top. Excess epoxy is used so that a curved surface is formed due to surface tension. This surface is then machined down with a fine grinder to ensure that any surface bubbles or discontinuities are eliminated.

The horizontal sandwich is designed using the same configuration of piezoceramic elements (Figure 4.18). A microscope slide is attached to the surface of the sandwich using Loctite E30-CL, pro- viding a perfectly flat surface which will be in contact with the specimen. A smooth and flexible surface is needed on the back of the sandwiches to prevent the elements or the shim stocks from puncturing the membranes. Hot glue is used for this purpose, a material with high workability when hot and a flexible solid consistency when cold.

The horizontal sandwich wires need to be routed from the side of the specimen, inside the membrane, to the connection on the base without affecting the specimen isolation from the cell fluid. Plumbing caulk is used around the bottom cap covering the wires and providing a continuous surface, so the O rings that seal the membrane press against this flexible material (Figure 4.19). The ends of the actuator wires were sealed with hot glue to prevent any leakage through the wires.

4.4.2 Actuator Calibration

There is a lag in the arrival time of signals received by the oscilloscope. This lag represents the time it takes for the signal to travel across the electronics and wires before it arrives at the oscilloscope. Additionally, there is a lag time due to the physical separation between the piezoceramic elements and the specimen surface caused by the epoxy between the elements, as well as the S-wave elements that are directly between the two P-wave elements. This lag time (t_L) is determined experimentally in each of the three directions by testing different length spacers and back calculating the travel time for a spacer with zero length using linear extrapolation. The material used for the spacers was PVC (Polyvinyl chloride), which is soft and has low dispersive behavior. It also has significantly more attenuation for the S-wave than the P-wave.

PVC rods were cut into different lengths and used to calibrate the caps (vertical

setup) and study the velocity range in the material. The PVC rods were cut into 2.78, 4.65, 7.9, 14.35, 47.48 and 102.11 mm pieces with 35 mm diameter, and the arrival times were picked from the signals. Rather than show all the figures for the different wave types in different directions, the procedure will be presented for vertical P-waves in PVC rods.

Figure 4.20 shows the vertical compressional P-waves in different length rods and the arrival times picked based on the first jump in the voltage. Figure 4.21 shows the P-wave arrival times for each respective length of spacer. The best fit linear line for the six data points provides an equation of the form $y = mx + b$. b is the y-intercept of the line, which corresponds to a spacer with zero height and the inverse of the slope is the P-wave velocity in this material. The lag time (t_L) is subtracted from the arrival time, when calculating the velocities.

The PVC pieces were also sent to Fugro Houston Laboratory for velocity measurements. No information on the instrumentation or the signal processing were provided. Velocities measured in TAG Lab on the same pieces are compared to Fugro results in Figure 4.22. The average P-wave value obtained in TAG lab was 2404 m/s, whereas the average value reported by Fugro was 2288 m/s. Theoretically the velocities should be independent of the length, however when measured, they would have slight variabilities due to errors such as signal quality and erroneous arrival pick, distance measurement, coupling, and the lag time accuracy. These errors tend to be negligible when the specimen length is greater than 2 cm. The velocity calculated based on the slope of the trendline in Figure 4.21 is 2293 m/s, which is shown with the red line in Figure 4.22. It is clear that the velocities are nearing 2293 m/s as the sample gets taller.

A similar procedure was followed to determine the lag times for P and S-waves propagating in horizontal and inclined directions. A piece of PVC brick was used (as shown in Figure 4.23), for this purpose, to ensure coupling between the sandwiches and the spacer. The side sandwiches are stuck on the two sides of the brick with a layer of vacuum grease, facing each other. For a horizontal wave, one acts as generator and the other one as a receiver. For an inclined wave, one side sandwich

generates the signal and one of the vertical caps (top cap in this case) receives the output signal. Depending on the direction, the lag times in this research varry between 0.75 µs and 2.5 µs for P-wave, and 0.1 µs and 0.4 µs for S-wave.

4.4.3 Travel Distance Determination for Inclined Wave Velocity Calculations

The piezoceramic elements used in this study have an area of roughly 1 cm^2, which makes them nonpoint sources considering the specimen dimensions. A single value is needed for the travel distance to calculate the velocity for each signal. In configurations where the sandwiches are parallel to and on-axis with one another the travel distance is the length between the sandwich surfaces. However, in cases where the sandwiches are on perpendicular and horizontally offset surfaces, to measure the inclined velocities, there are different ways of interpreting the distance. The various interpretations are explored in this section. Figure 4.24 shows a series of P-wave velocity measurements that are conducted on an isotropic PVC brick. The axial velocities are measured in all three directions (three distances) of by flipping the brick and using the vertical velocity caps placed on each of the three parallel surfaces. The inclined signals are sent from a side transmitter (with different vertical locations), while using the top cap as the receiver to measure the inclined velocities. Figure 4.24 shows the axial (acquired using the top and bottom caps) and inclined signals (acquired using the side sandwich and the top cap) collected on the same PVC brick. Comparing the axial and inclined signals propagating through the shortest distance (~ 80 mm), the yellow and the red, it is clear that the waveforms are different. The axial signal has a sharper arrival and a higher first peak amplitude, whereas the inclined signal has a smaller first peak amplitude and a relatively more gradual arrival, tilting the waveform to the right. The arrival times are shown with black dots.

Figure 4.25 schematically shows the three different geometrical paths, between two actuators on two perpendicular surfaces: longest (red), middle to middle (green) and shortest paths (blue).

Figure 4.26 shows the axial velocities (green points) and the inclined velocities

calculated using the longest, middle to middle and shortest paths between the sandwiches. The velocities in isotropic material are independent of both direction and distance. Also the group and phase velocities are equal due to the isotropic nature. As shown in Figure 4.26, the middle to middle path gives an average inclined velocity of 2276 m/s and 5.57 m/s SD, and the axial measurements have an average of 2271 m/s and 4.45 m/s SD. These two sets of measurements are practically equal to one another and independent of the distance.

While the physics of the phenomena in unknown, our observations support the use of middle to middle distance for laboratory testing purposes. However, in longer distances the elements resemble point sources. As shown in Figure 4.26, with the distance increasing, the velocities calculated using the shortest and the longest paths are converging.

4.5 Wave Propagation Electronics

The electronic setup used in this study was developed in TAG Lab by the author. The setup consists of a signal generator, custom-made circuit box and an oscilloscope, which will be discussed in this section. Also, a summary of the noise problem will be provided, as well as the signal processing methods.

4.5.1 Wave propagation Setup Components

- **Signal Generator**: A *B&K* Precision 3003 Function Generator (Figure 4.27) used in this research delivers clean and accurate DC to 10 MHz waveforms with frequency accuracy of 0.02% and 0.1 Hz frequency resolution. The settings of the pulser are set to send a ±5 V square pulse with a frequency of 115 Hz, the repetition of these square waves is set at a low frequency, f = 0.11 kHz. The elements are energized using a step function because it includes infinite frequencies and allows the wave to propagate at an optimal frequency. The generator is connected to the circuit box using a BNC connector with a 50 Ω terminal.

The ideal input frequency would return the strongest and clearest signals. Also, the specimen's optimal propagation frequency is unknown. So for this study's purposes, the goal is to select a frequency that 1) keeps the voltage at peak until after arrival, ensuring that the arrival will not coincide with the down going part of the square signal, and 2) allows the transducer-specimen-transducer system to vibrate at its natural frequency. Marjanovic [103] investigated the best frequency pick for the input square signal, and suggested that at higher stresses, a larger wavelength is a more appropriate choice for output signal clarity. Thus, this research used a square wave with a large wavelength for all the subsequent velocity results (0.11 kHz frequency).

- **Circuit Box**: The velocity circuit box was designed and custom-made at TAG Lab. The schematic of the system can be seen in Figure 4.28 and the actual circuit is shown in Figure 4.29.

  The electrical circuit was built inside a metal box, acting as a Faraday cage to help minimize the Electromagnetic Interference (EMI). A capacitor was used to increase the stability of the signal and provide more driving current. Resistors 2-4 were used as voltage dividers to feed the input signal from the pulse generator into the oscilloscope. The operational amplifier can be used as a tool to reduce the noise and create a clearer signal. The system was powered by a DC Power Supply at 23 V. The MOSFET transistor is used since the actuators are current-limited. A MOSFET passes high current while running on a small current itself. The part numbers and properties of the various parts are as follows:

  - **Ultrafast MOSFET driver (IC1)**: IXDD614PI
  - **Operational amplifier (IC2)**: LT 1210 CT7
  - **Capacitor**: 10 μF
  - **Resistor 1**: 5.1 $k\Omega$
  - **Resistor 2**: 75 $k\Omega$

  - **Resistor 3**: 10 $k\Omega$
  - **Resistor 4**: 0.22 $k\Omega$

- **Oscilloscope**: A Tektronix TBS1072B-EDU Digital Oscilloscope (Figure 4.30) was used in this research. This oscilloscope allows for two signals (input and output) to be recorded simultaneously on two different channels. The measurements are taken with an oscilloscope, every 128 pulses are averaged continuously and have a sampling rate of 5-25 Mega-samples/s ($4 \times 10^8 - 2 \times 10^7$ resolution).

4.5.2 Noise and Electromagnetic Interference

Electromagnetic interference and other types of electric noise negatively affect the quality of the waveforms ans the signal interpretations. This section identifies the sources of noise and some hardware solutions used to reduce them. The triaxial cell is a steel chamber in which the soil specimen is surrounded by pressurized, non-conductive fluid (silicon oil). This means any wire inside the cell needs to go through a pressure tight electronic connection placed in the base. This connection appears to add a high amplitude noise to the beginning of a signal. Whether or not this noise causes a significant problem for signal interpretation depends on the travel distance and the velocity. In shorter specimens, or higher velocity environments, the signal arrival is closer to the high amplitude noise, which gets combined with the output signal and makes the arrival time harder to pick. This noise can only be avoided by connecting the oscilloscope to the transducer with a continuous shielded cable, which is not practical in the current triaxial setup. Figure 4.31 shows two P-waves propagating through different soil specimens. In one setup the transducer is connected through the base and then the scope (Signal 1 shown in blue), and the other one is connected directly to the oscilloscope (Signal 2 shown in orange). In both tests the triaxial chamber was excluded to isolate the potential problem. Signal 1 contains the high amplitude noise in the beginning which lasts for much longer, compared to signal 2 in which the initial high amplitude noise decays very quickly.

While this initial high-amplitude noise is inevitable for the current triaxial testing setup, it is not an issue for the TCRS testing setup used in this research, since the sending and receiving wires are connected directly to the top and bottom caps.

There are several electronic devices around in the laboratory that also cause noise in the collected signals. This EMI has much higher frequencies and can have considerable amplitudes, especially compared to the shear signal amplitude. To minimize the effect of this noise Faraday cages are used whenever possible. In addition, some electronic devices in the room are shut off whenever practical while making a velocity measurement. It is worth mentioning that EMI is relatively easy to filter out during the signal processing phase because it has a high frequency and occurs continuously during signal acquisition.

Circular 9-pin connectors are used inside and outside of the triaxial cell, mounted into the base. The three wires coming out of each sandwich (the P, the S and the ground) are all connected to a female 9-pin connector. All the P and S wires amount to a total of 8, and the 4 ground wires are all connected to the ninth pin. A mirrored female 9-pin connector is connected to the base connector from the outside. From this connector the sending and receiving wires are separated into two ... cables, each connected to the circuit box with a circular 5-pin connector. Keeping the sending and receiving wires separate reduces the noise by decreasing the electrical interference between the two currents.

Furthermore, grounding is known to have a significant effect on noise levels. Also having too many sources of ground increases the noise in the signal. As a result, allowing a few of the ground sources to "float" while trying to maintain one definite "earth" would minimize the noise caused by ground loops. In this research the P and S actuators in each sandwich were grounded together, then the 4 grounds (vertical and horizontal P and S) were also soldered together, connecting to the ground wire in the circuit box. The author also found that using a separate wire connecting the triaxial cell (or the receiving cap itself in case of the TCRS test (yellow wire shown in Figure 4.32), helped stabilize the output signal received buy the oscilloscope.

Lastly, in any given material, compressional waves travel faster than shear waves.

This can cause inevitable interference between the two for various reasons. Sometimes, depending on the material type and geometry, it is possible to have the P signals reflect off the side of the top cap and arrive before the shear signal does, resulting in erroneous interpretation of arrival time, frequency content, and waveform. The signal interpretation and noise reduction procedures will be discussed in the next chapter.

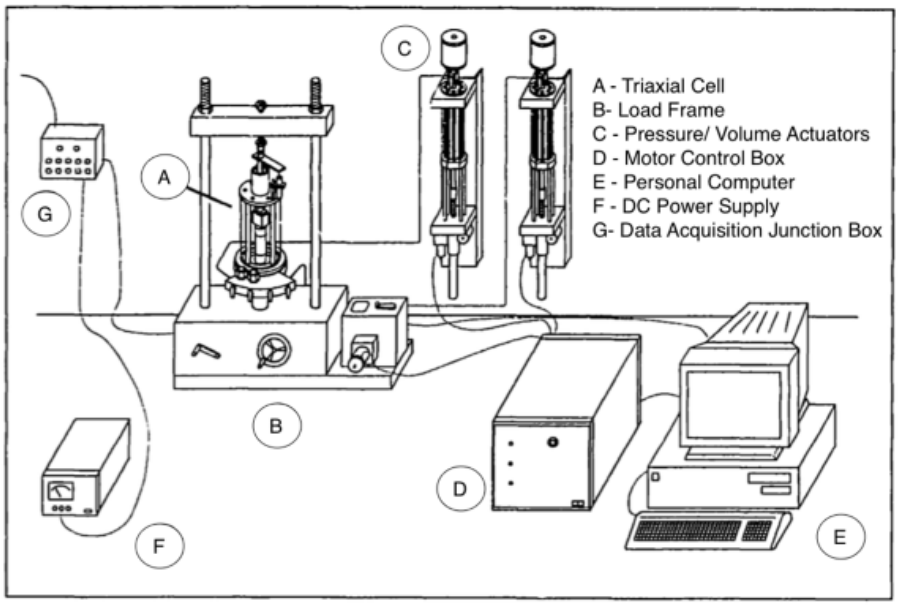

Figure 4.1: Major elements that are combined to create the triaxial cell system [136] (note that in the current the axial load is controled by a third PVA)

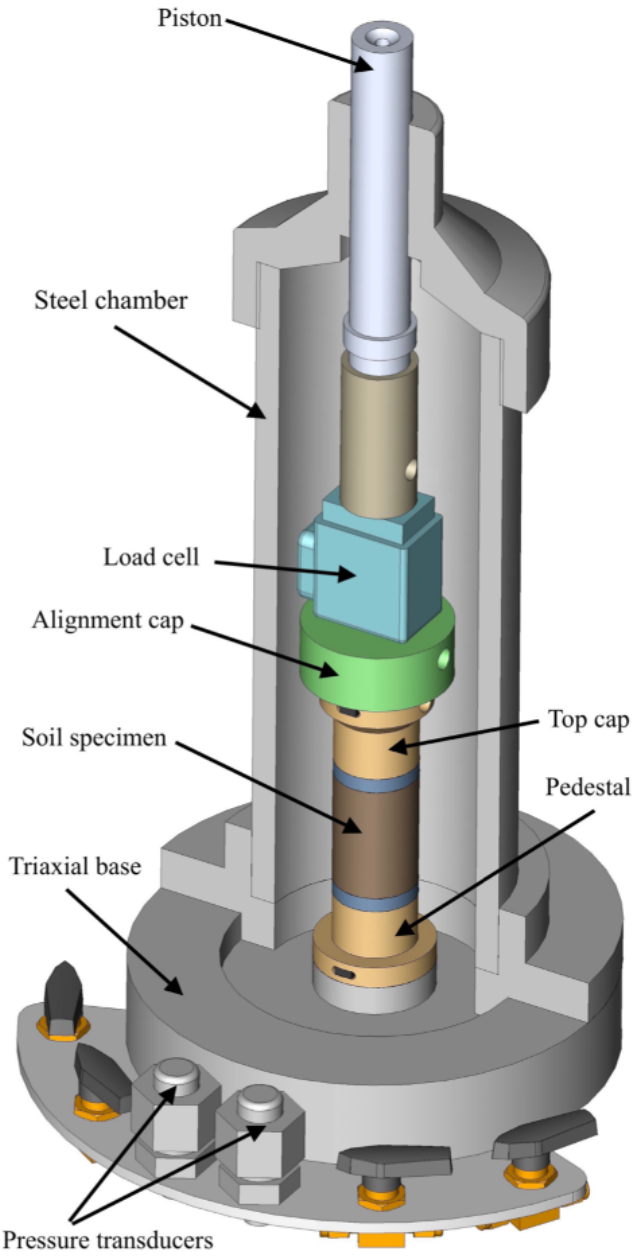

Figure 4.2: Three-dimensional schematic of a medium pressure triaxial cell [103]

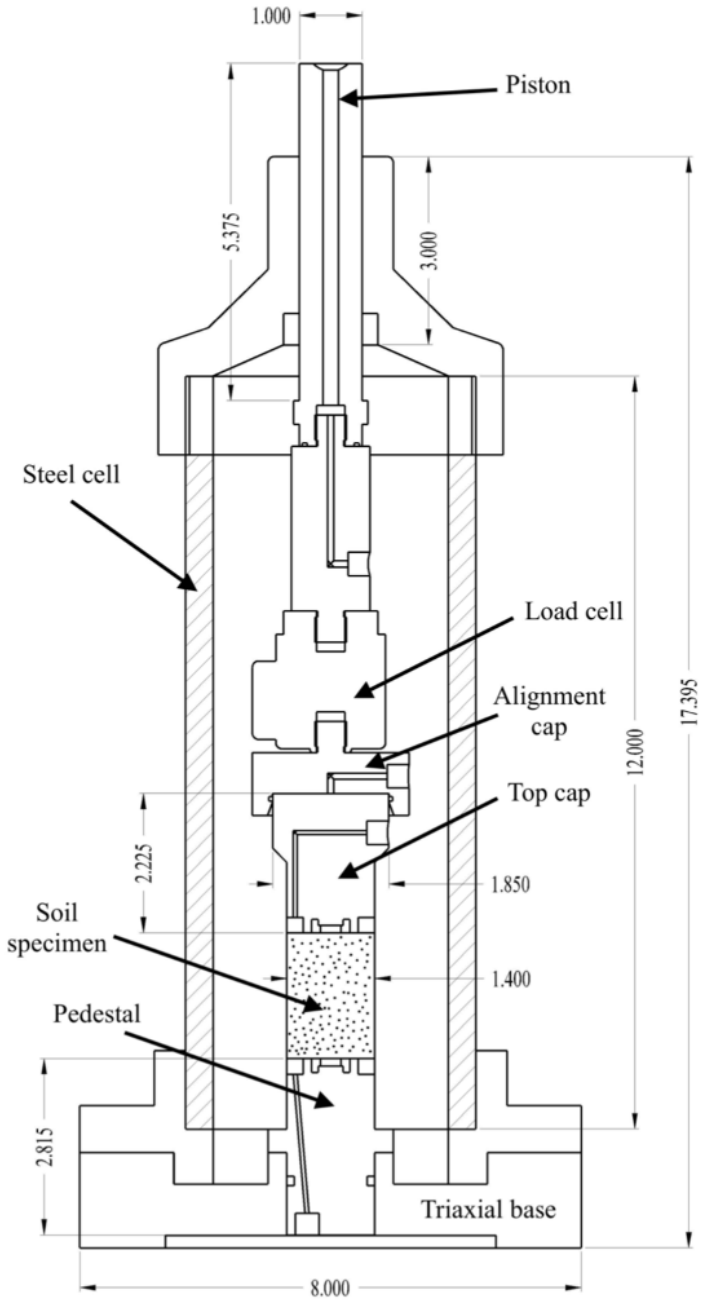

Figure 4.3: Section vied of a medium pressure triaxial cell (dimensions in inches [103]

Figure 4.4: The piston, attached to a spacer, then the load cell, and finally the alignment cap that fits with and aligns the top endcap. The alignment cap seen here has the ability to connect to the piston to enable suction; however, this was not used in this research. The standard top cap used in this research did not rigidly connect to the piston [103]

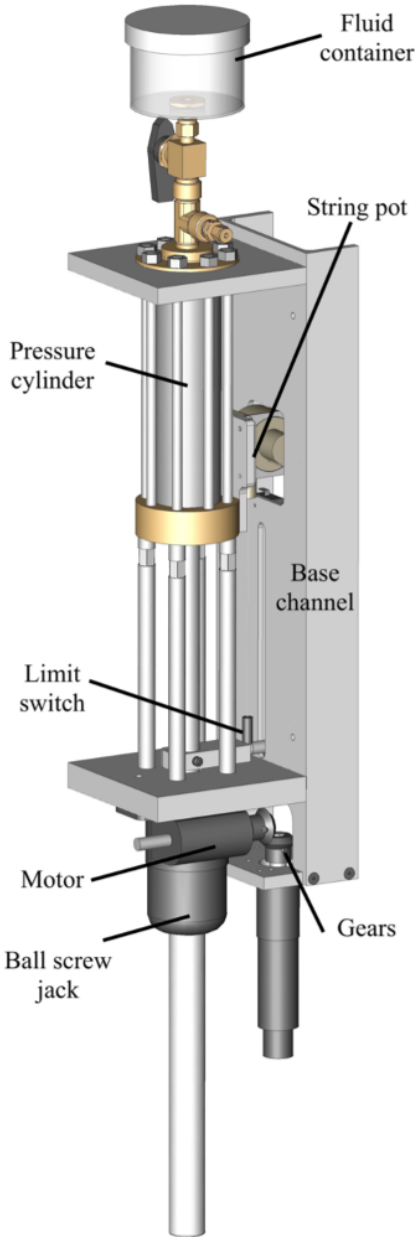

Figure 4.5: Schematic of a PVA [103]

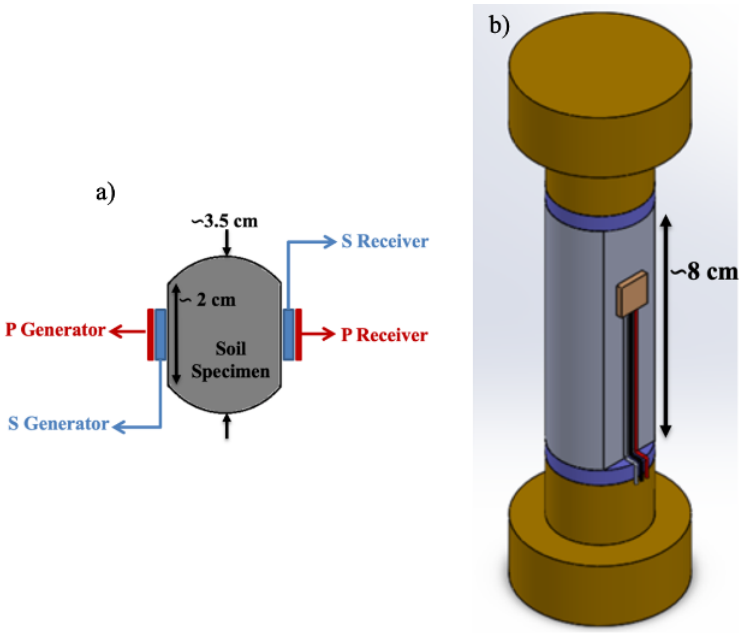

Figure 4.6: Schematics showing: a) cross section of the specimen and the side actuators, b) 3-D illustration of the specimen, the caps and the side actuators

Figure 4.7: The hollowed porous stone

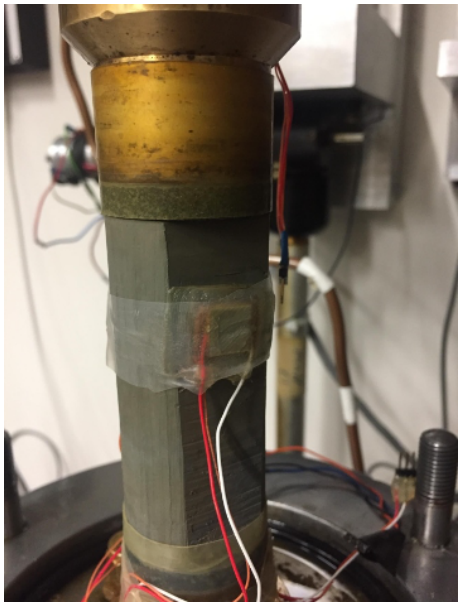

Figure 4.8: Side actuators are held in place with a small band of condom until the membrane is placed on the specimen

Figure 4.9: Final specimen configuration

Figure 4.10: TAG Lab TCRS testing setup

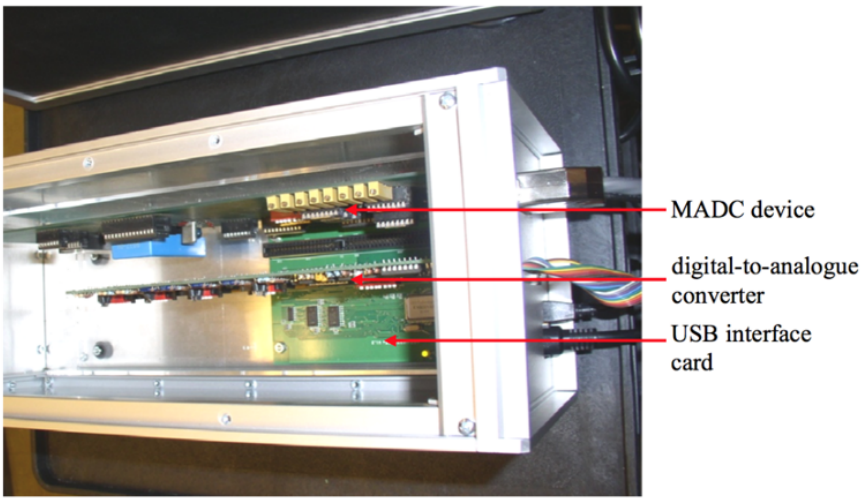

Figure 4.11: The MADC box houses the components needed to take an analog signal and feed it into a computer

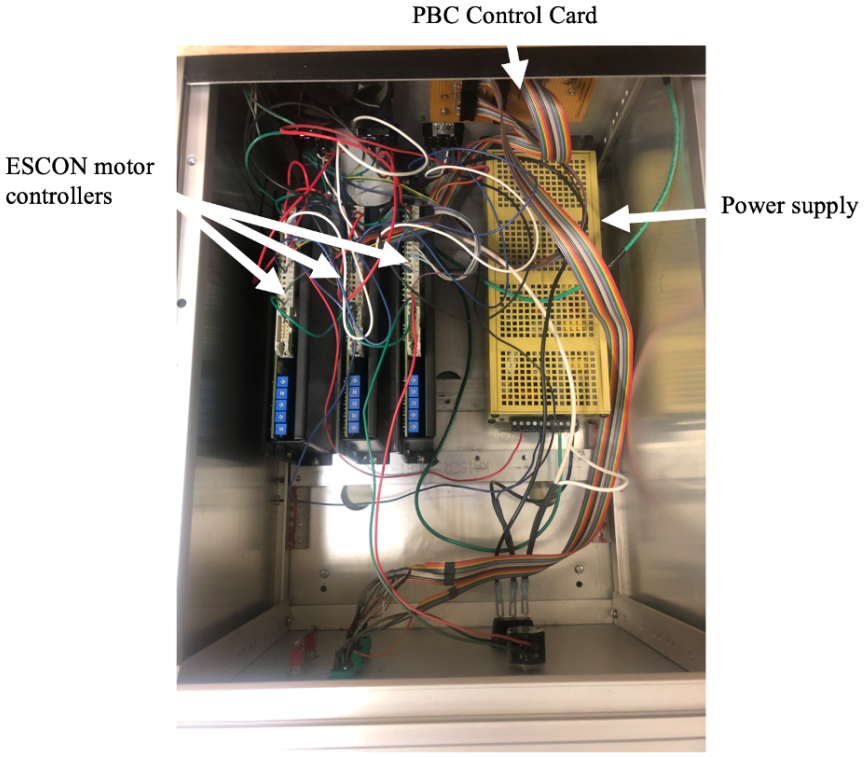

Figure 4.12: Updated computer control box [121]

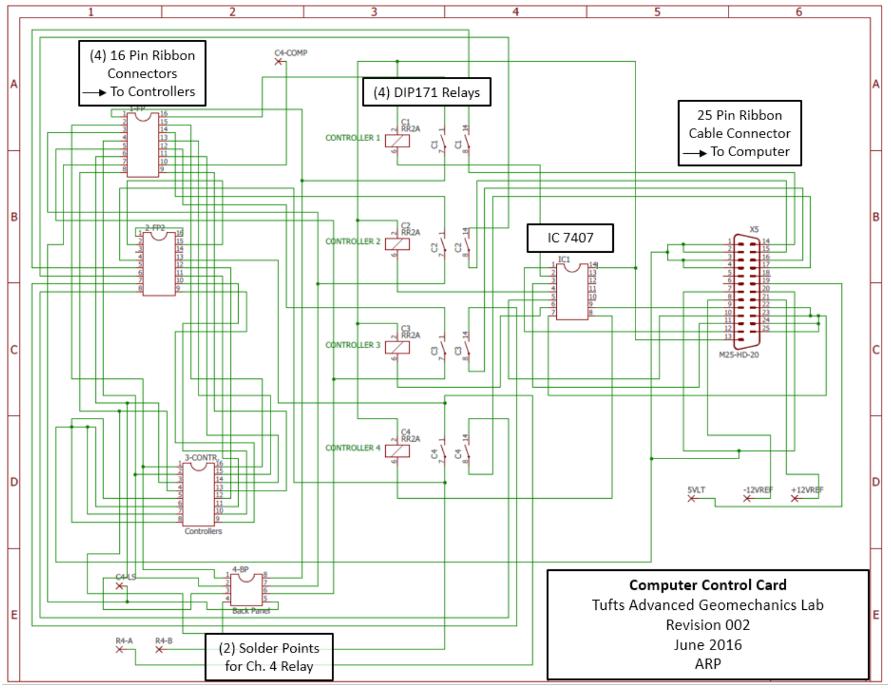

Figure 4.13: Updated computer control box [121]

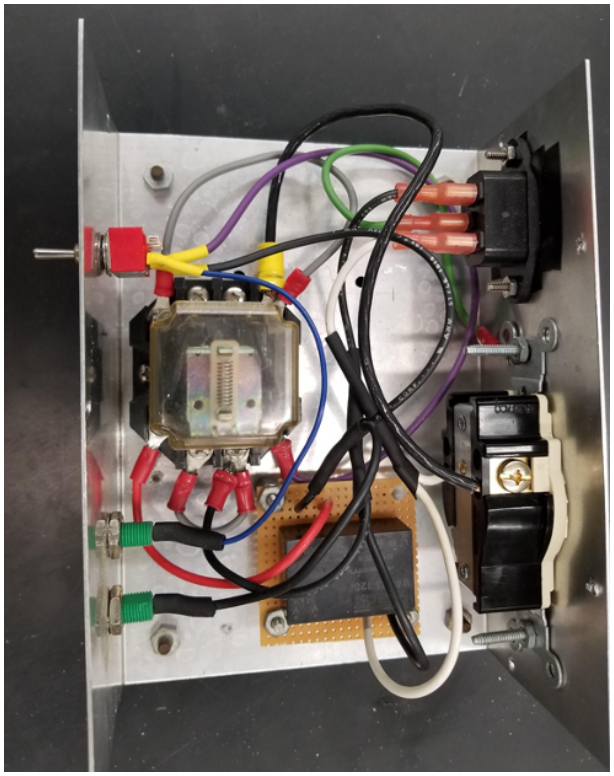

Figure 4.14: TCRS load frame junction box

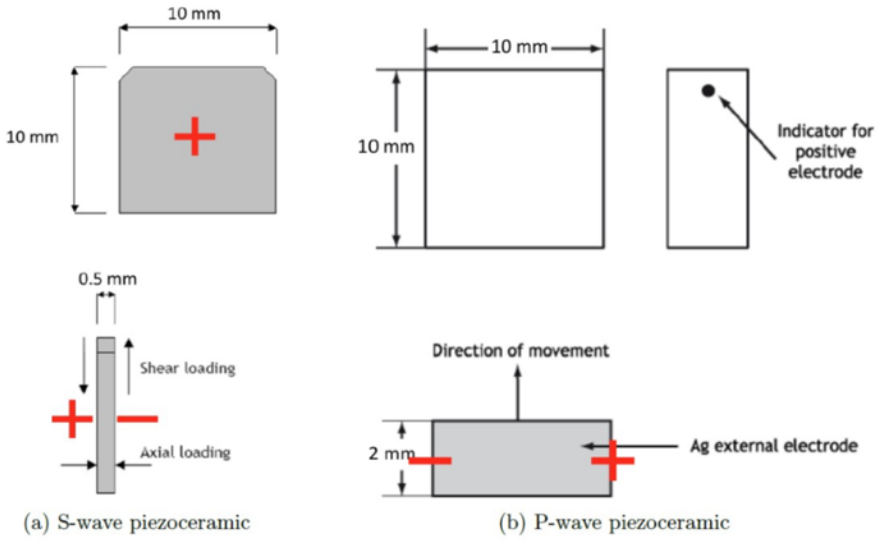

Figure 4.15: Schematics of the Noliac S-wave (CSAP03) and P-wave (NAC2015) Piezoceramic elements obtained from the Mictromechatronics, Inc. website

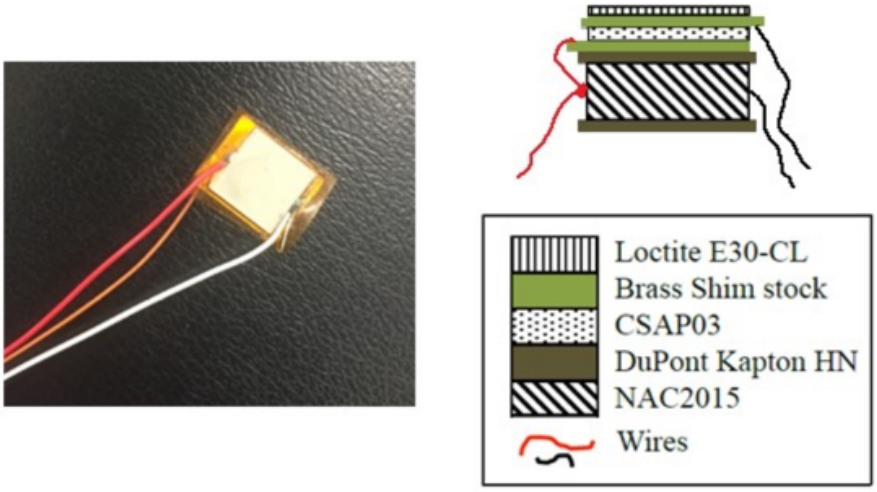

Figure 4.16: The sandwich including S-wave and P-wave piezoceramic elements

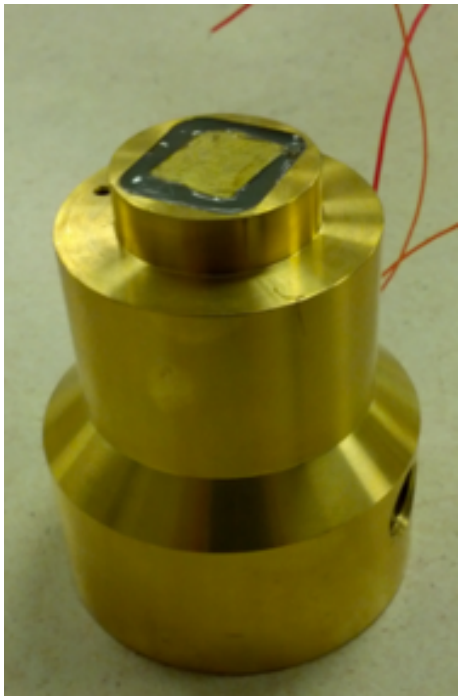

Figure 4.17: The custom made brass endcap

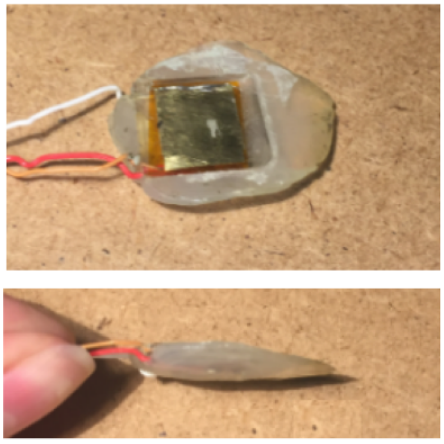

Figure 4.18: The surface touching the specimen was flattened using a microscope slide (a) and the surface in contact with the membranes is curved and flexible (b)

Figure 4.19: The horizontal sandwich wires permanently held in place on the bottom cap using plumbing caulk

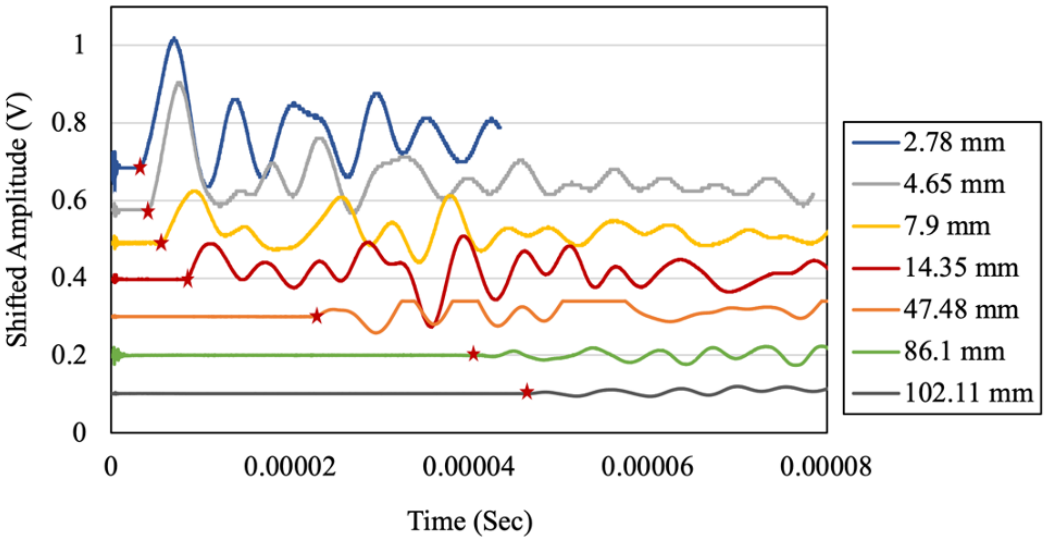

Figure 4.20: P-wave signals propagating through PVC rods with various lengths were collected. An arbitrary amplitude was added to each signal to separate them vertically

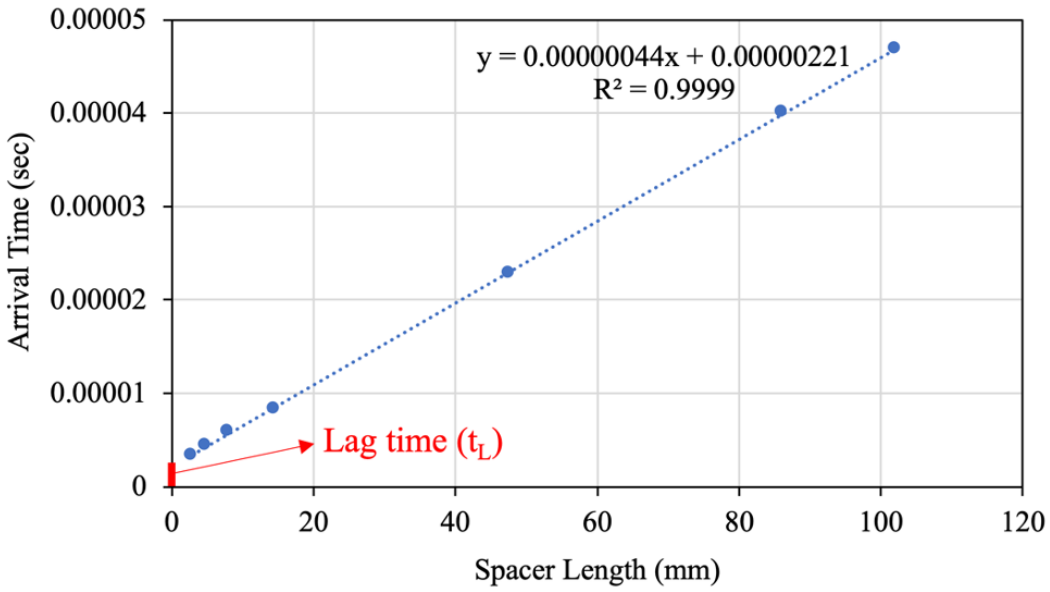

Figure 4.21: Interpreted arrival times of P-waves through various lengths of PVC rods

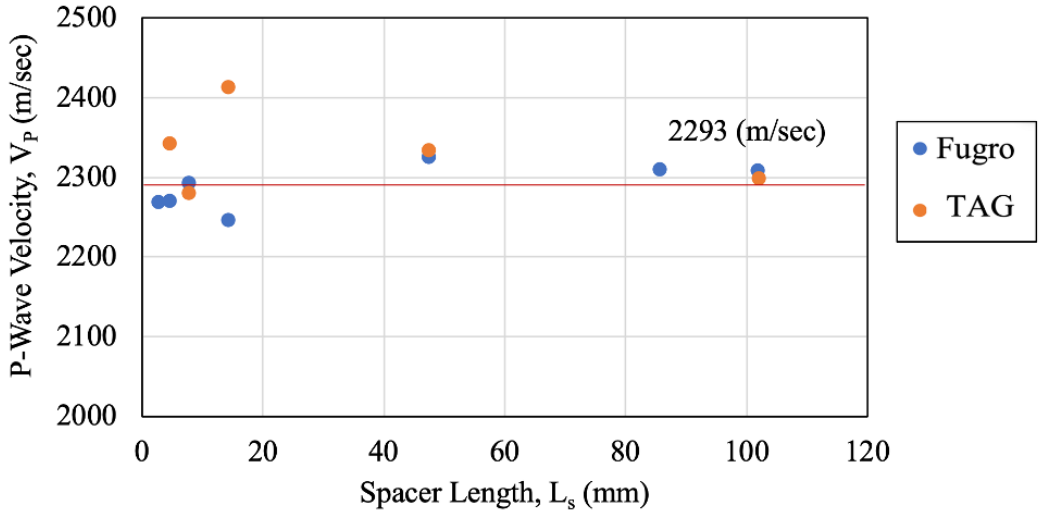

Figure 4.22: Vertical P-wave velocities measured in the same set of PVC rods by Fugro and at TAG Lab

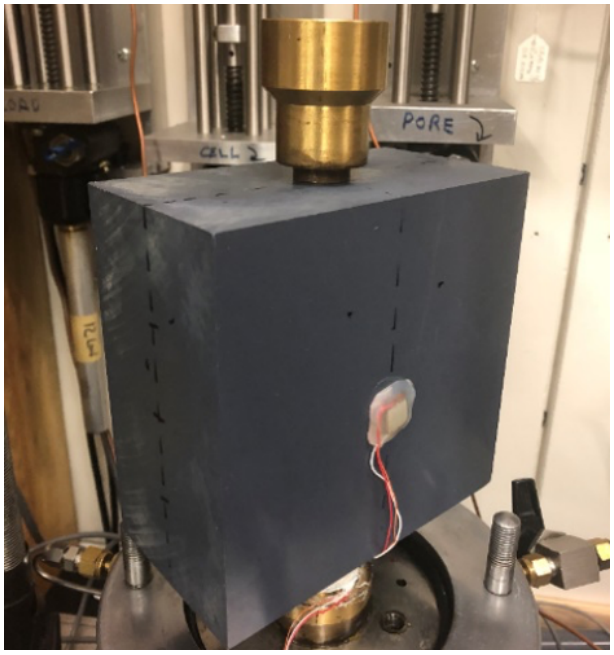

Figure 4.23: Horizontal and inclined calibration setup

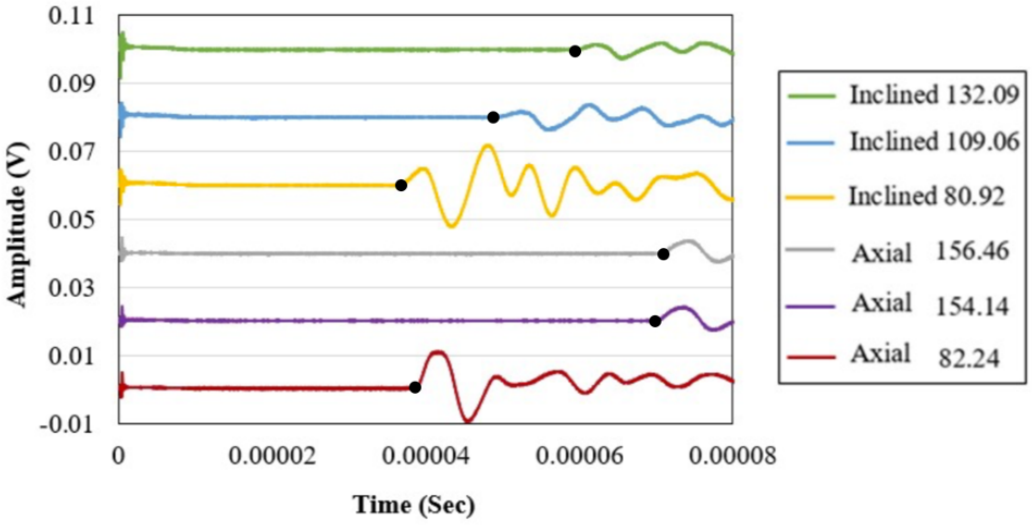

Figure 4.24: Inclined and axial P signals for different travel distances (in mm)

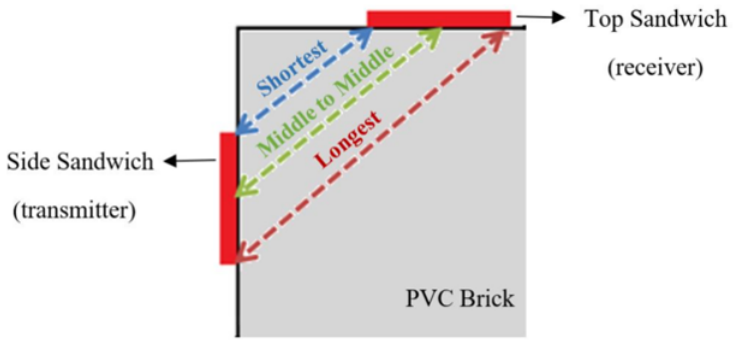

Figure 4.25: . The three paths used in inclined velocity calculations; shortest, middle to middle and longest

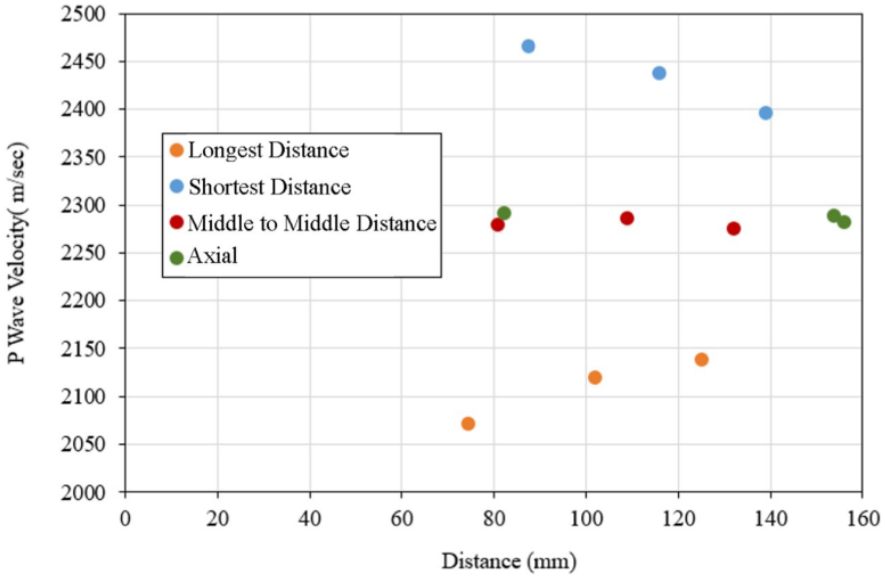

Figure 4.26: The three paths used in inclined velocity calculations; shortest, middle to middle and longest

Figure 4.27: *B&K* Precision 3003 Function Generator

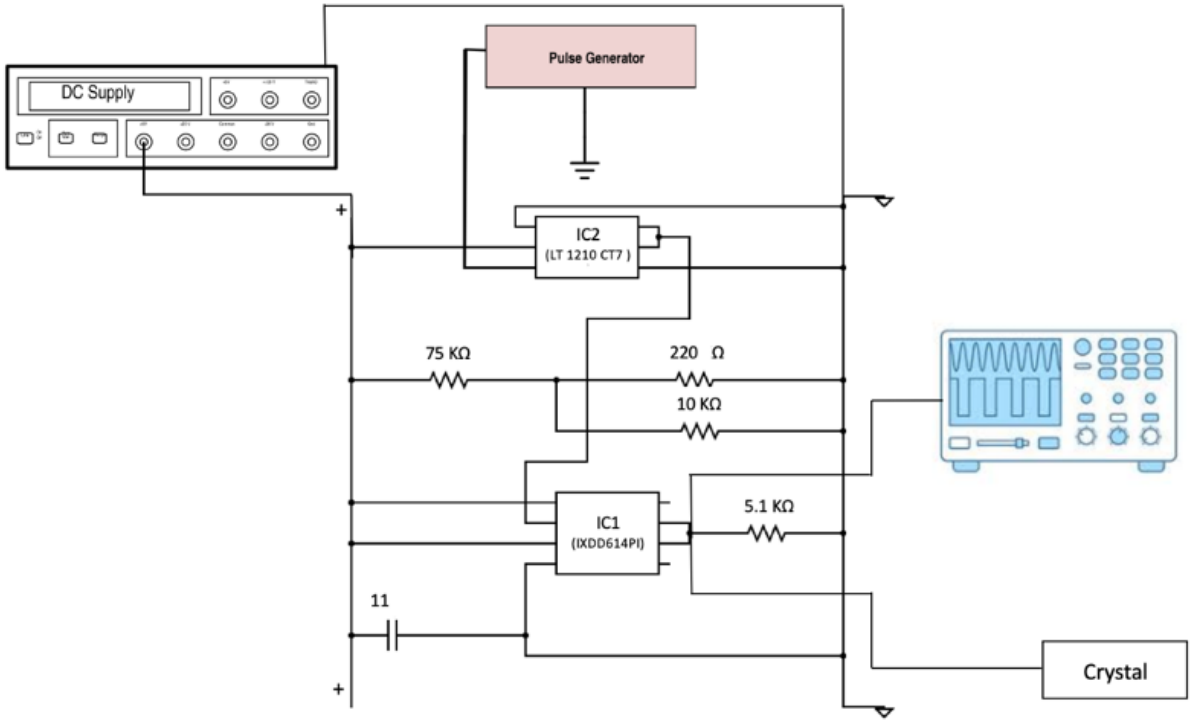

Figure 4.28: Circuit design schematic

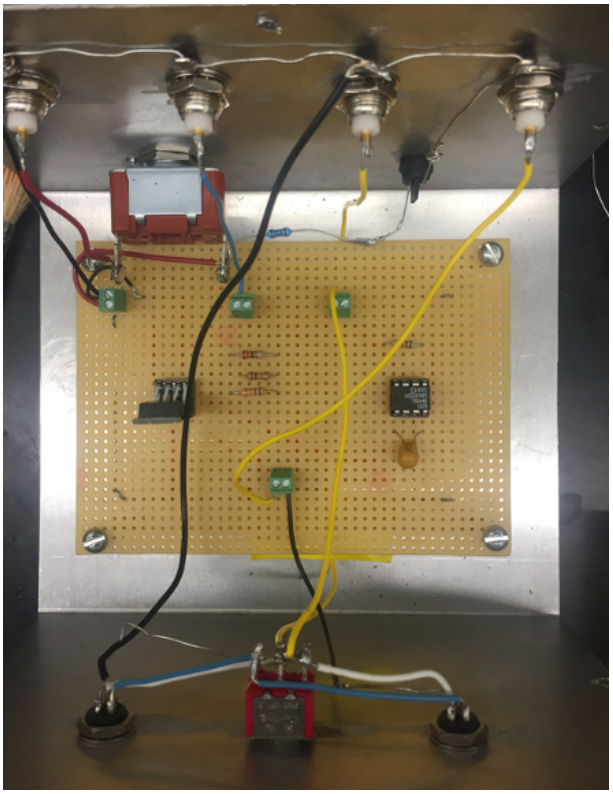

Figure 4.29: Custom-made circuit box

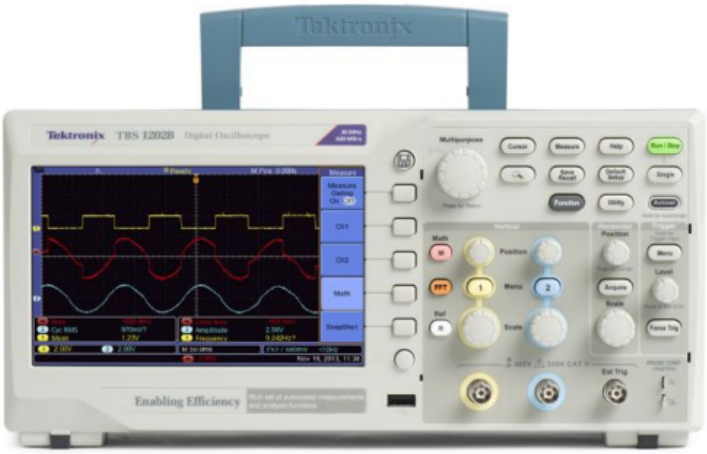

Figure 4.30: Tektronix TBS1072B-EDU Digital Oscilloscope

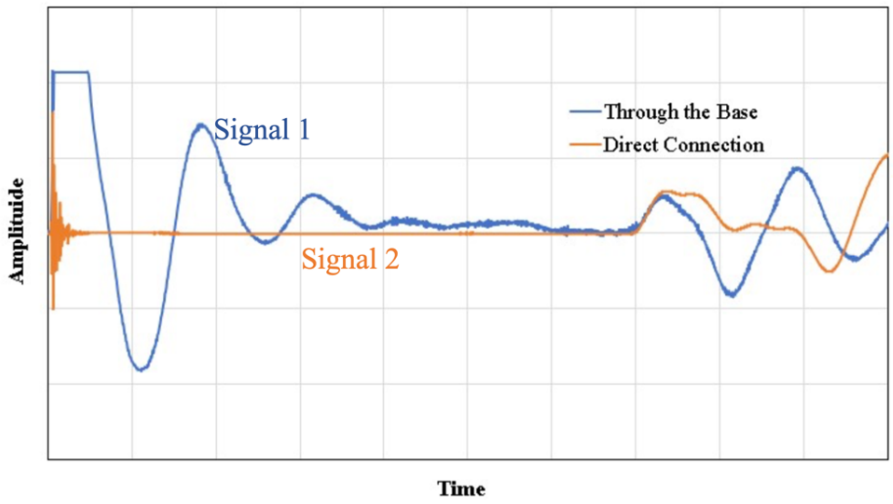

Figure 4.31: Signal 1, going through a soil specimen and the electrical connection in the base, and signal 2, going through another soil specimen but straight to the oscilloscope

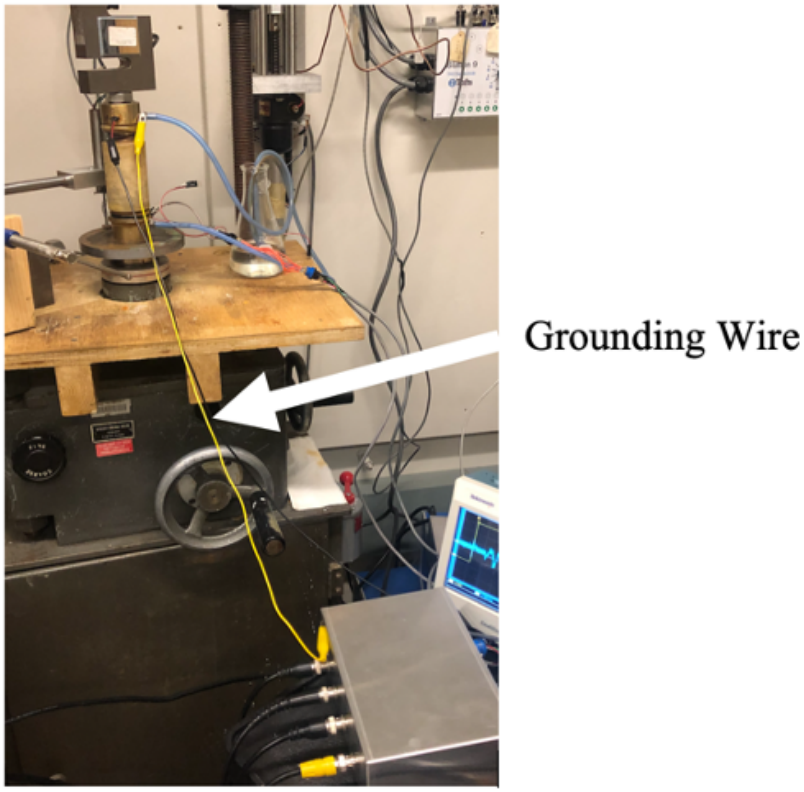

Figure 4.32: Alligator connector grounding the circuit box and the top cap

Chapter 5

Signal Interpretation and Test Corrections

As it is suggested by the title, this chapter will focus on some basics that are required for translating experimental measurements into coherent data. First, the effect of stress level, direction of propagation, testing setup and material on waveforms will be discussed, as well as the velocity calculation method. Next, the corrections applied to the measured vertical effective stress, excess pore pressure and sidewall friction, are explained.

5.1 Signal Interpretation

5.1.1 Various Waveforms and Interpretations

Regardless of the wave type (P or S) and test (triaxial or TCRS) type, a square signal is sent to the generating piezoelectric actuator, and the output signal is received using the oscilloscope (which averages every 128 readings) . Each time the output signal is collected, the corresponding input signal is always taken. Then the arrival is picked based on the signal type. It is worth noting that even the same type of waves (P or S) can have widely different waveforms depending on the stress level, testing setups, boundary condition, propagation direction and material.

Figure 5.1 shows the P and S-waves in different directions propagating through RGoM, under lowest (1.2 MPa) and highest (10 MPa) vertical effective stresses in the triaxial setup. All the compressional waves, regardless of direction of propagation or stress level have an initial, high amplitude interference signal. Despite having generally similar shapes and amplitudes, these initial signals change slightly with stress level and direction, making post processing much harder. As an example, Figure 5.2 shows the first 20 µs of the vertical P signals (Figure 5.1-a), where

the amplitudes are shifted vertically in an attempt to overlap the initial interference signals, and it clearly depicts the subtle discrepancies between the two. This high amplitude signal becomes more of a problem for smaller propagation distances (horizontal and inclined) and higher velocities (higher stresses). In such cases the arrival time is closer to zero, and the initial signal can interfere with the waveform, making the arrival interpretation harder. As shown in Figure 5.1-b and 5.1-c, the inclined and horizontal waveforms still have an unequivocal arrival, however, considering the short propagation distance (2-5 cm), even a small error in arrival time can cause a considerable error in the calculated velocity value. As an example, a 0.2 µs error in the arrival time for the inclined P at 10 MPa, results in a 30 m/s error in the velocity value. This is to say that while the author has paid the utmost attention in picking the arrival times, with the current technology a good portion of the human error associated with the task is simply inevitable.

Effect of the Stress Level

The same type of waves in the same directions tend to have very similar waveforms regardless of the stress level. However, as shown in Figure 5.1 and Figure 5.4 for the same input signal (23 V square wave) all five wave types have much stronger output signals, resulting in higher amplitudes, at higher stresses. This is due to better coupling between the soil surface and the piezoelectric sandwiches, as well as higher levels of contact between the clay particles. It also appears that at higher stress levels, P-wave signals dampen faster after the first arrival.

Comparing the signals at 1.2 and 10 MPa shown in Figure 5.1-d, it can be seen that the vertical shear signal at the lowest stress level has the poorest quality, hence is the hardest to interpret. However, with the increasing stresses, the coupling improves significantly, alleviating the problem to some extent. For weak S signals at low stresses a boxcar filter is used, such that the data is converted to the frequency domain using FFT, a range of desirable frequencies is selected, which the boxcar filter allows to pass, while eliminating any activity outside of this range. Figure 5.3 shows the low stress vertical S signal in Figure 5.1-d in much bigger scale (blue). It also

shows the signal after having been processed with a boxcar, zeroing the amplitude of the frequencies higher than 10 kHz (red). While the processed signal provides a much clearer signal and an easier arrival time interpretation, it does cause a small shift in the signal, which was calculated by Marjanovic [103] to correspond to 0.25% error in the arrival time.

Regardless of the wave type and direction, the arrival time was interpreted as the first major increase in the amplitude that has the same polarization as the input signal, in this case positive, in signals without the near-field effect [21]. The arrival times are marked with red stars on all the waveforms. As shown in Figure 5.1-d and 5.1-b, near-field effect was not observed in the shear waves collected from the triaxial setup. However, the TCRS specimens demonstrated slight near-field effect at low-medium stresses (less than 6 MPa) systematically, regardless of the material type (Figure 5.1-a). When the signal includes the near-field effect, Brignoli et al. [21] define the arrival time as the bottom of the initial upward curve, where the polarization changes direction (negative to positive) as shown by the red star in Figure 5.5.

Effect of the Propagation Direction

Figures 5.6 and 5.7 focus on the effect of propagation direction on the waveforms, at the same stress level. Figure 5.6 includes the P-waves in vertical, inclined and horizontal directions at 10 MPa. The output frequencies are obtained using half of the wavelength ($\lambda/2$ = second zero crossing- first zero crossing) with the equation $f = V/\lambda$. The horizontal P-wave output wave has the highest frequency (260 kHz) compared to the inclined (123 kHz) and vertical (113 kHz). This is potentially caused by the differences in particle alignment and boundary conditions in different directions, as well as the slight difference in the way the actuator sandwiches are placed on the specimen. It is also evident that the horizontal signal has a much sharper increase in the arrival amplitude compared to the other two. Figure 5.7 compares the S signals in horizontal and vertical directions at 10 MPa. Although the vertical signal is amplified by a factor of 5 for the sake of comparison, it still

has a much lower amplitude compared to the horizontal. Also, the noise level in the vertical shear is much higher that the horizontal, even without the amplification. The vertical S has a much smaller frequency (16 kHz), compared to the horizontal (52 kHz). Finally, similar to P signals, the S signal also has a much sharper arrival in horizontal direction.

Effect of the Testing Setup

The other factor affecting both the P and S-waveforms is testing setup. Figures 5.8 and 5.9 show the vertical P and S-waveforms, at the same stress level (10 MPa), propagating through RGoM-EI specimens undergoing K_0-consolidation in triaxial (blue) and TCRS (orange) testing setups. It is worth noting that the specimens had different heights at the time these signals were collected, hence the arrival times varied greatly. The most obvious difference between the P-waves shown in Figure 5.8 is the initial EMI in the triaxial signal and its absence in the TCRS signal. This is due to the connection configuration and was explained in Section 4.5. Although both signals have unequivocal arrival times (shown with red stars), they have significantly different waveforms. The TCRS demonstrates a sharper increase in amplitude at arrival, has a temporary drop in the amplitude at the first peak before going back up, and has a more unique shape. The triaxial signal however is much more sinusoidally shaped and has the highest amplitude in its second peak, instead of the first. The triaxial p signal also has a higher frequency (113 kHz) than the TCRS (91 kHz). Figure 5.9 includes the S-waves from the triaxial and TCRS tests at 10 MPa, both magnified by a factor of 5 to make comparison easier. It is obvious that the triaxial signal has a much higher level of noise, due to the wires going through the cell fluid and multiple connections. The TCRS signal exhibits initial curving, which is due to poor grounding. This issue can be mostly resolved by connecting the cap to the circuit box ground wire (Figure 4.32). Contrary to the triaxial S-wave, the TCRS S-waves is closer to a sine wave, and it has a higher frequency (28 kHz) than the triaxial (16 kHz).

Effect of the Material

Lastly, the material type can have an effect on the waveform. Figure 5.10 and 5.11 show vertical P and S signals propagating through RBBC and RGoM-EI specimens at almost 10 MPa, tested in the TCRS setup. The arrival times are shown with yellow stars. Figure 5.10 clearly shows that the two materials have quite similar waveforms and frequencies. S signals however are drastically different (Figure 5.11). The S signals are magnified by a factor 5 for clarity. The first peak amplitude of the RBBC signal is 4 times the RGoM-EI's. RBBC has a much higher frequency (51 kHz) compared to RGoM-EI (28 kHz), which causes a much sharper arrival. RBBC also exhibits a more pronounced near-field effect.

5.1.2 Signal Acquisition and Velocity Calculations

Waveforms are captured at regular intervals as axial stress increases (usually every 1 MPa for triaxial tests and 2 MPa for TCRS). Figure 5.13-5.19 show all the signals collected for RGoM-EI under K_0-consolidation in triaxial (TX 1408) and TCRS (TCRS 1582).

In both test types, the height of the specimen (the vertical dimension in this research) is known at any given time (L_t) as:

$$L_t = L_0 \left(1 - \frac{\epsilon_a}{100}\right) \tag{5.1}$$

where L_0 is the initial height and ϵ_a is the axial strain.

It is worth noting that given the nature of K_0-consolidation, the specimen area is constant throughout the test, hence the horizontal travel distance stays constant. Using the horizontal and vertical dimensions at a given time, the inclined distance (middle to middle, as explained in Section 4.4.3) can be calculated. Aslo, the apparatus compressibility, was not accounted for in this study.

Figure 5.12 shows an example of a square input signal (green) and a typical P-wave signal (blue) in vertical direction, propagating through a resedimented Boston Blue Clay (RBBC) specimen, as well as the input signal directly obtained from the

pulser (scaled down to $V/100$). There is usually a slight delay between the crosstalk and the actual input step pulse. The travel time is always obtained by analyzing both the direct input signal and the output signal. The real travel time (t_t) is the difference between the interpreted arrival (t_a, marked by red dots in Figure 5.12), first evidence of increased voltage in the input signal (t_0) and the lag time (t_L) (Section 4.4.2).

$$t_t = t_a - t_0 - t_L \tag{5.2}$$

With the travel distances and the travel times known, the velocities are simply calculated as:

$$V = \frac{L_t}{t_t} \tag{5.3}$$

5.2 Effective Stress Corrections

Before the stress dependant velocity data is presented, the effective stresses need to be studied, and corrected if needed, for two factors: excess pore pressure buildup and sidewall-friction. For the triaxial tetsing setup used in this study, the sidewall friction is not an issue, as the specimen is in a fluid chmber and is isolated with ekastic membranes. Also the computer controlled feedback loop is capable of controlling the pore fluid pressure and preventing any excess pore pressure from developing. Both of these factors however can cause issues in TCRS setup. This section will focus on the numerical effect each of these factors have on the vertical effective stress felt by the specimen.

5.2.1 Excess Pore Fluid Pressure

The purpose of this research is to study the velocity behavior in normally consolidated clays. To ensure that the soil is continuosly on the virgin consolidation curve, the loading rate must be slow enough to prevent excess pore pressure to build up and fast enough to avoid secondary compresssion. In reality this excess pore pressure

is not zero, regardless of how low the axial strain rate is kept. Wissa et al. [177] simplified Smith and Wahls' [149] linear stress-strain relationship, and simplified the hydraulic conductivity (k) as following:

$$k = \frac{\epsilon' H^2 \gamma_w}{2\Delta u_b} \tag{5.4}$$

where ϵ' is the axial strain rate, H is the drainage height, γ_w is the pore water density, and Δu_b is the excess pore pressure. Equation 1.4 was later modified by Gonzalez [53] to account for the finite strain to result in:

$$k = \frac{\epsilon' H_0 H \gamma_w}{2\Delta u_b} \tag{5.5}$$

where H_0 is the drainage specimen height,

Rearranging that equation, excess pore water pressure can be calculated as:

$$\Delta u_b = \frac{\epsilon' H_0 H \gamma_w}{2k} \tag{5.6}$$

As an example Figure 5.20 shows the excess pore pressures as a percentage of the vertical effective stress, plotted against the vertical effective stress, in TCRS1582. It is clear that although the values are not exactly zero, they are small enough to be deemed insignificant for the purposes of this research. The largest excess pore pressure in this test is 0.0098 kg/cm^2 at 7.16 MPa vertical effective stress (0.13%). The momentary jump seen in the excess pressure ratio around vertical effective strress of 16 MPa and the negative pore pressures are most likely due to erratic axial strain rates recorded after the computer program was reset, which are regulated after a short while. Considering the excess pore pressure analysis, it is safe to assume that the total and effective streeses are equal in TCRS tests run for this research.

5.2.2 Sidewall Friction

The effect of sidewall friction on the actual vertical effective stress was discussed in Section 2.11. The vertical effective stresses measured on the TCRS specimens in this

research need to be corrected for this frcition. The magnutide of the real pressure (measured pressuree minus the sidewall friction) in the middle of the specimen was calculated using the equation bellow, derived by Lovisa and Sivakugan [99]:

$$\sigma_P = qe^{-4K\tan\delta(\frac{z}{D})} \tag{5.7}$$

Considering that in this study the self-weight of the specimens is insignificant (maximum of 0.0005 MPa for a typical TCRS test) compared to the applied pressure, it is ignored in real pressure calculations. q is the stress that is measured by the load cell. The specimen diameter (D) is constant and z is calculated based on the initial height and the axial strains. The lateral stress ratio (K_0), is calculated using Casey's stress dependent lateral stress ratio equation, also δ is taken as half of the critical state friction angle of soil at each stress level (Figure 5.21, the red curve represents RGoM-EI and the blue curve RBBC) [26]. As an example, TCRS1582 will be studied again. Figure 5.22 compares the applied pressures to the calculated pressure in the middle, and the sidewall friction amounts to 20% (at 30 MPa) to 40% (at $<$1 MPa) of the applied vertical pressure. This however is the highest possible friction at each stress level, which is experienced in the middle of the specimen, hence a more realistic approach is required. In reality, the sidewall friction is parabolically distributed along the height of the specimen, however the author assumed this distribution to be linear for the sake of simplicity. Then the total amount of friction, at that particular stress level, was calculated and uniformly distributed with respect to the vertical location in the specimen. After the uniform distribution, the magnitude of the friction throughout the specimen was nearly 10% (at 30 MPa) to 20% (at $<$ 1 MPa). Figure 5.23 shows the real pressure and the uniformly distributed pressures. Similar corrections were made for all the TCRS test results. The final effect of this correction is shown in Figure 5.24. Similar corrections were made for all the TCRS test results.

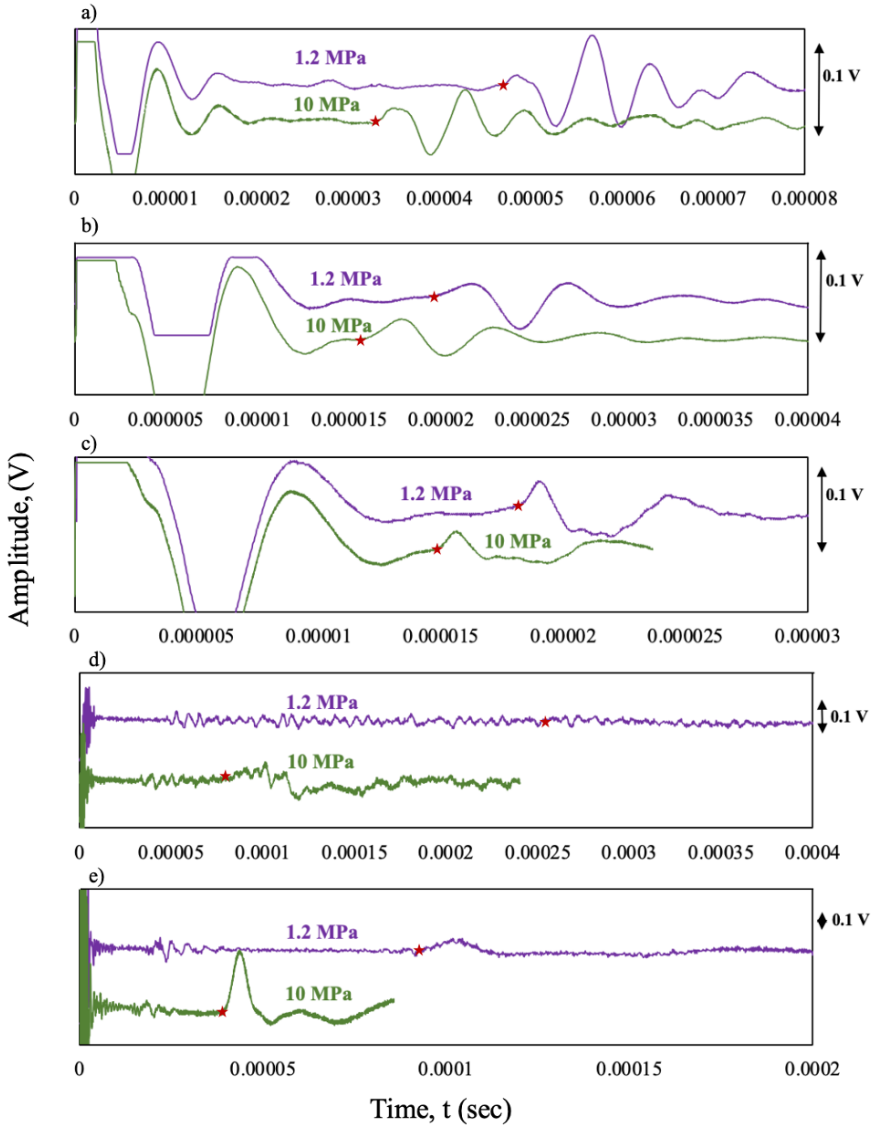

Figure 5.1: RGoM-EI specimen in triaxial setup at 1.2 and 10 MPa: a) Vertical P, b) Inclined P, c) Horizontal P, d) Vertical S, e) Horizontal S

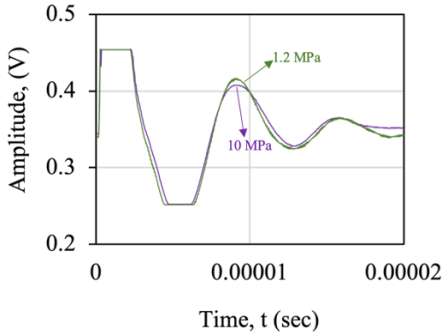

Figure 5.2: Initial high amplitude interference signal at 1.2 and 10 MPa

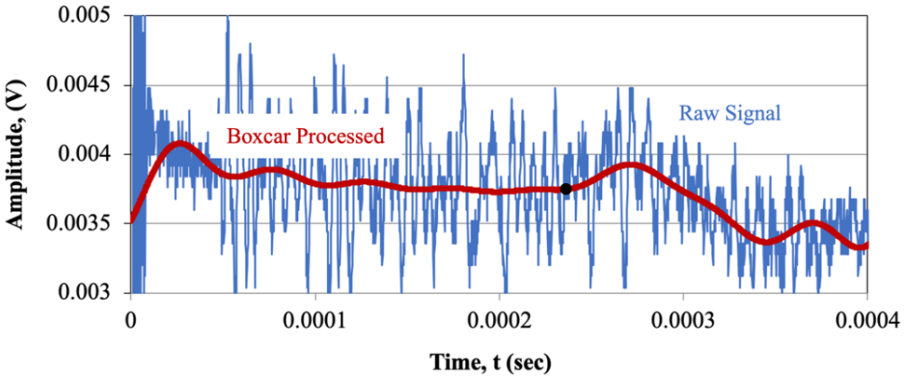

Figure 5.3: Raw S-wave signal (Figure 5.1-d) compared to the Boxcar processed signal (the black dot is the arrival time)

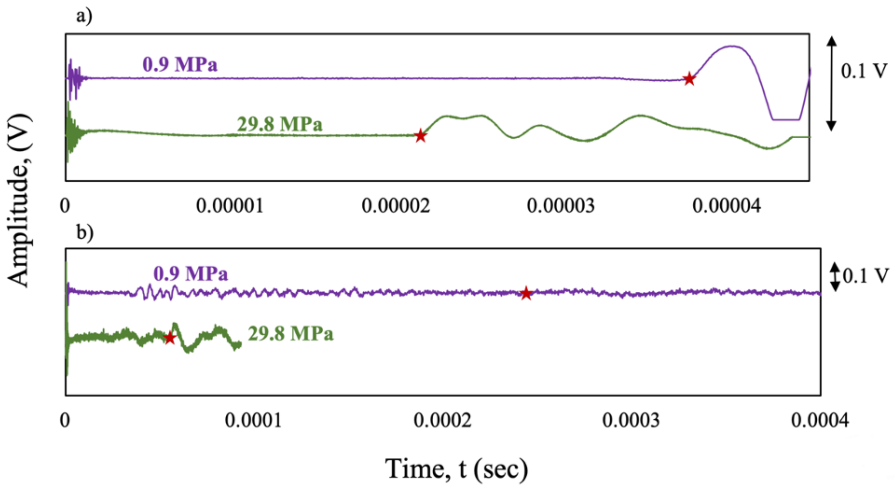

Figure 5.4: RGoM-EI specimen in TCRS setup at 0.9 and 29.8 MPa: a) Vertical P, b) Vertical S

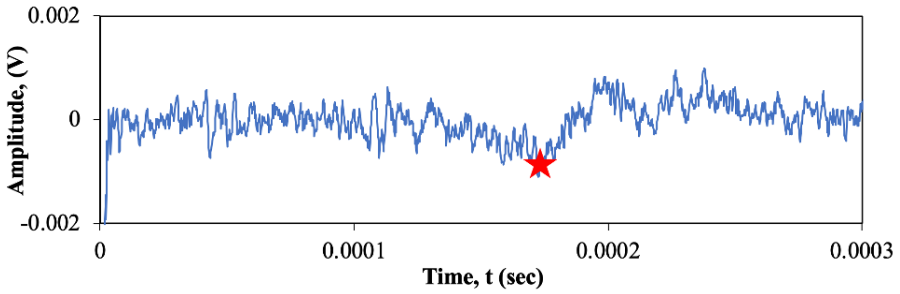

Figure 5.5: Shear wave in RGoM-EI (TX 1232) under 3.3 MPa vertical effective stress [103]

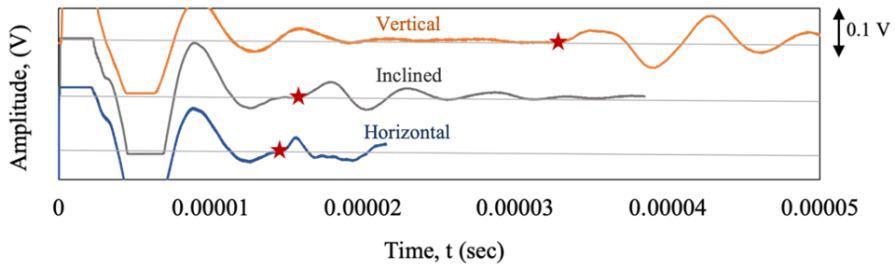

Figure 5.6: Horizontal, inclined and Vertical P signals propagating through triaxial RGoM at 10 MPa

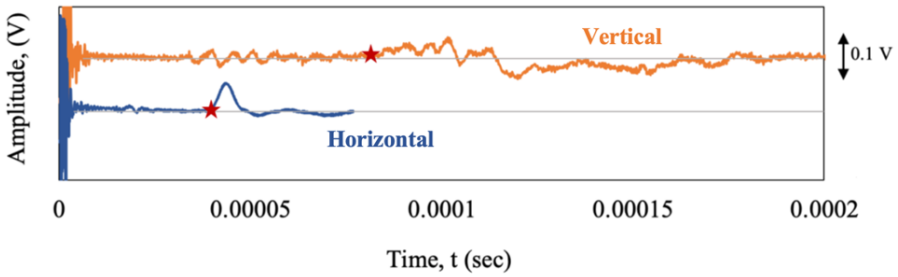

Figure 5.7: Horizontal and vertical S signals propagating through triaxial RGoM at 10 MPa

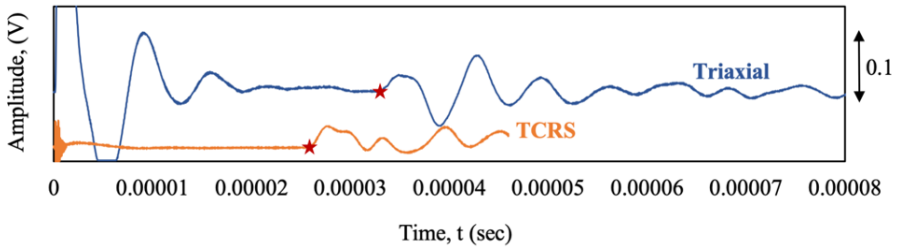

Figure 5.8: Vertical P signals propagating through RGoM at 10 MPa in triaxial and TCRS setup

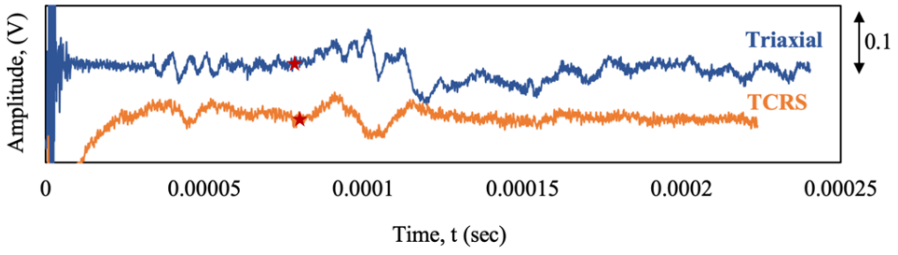

Figure 5.9: Vertical S signals propagating through RGoM at 10 MPa in triaxial and TCRS setup

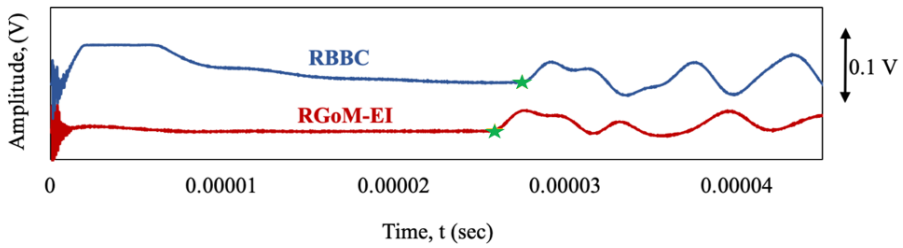

Figure 5.10: Figure 125. Vertical P signals propagating through RGoM and RBBC at 10 MPa in TCRS setup

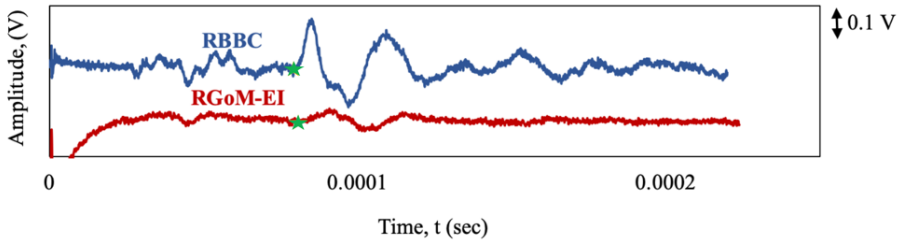

Figure 5.11: Vertical S signals propagating through RGoM and RBBC at 10 MPa in TCRS setup

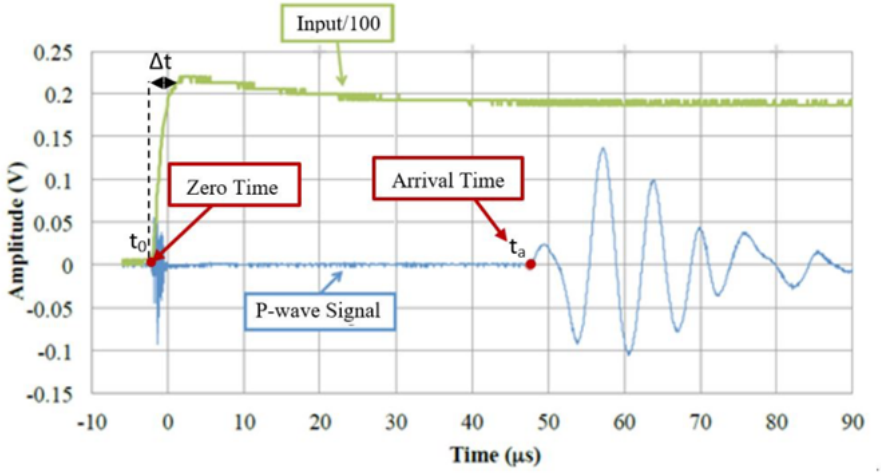

Figure 5.12: Arrival time selection for a representative P-wave signal through RBBC at 1 MPa (modified after [103])

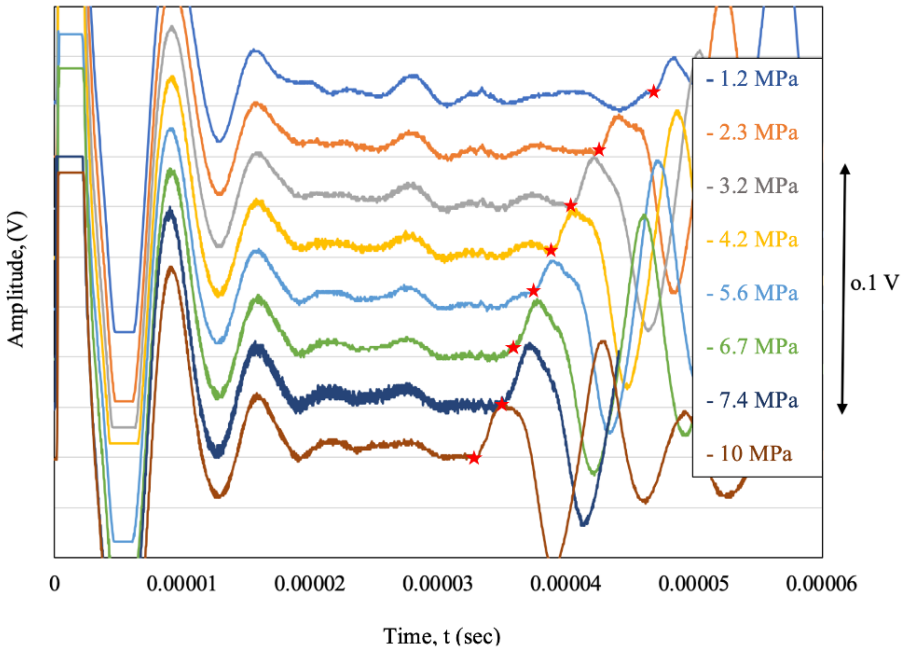

Figure 5.13: Vertical P signals propagating through RGoM at different stress levels (TX1408)

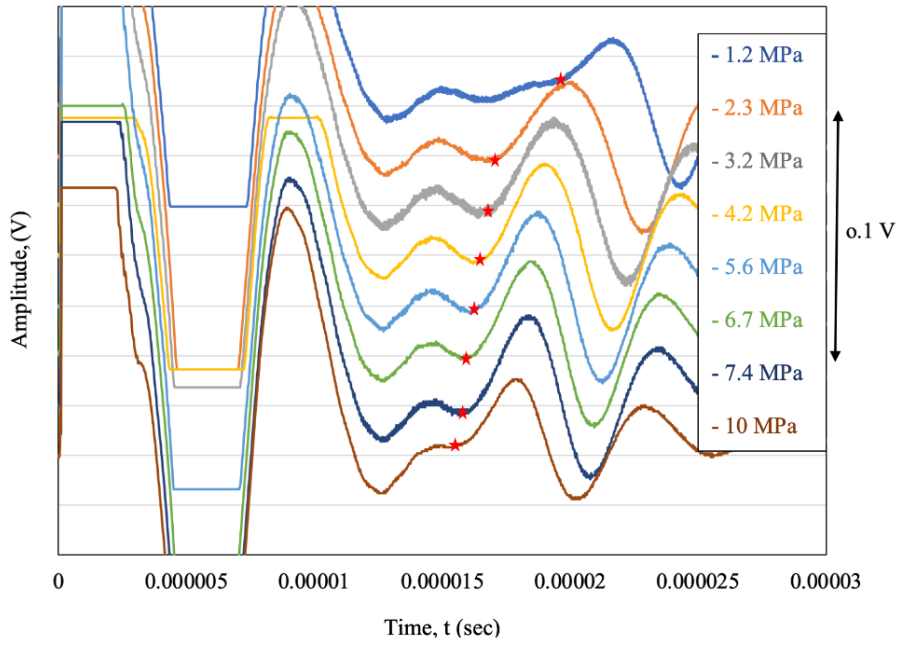

Figure 5.14: Inclined P signals propagating through RGoM at different stress levels (TX1408)

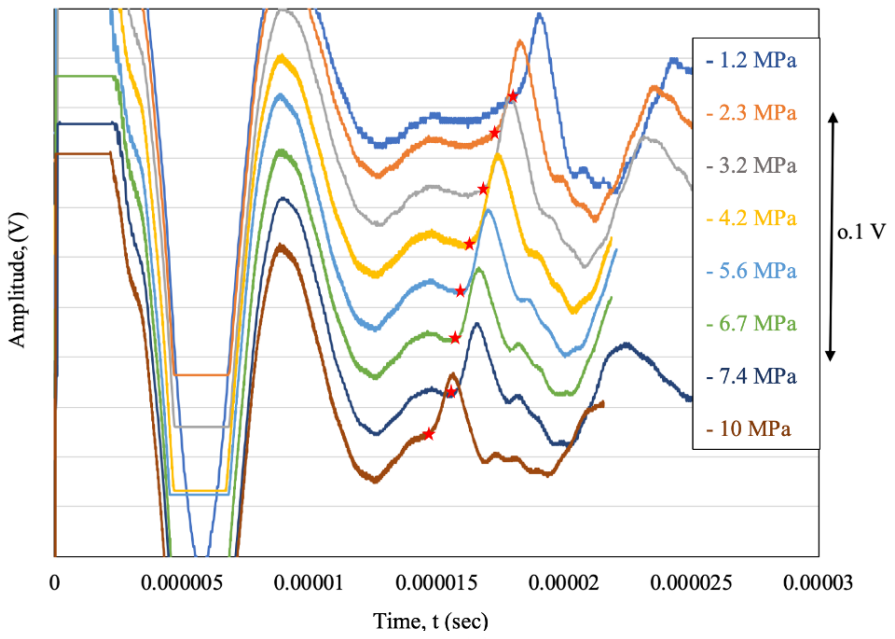

Figure 5.15: Horizontal P signals propagating through RGoM at different stress levels (TX1408)

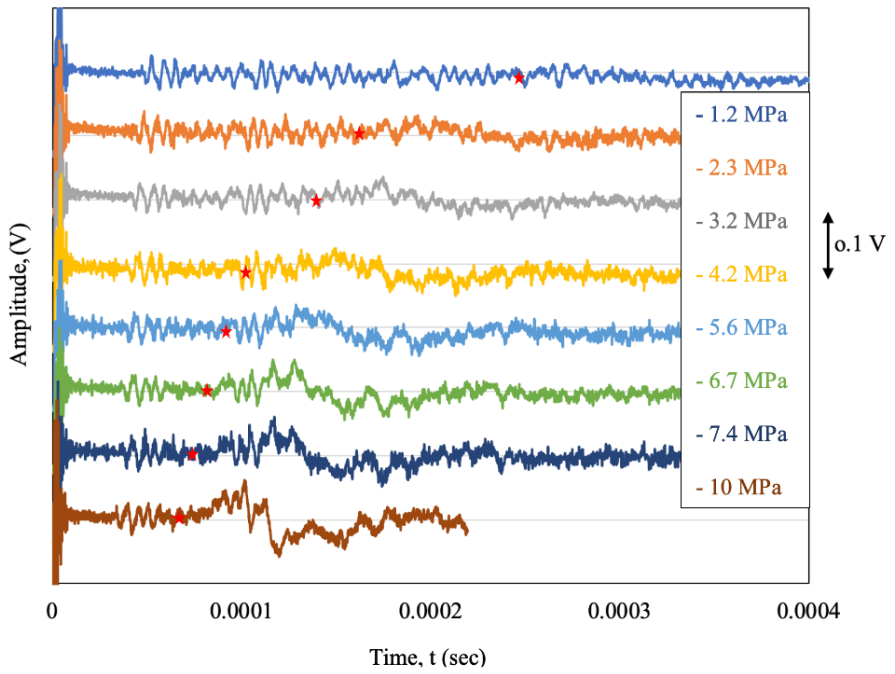

Figure 5.16: Vertical S signals propagating through RGoM at different stress levels (TX1408)

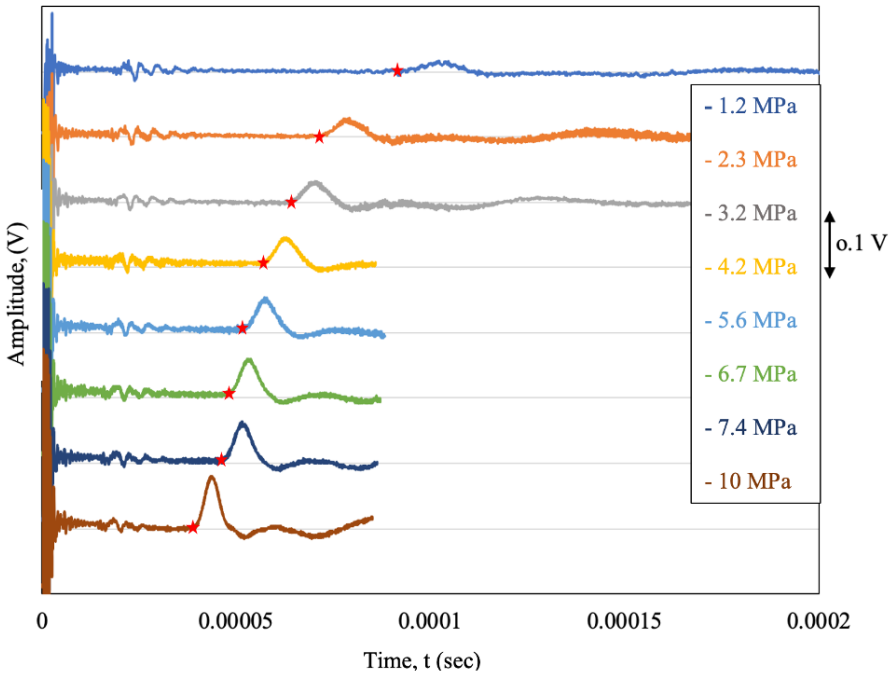

Figure 5.17: Horizontal S signals propagating through RGoM at different stress levels (TX1408)

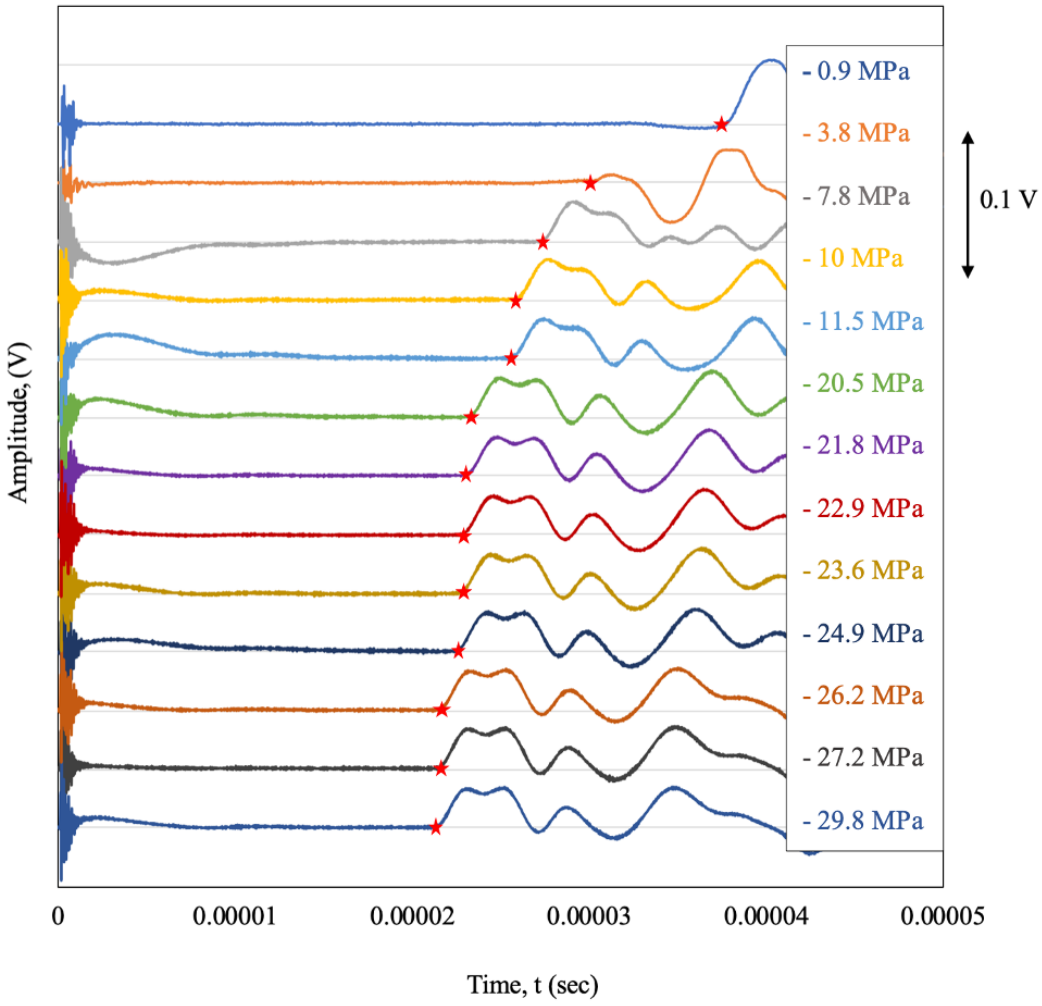

Figure 5.18: Vertical P signals propagating through RGoM at different stress levels (TCRS1582)

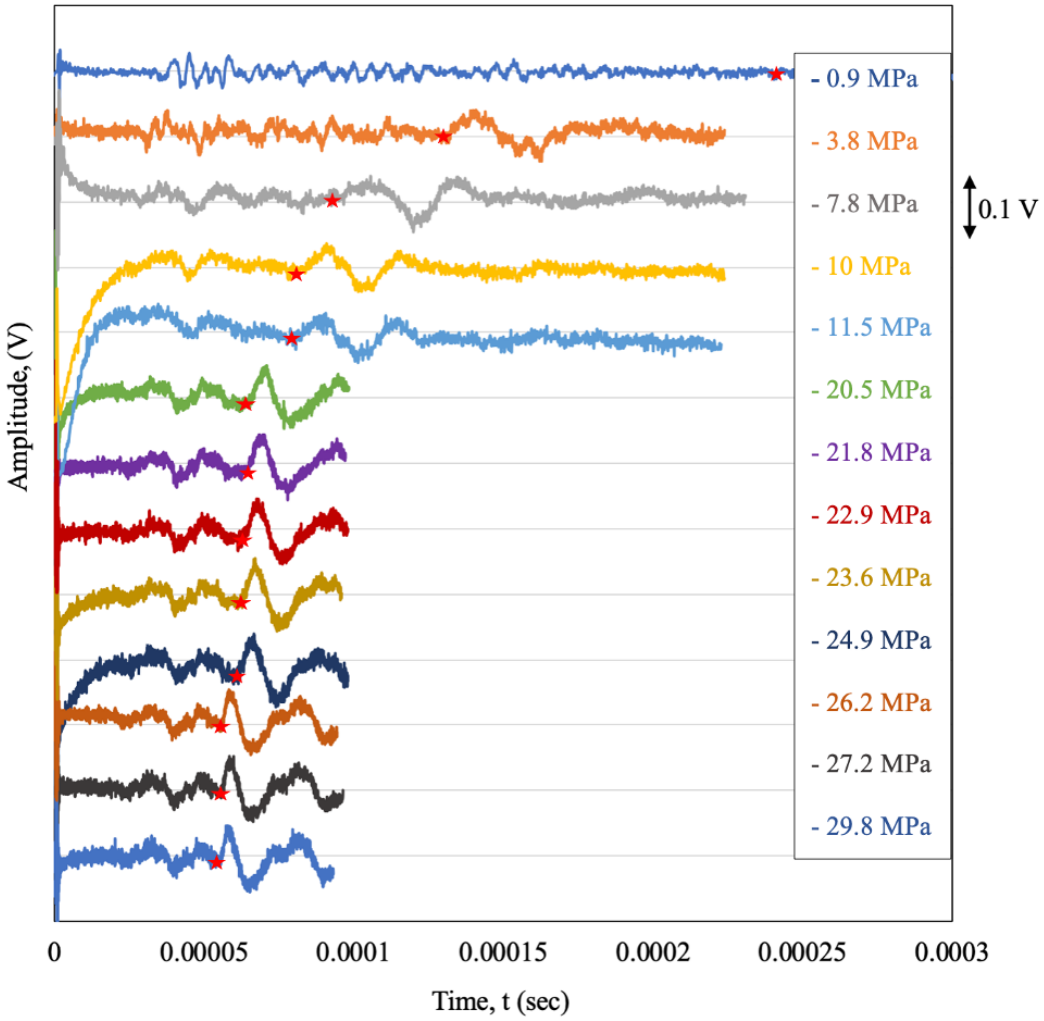

Figure 5.19: Vertical S signals propagating through RGoM at different stress levels (TCRS1582)

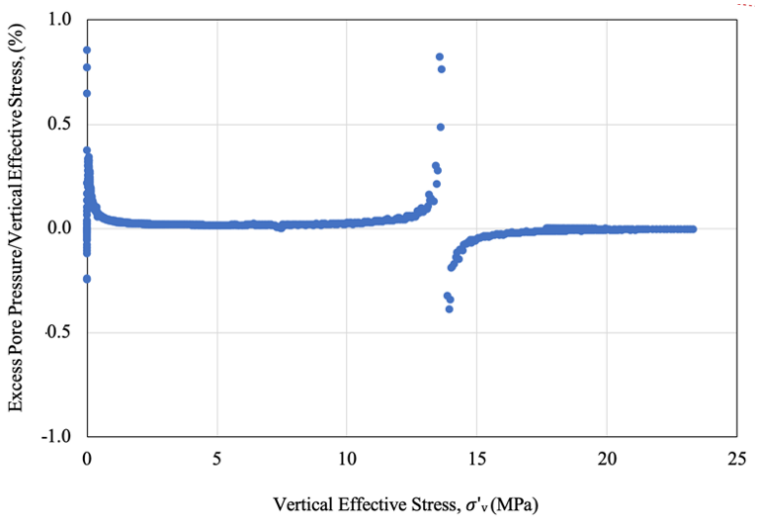

Figure 5.20: Excess pore water pressure analysis (TCRS1609)

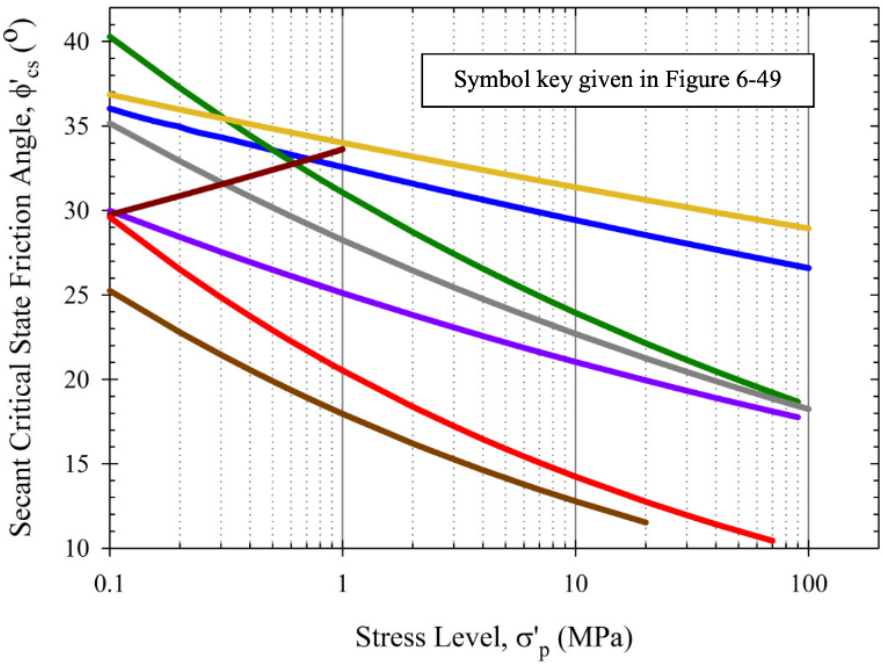

Figure 5.21: Regression lines of critical state friction angles of soils as a function of stress level (Figure 6-53 of [26])

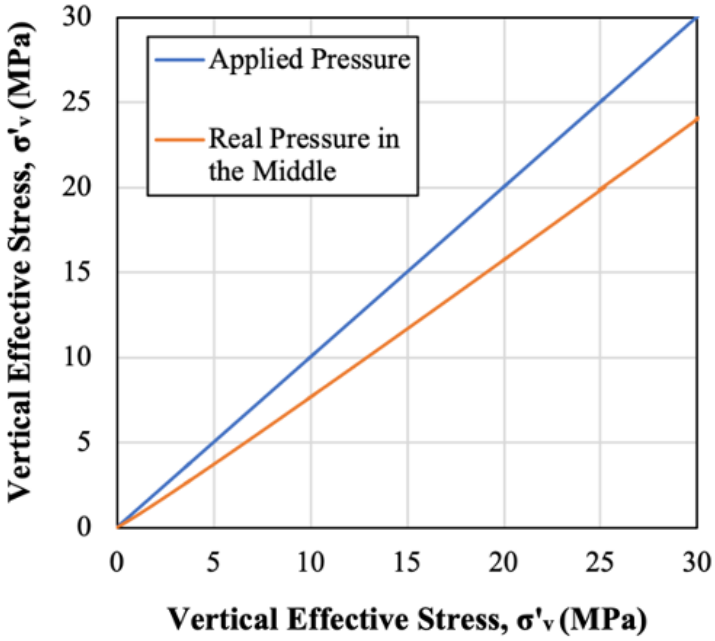

Figure 5.22: Applied pressure vs the calculated real pressure in the middle of the specimen height (TCRS1582)

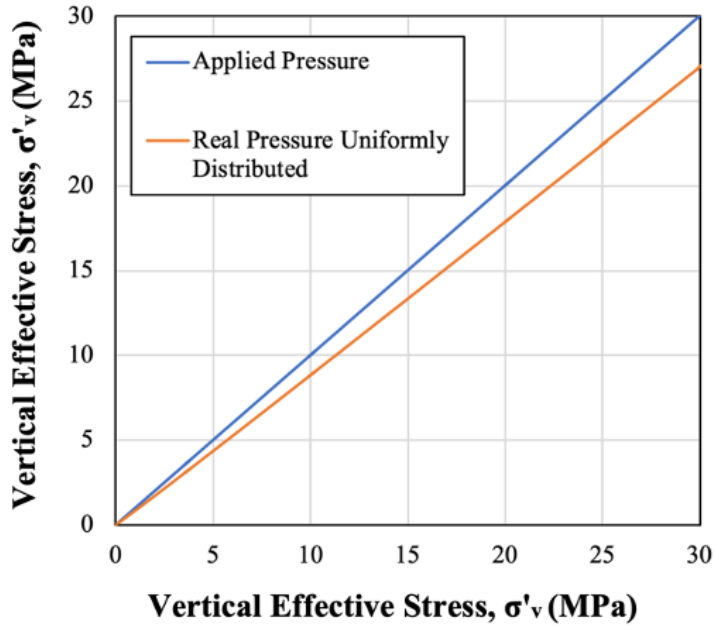

Figure 5.23: Applied pressure vs the uniformly distributed real pressure throughout the specimen height (TCRS1582)

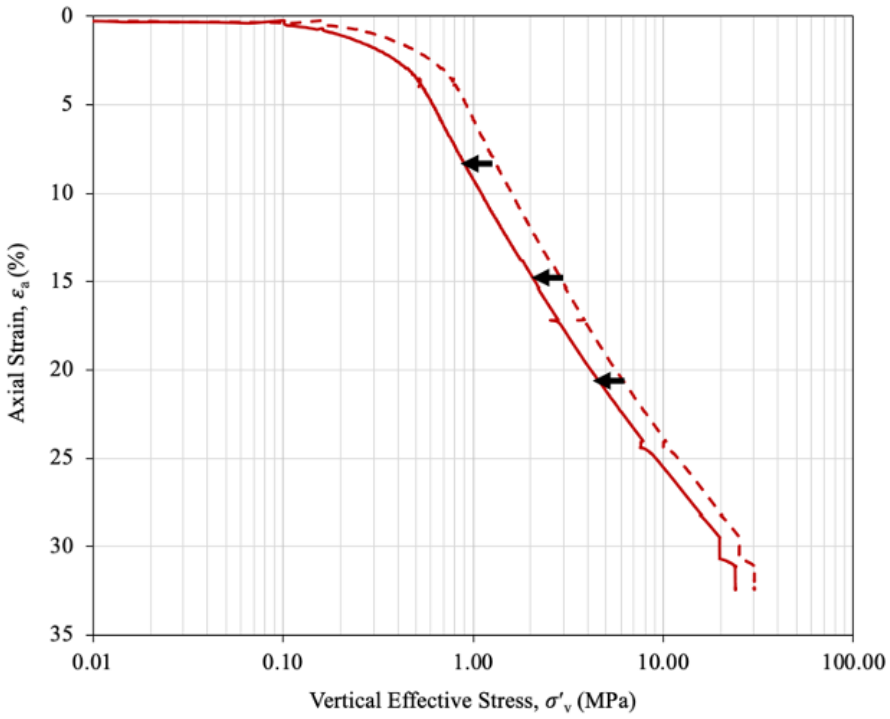

Figure 5.24: Compression curve before (right) and after (left) the vertical effective stress correction (TCRS1582)

Chapter 6

Experimental Results and Interpretations

This chapter presents the testing results for both the triaxial and TCRS test program. A summary of all the perfomed tests is presented in Table 6.1. The mechanical characteristic of the soil, such as compressional behavior and lateral stress ratios, will be discussed first. Next the focus will switch to the main objective of the thesis, seismic and anisotropic characteristics. Then the two will be correlated, presenting the stress-porosity-velocity trends and discussing the material behavior. And finally, the data from this research will be compared to some archive and published data.

6.1 Compression Behavior

6.1.1 Compression Curves

The K_0-consolidation compression curves are presented in Figures 6.1-6.7. The curves are plotted with either the void ratio or the axial strain as a function of vertical effective stress in logarithmic scale. The lines are color coordinated so that clusters of the same material are different shades of the same tone (red/orange for RGoM and blue/purple for RBBC). The compression curves obtained from the K_0-consolidation tests performed on RGoM in the medium pressure triaxial cell are shown in Figure 6.1 and Figure 6.2. In Figure 6.1, although there is a small shift ($< \pm 3\%$) between the void ratios on each two curves, the compression index (C_c) are seemingly very similar. C_c is the slope of the virgin compression line in void ratio-log effective stress space. The instability in the triaxial compression curves are mainly due to the system's difficulty in maintaining K_0-consolidation with low permeability samples, which is more of a problem in high smectite clays like GoM.

Tall constant rate of strain (TCRS) results for RGoM are shown in Figures 6.3

and 6.4. The resedimented specimens were continuously K_0-consolidated to 30 MPa vertical effective stress, except for TCRS1566, that was previously consolidated up to 1 MPa under step loading in an oedometer setup and then transferred to the TCRS setup. Figure 6.3 shows that although TCRS1587 had a lower initial void ratio and a stiffer response, the void ratios of all four tests converge after almost 2 MPa of vertical effective stress. This is mainly due to the fact that the different specimens only start behaving normally consolidated after a certain stress level. The final axial strain in this specimen is nearly 5% less than the other three, and the curve is flatter.

TCRS results for RBBC material are shown in Figure 6.5 and 6.6. The RBBC void ratios converge to similar values after 1 MPa of vertical effective stress, except for the TCRS1570 which appears to be an anomaly; starting from a much higher void ratio. Figure 6.6 shows that the axial strain measurements agree perfectly between different RBBC TCRS tests, suggesting that the issue causing the discrepancy in TCRS1570 is the initial void ratio.

Figure 6.7 contains all the compression curves mentioned above for comparison. It can be seen that while some discrepancies apply to individual tests, in general RGoM specimens start from a higher void ratio compared to RBBC and end up with lower void ratios. This is caused by higher compression indexes (C_c) since the high smectite materials experience greater deformations due to consolidation.

The shift in triaxial vs TCRS: Comparing the RGoM compression curves between TCRS and triaxial tests, for a given vertical effective stress level, triaxial tests have higher void ratios. These errors are caused by a combination of factors such as none-uniform specimen dimensions, dimension measurement error and internal leak.

6.1.2 Compression Curves Compared to Previous In-House Data

Compression behavior in both RGoM-EI and RBBC has been extensively studied over the years by researchers in Dr. Germaine's team. Casey [26] and Marjanovic [103] ran K_0-consolidation tests in triaxial setup, and Horan [64], Nordquist [117] and Parry [121] used the CRS setup. It should be noted that there are small differences

in the batching salinity of the various specimens tested. 6.8 compares the triaxial test compression curves obtained by the author to the curves provided by Marjanovic [103] (green) and Casey [24] (black). While the green curves have roughly the same slope as the red (and orange) curves, they are all vertically shifted, showing lower void ratios for the same stress level. While the black curve agrees with the red ones for the most part, it has a slightly smaller slope. All in all, it appears that the discrepancies in triaxial compression curves are mostly caused by a shift in initial void ratio. Figure 6.9 compares the RGoM-EI TCRS compression curves to the compression curves obtained from CRS test by Horan [64], Nordquist [117] and Parry [121], as well as the compression curve recommended by UT GeoFluids [70]. Both the slope and the values of the red curves agree with the GeoFluids recommended curve, with the biggest void ratio difference (3%) accruing around 25 MPa. However, the curves produced by Horan [64], Nordquist [117] and Parry [121], while in nearly perfect agreement with one another, exhibit lower void ratios, higher slope (lower stiffness) than the author's results. RBBC TCRS data are compared to the CRS compression curves from Horan [64], Nordquist [117] and GeoFluids [70] in Figure 6.10. It is clear that both the slope (stiffness) and the void ratios at each stress level from the author the other three sources agree, except for TCRS1570 which was discussed in the previous section.

6.1.3 Lateral Stress Ratio

Triaxial setup is capable of running K_0-consolidation tests using a PID controlled feedback loop that ensures zero lateral strain. The PID algorithm keeps the axial strain rate constant, while monitoring the axial and volumetric strains. The axial strain, which is measured using the external LVDT, when multiplied by the initial specimen area, needs to be equal to the volume of the pore fluid flowing into or out of the specimen. Using the strain measurements, the feedback loop continuously adjusts the cell pressure to maintain this equality. Fulfilling this condition means the cross-sectional area of the specimen is constant throughout the consolidation test, hence the lateral strain is zero. The stress dependent lateral stress ratio (K_0) of the

material is measured based on the applied axial and radial stresses. Figure 6.11 shows the lateral stress ratios changing with axial stress. The K_0 values in all four tests start from 1, since the specimens were unloaded to OCR=4 after resedimentation and then hydrostatically loaded during the initial pressure up and back pressure saturation phases. While on the reload curve (overconsolidated), K_0 values drop with stress level, however they start increasing once the preconsolidation pressure is exceeded and the specimen is once again normally consolidated. This increase is consistent with expected smectite behavior and the values agree with RGoM-EI results observed by Casey [24] and Marjanovic [103]. K_0 value at 1 MPa is between 0.66-0.7 and increases to 0.75-0.8 over the span of 9 MPa increase in vertical effective stress.

TCRS tests are performed on specimens that are placed inside a rigid ring, preventing any lateral deformation, which by definition results in K_0 consolidation. However, since only the axial stresses are measured, lateral stress ratios (K_0) cannot be measured in this setup. Casey [24] proposed the correlations shown in Figure 6.12 between the vertical effective stress and K_0, which were used for TCRS calculations when needed.

Equations 6.1 and 6.2 are extracted from Figure 6.12:

RGoM-EI:

$$K_0 = 0.6473{\sigma'_v}^{0.0834} \tag{6.1}$$

RBBC:

$$K_0 = 0.5215{\sigma'_v}^{0.0277} \tag{6.2}$$

6.2 Velocity Measurements

Velocity behavior should be studied with regards to the signal type (P or S), clay minerology and pore fluid chemistry. For example, despite S-waves, P-waves do propagate through fluids, which means P-wave velocity is more sensitive to both

porosity (hence the pore fluid ratio in a saturated medium) and the pore fluid chemistry. S-wave velocity on the other hand is thought to be more dependent on the clay minerology and particle interactions.

The diffuse double layer in clay was briefly mentioned in Section 2.6. There are two schools of thought about how the double layer behaves Ladd and Jen [88]:

- The double layer contributes to the cohesive strength of the material since it has a very high viscosity, which is responsible for the creep effect.
- The double layer behaves like a 2D liquid, highly resisting movement away from the clay surface, but is easily moved along the surface, thus not contributing to strength.

Although the exact effect of the diffuse double layer on the wave velocities is unknown, it is generally accepted that the double layer reduces the level of particle to particle contacts. Inter-particle contacts are also sensitive to pore fluid salinity in some clays. Horan [64] and Fahy [42] showed that GoM-EI clay is much more sensitive to salinity compared to BBC. GoM-EI exhibits much more flocculation with increased pore fluid salinity, whereas BBC is virtually unaffected by it. More flocculation results in more particle contact and expedited sedimentation. Mesri and Olson [109] report that flocculation also influences the size and shape of the void space, as well as the particle rotation and realignment.

The dominant mechanism and the magnitude at which each of these factors influence the velocity behavior varies significantly depending on the soil type. In this section, velocities measured in RGoM-EI and RBBC will be presented and the differences will be discussed.

6.2.1 Velocity Behavior as a Function of Stress

P-wave Velocity

Compressional wave velocities were measured in three directions: vertical (Figure 6.13), inclined (Figure 6.14) and horizontal (Figure 6.15) in triaxial setup, and in

vertical direction in TCRS setup (Figure 6.17), under 1-10 MPa and 1-30 MPa of vertical effective stress respectively. The same velocity data are also plotted against the mean effective stress.

The samples were batched to the same initial water content (105%), pore fluid salinity of 89.1 g/l (RGoM-EI) and 81.8 g/l (RBBC) and were resedimented to 0.8 MPa. This means that the specimens from each material type are in theory "identical", however in reality there are inevitable differences between specimens that affect the velocity behavior. The vertical P-wave propagates along the principal TI axis, which is perpendicular to the symmetry plane and the direction of particle alignment. The horizontal P-wave direction is parallel to this plane and the inclined wave is somewhere in between at angle Φ from the principle axis (Figure 2.3). It should be noted that the researcher does not have absolute control over the direction of the inclined measurement. The angle (Φ) is calculated based on the initial diameters and the strain values (30°-39°).

Figure 6.13-6.15 show the P-wave velocities in various directions, increasing with stress level. It is worth keeping in mind that while some tests have one or more "outlier readings", the individual tests have consistent velocity results for the most part, and trends will be discussed here rather than the individual data points. Comparing the data from the different tests however, there appears to be a systematic shift between the curves.

It can be seen in Figures 6.13-6.15 that for a given stress level, TX1394 and TX1408 have the highest and lowest P-wave velocities, and TX1399 and TX1404 values are somewhere in between. This is consistent with the initial void ratio of each specimen, which will be discussed in Section 6.2.2. The overall trends in P-wave velocity show about the same amount of increase in velocity (300 m/s) over a span of 9 MPa increase in the vertical effective stress (1-10 MPa). The scatter in the stress-velocity trends will be discussed in Section 6.2.3. The trends and scatter in the velocity data are similar in both vertical effective stress and the mean effective stress (caclulated from Equation 6.3) for vertical and horizontal directions, as the

horizontal effective stress is simply a fraction of the vertical effective stress. However, in inclined direction, the scatter is much higher in mean effective stress terms, although the trends are more or less the same as in vertical effectives stress terms. This behavior suggests the importance of lateral stress measurements on velocities in inclined direction. The stresses acting in the inclined direction are a function of vertical and horizontal directions, as well as the propagation angle.

$$\sigma'_m = \frac{\sigma'_v + \sigma'_h}{2} = \frac{\sigma'_1 + \sigma'_3}{2} \tag{6.3}$$

It is clear from Figure 6.16 that the velocities are the highest in horizontal direction and the lowest in vertical direction, and the inclined velocities are expectedly between these two values. As will be discussed in Section 6.2.3, the inclined velocities exhibit the most scatter due to a multitude of reasons.

Figure 6.17 shows the vertical P-wave velocity results of TCRS tests run on RGoM-EI and RBBC. While most RGoM-EI and RBBC tests are packed together, TCRS1609 has unusually high velocities. The applied vertical stresses (1-30 Mpa) were corrected for sidewall friction depending on the material type. Despite Heppard and Ebrom's suggestion that P-wave velocity for illitic clays are higher than smectitic clays [62], the research conducted by the author at TAG Lab, and previously by Marjanovic at MIT geotechnical lab, have consistently found the opposite to be true. The P-wave velocities in RGoM-EI specimens are clearly higher at any given stress level, although the difference is less pronounced in mean effective stress space. RGoM-EI has higher K_0 values, hence higher mean effective stresses for the same vertical effectives stress as an RBBC specimen. Also, RGoM-EI is a siltier clay, as opposed to clay-rich RBBC, which means RBBC clay particles are more prone to realignment causing the vertical velocities to be lower. Moreover, smectitic particles are much more sensitive to salinity, which means high pore fluid salinity (batching) shrinks the smectite double layer more, increasing the velocities disproportionately in RGoM-EI.

Triaxial and TCRS tests were performed on similar RGoM-EI samples, so the

velocities are expected to be the same at each stress level. The results from the two test types are plotted in Figure 6.18 and show great agreement between the two. However, the triaxial velocity trend has a slightly steeper slope than the TCRS trend, when plotted against the stresses.

S-wave Velocity

Shear wave velocities were measured in two directions: vertical (Figure 6.19) and horizontal (Figure 6.20) in triaxial setup, and in vertical direction in TCRS setup (Figure 6.22), under 1-10 MPa and 1-30 MPa of vertical effective stress respectively.

As can be seen in Figure 6.19 and 6.20 both vertical and horizontal S-wave velocities are increasing by roughly the same amount (400-450 m/s) over a 9 MPa increase in the vertical effective stress, which is almost 1.5 times the increase in P-wave velocities. However, in the vertical direction, the individual test trends are more jagged compared to P-wave velocities and horizontal S-wave velocities, which is caused by the more difficult interpretation of vertical S-waveforms and uncertainties in arrival times.

The horizontal S-wave velocities (shown in Figure 6.20) have the best trends yet, in that they are packed together and the difference between any two tests at each stress level does not exceed 60 m/s. This is likely due to the outstanding quality of the shear signals, as shown in Figure 5.17.

Figure 6.21 compares the vertical and horizontal S-wave velocities in stress space, highlighting two main points: 1) they both follow very similar trends, 2) there is not much of a difference between S-wave velocities in the vertical and horizontal directions. Both of these points suggest that the S-wave velocity anisotropy is very low in the RGoM-EI material, which will be discussed more thoroughly in Section 6.4.

It is worth noting that the specimen (TX1399) was kept at 5.2 MPa for more than 24 hours, undergoing significant secondary compression as a result. The effect of the secondary compression is exhibited as an increase in the velocities; however this jump is much more pronounced in S velocities than P velocities. The effect of secondary

compression on wave velocity behavior was investigated by Marjanovic [103] and will not be discussed here.

The S-wave velocities in RGoM-EI are slightly lower than they are in RBBC when plotted as a function vertical effective stress (Figure 6.22-a), but they seem to be a lot less material dependent compared to P-wave velocities (Figure 6.17). However, when plotted in mean effective stress space (Figure 6.22-b), the two materials separate slightly more, increasing the scatter in the data as a result. This is potentially due to the fact that S-wave has a vertical propagation and a horizontal motion, thus the S-wave feels the effects of the horizontally applied stress more than the P-wave.

Finally, Comparing the S-wave velocities from triaxial and TCRS tests, the two yield consistent results in both vertical and mean effective stress spaces (Figure 6.23).

6.2.2 Velocity as a Function of Density

In addition to the stress level, velocities are dependent on how "packed" the soil particles are. This quality can be represented by the soil density, void ratio or porosity. In other words, the velocity behavior cannot be described solely by the stress state of the material. It is possible for two specimens with different porosities to have notably different velocities at the same stress level. The higher the density (hence lower void ratio and porosity) the higher the velocities. However, the significance of this effect depends on the material type. On the other hand, when the modulus is kept constant, higher density means lower velocity. In this section the same results (as in Section 6.2.1) will be presented in density and porosity space.

P-wave Velocity

Directional P-wave velocities are presented as a function of bulk density and porosity: vertical (Figure 6.24 and 6.25), inclined (Figure 6.26 and 6.27) and horizontal (Figure 6.28 and 6.29) in triaxial setup, and in vertical direction in TCRS setup (Figure 6.30 and 6.31), under 1-10 MPa and 1-30 MPa of vertical effective stress respectively.

In triaxial tests, the densities increase by nearly 250 kg/m^3 (2050 kg/m^3 to 2300 kg/m^3) and the porosities decreased by almost 0.15 (0.48 to 0.33), as a result of the

K_0-consolidation. TX1394 and TX1408 mostly have the highest and lowest. TX1394 has the tightest particular structure with an initial void ratio of 0.93 (beginning of consolidation) and TX1408 has an initial void ratio of 1.005. However, this difference in the initial void ratio does not account for the velocity variability at a given void ratio (or porosity). The variability in porosity and density for a given velocity is less than ±2%, which is caused by the errors associated with void ratio and volumetric strain measurements.

Figure 6.30 and 6.31 include the P-wave velocities in RGoM-EI and RBBC as a function of bulk density and porosity respectively. The densities increase by nearly 400 kg/m^3 (2050 kg/m^3 to 2450 kg/m^3) and the porosities decreased by almost 0.18 (0.45 to 0.27), as a result of the K_0-consolidation. It seems that, except for TCRS 1609, in both density and porosity space the P-wave velocities for both materials are overlapping. This suggests that for the same density (or porosity), P-wave velocities are independent of the material for the most part, since the effect of diffuse double layer is eliminated. Figure 6.30 and 6.31 also show that the data scatter in higher densities (lower porosities) is much lower. This behavior is expected as in higher stresses the porosities vary ever slightly, making the errors inevitably small as a result.

S-wave Velocity

Directional S-wave velocities are presented as a function of bulk density and porosity: vertical (Figure 6.32 and 6.33) and horizontal (6.34 and 6.35) in triaxial setup, and in vertical direction in TCRS setup (Figure 6.36 and 6.37), under 1-10 MPa and 1-30 MPa of vertical effective stress respectively. Similar to the P-wave velocities, the scatter in the S-wave velocity data is much smaller in higher density, (higher stress, lower porosity).

6.2.3 Experimental Data Repeatability

As discussed in Section 2.10, there are many ways of fitting equations through experimental data. One of the simplest methods, especially when focusing only on

the normally consolidated behavior, is what is known as Bower's equation, which is simply a power equation in the following form:

$$V = C + A\sigma'^{B} \tag{6.4}$$

where V is the velocity, σ' is the effectives stress, and A, B and C are material specific constants. In this research, power equations were fit through the velocity data with respect to the vertical effective stresses and the results, A, B and C as well as the coefficient of determination (R^2), are shown in Table 6.2.

Multiple factors in laboratory testing and velocity measurements can cause errors and scatter in the data: electronic limitations, soil testing equipment limitations, velocity equipment sensitivity, material variability and human error. There has been a great effort to standardize the testing and signal interpretation procedure at Tufts Advanced Geomaterials Laboratory and at MIT Geotechnical Lab prior to that. While each individual test has significantly consistent results, various specimens tend to have slightly different velocity results. This section will focus on the data scatter and evaluate the repeatability between different tests.

This section focuses on evaluating the velocity results presented in Section 6.2. In Figures 6.38-6.41, the velocity data are plotted as a function of vertical effective stress (black dots). The figures also contain the fitted power equation (dashed red line) and an error bound (light blue). The error bound is populated by multiplying the power equation by (1+(±error%)) vertically. The error percentage is picked such that all the measurements are bound by the upper and lower envelope. This shows the scatter of the data when compared to the prediction curve. Each plot also shows the RMSD values. The RMSD or root-mean-square deviation or root-mean-square error (RMSE) is a measure of the differences between values (sample or population values) predicted by a model or an estimator and the values observed. In other words, the lower the RMSD, the lower the data scatter.

The RMSD of predicted values for times t of a regression's dependent variable with variables observed over T times, is computed for N different predictions as the

square root of the mean of the squares of the deviations:

$$RMSD = \sqrt{\frac{\sum_{n=1}^{N}(\hat{y}_n - y_n)^2}{N}} \tag{6.5}$$

Figure 6.38 and 6.39 show the directional RGoM-EI velocity results and the error bounds. P-wave velocities in the vertical direction seem to have the most repeatability with ±3% of errors, while the inclined and horizontal data are slightly more scattered but are still within ±4% error margins. Horizontal S-wave velocities (Figure 6.39) have less scatter (±5%) compared to the vertical data (±4%). This is expected considering the quality of the vertical S signals collected in the triaxial setup. The small tables shown in orange include the power equation constants and the RMSD parameters for each set of data. It is worth noting that the S-wave power equations are very similar, pointing at the fact that the shear velocity anisotropy in RGoM-EI is very low, which will be further discussed in Sections 6.4 and 6.6.

Figure 6.40 shows the vertical P and S velocities in RGoM-EI material tested in the TCRS setup. The P-wave error bound seems to be close to ±5%, mostly due to the outliner TCRS1609 that is shifted upwards, whereas the S-wave error bound is nearly ±8%. Figure 6.41 shows the vertical P and S velocities in RBBC material tested in the TCRS setup. The P-wave error bound seems to be close to ±3%, whereas the S-wave error bound is nearly ±8% within the medium stress range (1-10 MPa) but decreases at higher stress levels.

Marjanovic [103] determined the precision of the data collected with technologies and testing setups very similar to the ones used in this research, by analyzing the digital velocity signals and the possible error in the height measurements of the specimen, since these two factors are fundamental to the subsequent velocity measurement, which will not be discussed here.

6.2.4 Compressional and Shear Wave Velocity Relationships

The majority of the research focusing on V_p/V_s ratio in clayey material is performed on mudrocks, which are low porosity materials. This research focuses on the V_p/V_s

behavior in resedimented materials with much higher porosities compared to rocks, even under higher pressures.

Figure 6.42 shows the horizontal and vertical velocity ratios (V_p/V_s) as a function of vertical effective stress, in RGoM-EI tested in triaxial cell. Horizontal velocity ratios decrease from nearly 6 to 2.8 over a 9 MPa increase in vertical effective stress. Vertical velocity ratios have a similar range (5.7 to 2.6).

The velocity ratios in the two directions are plotted together in Figure 6.43 and 6.44. Figure 6.43 compares the two sets of data as a function of bulk density. While the trends in both are very similar, the values are vertically shifted resulting in higher horizontal velocity ratios. This is expected since the S-wave velocities are virtually the same in both directions but the P-wave velocities in the horizontal direction are higher. Figure 6.44 shows the same the data as a function of vertical effective stress in logarithmic space. Two logarithmic equations are fitted through the two sets of data, which have very close slopes (-1.156 and -1.167) but a slight vertical shift, which is consistent with the behavior seen in Figure 6.43.

Figure 6.45 presents the vertical velocity ratios (V_p/V_s) for RGoM-EI and RBBC specimens tested in TCRS. RGoM-EI velocity ratios tend to be slightly higher than RBBC and experience a 3.6 decrease with the increasing stress level. RBBC on the other hand exhibits a smaller change in the velocity ratio (2.8). This is expected since RGoM-EI material has higher porosities and thicker double layers for the same stress level, than the RBBC, causing the difference between the V_p and V_s to be more pronounced in this material.

Lastly all the vertical velocity ratio results, for both materials and test types, were plotted as a function of bulk density, as well as vertical effective stress in logarithmic space (Figure 6.46- 6.47). Figure 6.46 shows the RGoM-EI data have the same trend in both triaxial and TCRS tests, however the velocity ratios are consistently lower for triaxial tests. This is due to the P-wave velocities from the two test types being in agreement as opposed to the S-wave velocities being higher in triaxial testing. As Figure 6.47 shows, RGoM-EI tiaxial and TCRS data yield very similar logarithmic equations, RBBC velocity ratios seem to be starting from a lower value. Comparing

all three data sets however, it appears that at higher stresses the velocity ratios all converge.

6.3 Elastic Moduli and Stiffness Behavior

This section will focus on the stiffness properties of the tested materials, using the measured velocities. In both the geotechnical and geological fields, it is common to use elastic equations to calculate shear (G) and constrained moduli (M), as well as the Poisson's ratio (ν) from seismic velocities. The three elastic moduli can then be used to determine the young's and bulk moduli. As explained in Section 2.2 however, the underlying assumption for these equations is that the material is isotropic. Also the measured P and S waves are assumed to be plane waves, which might not be true given that sometimes the wavelengths are larger than the transducer and specimen dimensions. In this section, the moduli results will be presented, both calculated using the conventional isotropic equations, and using the stiffness matrix determined based on the measured directional velocities.

6.3.1 Isotropic Elasticity

The vertical and horizontal velocities measured in the RGoM-EI material tested in the triaxial cell are plugged in the equations bellow to calculate ν, G and M in two directions, assuming the material behaves isotopically:

$$\nu = \frac{\left(\frac{V_p}{V_s}\right)^2 - 2}{2\left[\left(\frac{V_p}{V_s}\right)^2 - 1\right]} \tag{6.6}$$

$$G = \rho \times {V_s}^2 \tag{6.7}$$

$$M = \rho \times {V_p}^2 \tag{6.8}$$

And the Young's modulus is calculated from G and M:

$$E = \frac{G(3M - 4G)}{M - G} \tag{6.9}$$

In a truly isotropic material, the velocities will be the same in all directions, hence the above values will be equal in the vertical and horizontal directions.

Figures 6.48-6.51 show the Poisson's ratios and velocity-derived elastic moduli in RGoM-EI under medium pressures (1-10 MPa), in vertical and horizontal directions that were determined using the isotropic equations. Figure 6.48 shows the Poisson's ratios calculated by inserting the vertical and horizontal velocities in Equation 6.6. The data in both directions start around 0.485, near the Poisson's ratio of water, and slightly diverge over the 9 MPa increase in the vertical effective stress, with the averages at the highest stress level around 0.435 and 0.425 for horizontal and vertical data respectively. The nearly 5% drop occurs as a result of the material getting stiffer in both directions. The elastic moduli on the other hand, are expectedly increasing with K_0-consolidation, but not at the same rate. The constrained moduli, shown in Figure 6.49, almost double in both directions. However, the constrained modulus in horizontal direction starts higher (6.5 GPa), increases at a faster rate, and ends up at a higher value (10.5 GPa), as opposed to the vertical values increasing from 5.5 GPa to 8.5 GPa. The vertical shift between the two data sets is due the horizontal P-wave velocities being consistently higher than vertical at all stress levels. Figure 6.50 shows that in both directions the shear moduli start around 0.2 GPa and climb up to 1.1 GPa, following the same curve. The shear moduli are practically the same regardless of the direction, which in turn alleviate the effect of P-wave anisotropy in Poisson's ratio and Young's modulus. As shown in Figure 6.51, the young's moduli start off around 0.5 GPa and increase by nearly seven times, finishing off at 3.5 GPa.

Although the TCRS testing setup increases the testing stress range to 25 MPa, the current technology only allows for vertical velocity measurements. Subsequently, the elastic parameters were only calculated in vertical direction, assuming the material is isotropic. The four elastic parameters (ν, G and M and E) calculated based on the measured velocities in RGoM-EI and RBBC are presented as a function of vertical effective stress.

Figures 6.52-6.55 show the velocity-derived elastic parameters in RGoM-EI, between 1 and 25 MPa of vertical effective stress. Similar to the triaxial results, the Poisson's ratio starts near 0.5 and decreases with the stress level, this time almost down to 0.4. It is important to note that while the data in Figure 6.52 seem more scattered after about 10 MPa of stress, the differences in Poisson's ratio are still within ±0.006. Figures 6.53-6.55 exhibit the increase in constrained modulus (6 to 11.5 GPa), Shear modulus(0.2 to 1.8 GPa), and young's modulus (0.5 to 5 GPa). Next, Figures 6.56-6.59 exhibit the decrease in Poisson's ratio (0.48 to 0.39), increase in constrained modulus (6 to 10.5 GPa), Shear modulus(0.2 to 1.8 GPa), and young's modulus (0.5 to 5 GPa). The results from the different materials and testing setups will be compared in

Lastly, vertical velocity-derived elastic moduli and the Poisson's ratios from the different test types are compared to one another (Figures 6.60-6.64). The Poisson's ratios in Figure 6.60 are intentionally shown in a wider vertical axis range in order to capture stress related variations and the data scatter more realistically. It is clear that although RBBC Poisson's ratios at the same vertical effective stress are slightly lower than the RGoM-EI's, the difference that the material type makes (0.01) is mostly within the data scatter associated with each material (±0.05) at lower stresses ($<$ 5 MPa). However, as the stress level goes higher the trends separate out and RGoM-EI end up with nearly 3% higher Poisson's ratio than RBBC at 25 MPa. Comparing the different testing methods performed on RGoM-EI, both the TCRS and triaxial results start from the same Poisson's ratios, but the triaxial data decreases with a steeper slope. The difference between the two at 10 MPa is nearly 0.015. Since Poisson's ratio is directly calculated from the measured V_p and V_s, Figure 6.60 does not include the effect of density, which is why the same data are also presented in porosity space (Figure 6.61). Considering the difference between the porosities in RGoM-EI and RBBC specimens at the same stress level, it is not surprising that data diverges for the two material when plotted in porosity terms. At a given stress level, RGoM-EI is stiffer than RBBC, which may well be explained by higher stress transfer between the grains in RGoM-EI, compared to RBBC. What

is surprising however, is that the Poisson's ratios calculated for triaxial RGoM-EI appear to be lower, by up to 0.05, than the ones for TCRS RGoM-EI. This is likely caused partly by the void ratio measurement errors and partly by the fact that Poisson's ratio includes the effect of both shear and constrained moduli (V_p and V_s). It could also have been affected by the lateral boundary condition, flexible membrane in triaxial versus rigid wall in TCRS, resulting in smaller lateral strain in triaxial tests for the same vertical effective stress as TCRS.

The determined elastic moduli (G, M and E) already include the effect of density/porosity, so presenting them as a function of stress level ensures that all participant agents (stress, velocity and porosity) are included. Shear and constrained moduli, shown in Figures 6.62 and 6.63, are calculated directly from the velocities and follow the same trends. Also, the level of scatter are higher than V_p and V_s scatter (±10% for M and ±15% for G), suggesting that the corrective effect that the density has on M and G, is not enough to compensate for the scatter caused by the fact that M and G take the velocity-squared term.

As shown in Figure 6.62, the RGoM-EI constrained moduli from triaxial and TCRS testing agree. On the other hand, RBBC results start from almost the same values as RGoM-EI (6 GPa) but increase with a smaller slope, ending up at a 9% lower constrained modulus (10.5 GPa) at 25 MPa. The normalized modulus M goes with about the 4th power of stress. Figure 6.63 shows the increasing shear moduli with increasing vertical effective stress. While the data apear to be more scattered at higher stresses, the two different materials follow the same trend, much like the vertical shear wave velocity (Figures 6.22 and 6.23). According to Figures 6.62 and 6.63, RGoM-EI has slightly higher M values, whereas RBBC has slightly higher G values, which seem to be cancelling each other out when calculating the E values. Using M and G, the Young's moduli are calculated and shown in Figure 6.64. It is clear that the results from both TCRS and triaxial, and the two very different material are highly overlapping. This is suggesting the Young's modulus results as a function of stress level are not material dependent.

6.3.2 Anisotropic Elasticity

Isotropic elastic equations do not apply to truly anisotropic material, as the stiffness behavior is direction dependent. Although only weakly anisotropic, the materials tested in this research are regarded to be transverse isotropic (TI) having a symmetrical stiffness matrix with five independent parameters (C_{11}, C_{33}, C_{44}, C_{66} and C_{13}) represents the stiffness behavior in TI material (Figure 6.65). Thomsen's method [158] is used to determine each of the elements in the stiffness matrix using 5 independent velocities (Vertical P (V_{pv}), Vertical S (V_{sv}), Horizontal P (V_{ph}), Horizontal S (V_{sh}) and Inclined P ($V_{p(\phi)}$)) the phase angle (θ) and the bulk density (ρ). This method was discussed in Section 2.2.

The C_{ij}s calculated using the measured directional velocities are shown in Figure 6.66. It should be noted that the matrix is symmetrical, and some elements are equal as a result. As a result of the velocity data being scattered, the stiffness matrix elements are also scattered. The inclined velocities (which have the most scatter) are only needed in calculating C_{13} (= C_{23} = C_{32} = C_{31}), making the results for this element the most scattered among the C_{ij}s. All in all, there is a clear increasing trend in all the elements as the vertical effective stress increases.

One way of eliminating the scatter in the C_{ij} data is to use the power equations presented in Figures 6.38-6.41 to attain the five velocities that are most representative of each stress level, and input those in the Thomsen's equations and calculate a single value for each C_{ij}. Figure 6.67 shows the results of this method. While C_{55} and C_{66} are practically the same, suggesting that the shear stiffness in the material is close to isotropic, the difference between C_{11} (dark blue) and C_{33} (red) is caused by the P-wave anisotropy. Also C_{13} (light blue) starts out closer to C_{11} and C_{33} (compressional behavior) and moves closer to C_{55} and C_{66} (shear behavior) at higher stresses. The values determined using the compliance matrix (inverse of the stiffness matrix (Figure 6.67)) will be presented here.

Figure 6.69 shows the Poisson's ratios calculated from the compliance matrix. The TI compliance matrix provides three Poisson's ratios for each stress level: 1)

when a stress is applied horizontally and the element deforms horizontally (perpendicular to the stress direction) (ν_{hh} in blue), 2) when a stress is applied horizontally and the element deforms vertically (ν_{hv} in gray) and 3) when a stress is applied vertically and the element deforms horizontally (ν_{vh} in orange). The figure shows two sets of data for each value, the dots and the curves. The individual results calculated from each set of velocity measurement are shown by dots. The Poisson's ratios calculated using the velocities at each stress level that were determined from the power equations (same as values used to get Figure 6.67 values) are shown as curves with the same color. It is clear that the individual ν_{hh} and ν_{hv} data are too scattered to suggest a trend. The scatter is, for the most part, caused by the matrix calculations being extremely sensitive to the inclined velocity and the inclination angle. For ν_{vh} on the other hand, the individual points (gray) are in great agreement with the curve (changing between 0.47 and 0.41). Considering that the material tested in this research has low anisotropy, the three Poisson's ratios being so different at lower stress levels is odd. A possible explanation could be the velocity ratio sensitivity of the stiffness matrix calculations.

Figure 6.70 was constructed by keeping all three P-wave velocities at 1 MPa and changing the S-wave velocities to get different velocity ratios (V_p/V_s). Then the Poisson's ratios were calculated using the compliance matrix for each velocity ratio. This figure clarifies the previous point about the sensitivity of the stiffness matrix method in higher velocity ratios (lower stresses). In lower stress levels, the specimen porosity is high, which assuming full saturation results in higher amounts of pore fluid trapped within the clay structure. Considering the fact that P-waves can propagate through fluid, but S-waves cannot, P-wave velocity is dominated by the pore fluid effect as opposed to the clay structure effect. Figure 6.70 shows that as the pore fluid drains with the increasing vertical effective stress, and the velocity ratios decrease, the five Poisson's ratios converge: at 1.9 velocity ratio, the biggest difference between the Poisson's ratios ($\nu_{hh} - \nu_{hv}$) is 0.06, which is reasonable given low anisotropy in the material.

Lastly, Figure 6.71 displays the matrix calculations' sensitivity to the inclined

velocity and angle interpretations. The interpreted velocities (power equations output) were used, however the inclined angle was assumed to be 45° and all the inclined velocities were assumed to be the average of the horizontal and vertical P-wave velocities at that stress level. The Poisson's ratios calculated based on these assumptions are shown in Figure 6.71. It is clear that the Poisson's ratios constructed for 45° are within a reasonable range from one another (given the material's low anisotropy) and are following very similar decreasing trends. Also, the method eliminates the unreasonably high or low values that are shown in Figure 6.69 and yields Poisson's ratios between 0.5 and 0.4. While the values shown in Figure 6.71 are not the real Poisson's ratios, this figure confirms that the Poisson's ratio calculations are extremely sensitive to the velocity ratios.

The TI Young's moduli (shown in Figure 6.72), are both increasing with similar slopes, despite being scattered at lower stress levels. Also expectedly, E_h is higher than E_v at all stress levels. As explained before, the two methods of calculating ν and E have a fundamental difference: one takes the material anisotropy into account, the other one assumes the material is isotropic.

Figure 6.73 shows the similar data for Young's modulus: a) where loading and deformation are in the vertical direction and b) where loading and deformation are in horizontal direction. Despite being scattered, due to the velocity measurement errors, the E values in both directions are similar for isotropic and TI assumptions. This could be caused by two factors (or a combination of the two): 1) the isotropy assumption provides good estimations of the stiffness behavior, even if the material is in reality transverse isotropic, 2) the behavior of the material tested here is closer to isotropic rather than TI. The anisotropy results will be discussed further in the next section.

6.4 Anisotropy Parameters

Thomsen [158] defines the three constants that describe the degree of anisotropy (ϵ, γ, and δ), in terms of the five constants C_{11}, C_{13}, C_{33}, C_{44}, and C_{66} as:

$$\epsilon = \frac{C_{11} - C_{33}}{2C_{33}} \tag{6.10}$$

$$\gamma = \frac{C_{66} - C_{44}}{2C_{44}} \tag{6.11}$$

$$\delta = \frac{(C_{13} + C_{44})^2 - (C_{33} - C_{44})^2}{2C_{33}(C_{33} - C_{44})} \tag{6.12}$$

Thomson's parameters (ϵ, γ, and δ) relate to the case of weak anisotropy described by small values ($\ll 1$). According to Sheriff [145] for most sedimentary rocks, the three parameters are of the same order of magnitude and usually much less than 0.2. Figures 6.74-6.76 show Thomson's parameters calculated for the RGoM-EI. The red dots are the individual test results, calculated using the set of 5 velocities measured on a particular specimen at a particular stress level. The scatter in the measured velocities is responsible for the scatter exhibited in the anisotropy parameters for the most part. Although the individual test results in Figures 6.74 and 6.75 (ϵ, γ) only roughly follow a trend, even that does not apply to the δ values (Figure 6.76). Alternatively, the author used the power equations fit through the velocities to calculate a likely set of five velocities, and the inclined angle, to determine the stiffness matrix at each stress level and calculate the anisotropy parameters accordingly (orange diamonds). This method results in an increasing trend in ϵ and δ, and a decreasing trend in γ, with an increasing vertical effective stress. However, it should be noted that the anisotropy parameters for RGoM-EI are low regardless, suggesting that the material behaves almost isotopically.

The special case of $\delta = \epsilon$ is known as elliptical anisotropy [94]. The ellipticity is associated with the shape of the wave-front expanding from a point source. Although its underlying theory is simpler than the general theory of anisotropy, elliptical anisotropy rarely occurs in nature (always in S_h [61]). Figure 6.77 shows the ϵ and δ results against the ellipticity line ($\delta = \epsilon$). It is clear that for the most part δ is higher than ϵ, with the interpreted data (as well as the majority of the individual

test results) being close but slightly higher than the ellipticity line. The individual test results are scatted vertically, displaying much bigger variations in δ rather than in ϵ.

Figure 6.78 shows that although ϵ and γ are the same order of magnitude, γ ($-0.04 < \gamma < 0.1$) tends to be lower than ϵ ($0.04 < \epsilon < 0.1$). This is expected as the difference between the horizontal and vertical P-wave velocities are more pronounced than that of the S-wave velocities. The interpreted values appear to be an acceptable estimate of the individual test results, capturing the "average" behavior.

6.5 Velocity Results Compared to Previous In-House Data

As mentioned previously, the author took over the velocity behavior research from the previous researcher at MIT Geotechnical Engineering Laboratory researcher, Jana Marjanovic [103]. The piezoelectric technology used by Marjanovic was modified and improved further by the author to measure directional velocities and study the material anisotropy. The testing setup was also altered to measure the vertical velocities in a more expansive range of stresses. In this section the result from the current research will be compared to the various testing results obtained by Marjanovic. Marjanovic measured the vertical velocities in RGoM-EI under K_0-consolidation in the triaxial cell. Figures 6.79 and 6.80 show the RGoM-EI data from tests performed by both researchers.

Figure 6.79-a depicts three sets of RGoM-EI P-wave velocity data as a function of vertical effective stress: the tests run by each researcher in the medium pressure triaxial setup, and the high pressure TCRS data. There seems to be a significant difference between the velocities measured by the author and Marjanovic. The Marjanovic data are starting from similar values, but increases with a much higher slope, resulting in a nearly 200 m/s difference at 10 MPa. As discussed before, a portion of this difference is potentially associated with the porosity discrepancies at the same stress level. To test this hypothesis the same data are then plotted in porosity space (Figure 6.79-b). When porosity is considered, the three sets of data have very similar

slopes, but shifted by the starting void ratio. Also, the two sets of triaxial velocities (green and pink) are shifted by 30-90 m/s, which is within the error bound of each data set. An arrival time shift of roughly 0.0000025 sec (2.5 µsec) shifts the velocities enough to compensate for the difference is porosity space.

Figure 6.80 shows the vertical S-wave velocities, both as a function of vertical effective stress and porosity. Opposite to the P-wave velocities, Marjanovic's S-wave velocities are slightly lower than the values measured in this research (nearly 10% at all stress levels). Upon investigating the possible reasons, the author discovered a major assumption difference in the way the two researchers had processed the S-waveforms. Figure 6.81 shows an example S-waveforms from Marjanovic. What she had considered the arrival time (the first zero intercept in the upwards portion) is shown with a black dot, and what Brignoli et al. [21] suggests for signals with near-field effect) is shown with a red star. This can cause up to 80 m/s difference in S-wave velocity depending on the waveform. Although re-analyzing all of the previous signals and adjusting them for the recent assumption would not have been possible, the author believes that correcting for this assumption would eliminate most of the difference between the two sets of data (red and pink versus green). As an example, correcting for the arrival time in the signal in Figure 6.81, which was taken at 6 MPa, the velocity increases by 35 m/s. After near-field effect consideration, a significant shift in the arrival time (0.00004-0.0001 sec) is still required to shift the green data in Figure 6.80-a. Hence the difference cannot be explained solely by arrival time errors.

Marjanovic measured vertical velocities in RBBC both in the MIT geotechnical laboratory (0.1-10 MPa) and off campus, using Shell high pressure technology (20-75 MPa). The author attempted to fill in the gap and connect the two data sets (1-30 MPa) Results from the current research (blue) are compared to Marjanovic's results (green) in Figures 6.82 and 6.83. The vertical effective stress results are presented in logarithmic scale to better capture the 3 orders of magnitude variability. The Shell data for P-wave velocities in stress space (Figures 6.82-a) are aligned with the data acquired by the author. However Marjanovic's triaxial P-wave velocities are

higher than both by as much as 8%. In porosity space, the Shell and triaxial P-wave velocities agree perfectly, with author's TCRS data following a similar trend but nearly 2% lower at each porosity. This is less than the experimental scatter in this research (3%) shown in Figure 6.38. RBBC S-wave velocities are shown in Figure 6.83-a in stress and Figure 6.83-b in porosity space. Marjanovic's triaxial data follow the same trend for the S-wave velocity, but have slightly higher P-wave velocities. Similar to the stress dependent behavior, Shell and current research data agree well in porosity space. The RBBC testing repeatability for P-wave velocity is ±5% and for S-wave velocity is ±9% from average.

The exact reason behind the difference in the velocity data measured by the two researchers is unknown. It could have been caused by a combination of subtly different testing procedures (such as the number of measurements, the measurement intervals, the oven drying time, etc.), difference in the resedimentation process or material (such as slurry water content, batched material, salinity, etc.) and degree of saturation after back pressure saturation (or the lack of in case of the TCRS tests).

6.6 Results Compared to other Published Data

6.6.1 Velocity

In this section the measured parameter will be compared to various published data. The results will be studied both as a function of stress and porosity. The data in the literature can be different than the data from current research in various ways. Most experimental velocity studies have been performed on lithified rock cores (Vernik and Liu [167], Hornby [66]), as opposed to resedimented clay specimens with relatively high porosity. Vernik and Liu [167] measured directional velocities and anisotropy for a variety of shales (dry, brine-saturated and silicon oil-saturated) including Bazhenov (Western Siberia), Niobrara (New Mexico) and Kimmeridge (North Sea). Their brine-saturated results are used for comparison in this study. Hornby [66] ran similar tests on Kimmeridge and Jurassic shales, that are included here. Perhaps the most comparable data was published by Nihei [116], from tests performed on intact Gulf

of Mexico- Green Canyon shale specimen. Finally, Johnston and Christenten [78] reported a data set, mostly collected from other publications, of vertical velocities measured in a wide variety of rocks (Sandstone, limestone, silty limestone, dolostone, and quartzite). These data are included in the vertical velocity figures (yellow dots). For reasons that will become clear shortly, the author only compared the data from the current research to a handful of published data that reported the porosity data, as well as the velocity data.

Figures 6.84-6.87 compare the velocity measurements from the current study, as well as the aforementioned data from the literature. They include the velocity values as a function of both stress and porosity. While in each plot the results from this research are clustered together at the higher end of the porosity axis with only small material-dependent variations, it is clear that when plotted against the vertical effective stress (shown on the left with a) there is no correlation between the different data sets. In contrast, when the velocities are plotted as a function of porosity (shown on the right with b), there is a clear increasing trend with decreasing porosity. This further shows that the stress level alone does not represent the velocity behavior. In the velocity versus porosity plots there are two separate clusters of data, high porosity (0.35-0.6) and low porosity (0-0.1) and a clear gap in between (0.1-0.35). Filling this gap in the porosity data requires expanding the stress level even further than 25 MPa. Vernik [164] and Issler [74] reported some velocity within this porosity range in shale. Vernik [165] proposed a linear correlation between the porosity and velocities in shale, within the range of 0-0.3 of porosity. However, based on the data presented in this research, the author believes such correlation would have to be of non-linear nature, presumably logarithmic. It is worth noting that most of the intact core samples tend to have low porosity, except for Nihei's. Nihei's sample was retrieved from 74 m below mudline, which is relatively shallow, and then consolidated to 7 MPa vertical effective stress. While the composition of GoM-Green Canyon (Typhoon field) shale is different than both RGoM-EI and RBBC, there is still a general agreement between the velocity results from Nihei [116] and this research, in both directions, further indicating relative material independence.

More data is needed for an accurate predictive model to be developed; however, it is clear that the velocities become gradually more sensitive to the porosity. At lower porosities the velocities are changing with much steeper slopes.

Figures 6.88 and 6.89 show the vertical and horizontal velocities as a function of porosity in logarithmic scale. The dotted lines in the two figures illustrate the logarithmic equations fitted through all the data from the current research and the dots are the same data shown in Figures 6.84-Figure 6.87 (on the right side). In the Figure 6.88-a the logarithmic line captures the average of V_{pv} data from the literature for porosities between 0.1 and 0.02, but at porosities lower than 0.02 (Johnston and Christenten [78]) the line lays below the experimental data. The Logarithmic V_{sv} line however lands at the higher end of velocities. Similar to the vertical P-wave velocity, the logarithmic line, fitted through the horizontal P-wave velocities, passes through the average V_{ph} values (Figure 6.89-a). Lastly, Figures 6.89-b shows that the logarithmic line does not capture the V_{sh} behavior and yields values much bigger than what was measured by various researchers.

6.6.2 Velocity Ratio

Another parameter affected by the porosity is velocity ratio (V_p/V_s). Figures 6.90 and 6.91 show the velocity ratios in vertical and horizontal directions. P-waves propagate through pore fluid, but S-waves do not, which results in higher V_p/V_s in more porous specimens compared to low porosity rocks. Hence the velocity ratios decrease as a result of decreasing porosity. This trend also appears to be more dependent on porosity than the material type. Virtually all published V_p/V_s data is less than 3, whereas this research and Nihei [116] have velocity ratios starting around 2.5, and as high as 7.3. His higher S-wave velocities are the driver for higher velocity ratios. Also, the velocity ratios from this research are very similar in both directions, because of the low anisotropy level (Figure 6.92).

Dutta et al. [37] compared a massive amount of log data from Gulf of Mexico-Green Canyon to Vernik's V_p/V_s equation for shale [166] and the mudrock relation by Greenberg and Castagna [54]. Figure 6.93 compares the RGoM-EI data from

this research (both from triaxial and TCRS testing, shown in yellow) the figure 8-a of Dutta et al. [37]. The velocities from the current research are on the lower end of the V_p versus V_s trends, since the resedimented specimens tested in TAG Lab have higher porosities and lower velocities. Also, the non-linear to linear transition portion of Vernik's shale equation seems to fit through the lab data almost perfectly. In contrary, the linear Castagna mudrock equation does not appear to be predicting the lower end of the velocities accurately. Figure 6.94 focuses on RGoM-EI data and how they compare to the models proposed by Greenberg and Castagna [54] (Equation 6.13) and Vernik et al. [166] (Equation 6.14).

$$V_s = 0.77V_p - 0.867 \tag{6.13}$$

$$V_s = \sqrt{-0.79 + 0.287{V_p}^2 + 0.00284{V_p}^4} \tag{6.14}$$

The author modified equation 6.14 to ensure that the S-wave velocity is zero at V_p=1584, which is the P-wave velocity through the 80 gr/l salt-water used in this research:

$$V_s = \sqrt{-0.738 + 0.287{V_p}^2 + 0.00284{V_p}^4} \tag{6.15}$$

As shown in Figure 6.94 for V_p values smaller than 1900 m/s, the RGoM-EI data are closely following the nonlinear trend suggested in equation 6.15. for V_p values higher than 1900 m/s however, RGoM-EI has slightly higher V_s values compared to the results from both models, that are overlapping for the most part.

6.6.3 Anisotropy

The majority of the velocity anisotropy studies focus on testing on lithified sedimentary rock cores, with low porosities ([126] [80] [168], [78] [79] [167] [66] [173] [124] [116], etc). They measured velocities in two perpendicular directions and one inclined angle, and calculated the anisotropy (Thomsen's) parameter. The anisotropy

in non-lithified and high porosity resedimented samples has been mostly avoided because of the dificulties making velocity measurements in soft materials. In this section, the anisotropy parameters determined in this research (Section 6.4) will be compared to some of the data published on shales.

Figure 6.95 includes the P-wave anisotropy parameter (epsilon, ϵ) and S-wave anisotropy (gamma, γ) calculated for RGoM-EI (both individual results and interpreted data (from the power equations in Section 6.2.3) to the published data on various shale formations. The first notable point is that the data from this research are at the lowest end of anisotropy (ϵ & $\gamma < 0.1$, hence weakly anisotropic), compared to virtually all of the published data. This behavior is likely due to two major factors. First, the resedimented specimens have much higher porosities, which means P-wave velocities are dominated by the pore fluid effect. Since V_p is independent of direction in fluid, higher porosity results in lower anisotropy. Moreover, RGoM-EI specimens are resedimented as opposed to intact and lithified. The effect of lithification on anisotropy was not covered in this study. While a good portion of the published data (nearly half) has less than 0.3 anisotropy, the rest seem to follow two parallel lines on each side of the ellipticity line. This signifies that in more anisotropic shales, one of the two anisotropy parameters is dominant. Hence the ellipticity assumption in more anisotropic shales (ϵ & $\gamma > 0.3$) is unrealistic.

Epsilon and gamma parameters only take the horizontal and vertical stiffnesses into consideration. Also, they are not very relevant to problems of near-vertical P-wave propagation, as the most commonly occurring type of anisotropy (transverse isotropy) masquerades as isotropy in near- vertical reflection profiling [87]. The delta parameter captures the position of C_{13} relative to the compressional (C_{11} and C_{33}) and shear (C_{44} and C_{66}) elements. The closer C_{13} is to the compressional elements, the higher delta is. Also C_{13} is higher at higher velocity ratios (RGoM-EI has quite high V_p/V_s ratios) which results in higher delta. Not all studies measured the inclined velocity (so ϵ & γ are the more common anisotropy parameters). Figure 6.96 compares the ϵ and δ values from this research to the data published in the literature on shales. While the interpreted RGoM-EI data seem to slightly above the

45° line (high γ), the individual test results are scattered rather vertically. Despite the RGoM-EI individual test results, virtually all the data from the literature are located either on or under the 45° line ($\epsilon \geq \delta$). This discrepancy further implicates that the variation in RGoM-EI delta (red dots) is most likely a product of the errors in inclined velocity measurements and the sensitivity of the δ parameter on this measurement, not a material behavior.

Test#	Sample#	Soil Type	Initial wc (%)	Final wc (%)	Initial e()	Final e()	Maximum Measured Vertical Effective Stress , σ'_{vmax} (MPa)
TX1394	RS493	RGoM-EI	33.3	17.6	0.98	0.54	9
TX1399	RS597	RGoM-EI	34.0	18.7	1.03	0.59	9.5
TX1404	RS576	RGoM-EI	33.7	19.2	1.00	0.552	9
TX1408	RS591	RGoM-EI	33.4	19.4	1.01	0.53	10
TCRS1566	RS608	RGoM-EI	33.3	14.2	0.97	0.352	27.1
TCRS1582	RS589	RGoM-EI	33.9	13.5	0.97	0.333	24.3
TCRS1587	RS630	RGoM-EI	32.5	15.2	0.94	0.401	25.3
TCRS1609	RS611	RGoM-EI	34.9	12.4	0.98	0.367	23.3
TCRS1570	RS620	RBBC	34.1	17.8	1.01	0.452	19.6
TCRS1577	RS622	RBBC	32.5	16.0	0.96	0.407	25.3
TCRS1583	RS600	RBBC	33.4	15.4	1.02	0.395	25.3
TCRS1598	RS641	RBBC	32.2	13.9	0.93	0.387	25.3

Table 6.1: Summary of triaxial and TCRS tests performed

Test Type	Triaxial	Triaxial	Triaxial	Triaxial	Triaxial	TCRS	TCRS	TCRS	TCRS
Direction	Vertical	Inclined	Horizontal	Vertical	Horizontal	Vertical	Vertical	Vertical	Vertical
Signal Type	P	P	P	S	S	P	S	P	S
Soil Type	RGoM-EI	RGoM-EI	RGoM-EI	RGoM-EI	RGoM-EI	RGoM-EI	RGoM-EI	RBBC	RBBC
A	113	141.2	215.5	314	324	144.4	314.3	69.9	320
B	0.56	0.519	0.392	0.37	0.366	0.415	0.314	0.611	0.317
C	1584	1584	1584	0	0	1584	0	1584	0
R^2	0.92	0.86	0.88	0.97	0.98	0.88	0.98	0.90	0.97
Error Bound (±%)	3	4	4	8	5	5	8	3	8
RMSD	23.1	33.6	40.1	24.3	18.6	40.6	26.7	23.1	24.7

Table 6.2: Experimental power correlations predicting the velocities as a function of stress level ($V = C + A\sigma'^{B}$)

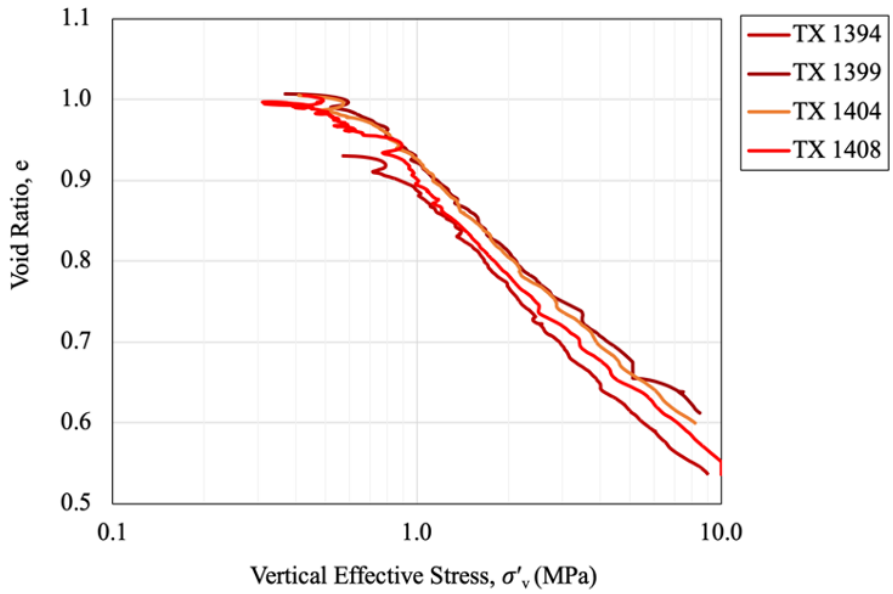

Figure 6.1: Void ratio curves for RGoM material K_0-condsolidated up to 10 MPa vertical effective stress using the triaxial setup

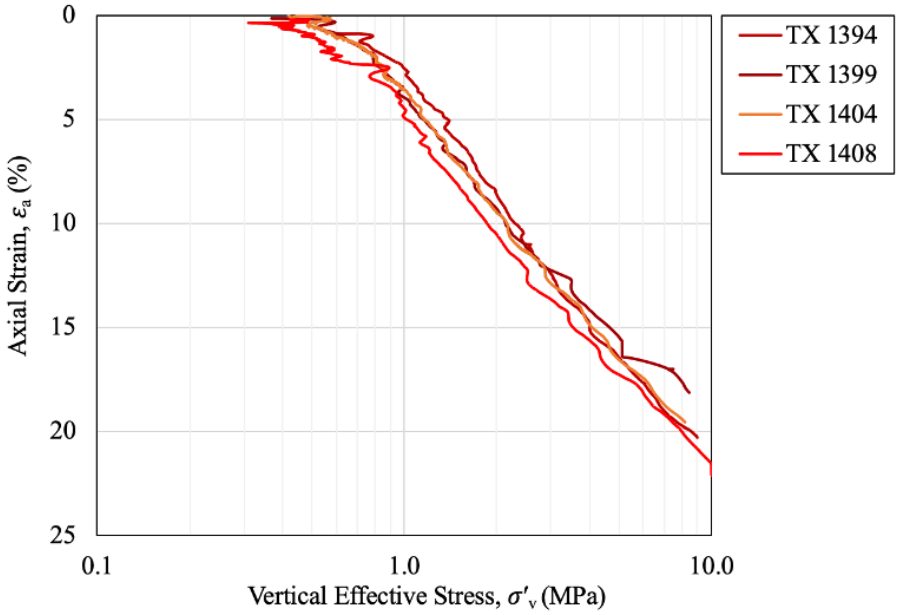

Figure 6.2: Axial strain curves for RGoM material K_0-condsolidated up to 10 MPa vertical effective stress using the triaxial setup

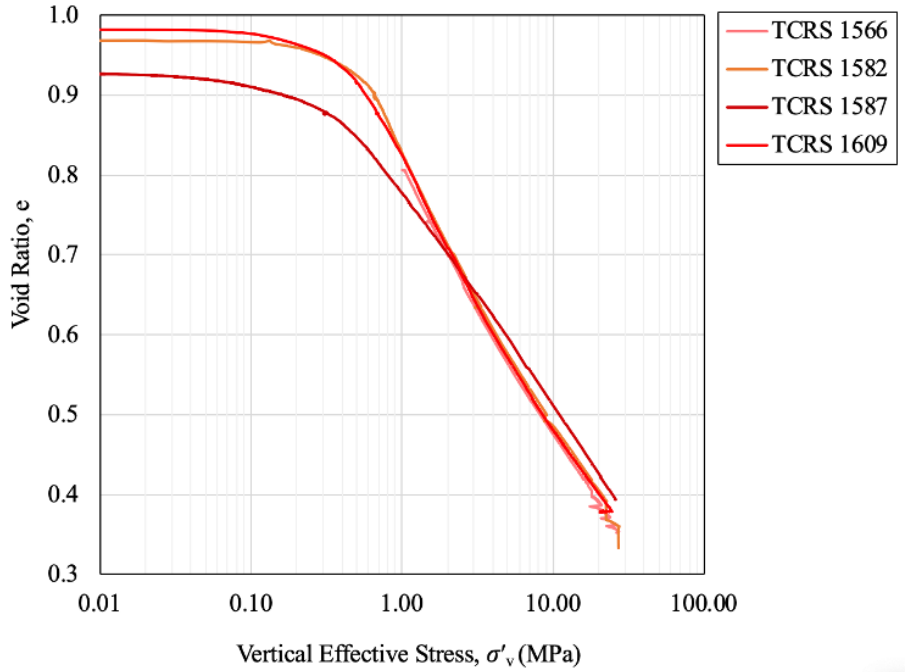

Figure 6.3: Void ratio curves for RGoM material K_0-condsolidated up to 30 MPa vertical effective stress using the triaxial setup

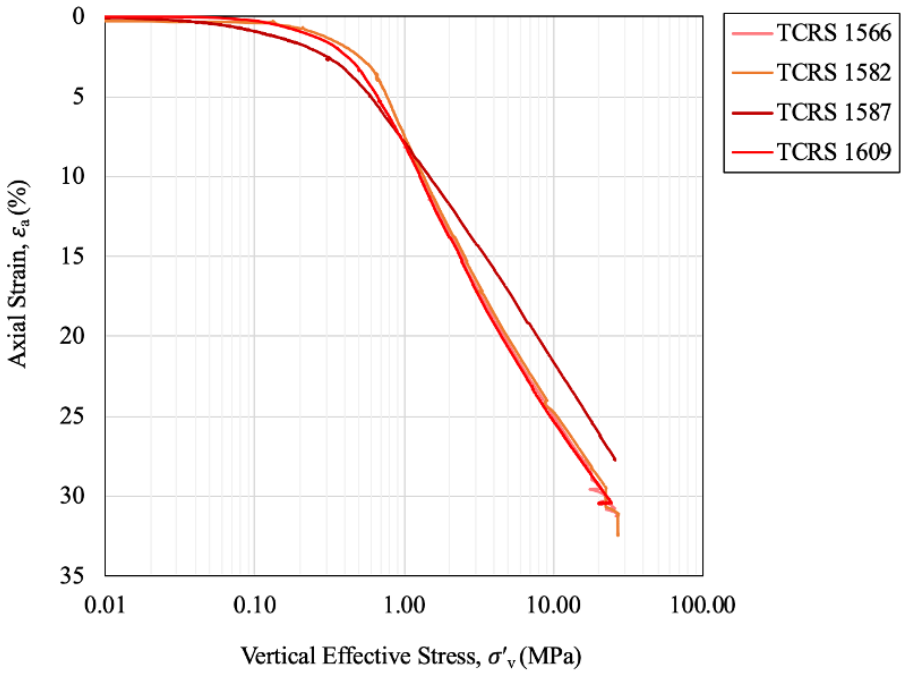

Figure 6.4: Axial strain curves for RGoM material K_0-condsolidated up to 30 MPa vertical effective stress using the triaxial setup

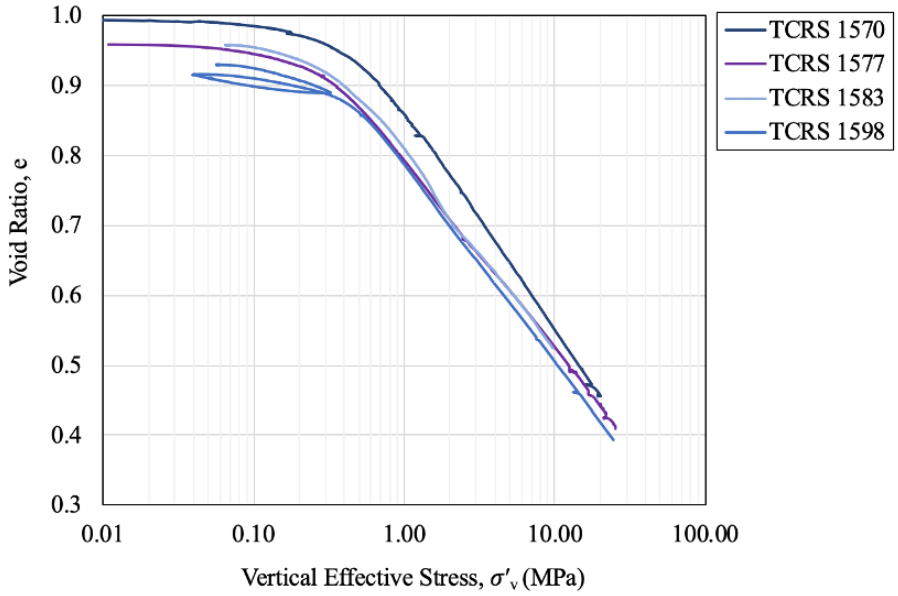

Figure 6.5: Void ratio curves for RBBC material K_0-condsolidated up to 30 MPa vertical effective stress using the triaxial setup

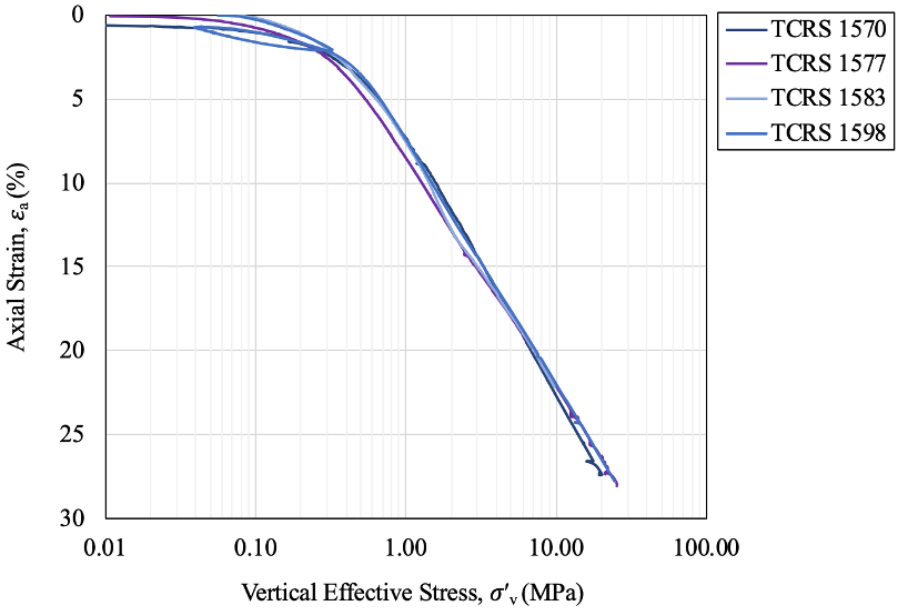

Figure 6.6: Axial strain curves for RBBC material K_0-condsolidated up to 30 MPa vertical effective stress using the triaxial setup

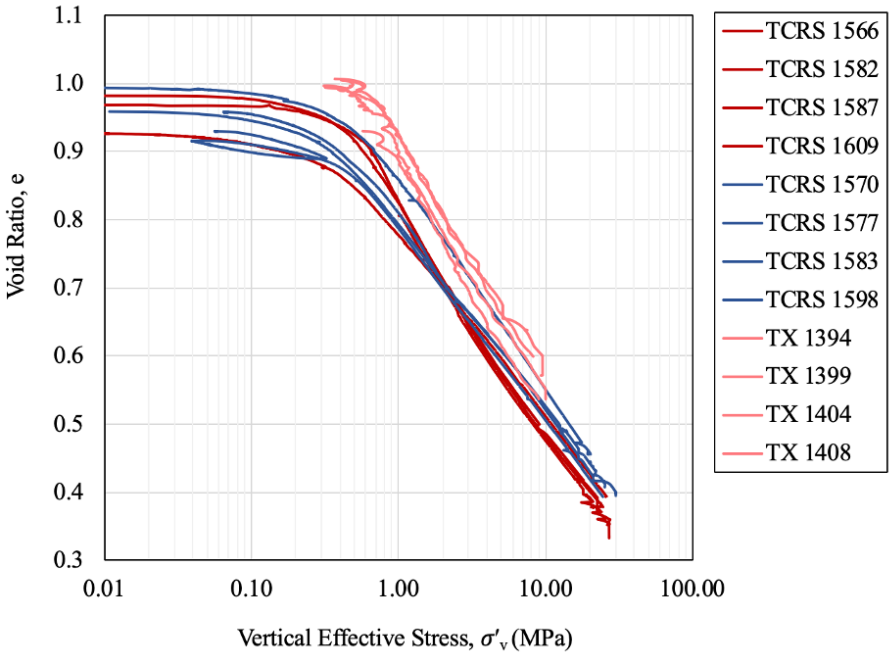

Figure 6.7: Compression curves comparison for RGoM and RBBC material K_0-condsolidated using the TCRS and triaxial setup

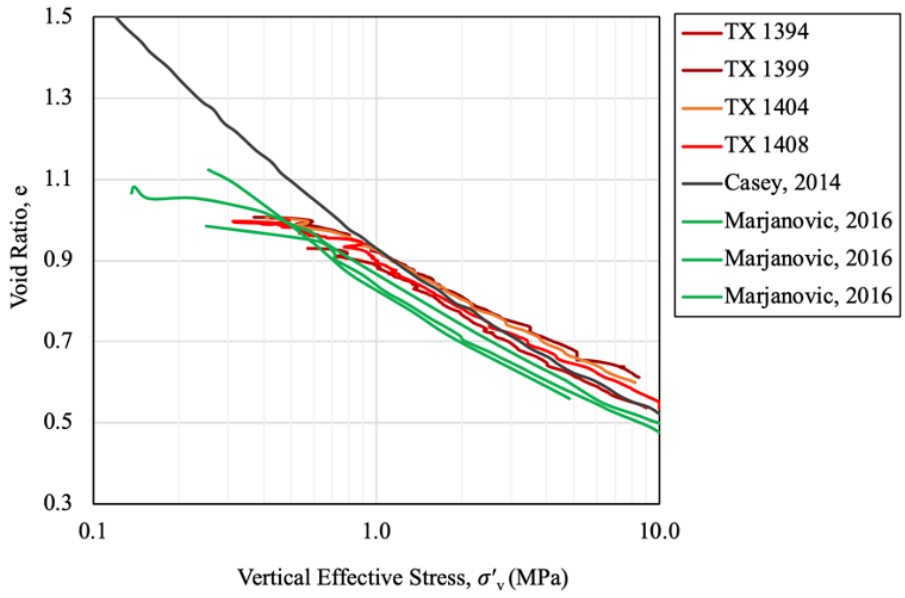

Figure 6.8: Compression curve comparison for triaxial RGoM tests performed by various researchers

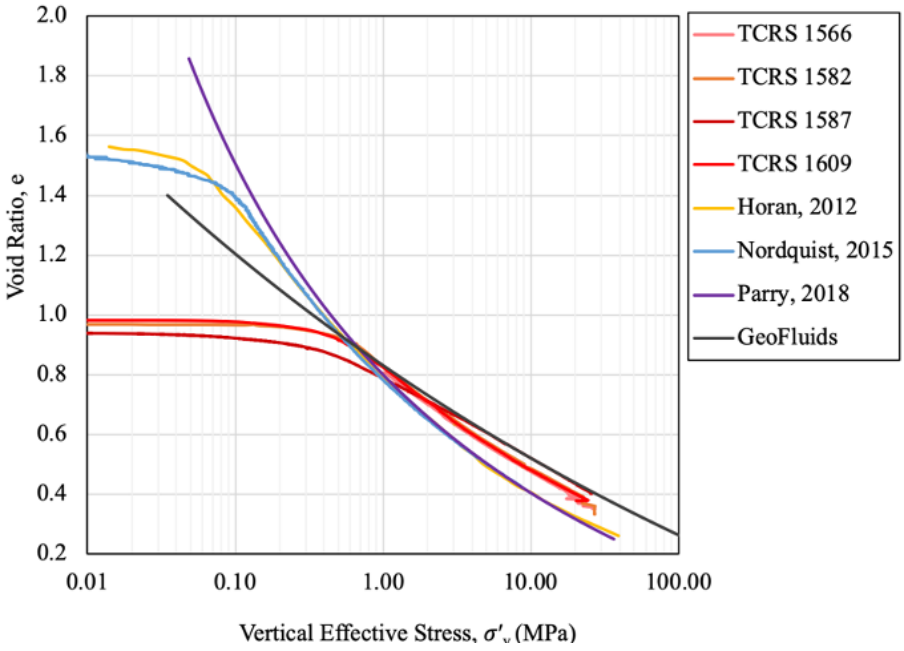

Figure 6.9: Compression curve comparison for TCRS RGoM-EI tests performed by various researchers

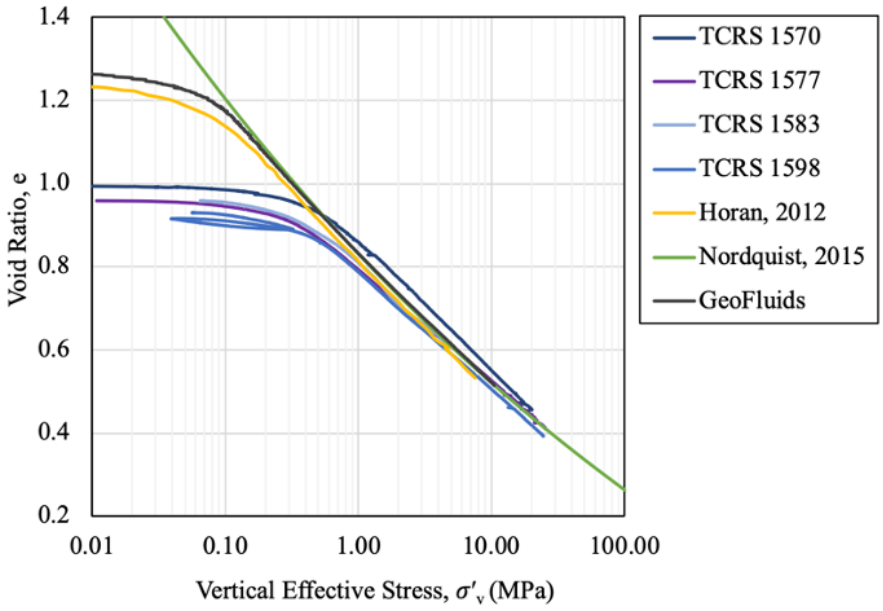

Figure 6.10: Compression curve comparison for TCRS RBBC tests performed by various researchers

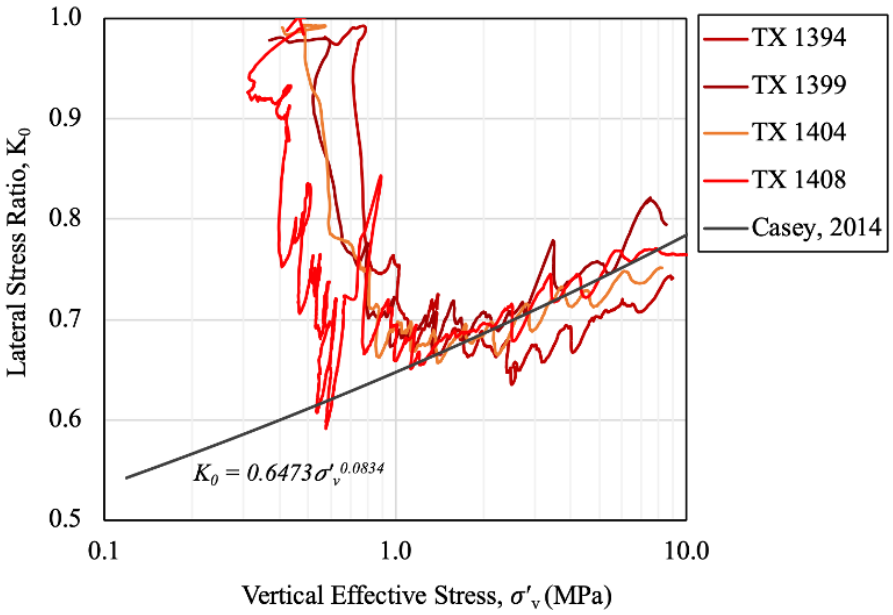

Figure 6.11: K_0 values measured during consolidation in triaxial cell

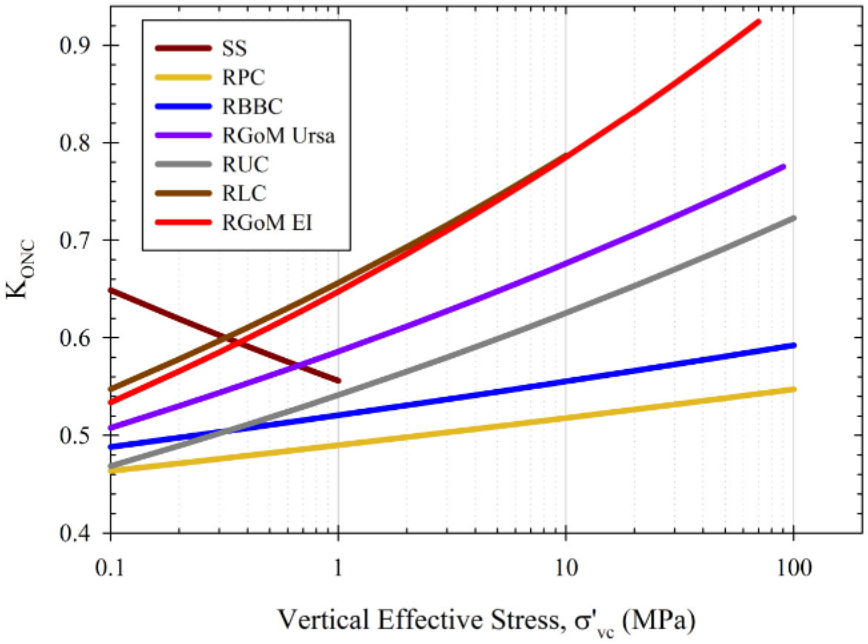

Figure 6.12: Normally consolidated K_0 for different materials [24]

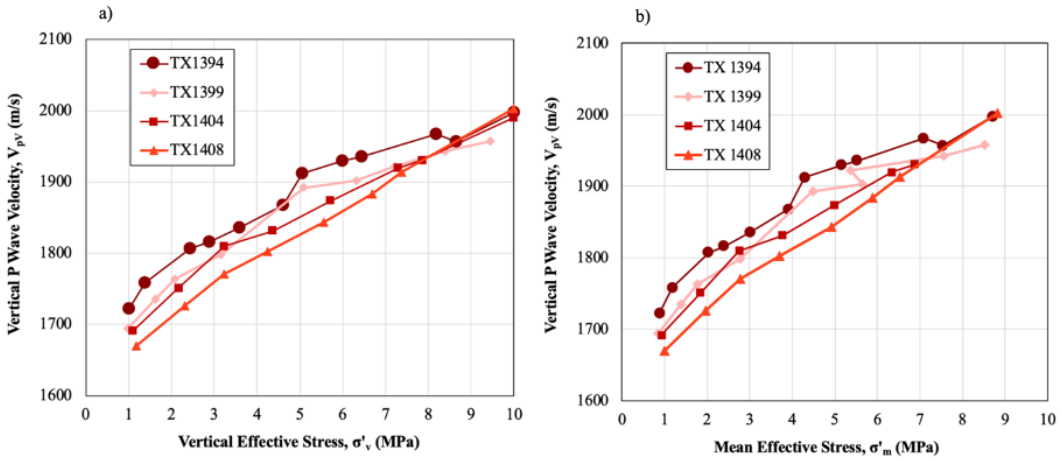

Figure 6.13: Vertical P-wave velocity results as a function of a) vertical effective stress and b) mean effective stress, for RGoM-EI specimens tested in triaxial cell

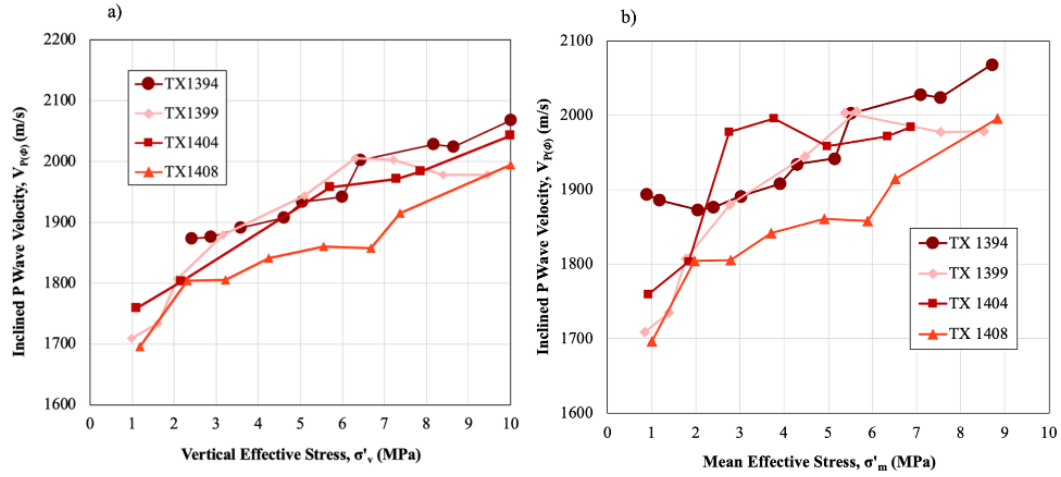

Figure 6.14: Inclined P-wave velocity results as a function of a) vertical effective stress and b) mean effective stress, for RGoM-EI specimens tested in triaxial cell

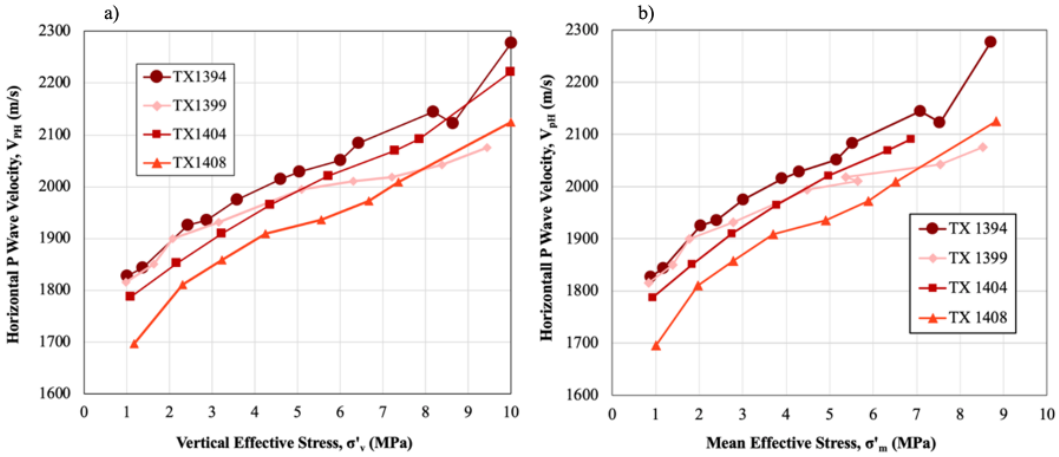

Figure 6.15: Horizontal P-wave velocity results as a function of a) vertical effective stress and b) mean effective stress, for RGoM-EI specimens tested in triaxial cell

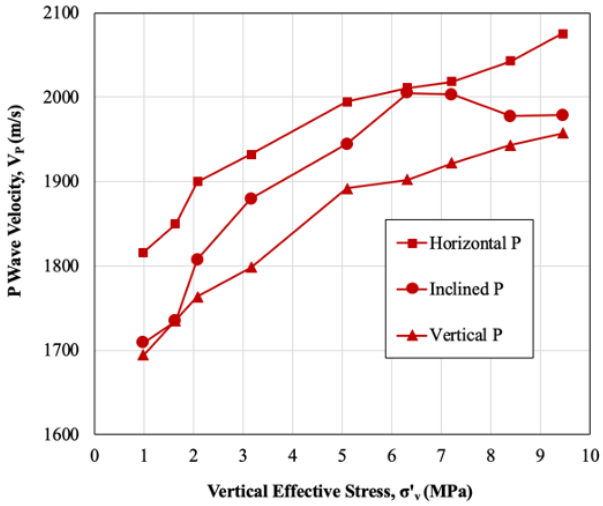

Figure 6.16: Vertical, inclined and horizontal P-wave velocity results as a function of vertical effective stress for RgoM-EI specimens tested in triaxial cell (TX1399)

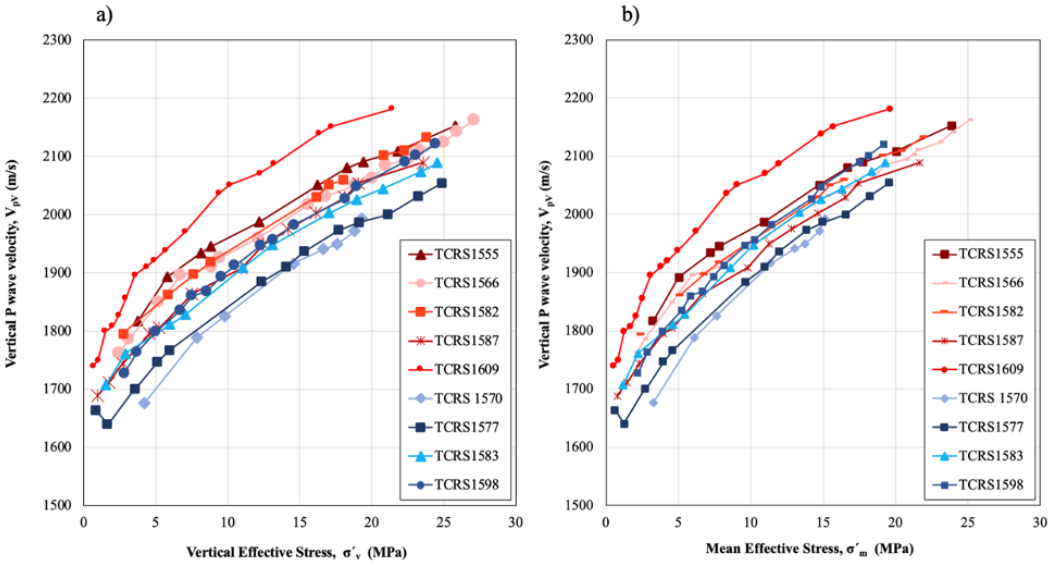

Figure 6.17: Vertical P-wave velocity results as a function of a) vertical effective stress and b) mean effective stress for RGoM-EI and RBBC specimens tested in TCRS

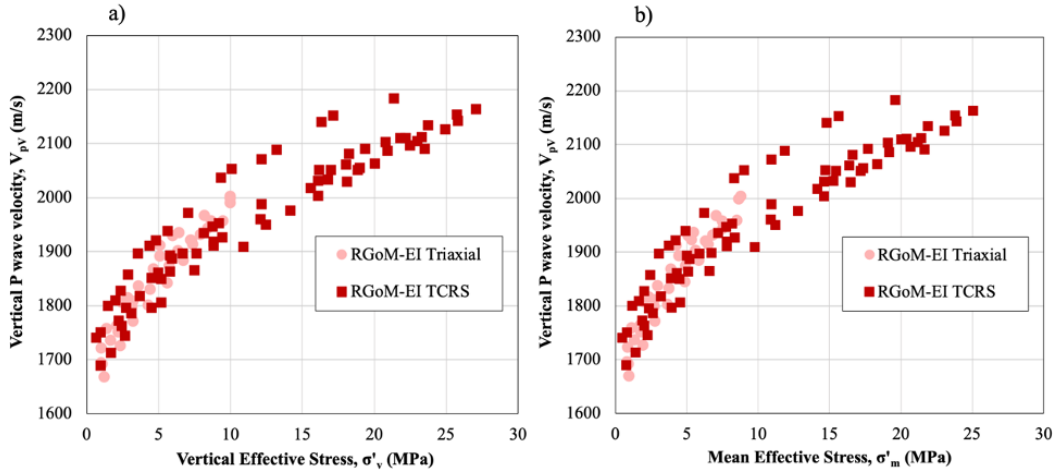

Figure 6.18: Vertical P-wave velocity results as a function of a) vertical effective stress and b) mean effective stress for RGoM-EI specimens tested in triaxial cell and TCRS

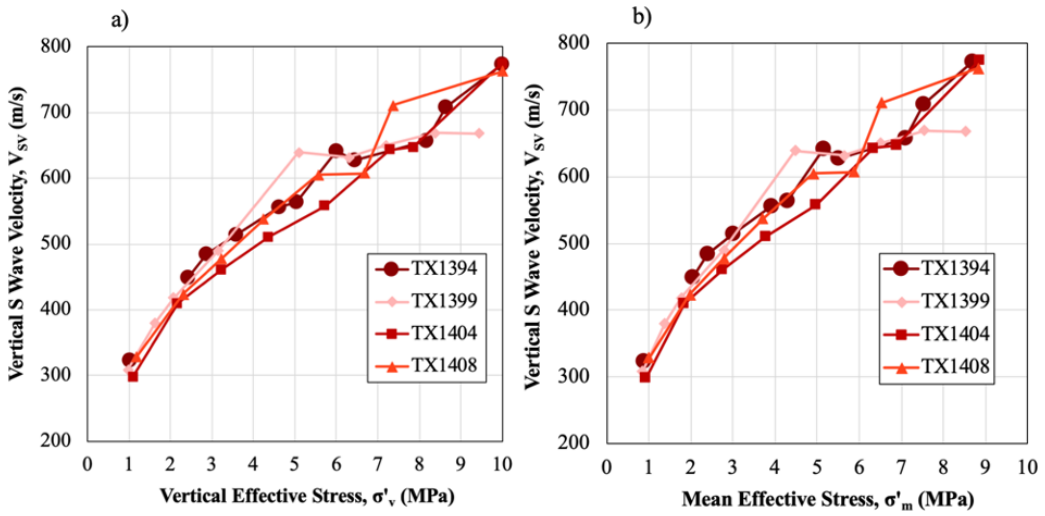

Figure 6.19: Vertical S-wave velocity results as a function of a) vertical effective stress and b) mean effective stress for RGoM-EI specimens tested in triaxial cell

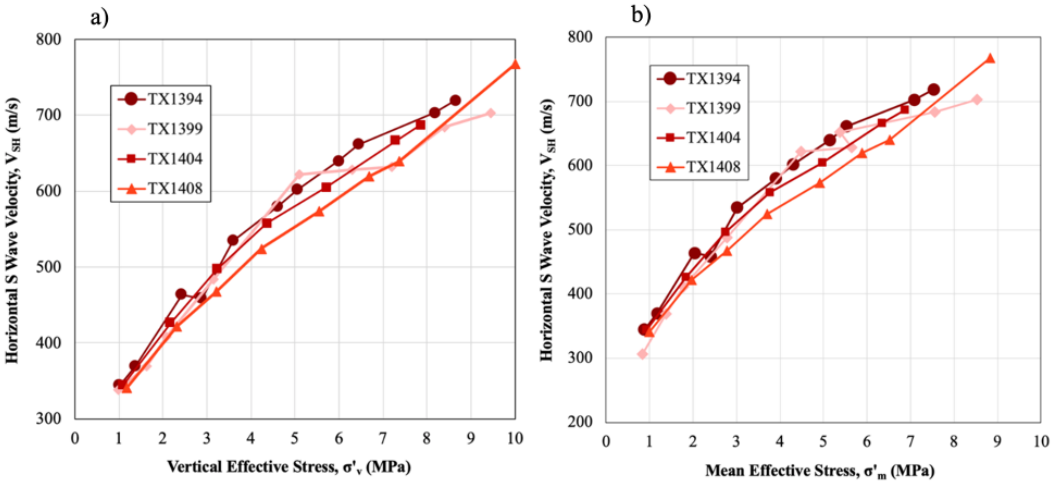

Figure 6.20: Horizontal S-wave velocity results as a function of a) vertical effective stress and b) mean effective stress for RGoM-EI specimens tested in triaxial cell

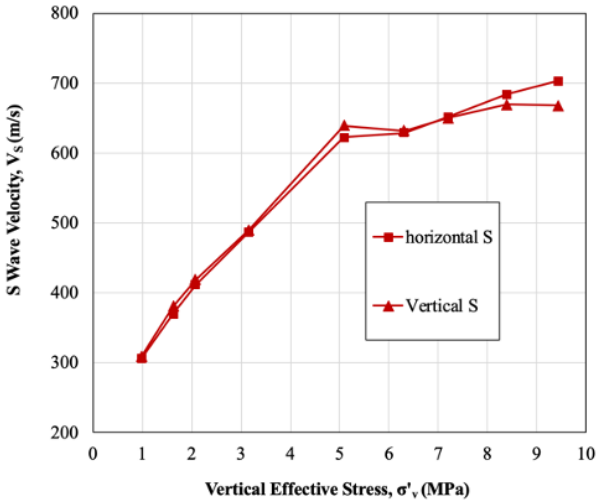

Figure 6.21: Vertical and horizontal S-wave velocity results as a function of vertical effective stress for RGoM-EI specimens tested in triaxial cell (TX1399)

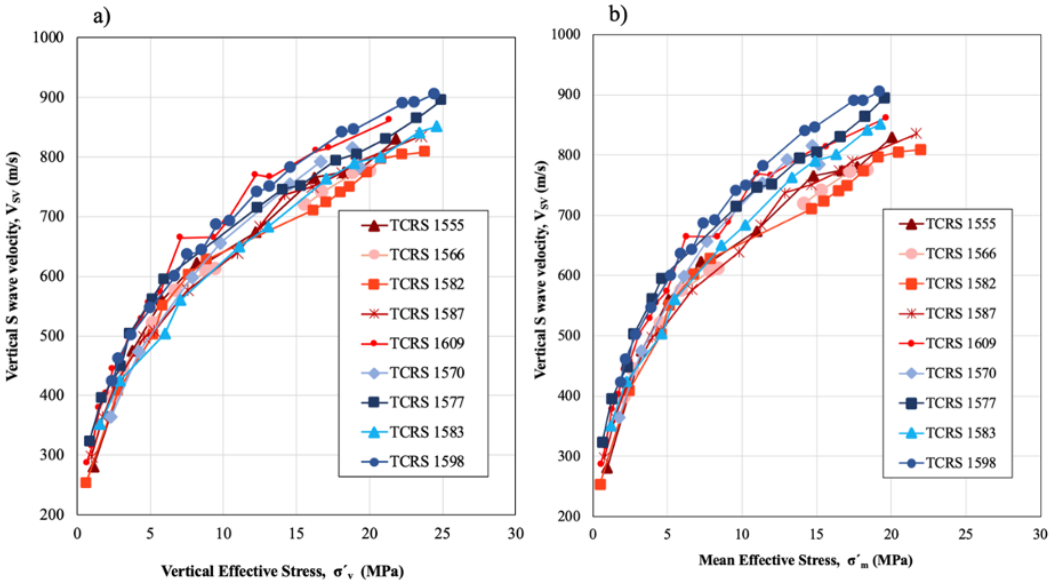

Figure 6.22: Vertical S-wave velocity results as a function of a) vertical effective stress and b) mean effective stress for RGoM-EI and RBBC specimens tested in TCRS

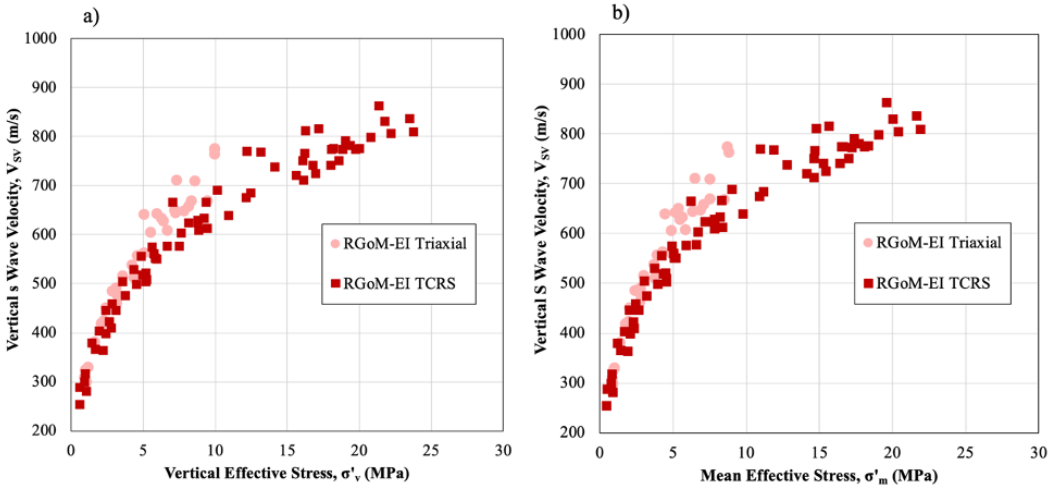

Figure 6.23: Vertical S-wave velocity results as a function of vertical effective stress for RGoM-EI and specimens tested in TCRS and triaxial cellS

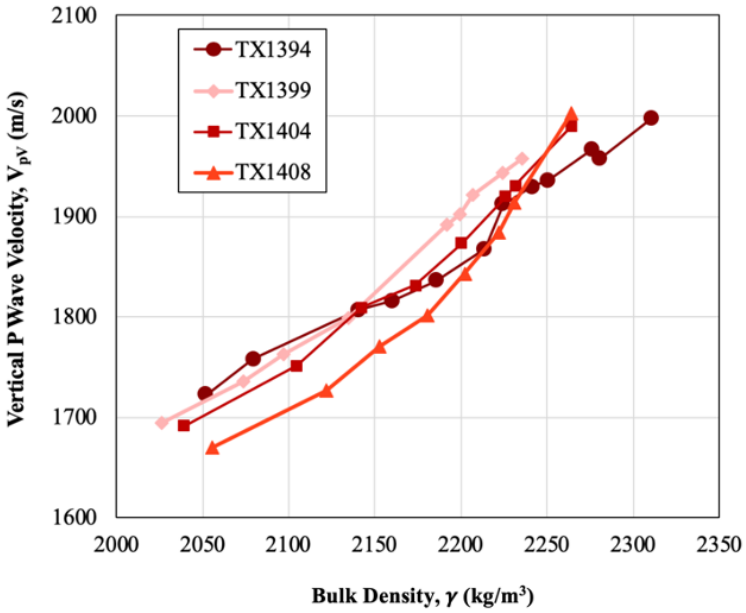

Figure 6.24: Vertical P-wave velocity results as a function of bulk density for RGoM-EI specimens tested in triaxial cell

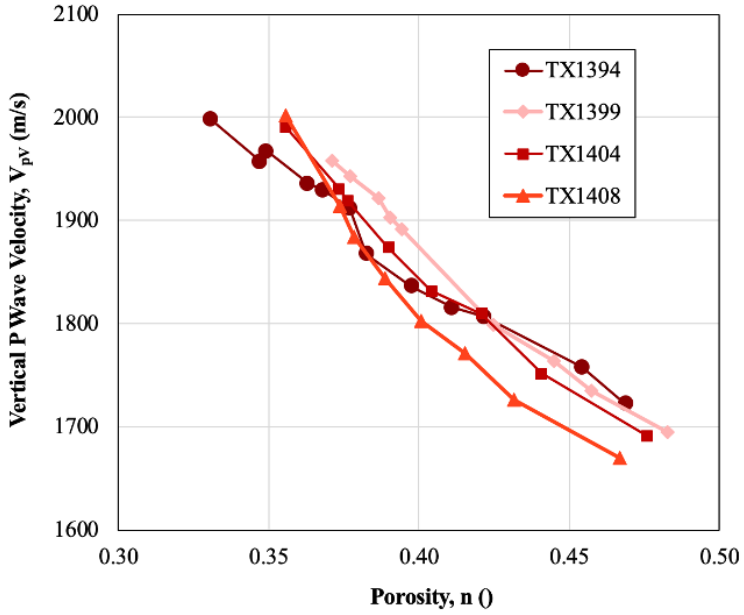

Figure 6.25: Vertical P-wave velocity results as a function of porosity for RGoM-EI specimens tested in triaxial cell

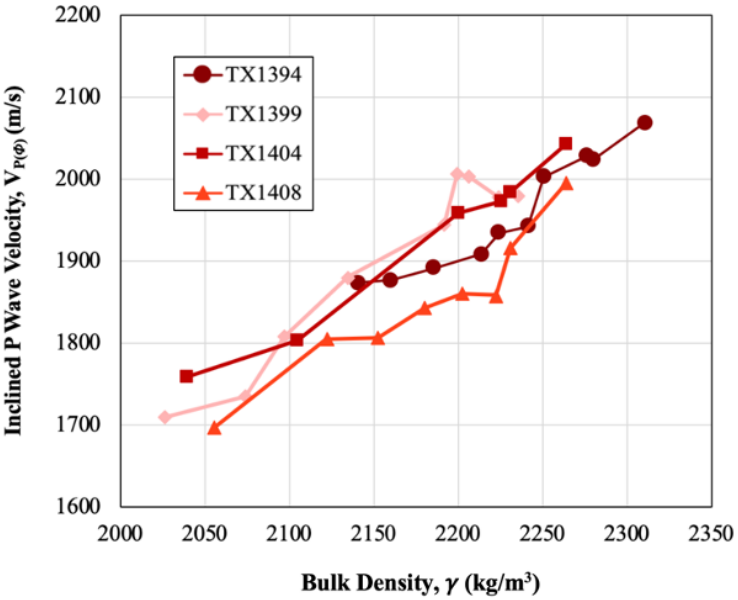

Figure 6.26: Inclined P-wave velocity results as a function of bulk density for RGoM-EI specimens tested in triaxial cell

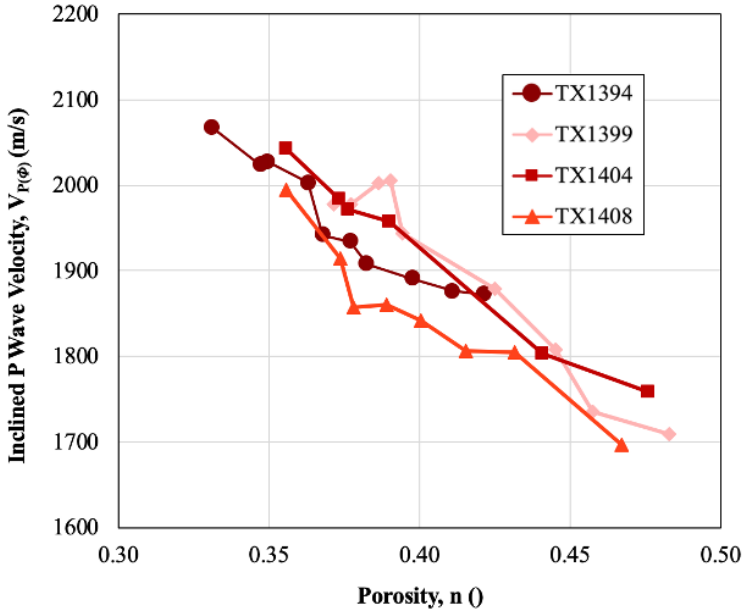

Figure 6.27: Inclined P-wave velocity results as a function of porosity for RGoM-EI specimens tested in triaxial cell

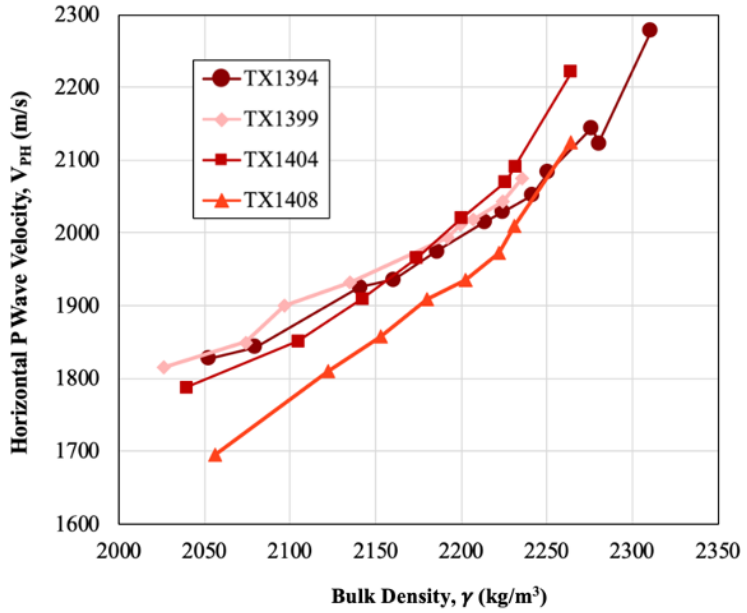

Figure 6.28: Horizontal P-wave velocity results as a function of bulk density for RGoM-EI specimens tested in triaxial cell

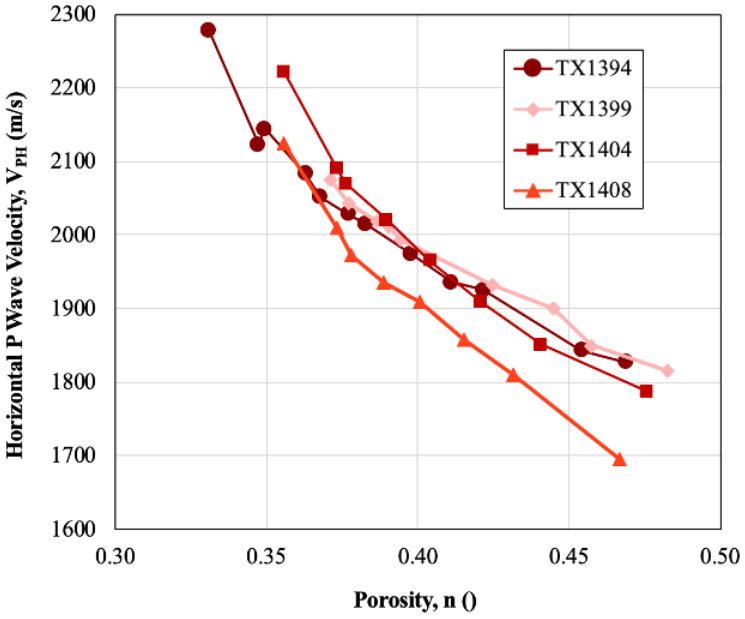

Figure 6.29: Horizontal P-wave velocity results as a function of porosity for RGoM-EI specimens tested in triaxial cell

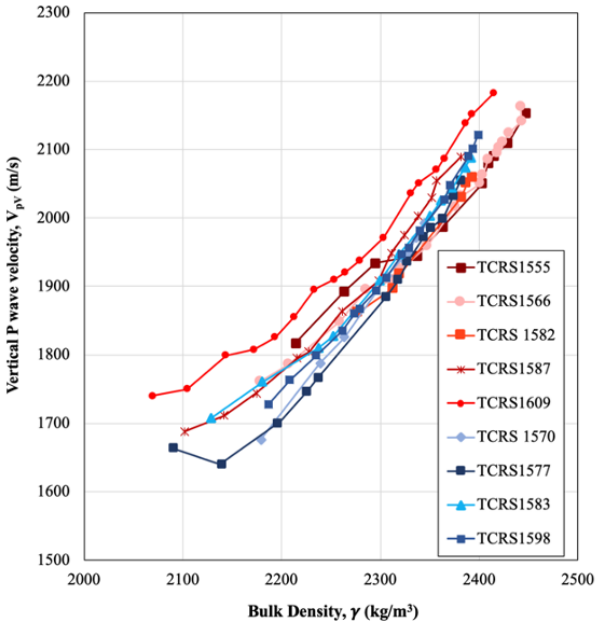

Figure 6.30: Vertical P-wave velocity results as a function of bulk density for RGoM-EI and RBBC specimens tested in TCRS

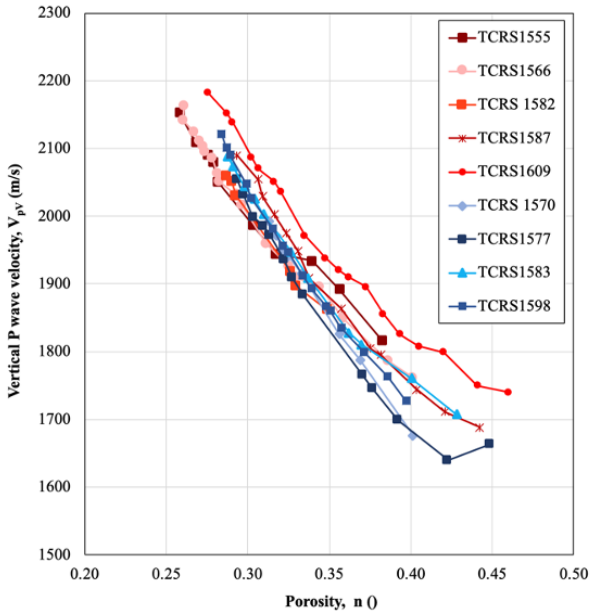

Figure 6.31: Vertical P-wave velocity results as a function of Porosity for RGoM-EI and RBBC specimens tested in TCRS

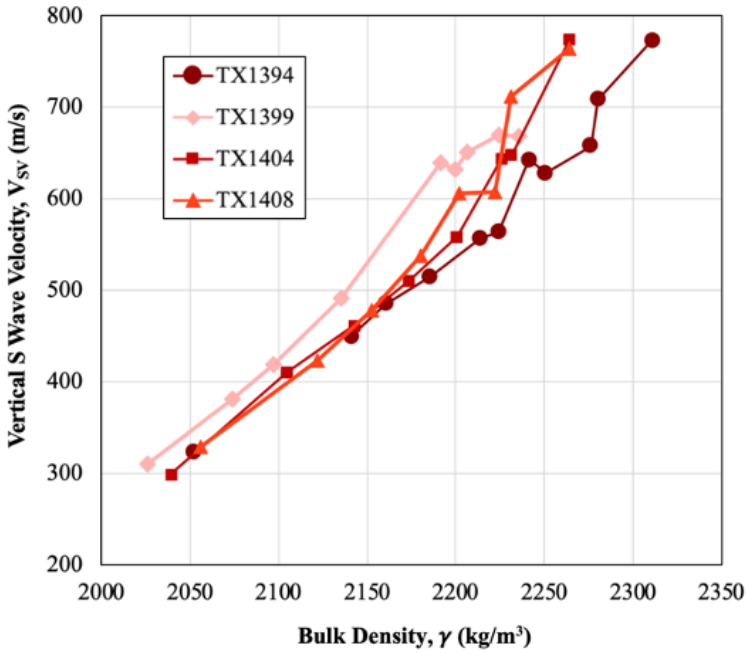

Figure 6.32: Vertical S-wave velocity results as a function of bulk density for RGoM-EI specimens tested in triaxial cell

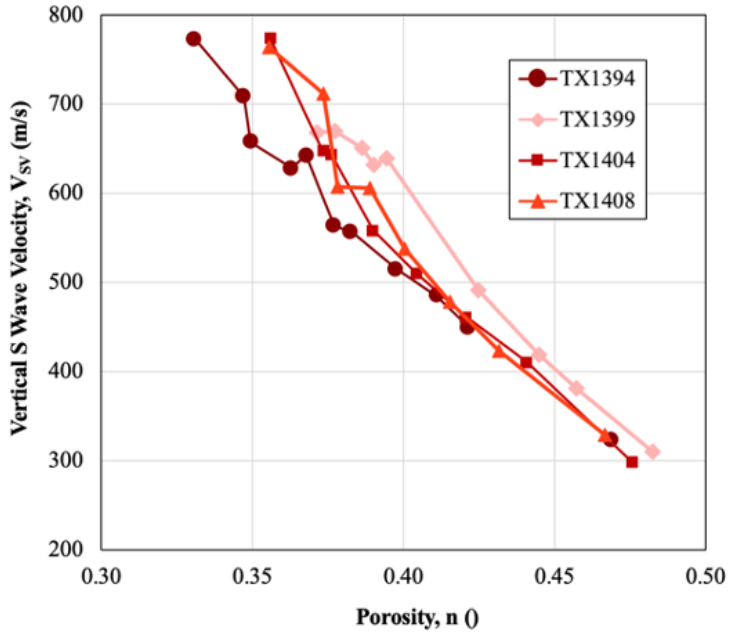

Figure 6.33: Vertical S-wave velocity results as a function of porosity for RGoM-EI specimens tested in triaxial cell

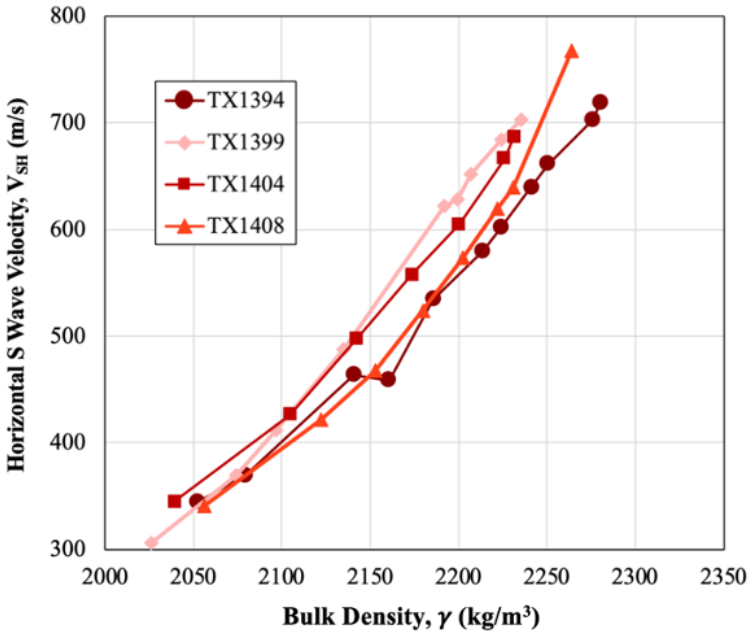

Figure 6.34: Horizontal S-wave velocity results as a function of bulk density for RGoM-EI specimens tested in triaxial cell

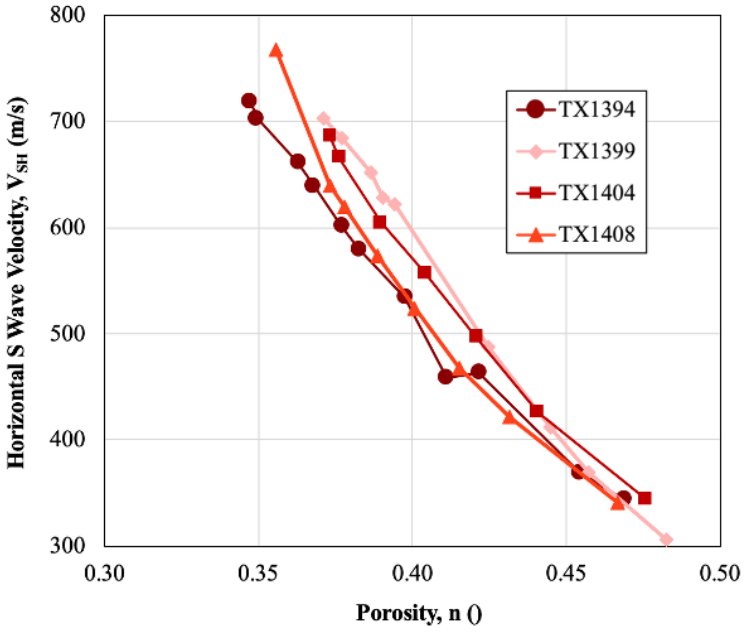

Figure 6.35: Horizontal S-wave velocity results as a function of porosity for RGoM-EI specimens tested in triaxial cell

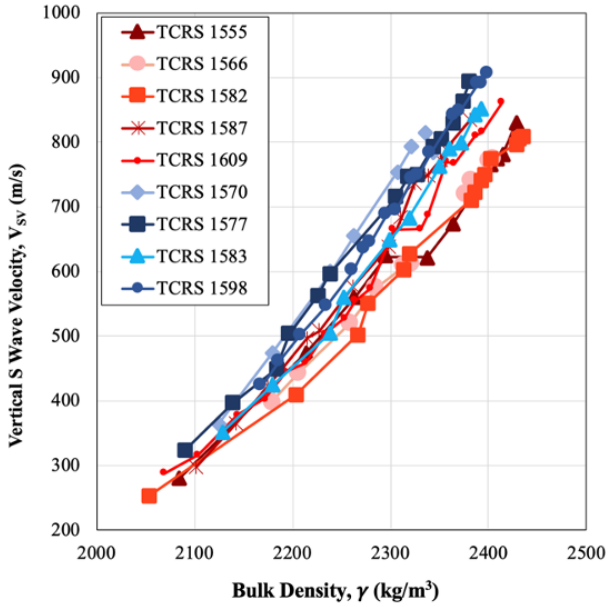

Figure 6.36: Vertical S-wave velocity results as a function of bulk density for RGoM-EI and RBBC specimens tested in TCRS

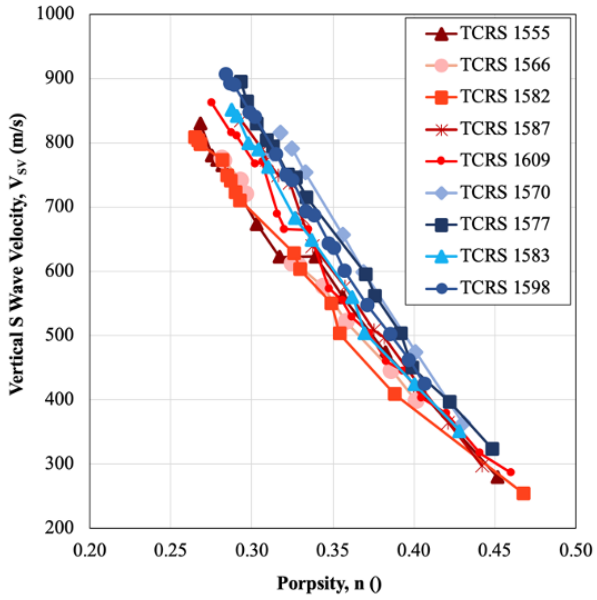

Figure 6.37: Vertical S-wave velocity results as a function of porosity for RGoM-EI and RBBC specimens tested in TCRS

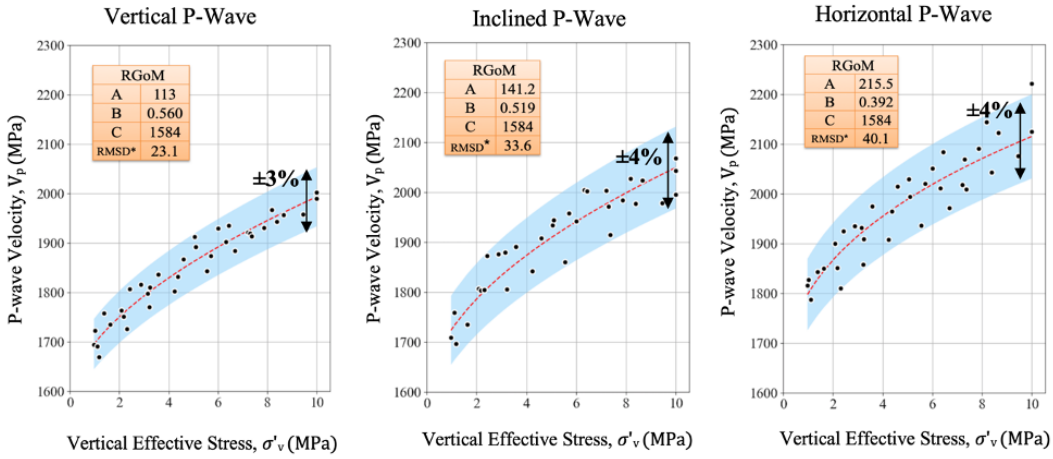

Figure 6.38: The data scatter in directional P-wave velocity results as a function of vertical effective stress for RGoM-EI specimens tested in triaxial cell

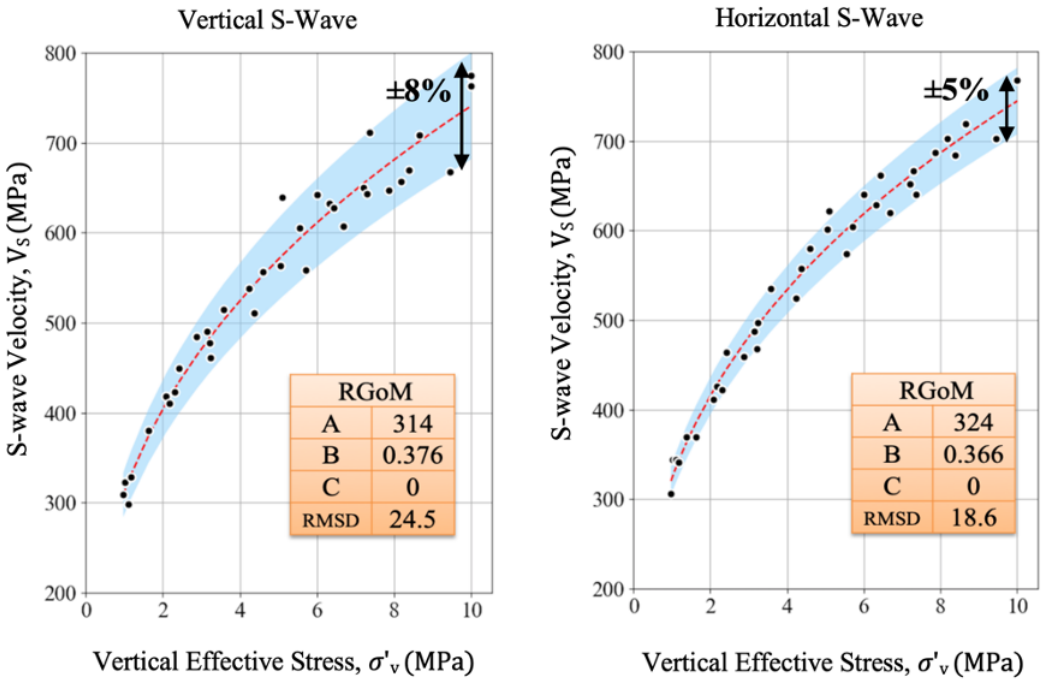

Figure 6.39: The data scatter in directional S-wave velocity results as a function of vertical effective stress for RGoM-EI specimens tested in triaxial cell

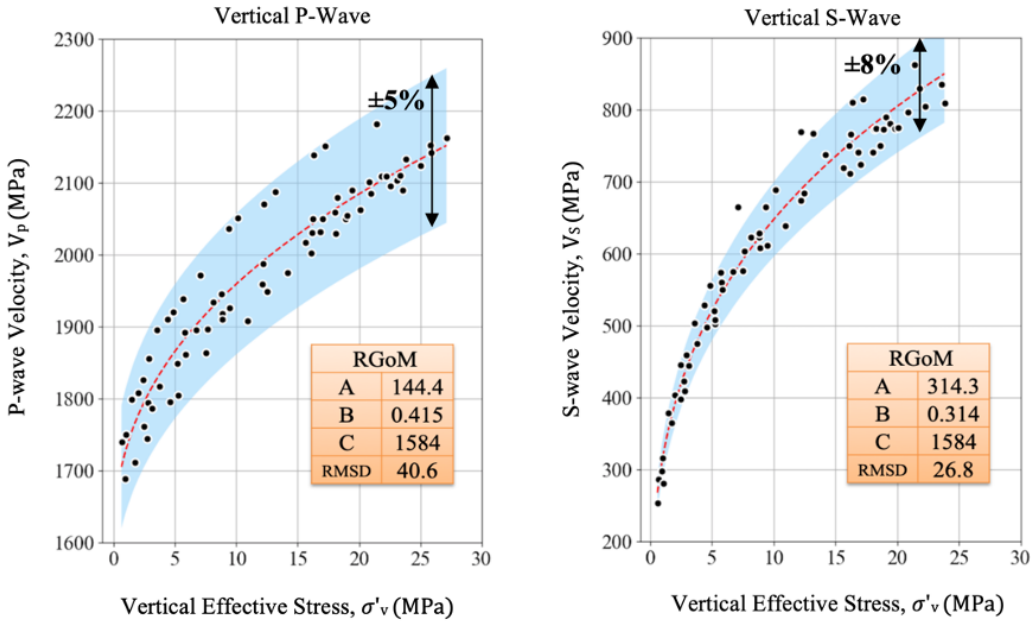

Figure 6.40: TThe data scatter in vertical P and S-wave velocity results as a function of vertical effective stress for RGoM-EI specimens tested in TCRS

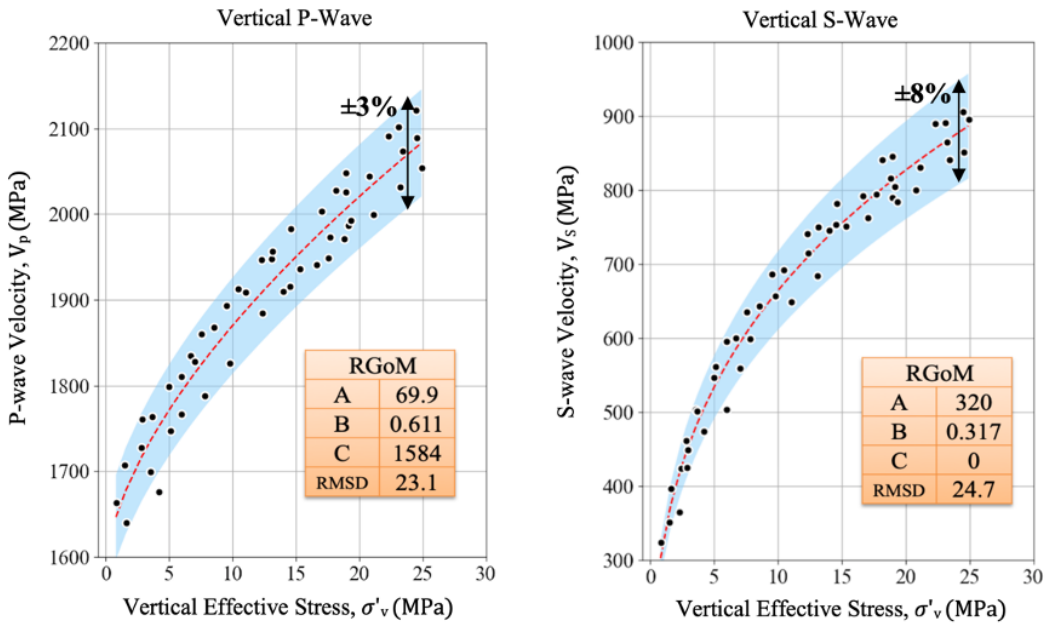

Figure 6.41: The data scatter in vertical P and S-wave velocity results as a function of vertical effective stress for RBBC specimens tested in TCRS

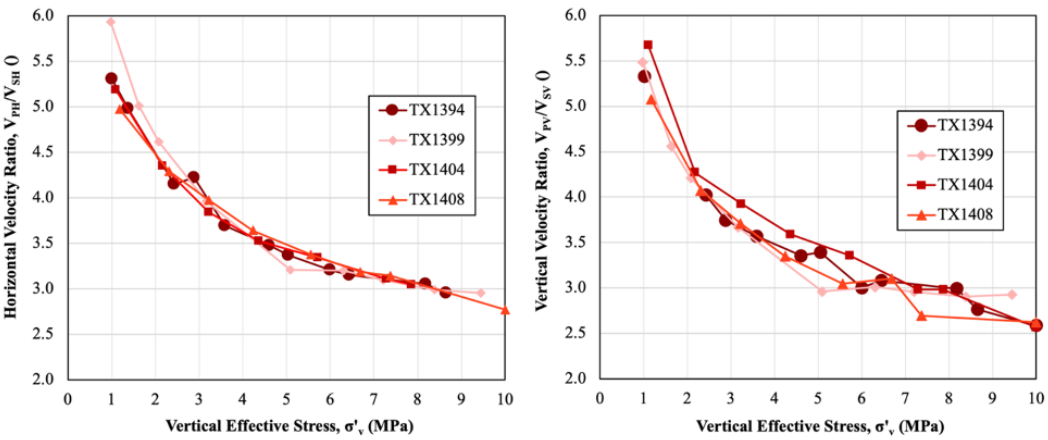

Figure 6.42: Vertical and horizontal velocity ratios as a function of vertical effective stress for RGoM-EI specimens tested in triaxial cell

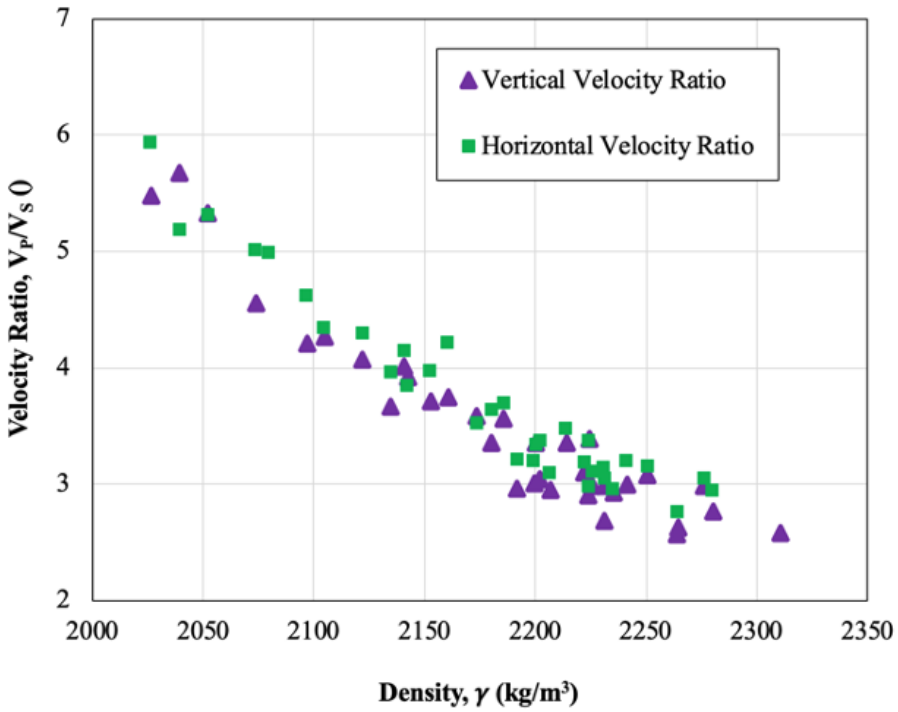

Figure 6.43: Vertical and horizontal velocity ratios as a function of bulk density in sRGoM-EI pecimens tested in triaxial cell

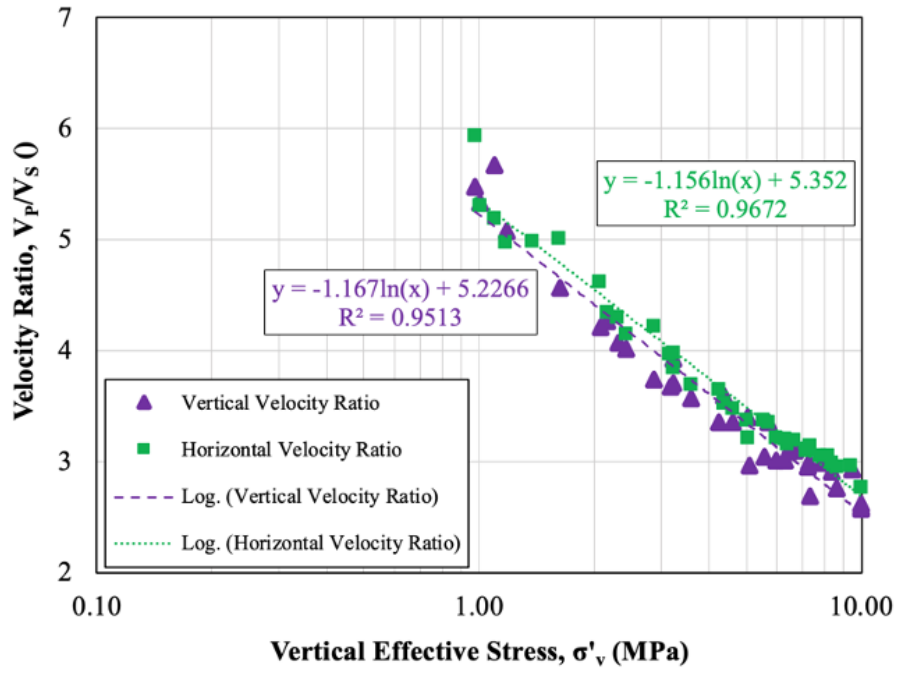

Figure 6.44: Vertical and horizontal velocity ratio comparison in RGoM-EI specimens tested in triaxial cell

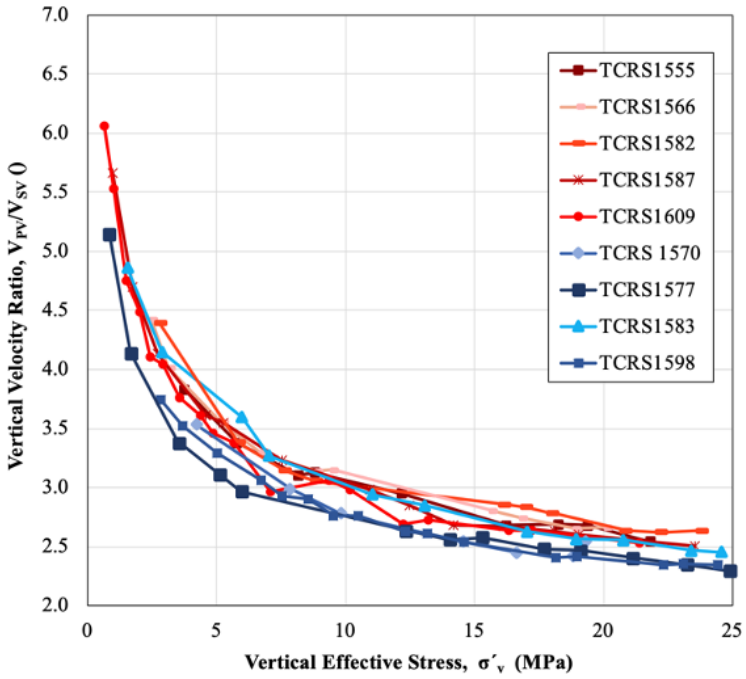

Figure 6.45: Vertical velocity ratios as a function of vertical effective stress for RGoM-EI specimens tested in TCRS

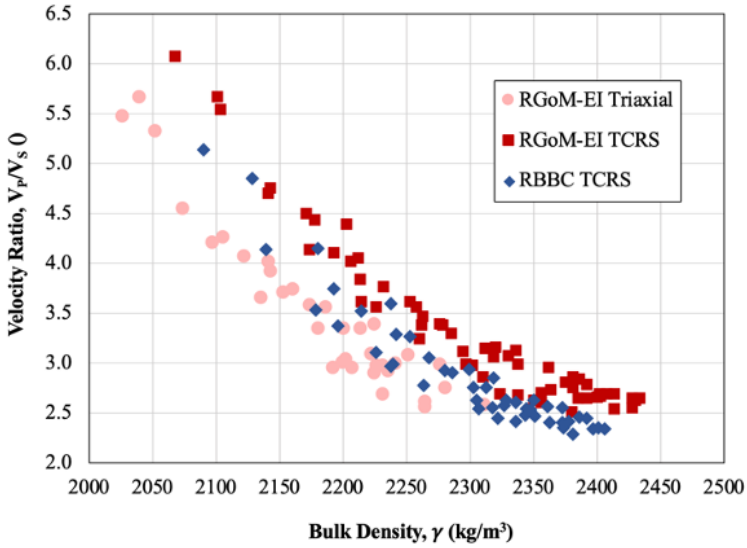

Figure 6.46: Vertical velocity ratio comparison in RGoM-EI and RBBC specimens tested in triaxial cell and TCRS, as a function of bulk density

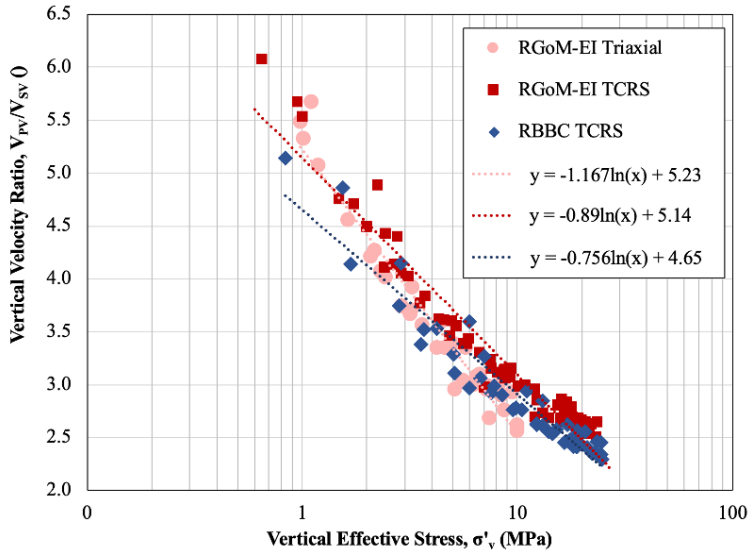

Figure 6.47: Vertical velocity ratio comparison in RGoM-EI and RBBC specimens tested in triaxial cell and TCRS, and the best fit lines

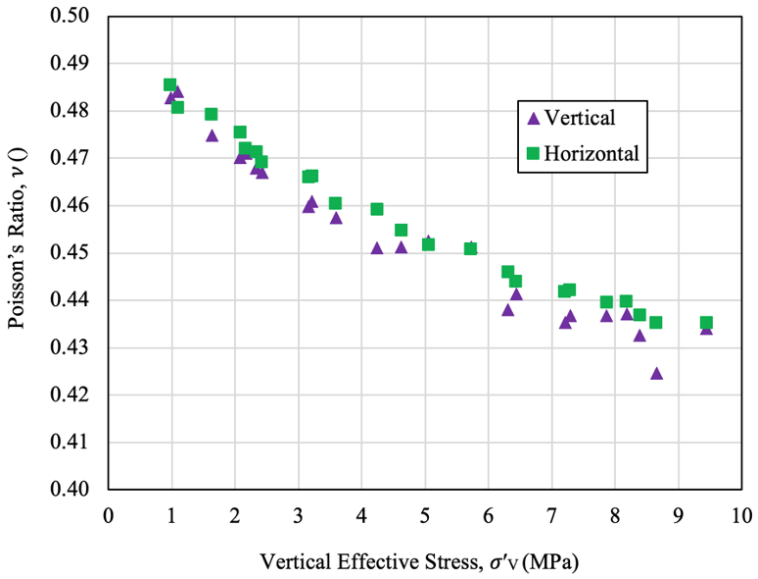

Figure 6.48: Vertical and horizontal Poisson's ratio in RGoM-EI tested in triaxial cell

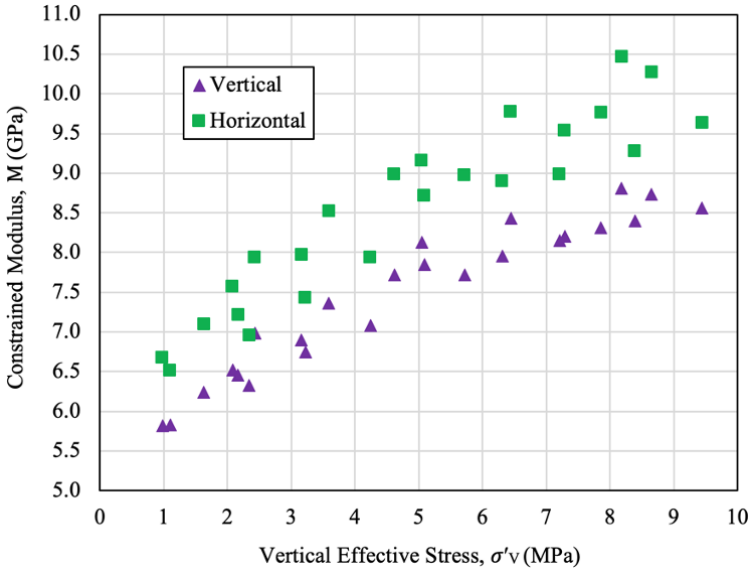

Figure 6.49: Vertical and horizontal constrained moduli in RGoM-EI tested in triaxial cell

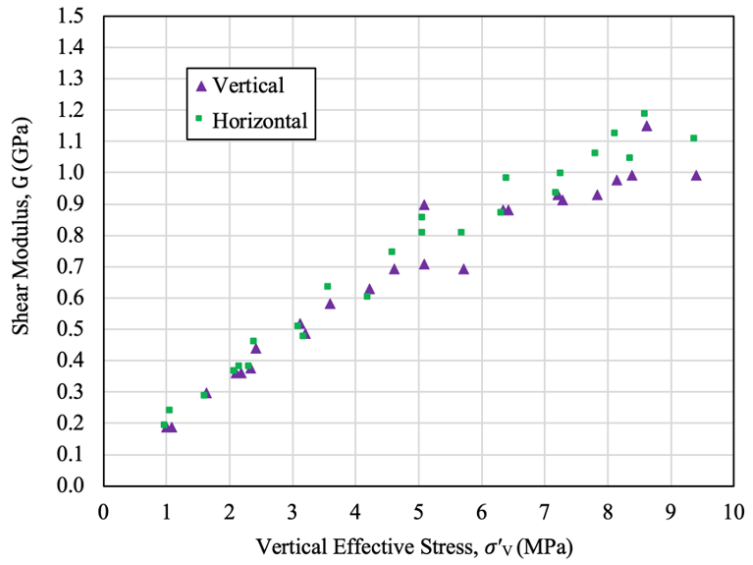

Figure 6.50: Vertical and horizontal shear moduli in RGoM-EI tested in triaxial cell

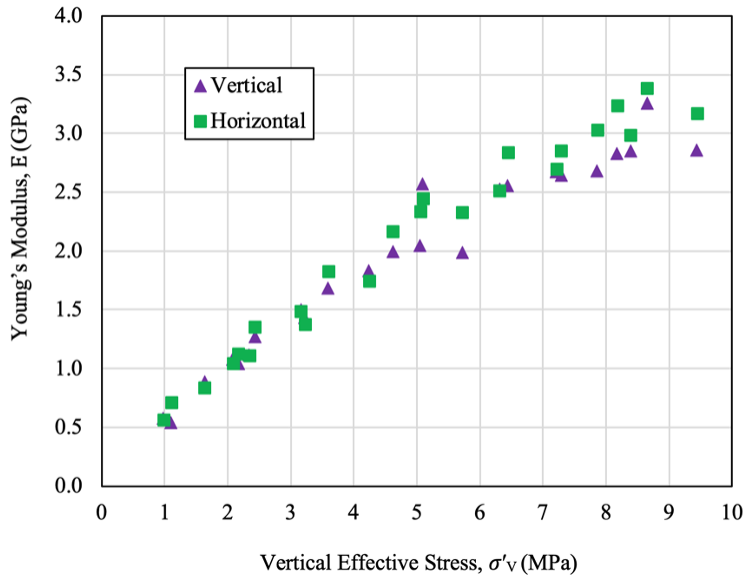

Figure 6.51: Vertical and horizontal Young's moduli in RGoM-EI tested in triaxial cell

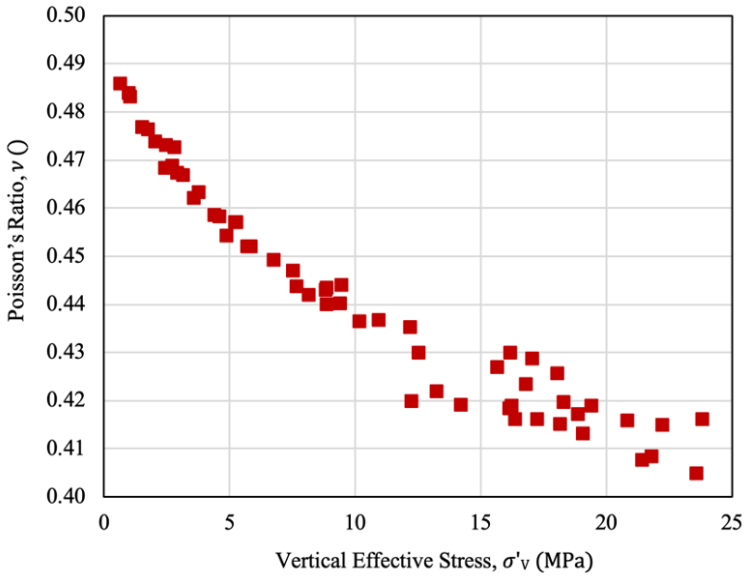

Figure 6.52: Vertical Poisson's ratio in RGoM-EI tested in TCRS

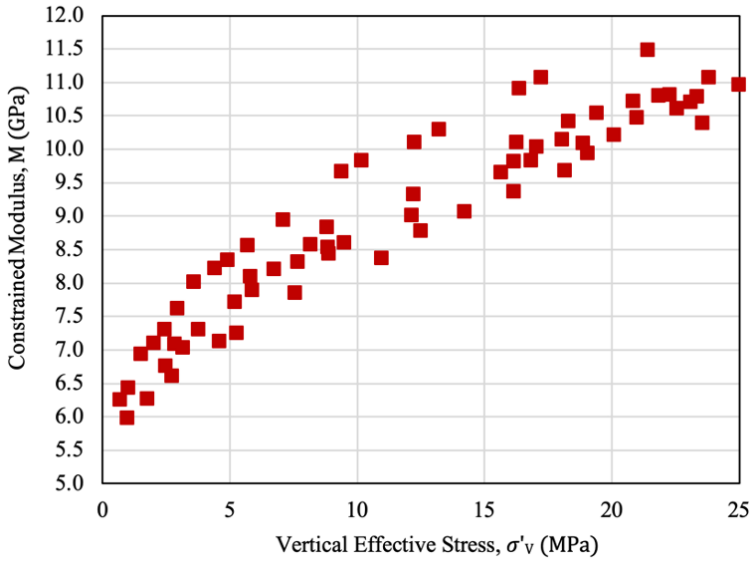

Figure 6.53: Vertical constrained moduli in RGoM-EI tested in TCRS

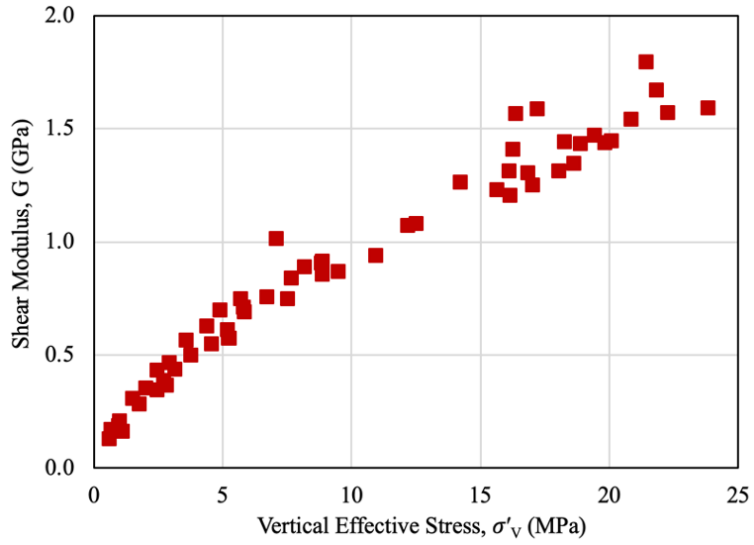

Figure 6.54: Vertical shear moduli in RGoM-EI tested in TCRS

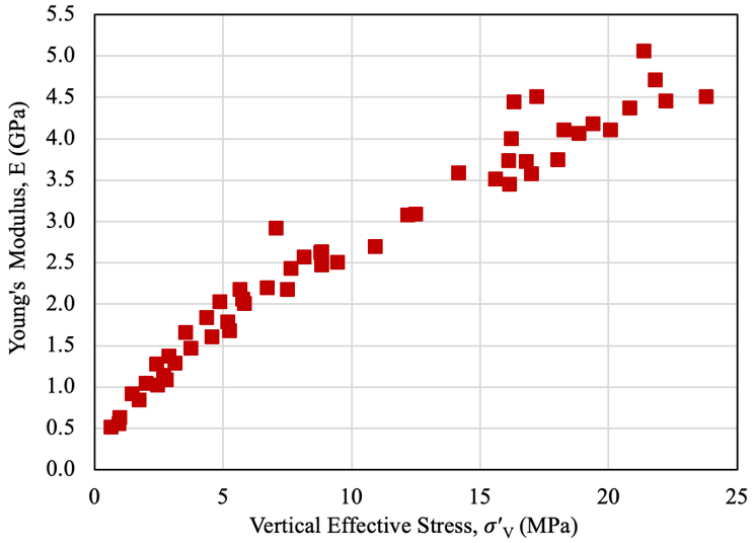

Figure 6.55: Vertical Young's moduli in RGoM-EI tested in TCRS

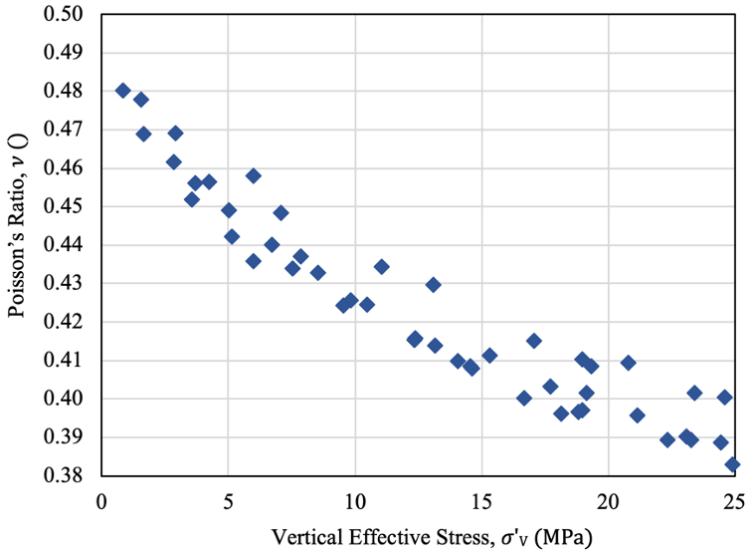

Figure 6.56: Vertical Poisson's ratio in RBBC tested in TCRS

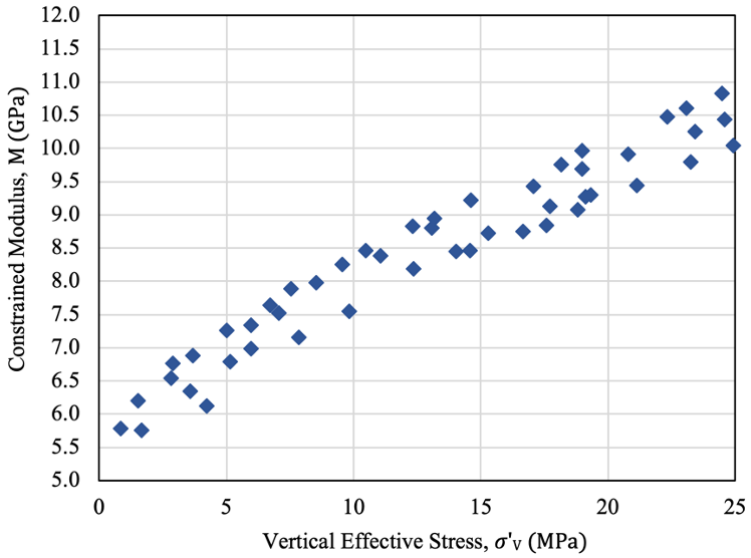

Figure 6.57: Vertical constrained moduli in RBBC tested in TCRS

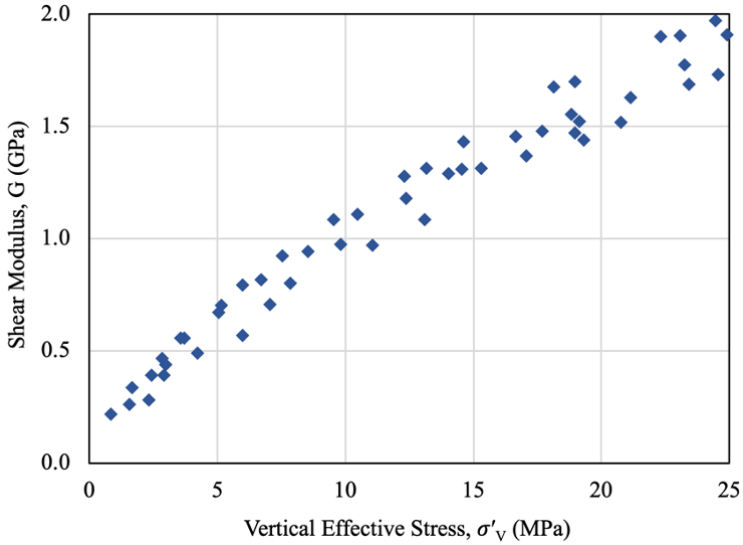

Figure 6.58: Vertical shear moduli in RBBC tested in TCRS

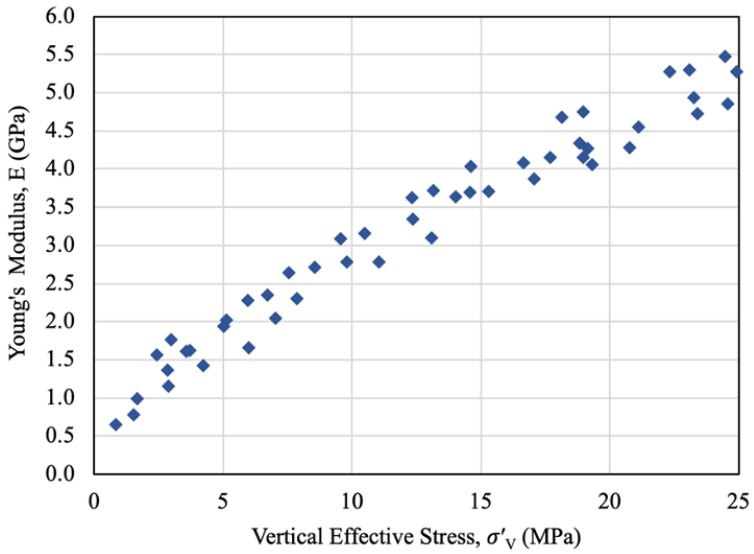

Figure 6.59: Vertical Young's moduli in RBBC tested in TCRS

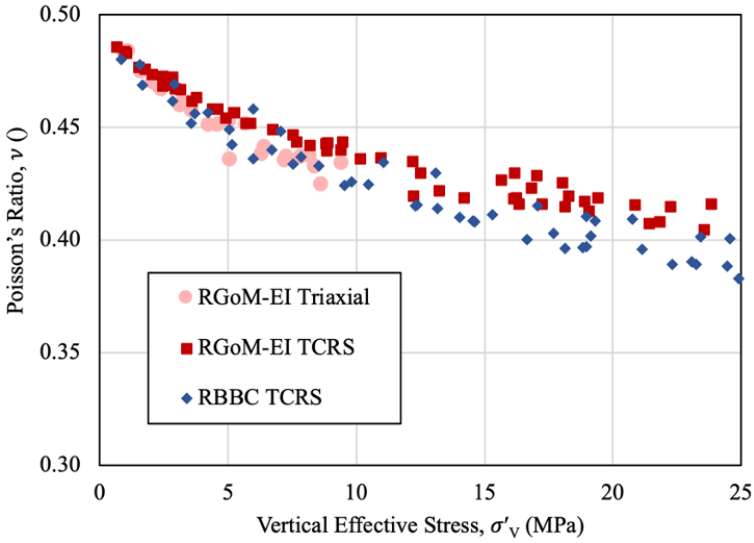

Figure 6.60: Velocity-derived vertical Poisson's ratio in RGoM-EI and RBBC in stress space

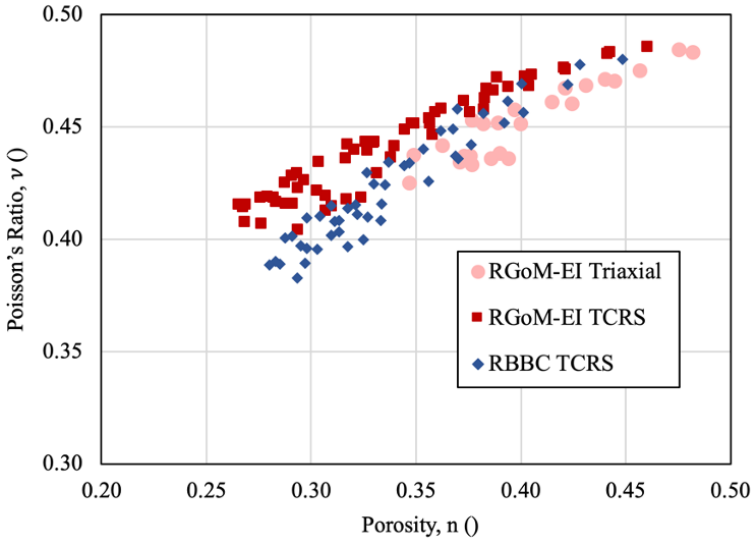

Figure 6.61: Velocity-derived vertical Poisson's ratio in RGoM-EI and RBBC in porosity space

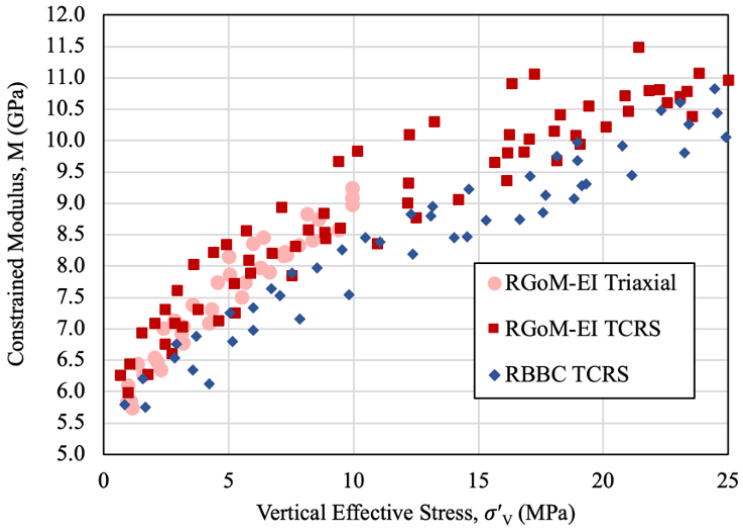

Figure 6.62: Velocity-derived vertical constrained moduli in RGoM-EI and RBBC in stress space

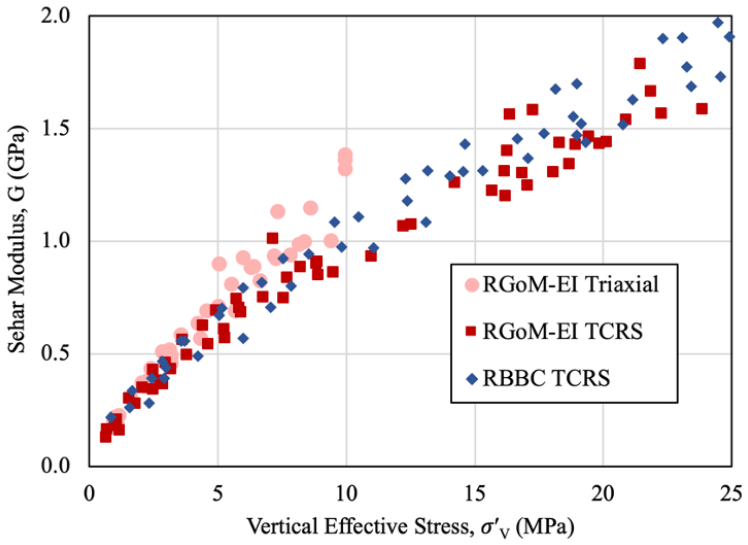

Figure 6.63: Velocity-derived vertical shear moduli in RGoM-EI and RBBC in stress space

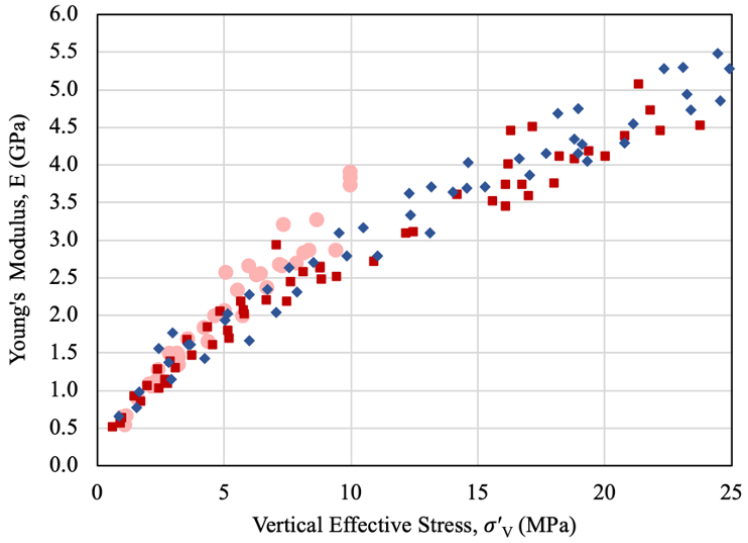

Figure 6.64: Velocity-derived vertical Young's moduli in RGoM-EI and RBBC in stress space

$$\begin{bmatrix} C_{11} & C_{12} & C_{13} & 0 & 0 & 0 \\ C_{21} & C_{22} & C_{23} & 0 & 0 & 0 \\ C_{31} & C_{32} & C_{33} & 0 & 0 & 0 \\ 0 & 0 & 0 & C_{44} & 0 & 0 \\ 0 & 0 & 0 & 0 & C_{55} & 0 \\ 0 & 0 & 0 & 0 & 0 & C_{66} \end{bmatrix}$$

Figure 6.65: Transverse Isotropic material stiffness matrix (C_{ij})

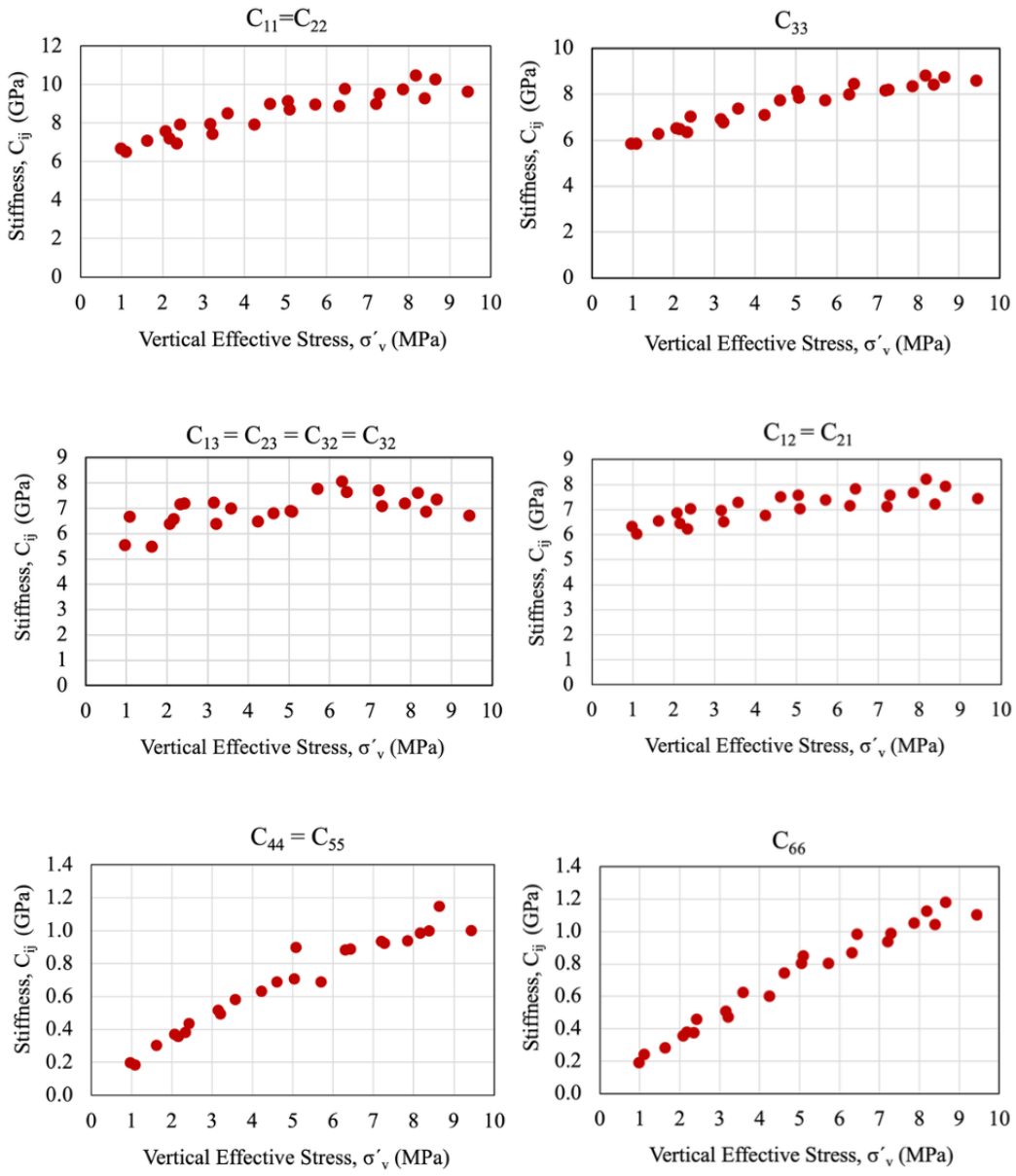

Figure 6.66: RGoM-EI stiffness matrix elements as a function of vertical effective stress

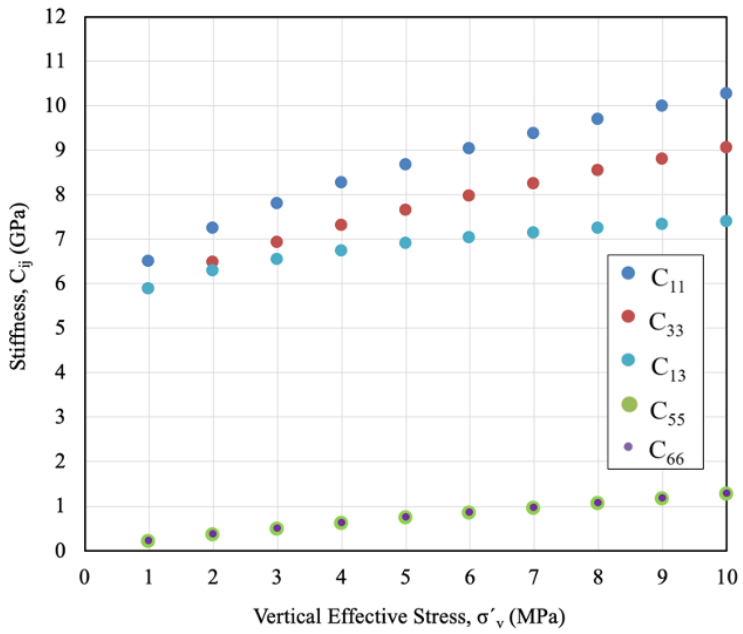

Figure 6.67: RGoM-EI stiffness matrix elements as a function of vertical effective stress

$$\begin{bmatrix} \frac{1}{E_h} & \frac{-\nu_{hh}}{E_h} & \frac{-\nu_{vh}}{E_v} & 0 & 0 & 0 \\ \frac{-\nu_{hh}}{E_h} & \frac{1}{E_h} & \frac{-\nu_{vh}}{E_v} & 0 & 0 & 0 \\ \frac{-\nu_{hv}}{E_h} & \frac{-\nu_{hv}}{E_h} & \frac{1}{E_v} & 0 & 0 & 0 \\ 0 & 0 & 0 & \frac{1}{2G_{vh}} & 0 & 0 \\ 0 & 0 & 0 & 0 & \frac{1}{2G_{vh}} & 0 \\ 0 & 0 & 0 & 0 & 0 & \frac{1}{2G_{hh}} \end{bmatrix}$$

Figure 6.68: Compliance matrix for TI material

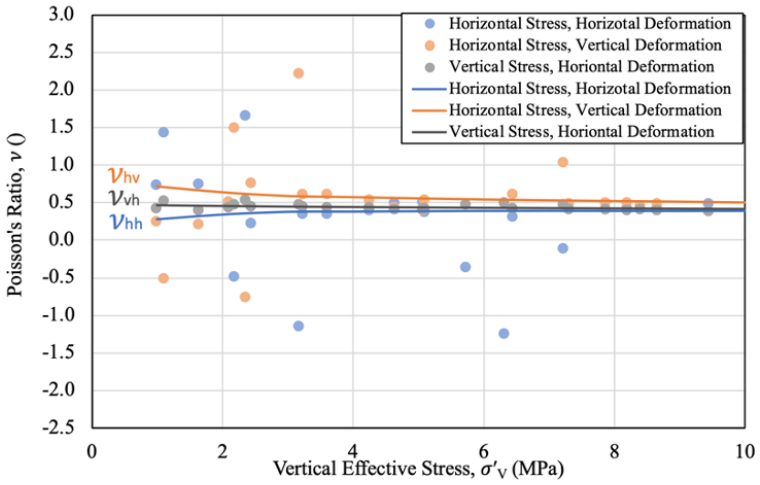

Figure 6.69: Anisotropic Poisson's ratio calculated based on the compliance matrix

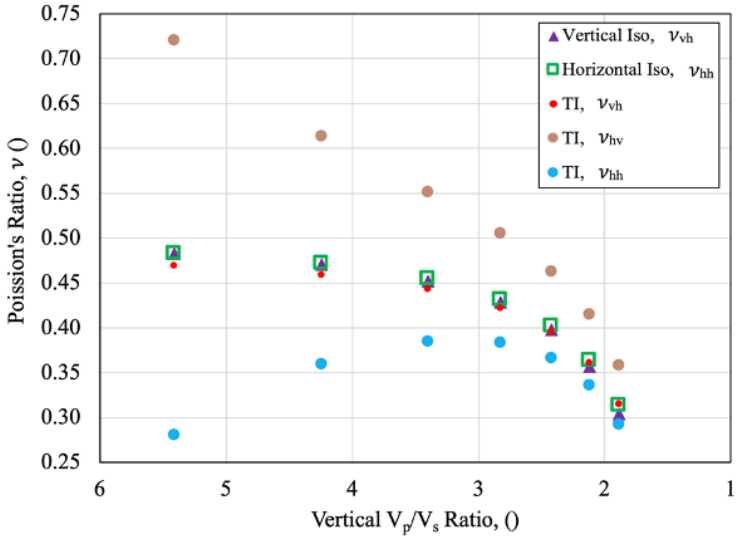

Figure 6.70: Constructed anisotropic (TI) and vertical isotropic Poisson's ratios as a function of velocity ratio (V_p/V_s) at 1 MPa

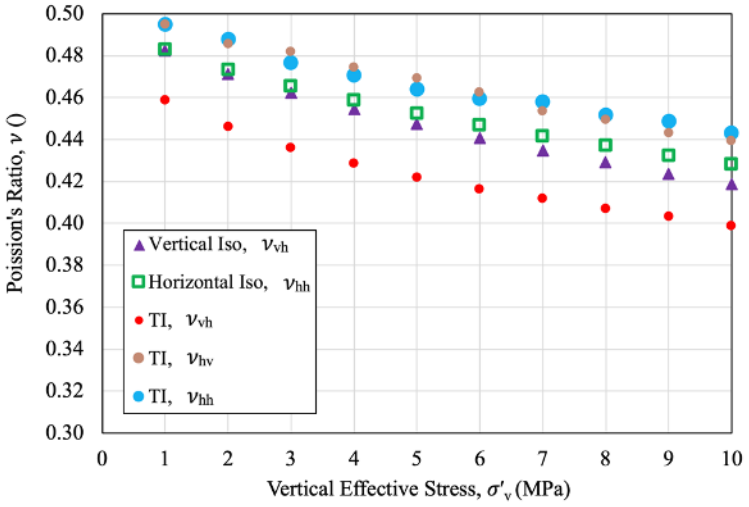

Figure 6.71: Constructed anisotropic (TI) and isotropic Poisson's ratios as a function of vertical effective stress

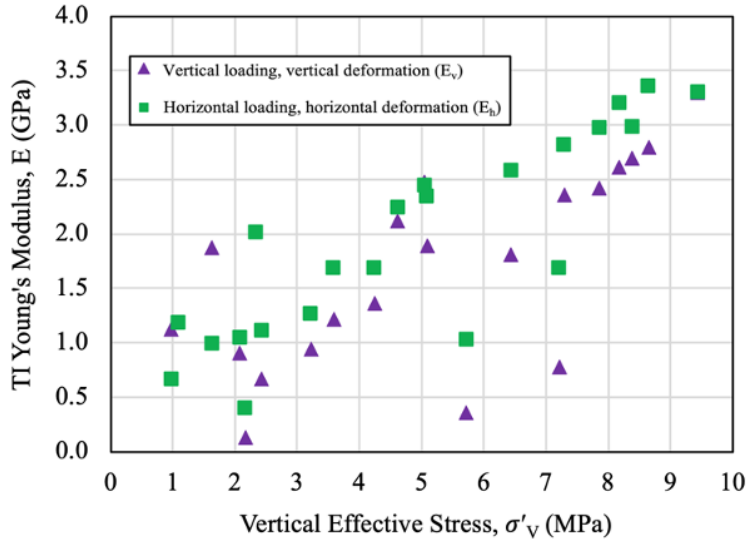

Figure 6.72: Anisotropic Young's modulus calculated based on the compliance matrix

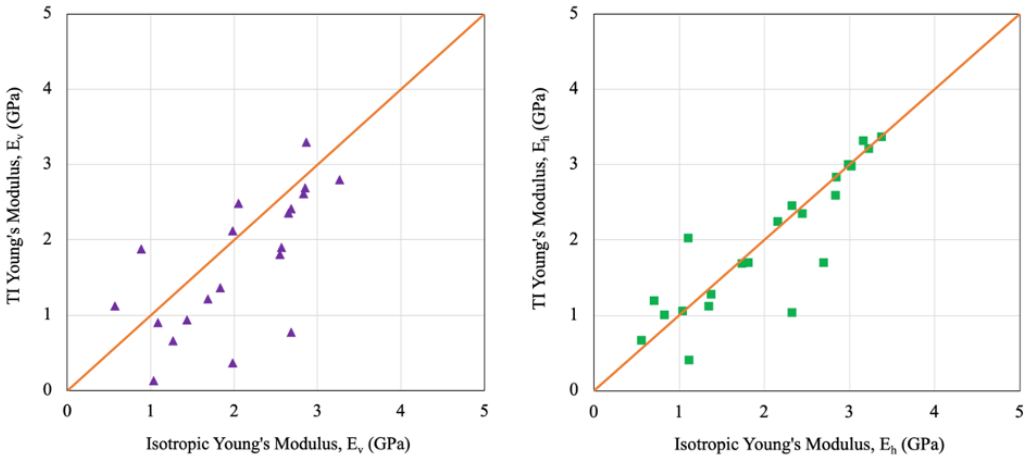

Figure 6.73: TI and isotropic Young's modulus comparison for a) vertical loading and vertical deformation and b) horizontal loading and horizontal deformation

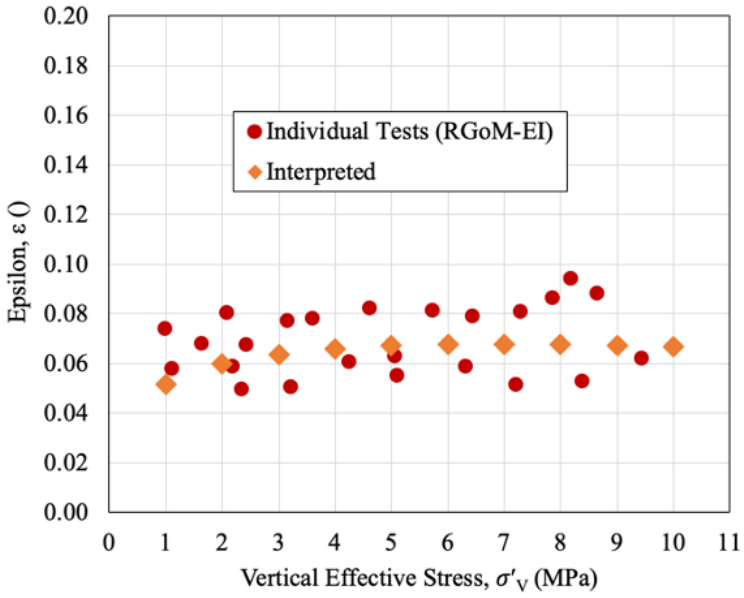

Figure 6.74: Epsilon (ϵ) as a function of vertical effective stress for individual test results (red) and the values determined using the velocities from the power equations

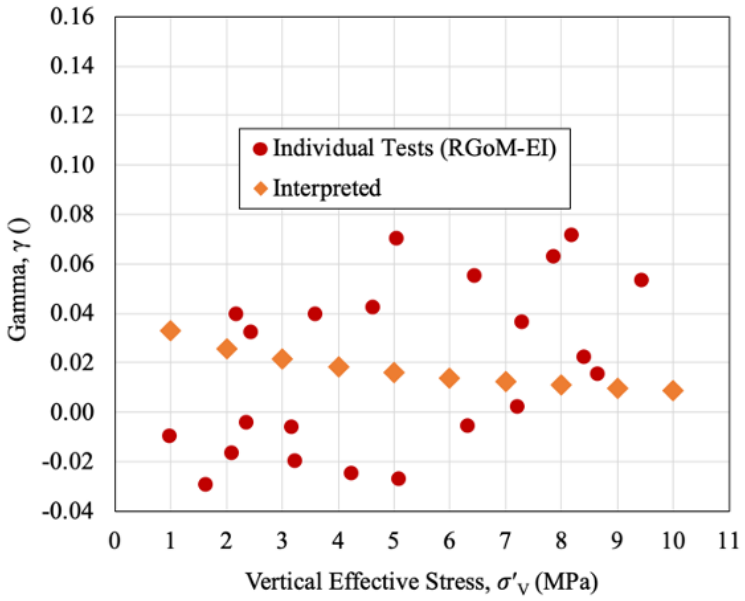

Figure 6.75: Gamma (γ) as a function of vertical effective stress for individual test results (red) and the values determined using the velocities from the power equations

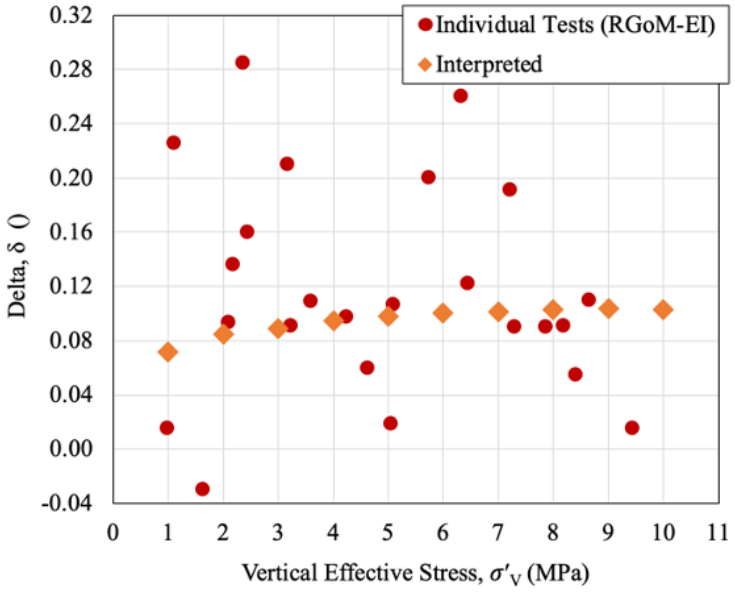

Figure 6.76: Delta (δ) as a function of vertical effective stress for individual test results (red) and the values determined using the velocities from the power equations

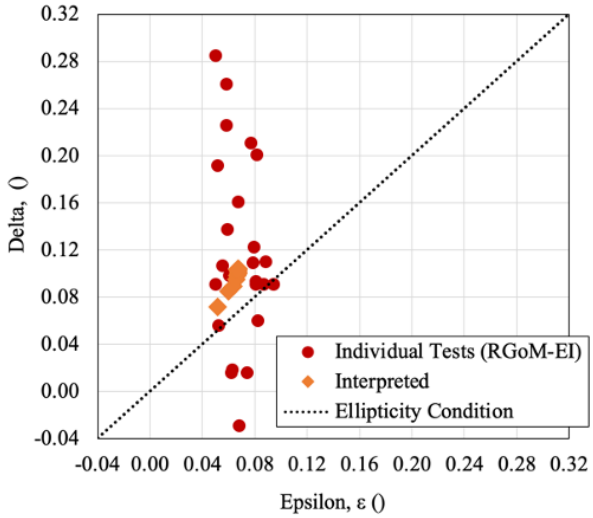

Figure 6.77: Delta and epsilon comparison against the ellipticity condition for both individual test results and interpreted values

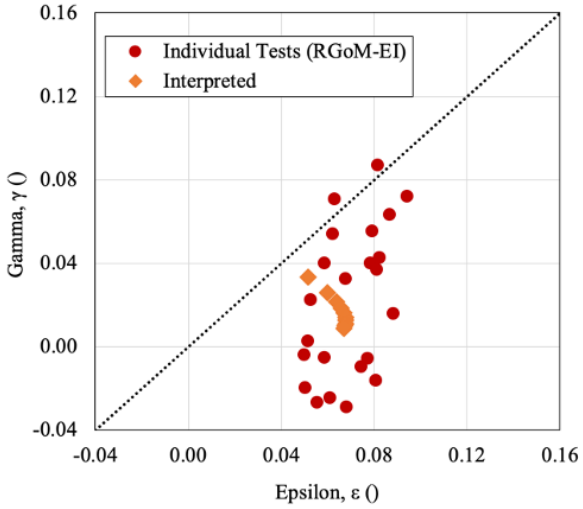

Figure 6.78: Gamma and epsilon comparison against the 45° line for both individual test results and interpreted values

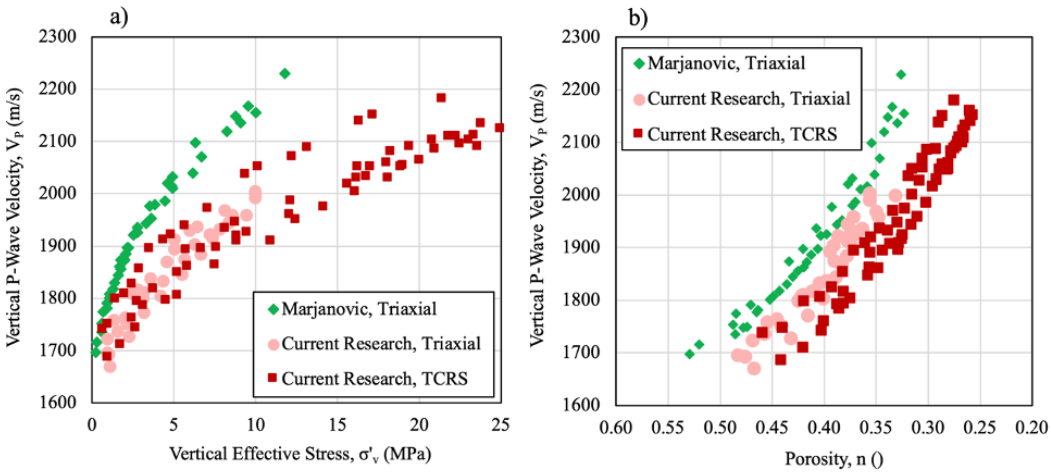

Figure 6.79: RGoM-EI vertical P-wave velocities compared to previous in-house results

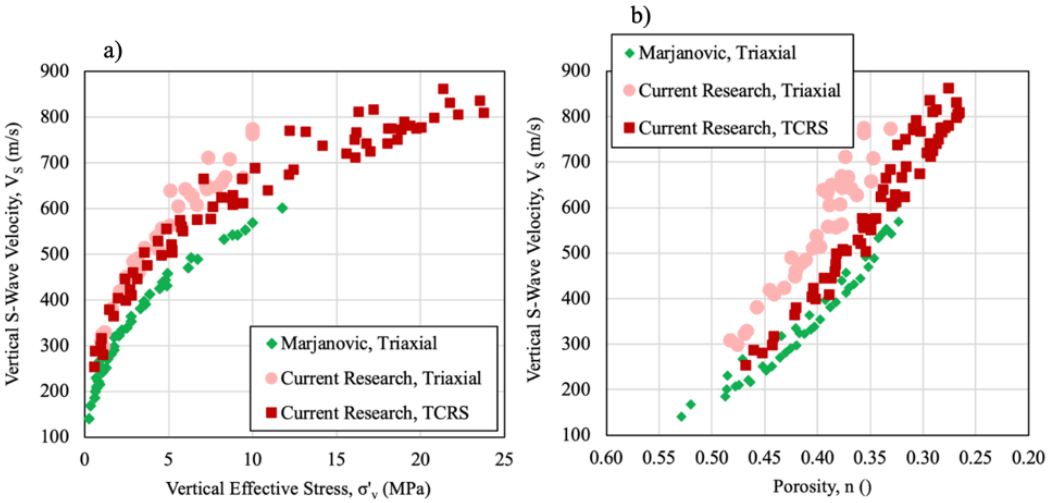

Figure 6.80: RGoM-EI vertical S-wave velocities compared to previous in-house results

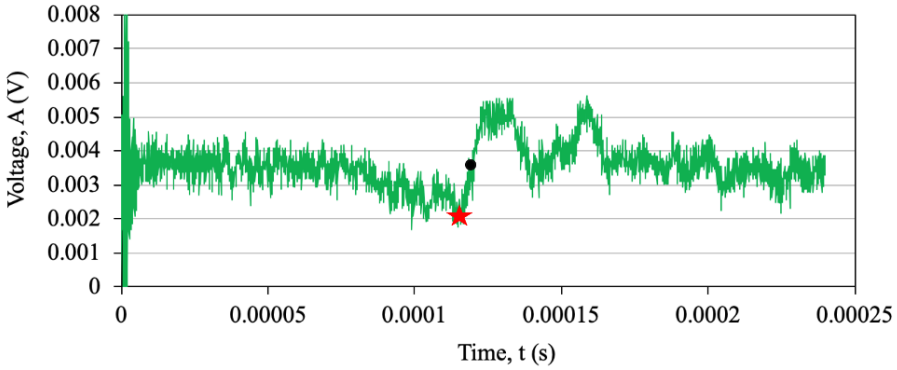

Figure 6.81: Vertical S-waveform at 6 MPa (TX1232), Marjanovic arrival interpretation (black dot) and the author's interpretation

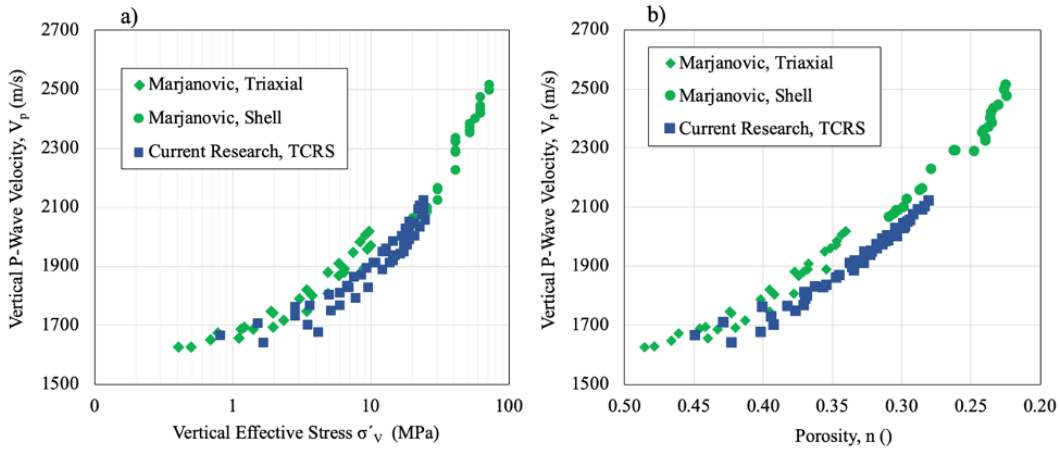

Figure 6.82: RBBC vertical P-wave velocities compared to previous in-house and Shell results

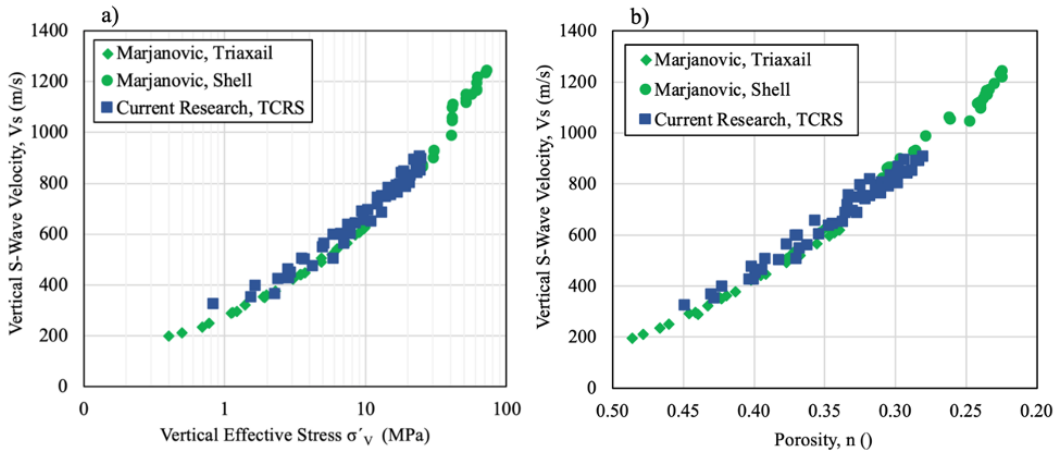

Figure 6.83: RBBC vertical S-wave velocities compared to previous in-house and Shell results

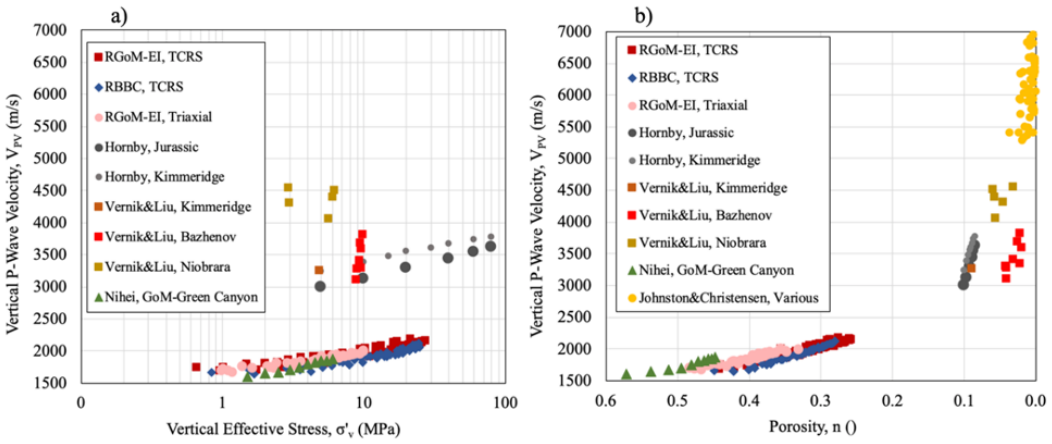

Figure 6.84: Vertical P-wave velocity comparison in vertical effective stress and porosity space

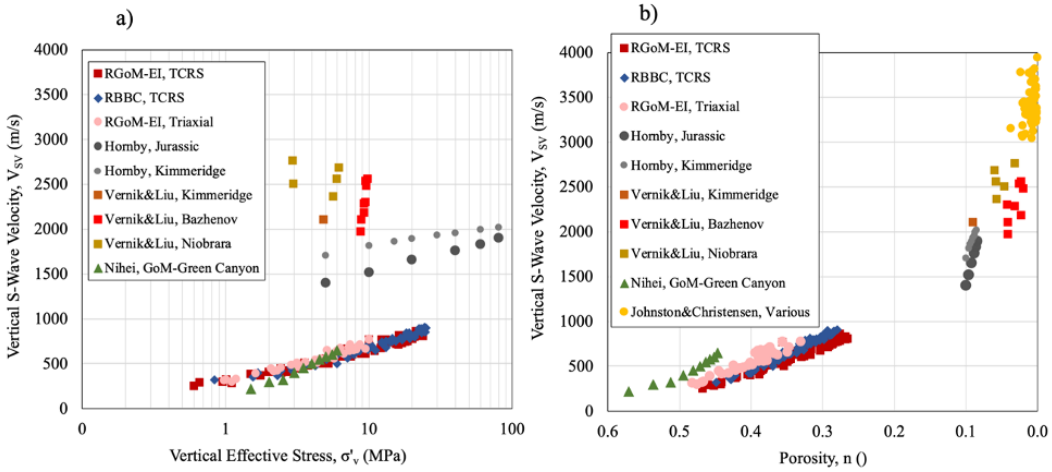

Figure 6.85: Vertical S-wave velocity comparison in vertical effective stress and porosity space

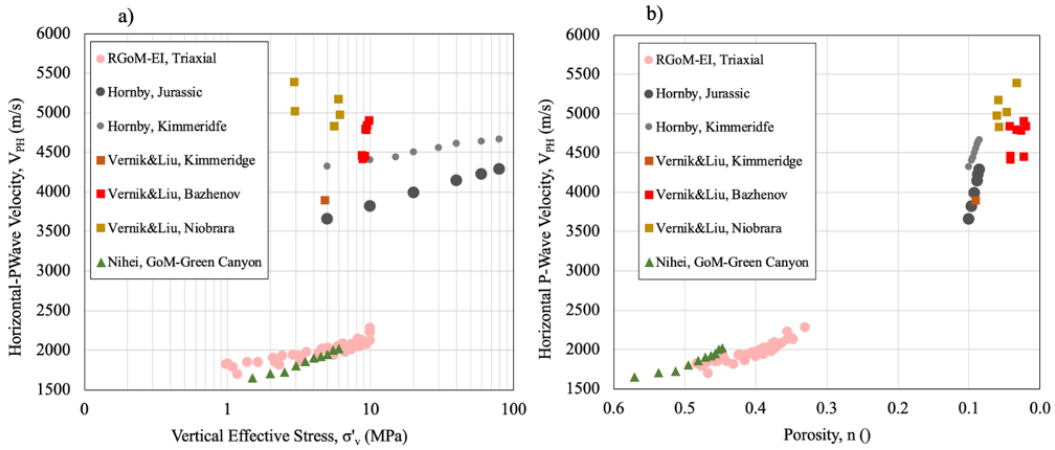

Figure 6.86: Horizontal P-wave velocity comparison in vertical effective stress and porosity space

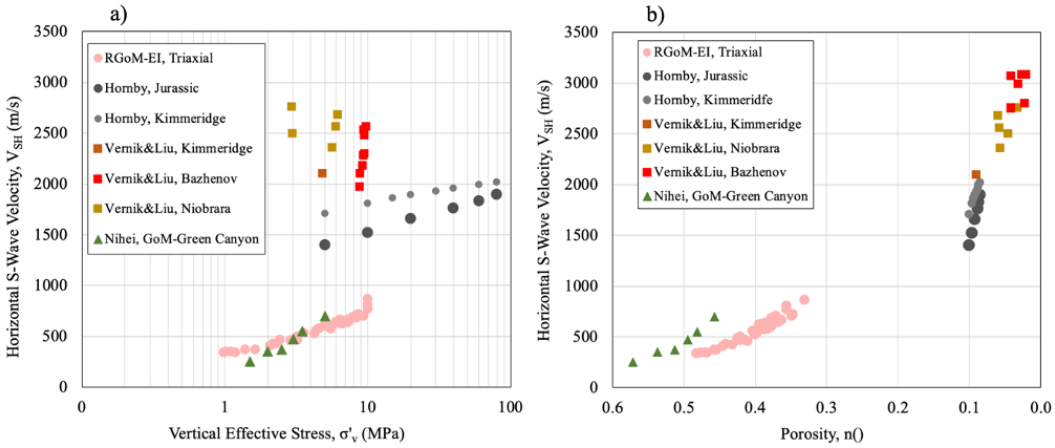

Figure 6.87: Horizontal S-wave velocity comparison in vertical effective stress and porosity space

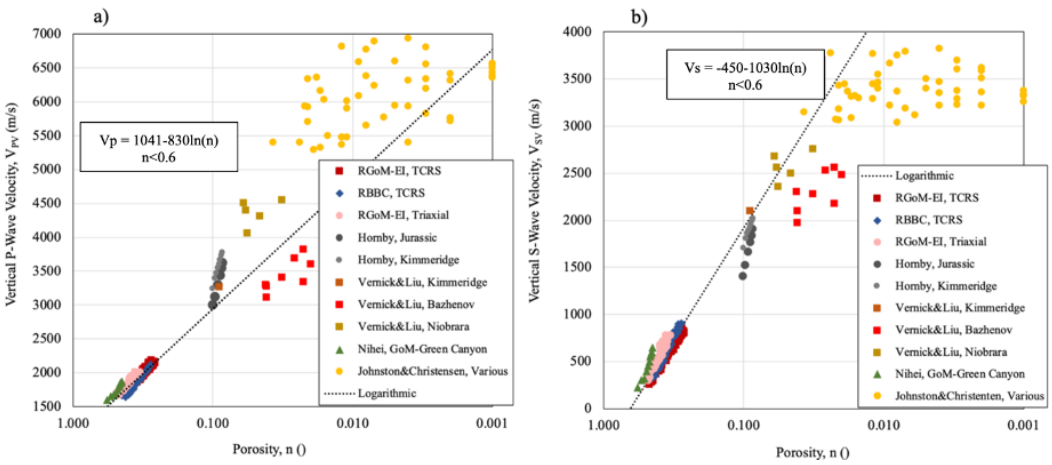

Figure 6.88: Vertical P and S velocities in logarithmic porosity space

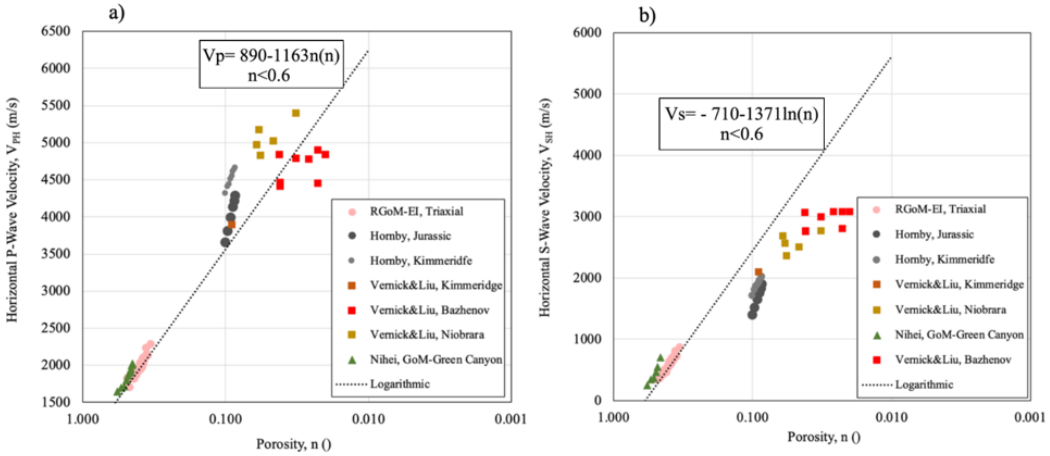

Figure 6.89: Horizontal P and S velocities in logarithmic porosity space

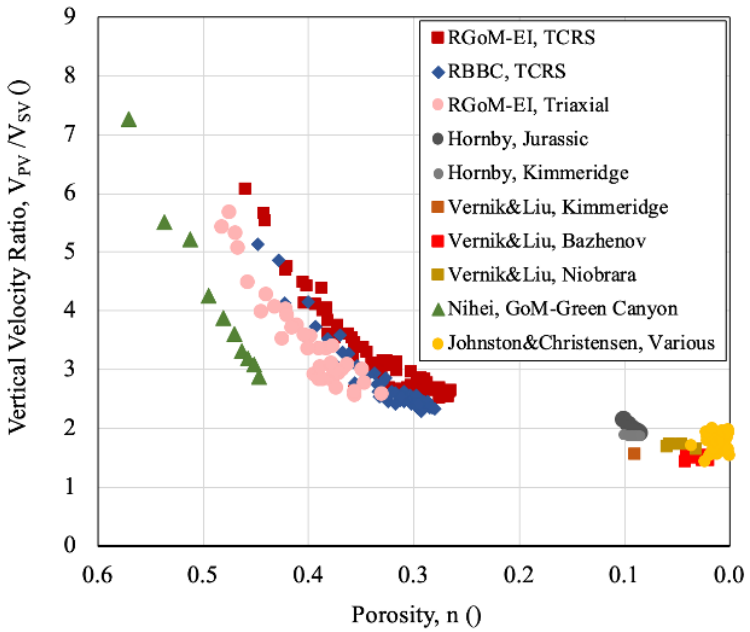

Figure 6.90: Current study vs published data vertical velocity ratio comparison

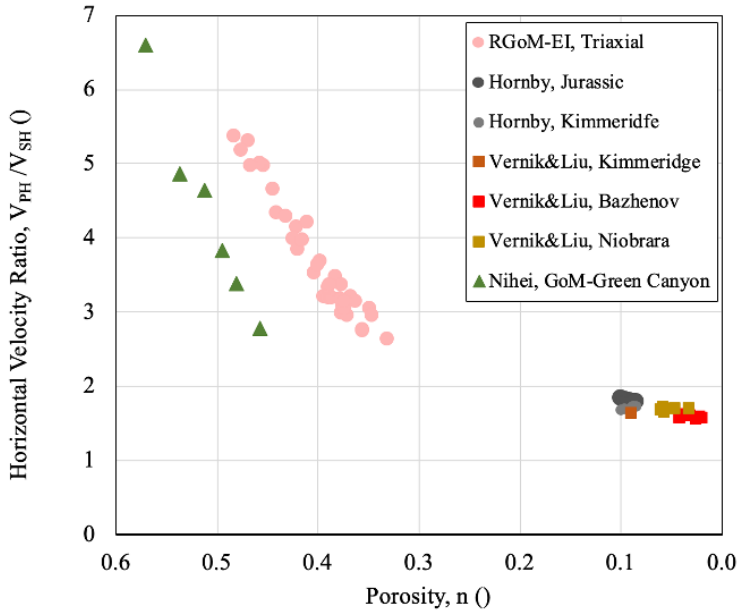

Figure 6.91: Current study vs published data horizontal velocity ratio comparison

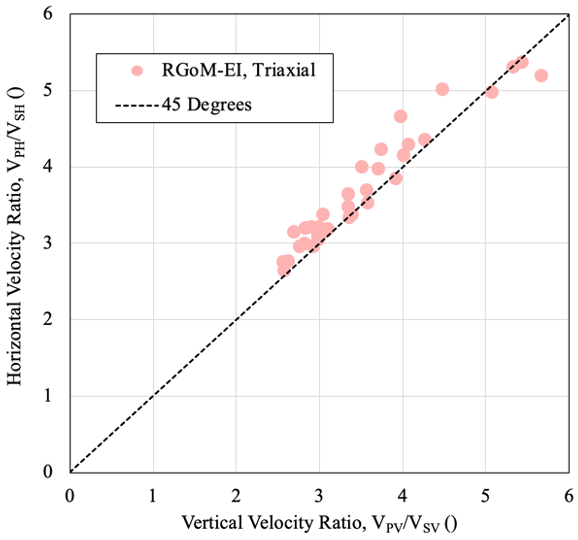

Figure 6.92: Vertical and horizontal velocity ratios comparison

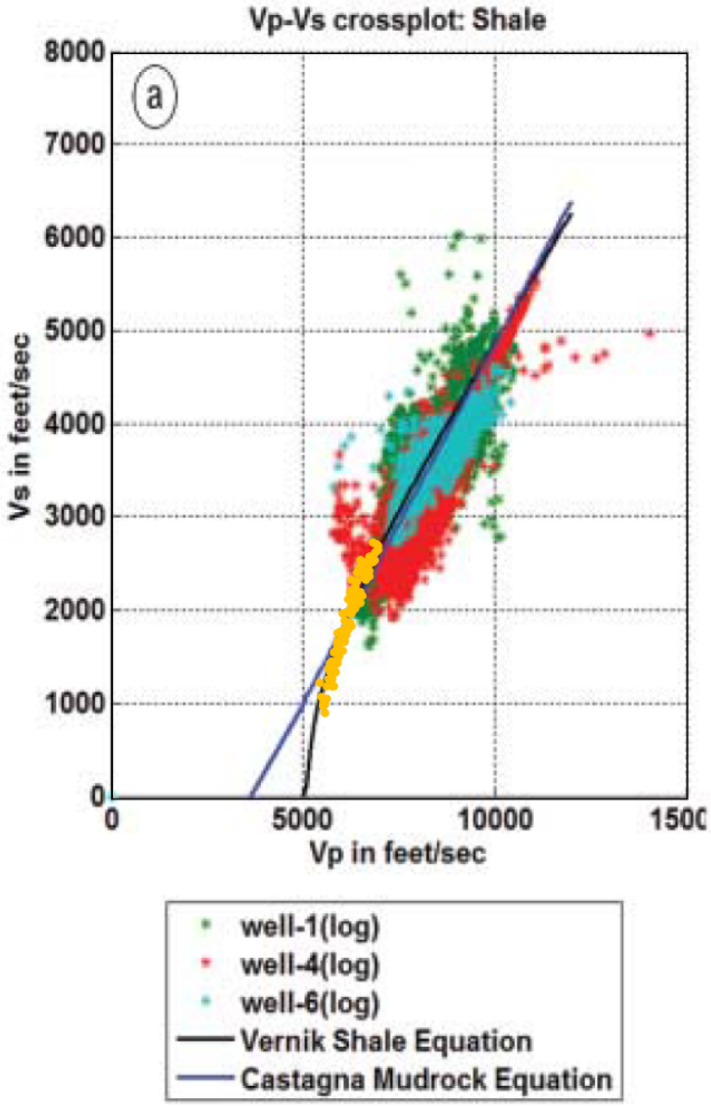

Figure 6.93: Vertical P and S-wave velocities in RGoM-EI compared to Vernik et al. [166] shale equation Greenberg and Castagna [54] mudrock equation

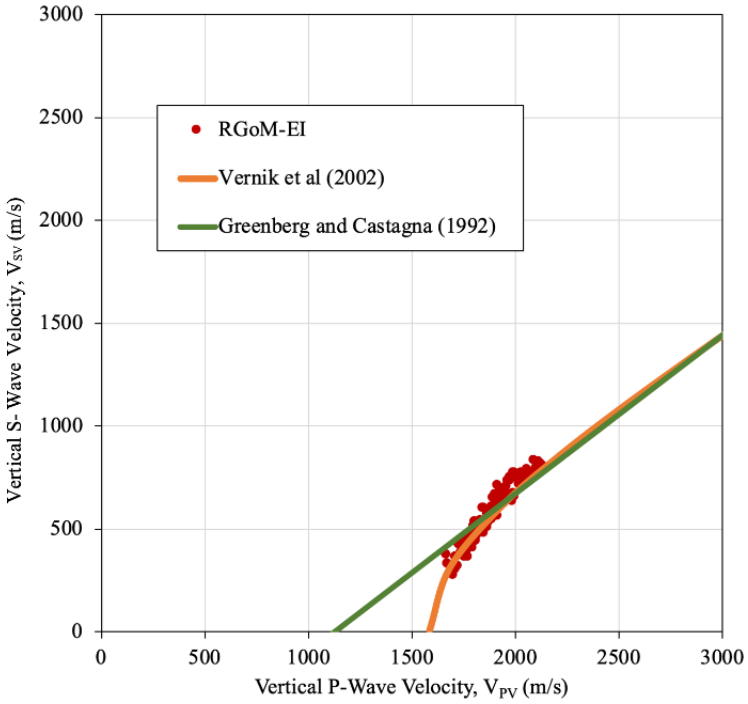

Figure 6.94: Vertical P and S-wave velocities compared to log data [37], Vernik et al. [166] shale equation and Greenberg and Castagna [54] mudrock equation

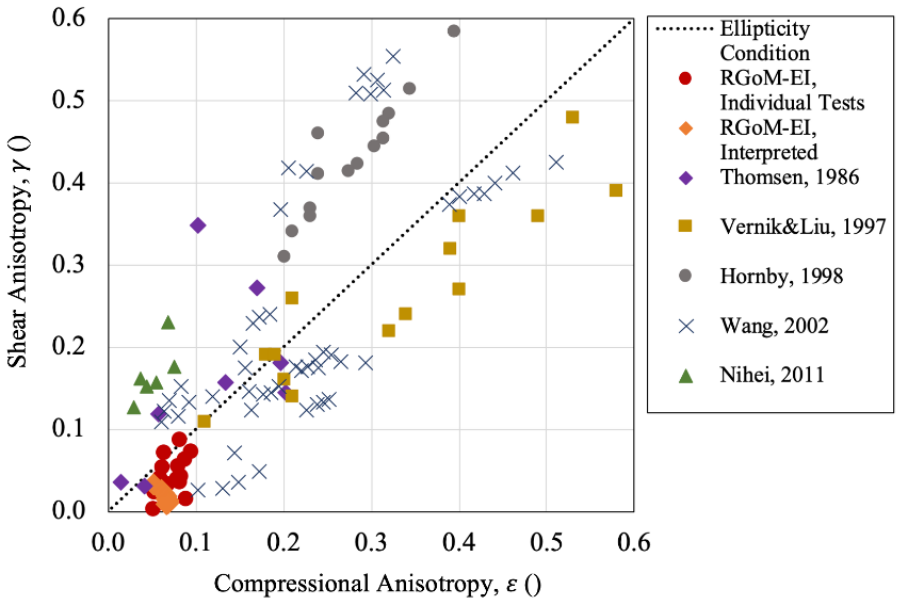

Figure 6.95: RGoM-EI, P-wave and S-wave anisotropy parameters (ϵ & γ) compared to the published data on various shales

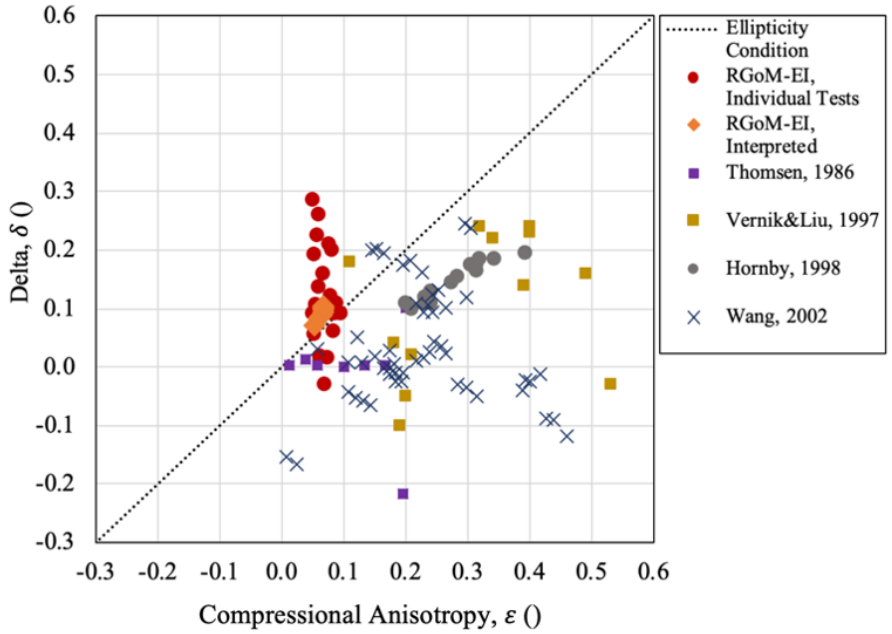

Figure 6.96: RGoM-EI, ϵ & δ anisotropy parameters compared to the published data on various shales

Chapter 7

Conclusions and Recommendations

7.1 Overview

Compressional and shear wave velocity measurement is a powerful tool to study material behavior. Wave velocity through soil is a function of elastic stiffness, and the elastic stiffness changes with soil type, soil structure and sedimentation, direction, porosity, stress level, saturation status, lithology, etc.

Clay can be found in the first 5 km of the Earth's crust, which corresponds up to approximately 50 MPa vertical effective stress. Furthermore, mudrocks, which are primarily composed of clay-sized particles, are the most abundant type of sedimentary rock. The geotechnical field has mostly tested soft clays ($n > 0.45$) in low stress ($\sigma_v{}' < 1$ MPa) regime, while the geophysics field has studied low porosity ($n < 0.25$) under high stresses (10 MPa $< \sigma_v{}'$). This research focuses on the high porosity clay, transitioning into low porosity mudrocks, under pressure. Two types of tests were performed: TCRS and triaxial. The triaxial tests were performed on RGoM-EI material starting at high porosity ($n \approx 0.5$) and low stress ($\sigma_v{}'$=0.8 MPa) and going down to low porosity ($n \approx 0.32$) as K_0-consolidated to 10 MPa. The compressional and shear velocities were measured in three directions (vertical, horizontal and inclined) throughout the test, using a newly developed piezoelectric technology. The main goal of the triaxial testing was to study anisotropy in a TI material and evaluate the increase of material stiffness with K_0-consolidation. The TCRS tests were performed on both RGoM-EI and RBBC specimens. The vertical effective stress increased from 1 MPa to 25 MPa under constant rate of strain compression, resulting in porosities decreasing by nearly 0.23 (~ 0.49 to ~ 0.26). The piezoelectric technology was adapted for the TCRS setup in order to increase the vertical effective stress span by 2.5 times and measure the vertical velocities in this stress range.

The results from both testing setups are applicable to both geotechnical engineering practice (foundation, tunnel, excavation and earth support system design) and material characteristics used in the oil industry (exploration and drilling). This research helps answer some of the important questions about seismic behavior of clays.

7.2 Key Findings and Developments

A significant portion of time and energy spent on this research was dedicated to developing the testing technology. The triaxial piezoelectric setup developed by Marjanovic was only capable of measuring vertical velocities. The author of this research designed and fabricated the side actuators that are capable of measuring V_p and V_s in horizontal direction. Also combined with the existing vertical caps, the horizontal setup allow for inclined velocity measurement. P-wave velocities were measured in vertical, horizontal and inclined directions, while S-wave velocities were measured vertically and horizontally. Another significant distinction of this testing setup is in that the specimens deform vertically, up to 25%. This is important because previously, most directional velocity measurements were limited to rocks with minimal deformations. Considering the stress level limit in the medium stress triaxial equipment (10 MPa in cell pressure), the TCRS equipment was a great innovation that would allow for the existing piezoelectric caps to be used at higher stress level. The setup was a modification of traditional CRS apparatus using a tall (8 cm) stainless-steel ring, that prevents lateral deformation, and two top caps, hosing P and S actuators, similar to the ones used in the triaxial setup. This setup increases the vertical effective stress limit by 2.5 times without adding an elaborate or expensive equipment. The top and bottom caps in the TCRS setup are directly connected to the circuit box (input) and the oscilloscope (output) eliminating a considerable portion of the noise and interference in the signals. Furthermore, although not included in this thesis, vertical velocities were successfully measured in TCRS specimens under vertical effective stresses as high as 50 MPa, emphasizing that the

technology is sufficient to expand the testing stresses even further than 25 MPa.

All the tests were run under K_0-consolidation (vertically consolidated while the lateral strain was kept at zero) and the compression curves were compared to the curves from other researchers that tested the same materials. The compression curves obtained from the triaxial tests on RGoM-EI agree well with Casey's results but have higher porosities than Marjanovic's. RGoM-EI material tested using the TCRS setup in this study has a similar compression curve to the GeoFluids recommended curve, but has higher porosities and stiffnesses compared to Horan, Nordquist and Parry's results. The RBBC compression curves obtained in this research, except for one outlier test (TCRS1570) are in agreement with the GeoFluids recommended curve, as well as Horan and Nordquist. The most important conclusion to be drawn from K_0-consolidation tests run by 7 researchers shows that the variation in initial void ratio is the factor dictating the exact location of the curve, however it does not affect the slope of it. The compression curves comparison proves that the novel TCRS testing setup is an appropriate alternative to traditional CRS testing to test taller specimens, however, further investigation into the wall friction calculations could improve the accuracy of the results.

Signal and arrival time interpretations is one of the most important factors affecting the velocity measurements. The quality of the waveforms and the clarity of the arrival time can depend on stress level, propagation direction, testing setup and material. It is shown that both signal types have much clearer arrival times at higher stress levels, however S-waves acquired by piezoelectric elements are particularly hard to process at stress levels lower than 2 MPa. This is mostly due to the lack of coupling between the piezoelectric elements and the clay specimen. The horizontal waveforms at the same stress level have sharper and stronger (higher amplitude) first peak arrivals. However, the initial high amplitude interference signal poses a bigger problem in horizontal and inclined directions, where the output signal is so close to this signal that the arrival time is much harder to pick. This issue is the main factor affecting the accuracy of the inclined velocity measurements. With regards to the testing setup, it was shown that the TCRS setup delivers better quality

signals compared to the triaxial setup, mainly due to the connection configuration. In the triaxial setup, the wires run through the cell base, causing the initial high amplitude interference in the P-wave and considerably more noise in the S-waves, both of which are alleviated by the direct connections (cap to circuit and cap to oscilloscope) in the TCRS setup. Lastly, both RGoM-EI and RBBC have similar P-waveforms, however, RBBC has a significantly higher frequency and amplitude and a sharper arrival. While some of the aspects causing lower quality waveforms, like the triaxial connection configuration or the EMI caused by other electronic in the lab, are inevitable for now, signal processing tools, other than the boxcar used in this research, could be deployed to further improve the interpretation process.

The velocity measurements were analyzed for repeatability. Power equations were fitted through the velocities as a function of vertical effective stress, the upper and lower bounds were stablished and the RMSD values were calculated. The maximum scatter from the power equation was ±5% for P-wave velocities and ±8% for S-wave velocities. Despite the uncertainties associated with the arrival time picks, these numbers suggest high quality velocity testing in both triaxial and TCRS setups.

The triaxial tests provide P-wave velocities in vertical, inclined and horizontal directions and the S-wave velocities in the vertical and horizontal directions, under 1-10 MPa vertical effective stress. The triaxial P-wave velocities in all three directions are increasing by nearly 300 m/s (+17%) throughout this stress span while the porosities are decreasing by almost 0.25. The triaxial S-wave velocities in vertical and horizontal velocities both increase by 350 m/s (+250%). The RGoM-EI TCRS results show a 450 m/s (+26%) increase in the P-wave velocity and 550 m/s (+283%) increase in the S-wave velocities, over a 1-25 MPa vertical effective stress and 0.47-26 porosity range. Similarly, the RBBC TCRS results show a 450 m/s (+27%) increase in the P-wave velocity and 600 m/s (+300%) increase in the S-wave velocities, over a 1-25 MPa vertical effective stress and 0.45-0.28 porosity range. The vast difference between how P and S wave velocities react to a stress increase can be explained by the effect of pore water. Since P-waves do travel through fluid, the P-wave velocity represents both the stiffness effect of the soil structure and the pore fluid. S-waves

on the other hand do not propagate through fluids, which is why the S-wave velocity is only affected by the soil structure stiffness. Since the first 1584 m/s of the P-wave velocity is solely due to P-wave propagation through salt-water, the increase in the P-wave velocity due to the stress increase is small compared to the increase in S-wave velocity.

Testing resedimented specimens from known materials (RGoM-EI and RBBC) in both triaxial and TCRS equipment granted the opportunity to compare the recent data to the previous in-house data [103] and compare the two setups to one another. Comparing the P-wave velocities measured for this research in porosity space, triaxial and TCRS results are in general agreement, however the triaxial results are slightly higher. Compared to Marjanovic's RGoM-EI data, the triaxial P-wave velocities acquired by the author are slightly lower and S-wave velocities are much higher. Comparing the RBBC velocities from the author to the results from Marjanovic obtained using the in-house and Shell technology, both P and S wave velocities are in agreement. The most significant reason behind the variations in velocity trends is the effect of void ratio measurement errors. Even the smallest variation in the measured void ratio, whether it is caused by an error in the dry mass, specimen dimensions or an internal leak, can distort the velocity interpretations. Moreover, individual discrepancies in testing process and signal interpretation is an important factor.

The repeatability analysis also establishes that for specimen within a certain range of porosity (0.25-0.6) the power equation format is an appropriate regression to represent the velocity data over an extended vertical effective stress range (1-25 MPa). However, over a broader span of porosity (0-0.6) there is no particular correlation between velocities and vertical effective stress. Four equations were fitted through all the velocity measurements from this research as a function of porosity in logarithmic scale. The logarithmic equations corelating P-wave velocities to porosities give a reasonable first order estimate of the P-wave velocities for a variety of materials with porosities lower than 0.6. The S-wave velocity equations however appear to overestimate the shear wave velocities at lower porosities ($n < 0.1$), when

compared to rock results from the literature. It should be noted that this research did not account for the effects of lithology and cementation on velocities.

Velocity ratios (V_p/V_s) in K_0-consolidated specimens were shown to have a considerable decreasing trend (6 to 2.5) with vertical effective stress (1-25 MPa) and can be represented by a logarithmic equation. The velocity ratios as a function of stress in RGoM-EI have roughly the same trend in both vertical and horizontal directions, which is caused by the material's weak elastic anisotropy. The vertical velocity ratios are lower in RBBC compared to RGoM-EI and decrease with a smaller slope (logarithmic scale). The materials tested in this study have much higher velocity ratios compared to results on rocks ($V_p/V_s<3$). Due to the higher levels of porosity, a larger portion of the soil structure in the resedimented materials is occupied by pore fluid rather than clay particles, resulting in higher P-wave velocities and lower S-wave velocities.

Thomsen's method can theoretically be used to calculate the stiffness matrix for a TI material at a certain stress level, using the five velocities (measured vertical and horizontal P, measured vertical and horizontal S, phase inclined P velocity) and the inclined angle. The inverse of the stiffness matrix is the compliance matrix, using the elements of which the elastic moduli and the Poisson's ratio can be determined. However, the accuracy of the results, depends on element C_{13}, the only element in the stiffness matrix that includes the effect of the inclined velocity and angle. It was shown that the Poisson's ratio is extremely sensitive even to the smallest changes in C_{13}. An inaccurate C_{13} introduces significant errors and scatter in Poisson's ratio and Young's modulus calculations. This sensitivity is exacerbated at lower stress levels, when the velocity ratios are high. The inclined velocity and angle range that would yield reasonable stiffness values is extremely narrow at higher velocity ratios. This suggests that the matrix method is greatly sensitive to the velocity ratios and can produce inaccurate results with the slightest inclined velocity error.

Constrained modulus and shear moduli are calculated in exactly the same way, whether they are being determined using the stiffness matrix elements (anisotropic elasticity) or directly from the velocity measurements (isotropic elasticity). Both

methods use the P and S velocities in each direction and the bulk density to calculate the constrained and shear modului respectively. The constrained modulus is higher in the horizontal direction, since the horizontal P-wave velocity is higher. Both constrained moduli (vertical and horizontal) nearly double as a result of 9 MPa increase in the vertical effective stress (1-10 MPa) following roughly the same linear trend. Since the S-wave velocities are virtually the same in both directions, so are the shear moduli, varying between 0.5 and 3.5 GPa. Although scattered, the TI young's moduli calculations suggest a seven times increase in E as a result of the vertical effective stress increase (1 MPa to 9 MPa).

The stiffness matrix elements were used to calculate Thomsen's anisotropy parameters (ϵ, γ and δ) for K_0-consolidated RGoM-EI. There is a slight increase in compressional (ϵ) anisotropy parameter (0.05-0.07) with a 9 MPa increase in the vertical effective stress, whereas the shear (γ) anisotropy parameter decreases (0.03-0.01) in the same stress span. The compressional and shear anisotropy parameters are both lower than 0.1, putting RGoM-EI in the the weak elastic anisotropy category based on Thomsen's definition. This characteristic becomes obvious when the ϵ and γ of RGoM-EI are compared to those of a variety of other materials. The weak anisotropy of RGoM-EI is mainly caused by higher porosity in RGoM-EI, which means more pore fluid, an anisotropic material, dominating the material behavior. Lastly, the delta parameter (δ) captures the position of C_{13} relative to the compressional (C_{11} and C_{33}) and shear (C_{44} and C_{66}) elements. Velocity ratio and C_{13} are directly corelated to the δ parameter. RGoM-EI has high velocity ratios and high C_{13}, resulting in higher δ values compared to other materials at the same level of anisotropy (comparable ϵ). While the current testing technology introduces a promising method to test soft materials for anisotropy, an improved stiffness matrix calculation model can improve the calculated C_{13} and the accuracy of Thomsen's parameters.

7.3 Recommendations for Future Work

- There is room for improving the velocity measurement setup to better the quality of the signals by reducing the noise levels. Also eliminating the initial high amplitude interference signal would significantly improve the inclined and horizontal P-wave velocity measurements, and every other parameter calculated based on those.

- New post processing methods can be tried on the collected signals to potentially eliminate the noise in the vertical S-waveform and the initial high amplitude interference signal in the P-waveforms.

- The effect of water on the measured P-wave velocities is potentially distorting our understanding of P-wave velocity, velocity ratio and velocity anisotropy. A deeper look into theoretical methods of eliminating the effect of water from the material stiffness and velocities through clays could certainly be beneficial. Moreover, a revised stiffness matrix calculation model could decrease the velocity ration sensitivity.

- The TCRS setup can be used to test specimens under up to 50 MPa of vertical effective stress. Increasing the highest stress level from 25 MPa to 50 MPa would close the porosity gap (0.10-0.25) between the soft and hard clays even further.

- The new directional velocity technology can explore the elastic properties for all sorts of conditions, including undrained shearing, unloading, secondary compression and loading paths other than K_0.

- Cementation might be an important factor dictating the material anisotropy. This can be studied by testing intact and resedimented specimens (of the same source) and comparing the velocities and the anisotropy parameters. Also, of all the materials generally tested for GeoFluids, only the GoM-EI was tested for anisotropy. There is benefit in testing other materials.

- A good portion of the velocity testing procedure is currently performed in person. An automated system recording signals at certain time or stress intervals without physical human interference can increase the data resolution significantly.

- An internal strain measurement technology can be attached to the specimen and used to measure directional strains. Combined with the stress measurements, these strains can be used to calculate the elastic moduli, as well as to further confirm the zero lateral strain condition during K_0-consolidation.

Bibliography

[1] N Abdulhadi and A Barghouthi, *Measurement of stiffness of rock from laboratory and field tests*, in Proceedings of the 5th Jordanian international civil engineering conference, 2012.

[2] Naeem Omar Abdulhadi, *An experimental investigation into the stress-dependent mechanical behavior of cohesive soil with application to wellbore instability*, PhD thesis, Massachusetts Institute of Technology, 2009.

[3] Ludmila Adam, Kasper van Wijk, Thomas Otheim, and Michael Batzle, *Changes in elastic wave velocity and rock microstructure due to basalt-co2-water reactions*, Journal of Geophysical Research: Solid Earth, 118 (2013), pp. 4039–4047.

[4] Amy Lynn Adams, *Permeability anisotropy and resistivity anisotropy of mechanically compressed mudrocks*, PhD thesis, Massachusetts Institute of Technology, 2014.

[5] Tarun K Agarwal and Isao Ishibashi, *Multi-directional wave velocity by piezoelectric crystals*, in Recent Advances in Instrumentation, Data Acquisition and Testing in Soil Dynamics, ASCE, 1991, pp. 102–117.

[6] Awad A Al-Karni and Mosleh A Al-Shamrani, *Study of the effect of soil anisotropy on slope stability using method of slices*, Computers and Geotechnics, 26 (2000), pp. 83–103.

[7] Sara Amoroso, P Monaco, BM Lehane, and D Marchetti, *Examination of the potential of the seismic dilatometer (sdmt) to estimate in-situ stiffness decay curves in various soil types*, Soils and Rocks, 37 (2014), pp. 177–194.

[8] Glen Robert Andersen, *Physical mechanisms controlling the strength and deformation behavior of frozen sand*, PhD thesis, Massachusetts Institute of Technology, 1991.

[9] RD Andrus, Jianping Zhang, BS Ellis, and CH Juang, *Guide for estimating the dynamic properties of south carolina soils for ground response analysis*, tech. report, 2003.

[10] JH Atkinson and G Sallfors, *Experimental determination of soil properties. general report to session 1*, in Proc. 10th ECSMFE, Florence, vol. 3, 1991, pp. 915–956.

[11] A Ayres and F Theilen, *Relationship between seismic velocities and geological and geotechnical properties of near surface marine sediments of the continental slope of the barents sea*, Geophysical Prospecting, 47 (1999), pp. 431–441.

[12] William Anthony Bailey, *The effects of salt on the shear strength of Boston blue clay*, PhD thesis, Massachusetts Institute of Technology, 1961.

[13] Laing Barden, *The influence of structure on deformation and failure in clay soil*, Geotechnique, 22 (1972), pp. 159–163.

[14] Laing Barden and Geoffrey R Sides, *Engineering behavior and structure of compacted clay*, Journal of Soil Mechanics & Foundations Div, (1970).

[15] M Batzle, Ronny Hofmann, Manika Prasad, Gautam Kumar, L Duranti, and De-hua Han, *Seismic attenuation: Observations and mechanisms*, in SEG Technical Program Expanded Abstracts 2005, Society of Exploration Geophysicists, 2005, pp. 1565–1568.

[16] Debra Robin Berman, John T Germaine, and Charles Cushing Ladd, *Characterization of the engineering properties of boston blue clay at the mit campus*, master's thesis, Massachusetts Institute of Technology, Dept. of Civil and Environmental ..., 1993.

[17] WS Betts, *Compression and permeability behavior of Gulf of Mexico Mudrocks, resedimented and in-situ*, PhD thesis, MS thesis, Univ. of Texas at Austin, Austin, TX, 2014.

[18] Maurice Anthony Biot, *Thermoelasticity and irreversible thermodynamics*, Journal of Applied Physics, 27 (1956), pp. 240–253.

[19] J Blewett, IJ Blewett, and PK Woodward, *Phase and amplitude responses associated with the measurement of shear-wave velocity in sand by bender elements*, Canadian Geotechnical Journal, 37 (2000), pp. 1348–1357.

[20] Glenn L Bowers et al., *Pore pressure estimation from velocity data: Accounting for overpressure mechanisms besides undercompaction*, SPE Drilling & Completion, 10 (1995), pp. 89–95.

[21] Enrico GM Brignoli, Marino Gotti, and Kenneth H Stokoe, *Measurement of shear waves in laboratory specimens by means of piezoelectric transducers*, Geotechnical Testing Journal, 19 (1996), pp. 384–397.

[22] AP Butcher and JJM Powell, *Practical considerations for field geophysical techniques used to assess ground stiffness*, in ADVANCES IN SITE INVESTIGATION PRACTICE. PROCEEDINGS OF THE INTERNATIONAL CONFERENCE HELD IN LONDON ON 30-31 MARCH 1995, 1996.

[23] Bok S Byun, *Seismic parameters for transversely isotropic media*, Geophysics, 49 (1984), pp. 1908–1914.

[24] Brendan Casey and John T Germaine, *An evaluation of three triaxial systems with results from 0.1 to 100 mpa*, Geotechnical Testing Journal, 37 (2014), pp. 1068–1074.

[25] Brendan Brendan Anthony Casey, *The significance of specimen end restraint in high pressure triaxial testing of cohesive soil*, PhD thesis, Massachusetts Institute of Technology, 2011.

[26] ——, *The consolidation and strength behavior of mechanically compressed fine-grained sediments*, PhD thesis, Massachusetts Institute of Technology, 2014.

[27] JP Castagna, ML Batzle, TK Kan, and MM Backus, *Rock physics—the link between rock properties and avo response*, Offset-dependent reflectivity—Theory and practice of AVO analysis: SEG, 8 (1993), pp. 135–171.

[28] John P Castagna and Milo M Backus, *Offset-dependent reflectivity—Theory and practice of AVO analysis*, Society of Exploration Geophysicists, 1993.

[29] John P Castagna, Michael L Batzle, and Raymond L Eastwood, *Relationships between compressional-wave and shear-wave velocities in clastic silicate rocks*, geophysics, 50 (1985), pp. 571–581.

[30] Douglas Frederick Cauble, *An experimental investigation of the behavior of a model suction caisson in a cohesive soil.*, (1998).

[31] CRI Clayton, *Stiffness at small strain: research and practice*, Géotechnique, 61 (2011), pp. 5–37.

[32] Patrick F Daley and F Hron, *Reflection and transmission coefficients for transversely isotropic media*, Bulletin of the seismological society of America, 67 (1977), pp. 661–675.

[33] M Darot and T Reuschlé, *Acoustic wave velocity and permeability evolution during pressure cycles on a thermally cracked granite*, International Journal of Rock Mechanics and Mining Sciences, 37 (2000), pp. 1019–1026.

[34] Ruarri J Day-Stirrat, Anja M Schleicher, Julia Schneider, Peter B Flemings, John T Germaine, and Ben A van der Pluijm, *Preferred orientation of phyllosilicates: Effects of composition and stress on resedimented mudstone microfabrics*, Journal of Structural Geology, 33 (2011), pp. 1347–1358.

[35] Pierre Delage and Guy Lefebvre, *Study of the structure of a sensitive champlain clay and of its evolution during consolidation*, Canadian Geotechnical Journal, 21 (1984), pp. 21–35.

[36] Joseph J Durek and Göran Ekström, *A radial model of anelasticity consistent with long-period surface-wave attenuation*, Bulletin of the Seismological Society of America, 86 (1996), pp. 144–158.

[37] Tanima Dutta, Gary Mavko, Tapan Mukerji, and Tim Lane, *Compaction trends for shale and clean sandstone in shallow sediments, gulf of mexico*, The Leading Edge, 28 (2009), pp. 590–596.

[38] Jack Dvorkin, Gary Mavko, and Amos Nur, *Squirt flow in fully saturated rocks*, Geophysics, 60 (1995), pp. 97–107.

[39] D Eberhart-Phillips, DH Han, and MD Zoback, *Empirical relationships among seismic velocity, effective pressure, porosity, and clay content in sandstone*, Geophysics, 54 (1989), pp. 82–89.

[40] EA Ellis, K Soga, MF Bransby, and M Sato, *Resonant column testing of sands with different viscosity pore fluids*, Journal of geotechnical and geoenvironmental engineering, 126 (2000), pp. 10–17.

[41] Wolf von Engelhardt and Karl H Gaida, *Concentration changes of pore solutions during compaction of clay sediments*, Journal of Sedimentary Research, 33 (1963), pp. 919–930.

[42] Brian Patrick Fahy, *The influence of salinity on the mechanical behavior of high plasticity soils*, PhD thesis, Massachusetts Institute of Technology, 2014.

[43] Manzar Fawad, Nazmul Haque Mondol, Jens Jahren, and Knut Bjørlykke, *Mechanical compaction and ultrasonic velocity of sands with different texture and mineralogical composition*, Geophysical Prospecting, 59 (2011), pp. 697–720.

[44] Vincenzo Fioravante, *Anisotropy of small strain stiffness of ticino and kenya sands from seismic wave propagation measured in triaxial testing*, Soils and foundations, 40 (2000), pp. 129–142.

[45] Vincenzo Fioravante, Daniela Giretti, and M Jamiolkowski, *Small strain stiffness of carbonate kenya sand*, Engineering geology, 161 (2013), pp. 65–80.

[46] Peter B Flemings, Beth B Stump, Thomas Finkbeiner, and Mark Zoback, *Flow focusing in overpressured sandstones: Theory, observations, and applications*, American Journal of Science, 302 (2002), pp. 827–855.

[47] GHF Gardner, LW Gardner, and AR Gregory, *Formation velocity and density—the diagnostic basics for stratigraphic traps*, Geophysics, 39 (1974), pp. 770–780.

[48] GHF Gardner, MH Harris, et al., *Velocity and attenuation of elastic waves in sands*, in SPWLA 9th Annual Logging Symposium, Society of Petrophysicists and Well-Log Analysts, 1968.

[49] GHF Gardner, MRJ Wyllie, DMi Droschak, et al., *Effects of pressure and fluid saturation on the attenuation of elastic waves in sands*, Journal of Petroleum Technology, 16 (1964), pp. 189–198.

[50] Fritz Gassmann, *Elastic waves through a packing of spheres*, Geophysics, 16 (1951), pp. 673–685.

[51] Rajeeb Gautam and Ron CK Wong, *Transversely isotropic stiffness parameters and their measurement in colorado shale*, Canadian Geotechnical Journal, 43 (2006), pp. 1290–1305.

[52] John T Germaine, *Development of the directional shear cell for measuring cross-anisotropic clay properties*, ScD Thesis, Massachusetts Inst. of Tech., (1982).

[53] Jorge Hugo González, *Experimental and theoretical investigation of constant rate of strain consolidation*, PhD thesis, Massachusetts Institute of Technology, 2000.

[54] ML Greenberg and JP Castagna, *Shear-wave velocity estimation in porous rocks: theoretical formulation, preliminary verification and applications1*, Geophysical prospecting, 40 (1992), pp. 195–209.

[55] Fred J Griffiths and Ramesh C Joshi, *Clay fabric response to consolidation*, Applied clay science, 5 (1990), pp. 37–66.

[56] De-hua Han, Amos Nur, and Dale Morgan, *Effects of porosity and clay content on wave velocities in sandstones*, Geophysics, 51 (1986), pp. 2093–2107.

[57] BO Hardin, *Anisotropic shear modulus due to stress anisotropy*, JOURNAL OF THE GEOTECHNICAL ENGINEERING DIVISION-ASCE, 106 (1980), pp. 956–958.

[58] Bobby O Hardin, *The nature of stress-strain behavior for soils*, in From Volume I of Earthquake Engineering and Soil Dynamics–Proceedings of the ASCE Geotechnical Engineering Division Specialty Conference, June 19-21, 1978, Pasadena, California. Sponsored by Geotechnical Engineering Division of ASCE in cooperation with:, no. Proceeding, 1978.

[59] Bobby O Hardin and George E Blandford, *Elasticity of particulate materials*, Journal of Geotechnical Engineering, 115 (1989), pp. 788–805.

[60] Wei He, David Williams, and Ali Shokouhi, *Numerical study of slurry consolidometer tests taking into account the influence of wall friction*, Computers and Geotechnics, 91 (2017), pp. 39–47.

[61] Klaus Helbig, *Elliptical anisotropy—its significance and meaning*, Geophysics, 48 (1983), pp. 825–832.

[62] Phil Heppard and Dan Ebrom, *Compaction and overpressure in shales: Practice and theory*, (2010).

[63] Pierre Yves Hicher, H Wahyudi, and Dominique Tessier, *Microstructural analysis of inherent and induced anisotropy in clay*, Mechanics of Cohesive-frictional Materials: An International Journal on Experiments, Modelling and Computation of Materials and Structures, 5 (2000), pp. 341–371.

[64] Aiden James Horan, *The mechanical behavior of normally consolidated soils as a function of pore fluid salinity*, PhD thesis, Massachusetts Institute of Technology, 2012.

[65] Ian W Horn, *Some laboratory experiments on shear wave propagation in unconsolidated sands*, Marine Georesources & Geotechnology, 4 (1980), pp. 31–54.

[66] Brian E Hornby, *Experimental laboratory determination of the dynamic elastic properties of wet, drained shales*, Journal of Geophysical Research: Solid Earth, 103 (1998), pp. 29945–29964.

[67] SA Horne, *A statistical review of mudrock elastic anisotropy*, Geophysical Prospecting, 61 (2013), pp. 817–826.

[68] Robert Donald House, *A comparison of the behavior of intact and resedimented Boston Blue Clay (BBC)*, PhD thesis, Massachusetts Institute of Technology, 2012.

[69] Jens M Hovem, *Acoustic waves in finely layered media*, Geophysics, 60 (1995), pp. 1217–1221.

[70] http://www-udc.ig.utexas.edu/geofluids/.

[71] DS Hughes, WL Pondrom, and RL Mims, *Transmission of elastic pulses in metal rods*, Physical Review, 75 (1949), p. 1552.

[72] Darrell Stephen Hughes and J Harvey Cross, *Elastic wave velocities in rocks at high pressures and temperatures*, Geophysics, 16 (1951), pp. 577–593.

[73] William M Isenhower, Kenneth H Stokoe, and Jimmy C Allen, *Instrumentation for torsional shear/resonant column measurements under anisotropic stresses*, Geotechnical Testing Journal, 10 (1987), pp. 183–191.

[74] DR Issler, *A new approach to shale compaction and stratigraphic restoration, beaufort-mackenzie basin and mackenzie corridor, northern canada (1)*, AAPG bulletin, 76 (1992), pp. 1170–1189.

[75] Toshio Iwasaki, Fumio Tatsuoka, and Yoshikazu Takagi, *Shear moduli of sands under cyclic torsional shear loading*, Soils and Foundations, 18 (1978), pp. 39–56.

[76] M Jamiolkowski, R Lancellotta, and DCF Lo Presti, *Remarks on the stiffness at small strains of six italian clays*, Pre-failure deformation of geomaterials, 2 (1995), pp. 817–836.

[77] David Hervey Johnston, MN Toksöz, and A Timur, *Attenuation of seismic waves in dry and saturated rocks: Ii. mechanisms*, Geophysics, 44 (1979), pp. 691–711.

[78] JE Johnston and NI Christensen, *Compressional to shear velocity ratios in sedimentary rocks*, in International journal of rock mechanics and mining sciences & geomechanics abstracts, vol. 30, Elsevier, 1993, pp. 751–754.

[79] Joel E Johnston and Nikolas I Christensen, *Seismic anisotropy of shales*, Journal of Geophysical Research: Solid Earth, 100 (1995), pp. 5991–6003.

[80] Leonie EA Jones and Herbert F Wang, *Ultrasonic velocities in cretaceous shales from the williston basin*, Geophysics, 46 (1981), pp. 288–297.

[81] Vojkan Jovičić and MR Coop, *Stiffness of coarse-grained soils at small strains*, Géotechnique, 47 (1997), pp. 545–561.

[82] Vojkan Jovičić and MP Coop, *The measurement of stiffness anisotropy in clays with bender element tests in the triaxial apparatus*, Geotechnical Testing Journal, 21 (1998), pp. 3–10.

[83] Xin Kang, Bate Bate, and Louis Ge, *Characterization of shear wave velocity and its anisotropy in uniform granular materials*, in Geo-Congress 2014: Geo-characterization and Modeling for Sustainability, 2014, pp. 2029–2041.

[84] X Kang, G-C Kang, and B Bate, *Measurement of stiffness anisotropy in kaolinite using bender element tests in a floating wall consolidometer*, Geotechnical Testing Journal, 37 (2014), pp. 869–883.

[85] TC Kenney, *Sea-level movements and the geologic histories of the post-glacial marine soils at boston, nicolet, ottawa and oslo*, Geotechnique, 14 (1964), pp. 203–230.

[86] Dong-Soo Kim, Kenneth H Stokoe, and JM Roesset, *Characterization of material damping of soils using resonant column and torsional shear tests*, Unknown Journal, (1991), pp. 189–200.

[87] Th Krey and K Helbig, *A theorem concerning anisotropy of stratified media and its significance for reflection seismics*, Geophysical Prospecting, 4 (1956), pp. 294–302.

[88] Charles Ladd and Lucy C. Jen, *Advanced soil mechanics*, 1996.

[89] T William Lambe, *The engineering behavior of compacted clay*, Journal of the Soil Mechanics and Foundations Division, 84 (1958), pp. 1–35.

[90] T William Lambe and Robert V Whitman, *Soil mechanics, 553 pp*, 1969.

[91] Melissa M Landon, Don J DeGroot, and Thomas C Sheahan, *Nondestructive sample quality assessment of a soft clay using shear wave velocity*, Journal of geotechnical and geoenvironmental engineering, 133 (2007), pp. 424–432.

[92] Frederick V Lawrence Jr, *Ultrasonic shear wave velocities in sand and clay*, tech. report, MASSACHUSETTS INST OF TECH CAMBRIDGE DEPT OF CIVIL ENGINEERING, 1965.

[93] E Cahyandy Leong, J Cahyadi, and Harianto Rahardjo, *Measuring shear and compression wave velocities of soil using bender–extender elements*, Canadian geotechnical journal, 46 (2009), pp. 792–812.

[94] Franklyn K Levin, *The reflection, refraction, and diffraction of waves in media with an elliptical velocity dependence*, Geophysics, 43 (1978), pp. 528–537.

[95] Marshall Lew and Kenneth W Campbell, *Relationships between shear wave velocity and depth of overburden*, in Measurement and use of shear wave velocity for evaluating dynamic soil properties, ASCE, 1985, pp. 63–76.

[96] Suched Likitlersuang, Supot Teachavorasinskun, Chanaton Surarak, Erwin Oh, and Arumugam Balasubramaniam, *Small strain stiffness and stiffness degradation curve of bangkok clays*, Soils and Foundations, 53 (2013), pp. 498–509.

[97] ML Lings, DS Pennington, and DFT Nash, *Anisotropic stiffness parameters and their measurement in a stiff natural clay*, Géotechnique, 50 (2000), pp. 109–125.

[98] Van LR Loon et al., *Preferred orientations and anisotropy in shales: Callovo-oxfordian shale (france) and opalinus clay (switzerland)*, Clays and clay minerals, 56 (2008), pp. 285–306.

[99] Julie Lovisa and Nagaratnam Sivakugan, *Tall oedometer testing: method to account for wall friction*, International Journal of Geomechanics, 15 (2015), p. 04014045.

[100] Claudio Mancuso, Roberto Vassallo, and Anna d'Onofrio, *Small strain behavior of a silty sand in controlled-suction resonant column torsional shear tests*, Canadian Geotechnical Journal, 39 (2002), pp. 22–31.

[101] Silvano Marchetti, Paola Monaco, Gianfranco Totani, and Diego Marchetti, *In situ tests by seismic dilatometer (sdmt)*, in From research to practice in geotechnical engineering, 2008, pp. 292–311.

[102] Hendrikus Marcus, *The permeability of a sample of an anisotropic porous medium*, Journal of Geophysical Research, 67 (1962), pp. 5215–5225.

[103] Jana Marjanovic, *Stiffness characterization of mechanically-compressed cohesive soils using wave propagation*, PhD thesis, Massachusetts Institute of Technology, 2016.

[104] Jana Marjanovic and John T Germaine, *Experimental study investigating the effects of setup conditions on bender element velocity results*, Geotechnical Testing Journal, 36 (2013), pp. 187–197.

[105] R Torrence Martin and Charles C Ladd, *Fabric of consolidated kaolinite*, Clays and Clay Minerals, 23 (1975), pp. 17–25.

[106] David Mašín and Josef Rott, *Small strain stiffness anisotropy of natural sedimentary clays: review and a model*, Acta Geotechnica, 9 (2014), pp. 299–312.

[107] Gerald Mavko and Amos Nur, *Melt squirt in the asthenosphere*, Journal of Geophysical Research, 80 (1975), pp. 1444–1448.

[108] Paul W Mayne, *Stress anisotropy effects on clay strength*, Journal of Geotechnical Engineering, 111 (1985), pp. 356–366.

[109] Gholamreza Mesri and Roy E Olson, *Mechanisms controlling the permeability of clays*, Clays and Clay minerals, 19 (1971), pp. 151–158.

[110] James Kenneth Mitchell, *The importance of structure to the engineering behavior of clay*, PhD thesis, Massachusetts Institute of Technology. Department of Civil Engineering, 1956.

[111] Nazmul H Mondol, Knut Bjørlykke, Jens Jahren, and Kaare Høeg, *Experimental mechanical compaction of clay mineral aggregates—changes in physical properties of mudstones during burial*, Marine and Petroleum Geology, 24 (2007), pp. 289–311.

[112] Nazmul Haque Mondol, Jens Jahren, Knut Bjørlykke, and Ivar Brevik, *Elastic properties of clay minerals*, The Leading Edge, 27 (2008), pp. 758–770.

[113] Sung-Woo Moon and Taeseo Ku, *Development of global correlation models between in-situ stress-normalized shear wave velocity and soil unit weight for plastic soils*, Canadian Geotechnical Journal, 53 (2016), pp. 1600–1611.

[114] Tanaka Mori and K Tanaka, *Average stress in matrix and average elastic energy of materials with misfitting inclusions*, Acta metallurgica, 21 (1973), pp. 571–574.

[115] Tobias M Müller, Boris Gurevich, and Maxim Lebedev, *Seismic wave attenuation and dispersion resulting from wave-induced flow in porous rocks—a review*, Geophysics, 75 (2010), pp. 75A147–75A164.

[116] Kurt T Nihei, Seiji Nakagawa, Frederic Reverdy, Larry R Myer, Luca Duranti, and Greg Ball, *Phased array compaction cell for measurement of the transversely isotropic elastic properties of compacting sediments*, Geophysics, 76 (2011), pp. WA113–WA123.

[117] Taylor James Nordquist, *Permeability anisotropy of resedimented mudrocks*, PhD thesis, Massachusetts Institute of Technology, 2015.

[118] NEAL R O'BRIEN, *Origin of pennsylvanian underclays in the illinois basin*, Geological Society of America Bulletin, 75 (1964), pp. 823–832.

[119] Richard J O'Connell and Bernard Budiansky, *Viscoelastic properties of fluid-saturated cracked solids*, Journal of Geophysical Research, 82 (1977), pp. 5719–5735.

[120] Harold W Olsen, *Hydraulic flow through saturated clays*, Clays and Clay Minerals, 9 (1960), pp. 131–161.

[121] Amanda Renee Parry, *The Effect of Temperature and Variation of Salinity during One Dimensional Compression*, PhD thesis, Tufts University, 2018.

[122] C Pastén, M Sáez, S Ruiz, F Leyton, J Salomón, and P Poli, *Deep characterization of the santiago basin using hvsr and cross-correlation of ambient seismic noise*, Engineering Geology, 201 (2016), pp. 57–66.

[123] Frederic L Pellet and Geraldine Fabre, *Damage evaluation with p-wave velocity measurements during uniaxial compression tests on argillaceous rocks*, International journal of geomechanics, 7 (2007), pp. 431–436.

[124] C Delle Piane, DN Dewhurst, AF Siggins, and MD Raven, *Stress-induced anisotropy in brine saturated shale*, Geophysical Journal International, 184 (2011), pp. 897–906.

[125] George R Pickett et al., *Acoustic character logs and their applications in formation evaluation*, Journal of Petroleum technology, 15 (1963), pp. 659–667.

[126] AL Podio, AR Gregory, KE Gray, et al., *Dynamic properties of dry and water-saturated green river shale under stress*, Society of Petroleum Engineers Journal, 8 (1968), pp. 389–404.

[127] GW Postma, *Wave propagation in a stratified medium*, Geophysics, 20 (1955), pp. 780–806.

[128] J Gl Potyondy, *Skin friction between various soils and construction materials*, Geotechnique, 11 (1961), pp. 339–353.

[129] Manika Prasad, *Acoustic measurements in unconsolidated sands at low effective pressure and overpressure detection*, Geophysics, 67 (2002), pp. 405–412.

[130] RM Quigley, *The engineering properties of illite related to fabric and pore water composition*, Crawford, CB; Hamilton, JJ, 12 (1962), p. 5.

[131] RM Quigley and CD Thompson, *The fabric of anisotropically consolidated sensitive marine clay*, Canadian Geotechnical Journal, 3 (1966), pp. 61–73.

[132] S Rampello, GMB Viggiani, and A Amorosi, *Small-strain stiffness of reconstituted clay compressed along constant triaxial effective stress ratio paths*, Géotechnique, 47 (1997), pp. 475–489.

[133] Michael D Richardson, Enrico Muzi, Luigi Troiano, and Bruno Miaschi, *Sediment shear waves: A comparison of in-situ and laboratory measurements*, in Microstructure of Fine-Grained Sediments, Springer, 1991, pp. 403–415.

[134] Stephan K Roesler, *Anisotropic shear modulus due to stress anisotropy*, Journal of the Geotechnical Engineering Division, 105 (1979), pp. 871–880.

[135] Marika Santagata, John T Germaine, and Charles C Ladd, *Factors affecting the initial stiffness of cohesive soils*, Journal of Geotechnical and Geoenvironmental Engineering, 131 (2005), pp. 430–441.

[136] Maria Caterina Santagata, *Factors affecting the initial stiffness and stiffness degradation of cohesive soils*, PhD thesis, Massachusetts Institute of Technology, 1999.

[137] Joël Sarout, Laurent Molez, Yves Guéguen, and Nasser Hoteit, *Shale dynamic properties and anisotropy under triaxial loading: Experimental and theoretical investigations*, Physics and Chemistry of the Earth, Parts A/B/C, 32 (2007), pp. 896–906.

[138] Wojciech Sas and Katarzyna Gabryś, *Laboratory measurement of shear stiffness in resonant column apparatus*, ACTA Scientiarium Polonorum, series Architectura, 11 (2012), pp. 29–39.

[139] Auckpath Sawangsuriya, Peter J Bosscher, and Tuncer B Edil, *Laboratory evaluation of the soil stiffness gauge*, Transportation research record, 1808 (2002), pp. 30–37.

[140] Colin M Sayers and Lennert D den Boer, *Velocity-density relations for deepwater subsalt gulf of mexico shales*, in SEG Technical Program Expanded Abstracts 2011, Society of Exploration Geophysicists, 2011, pp. 2302–2307.

[141] Tian Ho Seah, *Anisotropy of resedimented Boston blue clay*, PhD thesis, Massachusetts Institute of Technology, 1990.

[142] SA Shapiro and G1 Kneib, *Seismic attenuation by scattering: theory and numerical results*, Geophysical Journal International, 114 (1993), pp. 373–391.

[143] Dorothy Sheahan, *The Social Origins of American Nursing and Its Movement into the University*, PhD thesis, PhD. dissertation, New York University, AM Arbor: UMI Dis-sertation ..., 1991.

[144] Peter M Shearer, *Introduction to seismology*, Cambridge university press, 2019.

[145] Robert E Sheriff, *Encyclopedic dictionary of applied geophysics*, Society of exploration geophysicists, 2002.

[146] S Shibuya, SC Hwang, and T Mitachi, *Elastic shear modulus of soft clays from shear wave velocity measurement*, Geotechnique, 47 (1997), pp. 593–601.

[147] Donald J Shirley and Aubrey L Anderson, *In situ measurement of marine sediment acoustical properties during coring in deep water*, IEEE Transactions on Geoscience Electronics, 13 (1975), pp. 163–169.

[148] Donald J Shirley and Loyd D Hampton, *Shear-wave measurements in laboratory sediments*, The Journal of the Acoustical Society of America, 63 (1978), pp. 607–613.

[149] Ronald E Smith and Harvey E Wahls, *Consolidation under constant rates of strain*, Journal of Soil Mechanics & Foundations Div, (1969).

[150] Carl H Sondergeld, *The rock physics handbook: Tools for seismic analysis of porous media, gary mavko, tapan mukerji, jack dvorkin, springer (2010), $84 (us),£ 48 (uk). isbn-13: 9780521861366*, 2011.

[151] Hartmut Spetzler and Don L Anderson, *The effect of temperature and partial melting on velocity and attenuation in a simple binary system*, Journal of Geophysical Research, 73 (1968), pp. 6051–6060.

[152] Seth Stein and Michael Wysession, *An introduction to seismology, earthquakes, and earth structure*, John Wiley & Sons, 2009.

[153] KH STOKOE II, SK Hwang, JN-K Lee, and Ronald D Andrus, *Effects of various parameters on the stiffness and damping of soils at small to medium strains*, in PRE-FAILURE DEFORMATION OF GEOMATERIALS. PROCEEDINGS OF THE INTERNATIONAL SYMPOSIUM, 12-14 SEPTEMBER 1994, SAPPORO, JAPAN. 2 VOLS, 1995.

[154] Robert D Stoll and George M Bryan, *Wave attenuation in saturated sediments*, The journal of the acoustical society of America, 47 (1970), pp. 1440–1447.

[155] Robert H Tatham, *V p/v s and lithology*, Geophysics, 47 (1982), pp. 336–344.

[156] Supot Teachavorasinskun, Hiroyuki Kato, Satoru Shibuya, Noriyuki Horii, and Fumio Tatsuoka, *Stiffness and damping of sands in torsion shear*, (1991).

[157] Fu-Chen Teng, Chang-Yu Ou, and Pio-Go Hsieh, *Measurements and numerical simulations of inherent stiffness anisotropy in soft taipei clay*, Journal of Geotechnical and Geoenvironmental Engineering, 140 (2014), pp. 237–250.

[158] Leon Thomsen, *Weak elastic anisotropy*, Geophysics, 51 (1986), pp. 1954–1966.

[159] MN Toksöz, David H Johnston, and Aytekin Timur, *Attenuation of seismic waves in dry and saturated rocks: I. laboratory measurements*, Geophysics, 44 (1979), pp. 681–690.

[160] Carol Tosaya and Amos Nur, *Effects of diagenesis and clays on compressional velocities in rocks*, Geophysical Research Letters, 9 (1982), pp. 5–8.

[161] Christophe Tournassat, Ian C Bourg, Carl I Steefel, and Faïza Bergaya, *Surface properties of clay minerals*, in Developments in clay science, vol. 6, Elsevier, 2015, pp. 5–31.

[162] Celestino Valle-Molina, *Measurements of Vp and Vs in dry, unsaturated and saturated sand specimens with piezoelectric transducers*, PhD thesis, The University of Texas at Austin, 2006.

[163] Paul J Vardanega and Malcolm D Bolton, *Stiffness of clays and silts: Normalizing shear modulus and shear strain*, Journal of Geotechnical and Geoenvironmental Engineering, 139 (2013), pp. 1575–1589.

[164] L Vernik, *Predicting lithology and transport properties from acoustic velocities based on petrophysical classification of siliciclastics*, Geophysics, 59 (1994), pp. 420–427.

[165] Lev Vernik, *Predicting porosity from acoustic velocities in siliciclastics: A new look*, Geophysics, 62 (1997), pp. 118–128.

[166] L Vernik, D Fisher, and S Bahret, *Estimation of net-to-gross from p and s impedance in deepwater turbidites*, The Leading Edge, 21 (2002), pp. 380–387.

[167] Lev Vernik and Xingzhou Liu, *Velocity anisotropy in shales: A petrophysical study*, Geophysics, 62 (1997), pp. 521–532.

[168] Lev Vernik and Amos Nur, *Ultrasonic velocity and anisotropy of hydrocarbon source rocks*, Geophysics, 57 (1992), pp. 727–735.

[169] Giulia Viggiani, *Small strain stiffness of fine grained soils*, PhD thesis, City University London, 1992.

[170] JB Walsh, *Seismic wave attenuation in rock due to friction*, Journal of Geophysical Research, 71 (1966), pp. 2591–2599.

[171] ——, *Attenuation in partially melted material*, Journal of Geophysical Research, 73 (1968), pp. 2209–2216.

[172] ——, *New analysis of attenuation in partially melted rock*, Journal of Geophysical Research, 74 (1969), pp. 4333–4337.

[173] Zhijing Wang, *Seismic anisotropy in sedimentary rocks, part 1: A single-plug laboratory method*, Geophysics, 67 (2002), pp. 1415–1422.

[174] JE White, *Computed seismic speeds and attenuation in rocks with partial gas saturation*, Geophysics, 40 (1975), pp. 224–232.

[175] Benjamin E Wickland, G Ward Wilson, and Dharma Wijewickreme, *Hydraulic conductivity and consolidation response of mixtures of mine waste rock and tailings*, Canadian Geotechnical Journal, 47 (2010), pp. 472–485.

[176] Kenneth W Winkler and Amos Nur, *Seismic attenuation: Effects of pore fluids and frictional-sliding*, Geophysics, 47 (1982), pp. 1–15.

[177] AE Wissa, *Consolidation at constant rate of strain*, Journal of Soil Mechanics & Foundations Div, (1971).

[178] RCK Wong, DR Schmitt, D Collis, and R Gautam, *Inherent transversely isotropic elastic parameters of over-consolidated shale measured by ultrasonic waves and their comparison with static and acoustic in-situ log measurements*, Journal of Geophysics and Engineering, 5 (2008), pp. 103–117.

[179] Angelika-M Wulff, Toshiyuki Hashida, Kimio Watanabe, and Hideaki Takahashi, *Attenuation behaviour of tuffaceous sandstone and granite during microfracturing*, Geophysical Journal International, 139 (1999), pp. 395–409.

[180] Malcolm Robert Jesse Wyllie, Alvin Ray Gregory, and Louis Wright Gardner, *Elastic wave velocities in heterogeneous and porous media*, Geophysics, 21 (1956), pp. 41–70.

[181] M Zimmer, *Seismic velocities in unconsolidated sands: Measurements of pressure, sorting, and compaction effects*, Ph. D. thesis, (2003).